Ultrafast lattice dynamics and microscopic energy flow in ferromagnetic metals and in an anisotropic layered semiconductor

Dissertation

zur Erlangung des Grades eines
Doktors der Naturwissenschaften

am Fachbereich Physik
der Freien Universität Berlin

vorgelegt von

Daniela Zahn

Berlin 2022

Abstract

Many properties in solids are determined by interactions between electronic, magnetic, and phononic degrees of freedoms. Ultrafast pump-probe techniques are ideally suited to access these interactions: they allow observing relaxation pathways of laser-excited solids on femtosecond timescales. These pathways are determined by the interplay of different microscopic interactions. In this thesis, femtosecond electron diffraction was employed to access the response of the crystal lattice to laser excitation. Several technologically relevant materials were investigated: the layered semiconductor black phosphorus, the $3d$ ferromagnets cobalt, iron, and nickel, and the $4f$ ferromagnets gadolinium and terbium.

Black phosphorus is a layered van der Waals crystal with a narrow band gap and an extraordinary in-plane anisotropic structure. In this work, the ultrafast structural response of the material to laser excitation was studied, in particular the impact of the in-plane anisotropy. Following laser excitation, electron-phonon coupling leads to a highly nonthermal phonon population, which is characterized by a large occupation of high-energy phonon modes and a transient modification of the anisotropy of the atomic vibrations. On timescales of tens of picoseconds, thermal equilibrium of the lattice is reestablished via phonon-phonon coupling. The results presented in this work provide detailed insights into the nonthermal evolution of the black phosphorus lattice following laser excitation and the underlying coupling mechanisms. In addition, the influence of several experimental parameters on the ultrafast lattice response was investigated to identify pathways to control properties of the transient non-equilibrium state.

The $3d$ ferromagnets iron, cobalt, and nickel exhibit ultrafast demagnetization on timescales of hundreds of femtoseconds following laser excitation [Bea96; Kam02; Koo10]. Here, three subsystems contribute to the observed ultrafast response: electrons, spins, and the lattice. In this work, the microscopic energy flow between these three subsystems was studied quantitatively. Experimental results for the lattice dynamics were combined with density functional theory calculations and several energy flow models. The comparison of the models with the experimental data unambiguously demonstrates the pronounced influence of the spin dynamics on the lattice dynamics: the combination of energy flow into and out of the spin system leads to significant slowing down of the lattice dynamics. This work shows that energy-conserving atomistic spin dynamics simulations offer a quantitative description of the microscopic energy flow in all three elemental $3d$ ferromagnets. Furthermore, transient nonthermal states of the spin system were observed in the simulations, showing that thermal descriptions, e.g. with temperature models, cannot capture the full non-equilibrium dynamics in magnetic materials.

In contrast to the itinerant $3d$ ferromagnets, the dominant contribution to the magnetic moment in gadolinium and terbium, the $4f$ moment, is much more localized. Only a small contribution, the $5d$ moment, is delocalized. This has consequences for the interaction mechanisms of spins with other subsystems and increases the complexity of the laser-induced response. This work provides detailed femtosecond electron diffraction studies on gadolinium and terbium, both in the ferromagnetic and paramagnetic phases. The diffraction experiments were complemented by time-resolved magneto-optical Kerr effect studies on terbium. Several observations that are at odds with a thermal description of the ultrafast dynamics were identified. This work provides the lattice perspective on the ultrafast response of gadolinium and terbium to laser excitation, which constitutes a basis for a full understanding of the complex ultrafast dynamics in $4f$ ferromagnets.

Kurzfassung

Viele Eigenschaften von Festkörpern werden durch Wechselwirkungen zwischen elektronischen, magnetischen und phononischen Freiheitsgraden bestimmt. Ultraschnelle Pump-Probe-Methoden sind ideal dafür geeignet, Zugang zu diesen Wechselwirkungen zu erhalten: Sie erlauben es, den Verlauf der Relaxierung von laserangeregten Festkörpern auf Femtosekundenzeitskalen zu beobachten. Dieser wiederum wird durch das Zusammenwirken verschiedener mikroskopischer Wechselwirkungen bestimmt. In dieser Arbeit wurde Femtosekunden-Eletronenbeugung verwendet, um Zugang zur Reaktion des Kristallgitters auf Laseranregung zu erhalten. Verschiedene technologierelevante Materialien wurden untersucht: der halbleitende Schichtkristall schwarzer Phosphor, die $3d$-Ferromagneten Kobalt, Eisen und Nickel sowie die $4f$-Ferromagneten Gadolinium und Terbium.

Schwarzer Phosphor ist ein Van-der-Waals-Kristall mit einer schmalen Bandlücke und einer speziellen Kristallstruktur, die Anisotropie in den einzelnen Kristallschichten aufweist. In dieser Arbeit wurde die ultraschnelle Reaktion des Kristallgitters auf Laseranregung untersucht, insbesondere die Folgen der Struktur-Anisotropie. Nach Laseranregung führt Elektron-Phonon-Kopplung zu einer nicht-thermischen Phononenbesetzung mit hoher Besetzung von hochenergetischen Phononen und einer Änderung in der Anisotropie der Atombewegungen. Durch Phonon-Phonon-Kopplung wird das thermische Gleichgewicht des Gitters in einigen zehn Pikosekunden wieder hergestellt. Die hier präsentierten Ergebnisse bieten detaillierte Einblicke in die nicht-thermische ultraschnelle Dynamik von schwarzem Phosphor und die zugrunde liegenden Kopplungsmechanismen. Außerdem wurde der Einfluss verschiedener experimenteller Parameter untersucht, um Möglichkeiten der Einflussnahme auf den transienten Nichtgleichgewichtszustands zu finden.

Die $3d$-Ferromagneten Eisen, Kobalt und Nickel zeigen ultraschnelle Entmagnetisierung auf Zeitskalen von Hunderten von Femtosekunden nach Laseranregung [Bea96; Kam02; Koo10]. In diesem Fall tragen drei Subsysteme zur beobachteten ultraschnellen Reaktion bei: Elektronen, Spins und das Kristallgitter. In dieser Arbeit wurde der mikroskopische Energiefluss zwischen diesen drei Subsystemen quantitativ untersucht. Experimentelle Ergebnisse für die Gitterdynamik wurden mit Dichtefunktionaltheorie-Rechnungen und verschiedenen Energieflussmodellen kombiniert. Der Vergleich der Modelle mit den experimentellen Ergebnissen zeigt eindeutig den starken Einfluss der Spindynamik auf die Gitterdynamik: Die Kombination von Energiefluss in das Spinsystem und aus dem Spinsystem heraus führt zu einer deutlichen Verlangsamung der Gitterdynamik. Diese Arbeit zeigt, dass energieerhaltende atomistische Spinsimulationen eine quantitative Beschreibung des mikroskopischen Energieflusses in allen drei $3d$-Ferromagneten bieten. Außerdem wurden in den Simulationen vorübergehende nicht-thermische Zustände des Spinsystems beobachtet. Dies zeigt, dass thermische Beschreibungen (z.B. mit Temperaturmodellen) die Nichtgleichgewichtsdynamik in magnetischen Materialien nicht vollständig erfassen können.

Im Gegensatz zu den hier betrachteten $3d$-Ferromagneten ist der Großteil des magnetischen Moments in Gadolinium und Terbium, das $4f$-Moment, viel lokalisierter. Nur ein kleiner Teil, das $5d$-Moment, ist delokalisiert. Dies hat Konsequenzen für die Wechselwirkungsmechanismen der Spins und erhöht die Komplexität der Reaktion auf Laseranregung. Diese Arbeit stellt detaillierte Ergebnisse der Femtosekunden-Elektronenbeugung sowohl im ferromagnetischen als auch im paramagnetischen Zustand zur Verfügung. Die Beugungsexperimente wurden durch

zeitaufgelöste Messungen des magneto-optischen Kerr-Effekts an Terbium ergänzt. Einige der Beobachtungen passen nicht zu einer thermischen Beschreibung der ultraschnellen Dynamik. Diese Arbeit zeigt die Gitterperspektive der ultraschnellen Reaktion von Gadolinium und Terbium auf Laseranregung, welche als Basis für ein vollständiges Verständnis der komplexen ultraschnellen Dynamik in 4f-Ferromagneten dient.

Contents

Chapter 1

Introduction

1.1 Probing microscopic interactions in the time domain

Many macroscopic properties of solids are determined by the interactions between electronic, magnetic, and lattice degrees of freedom. For example, the electrical conductivity of a material is largely determined by scattering of electrons with phonons. Magnetostrictive effects (dimension changes of a material upon changes in the magnetization) are due to the interactions between magnetic and lattice degrees of freedom. Mott insulators don't conduct electricity due to the interactions between electrons. These are just a few examples of the many cases in which microscopic interactions between different degrees of freedom are decisive for the macroscopic properties of a material, which in turn determine the functionality of any device made thereof. In order to create devices with new functionalities or to improve existing designs, a fundamental understanding of the different microscopic interaction mechanisms is therefore desired. One approach is to infer microscopic interaction mechanisms from measurements of different macroscopic properties. A variety of tuning knobs are available, e.g. temperature or pressure, which help to disentangle contributions of different effects. For example, temperature-dependent measurements of the electrical conductivity allow quantifying the contribution of phonons to the resistance and thus provide insights into electron-phonon coupling. Similarly, thermal conductivity measurements at different temperatures yield insights into phonon-phonon coupling. Another powerful approach to access coupling strengths are linewidth analyses, e.g. in static photoemission data. Since the linewidth of a state depends on its lifetime (among other contributions), it can yield information on its coupling to other degrees of freedom. However, there are limits to measurements in thermal equilibrium. Since many different interactions contribute to the observations, it can be challenging or even impossible to fully disentangle them.

Another approach to disentangle different interactions is to separate them in the time domain, by their interaction strength. This is not possible in thermal equilibrium. However, if the material is suddenly driven out of equilibrium, its relaxation pathway back to equilibrium will depend on the interplay of different interactions. The strongest interactions will induce the fastest relaxation processes, followed by additional ones mediated by less efficient interactions. Hence, by following the relaxation pathway back to equilibrium, it is possible to separate different equilibration processes in the time domain, enabling insights into the underlying interactions that would not be possible in thermal equilibrium.

In solid-state systems, the typical relaxation timescales of electrons, phonons, and spins are on the order of femto- to nanoseconds. Changes on such timescales cannot be directly recorded, because they exceed the speed of even the fastest electronics. Instead, femtosecond laser pulses in combination with a pump-probe approach are employed: first, the material is driven out of equilibrium with an ultrashort laser pulse (pump). After a certain time delay, a second laser pulse is employed to investigate the material's response to laser excitation (probe). The elegance of the pump-probe technique lies in the spectroscopic pumping and probing: since the probe pulse interrogates the state of the material only at a certain time delay after the pump pulse, the detection of the probe signal can be time-integrated. Time resolution is then achieved by repeating the measurement for many different time delays between pump and probe pulses, thus obtaining a "movie" of the material's response to laser excitation.

Different probing methods are available to investigate different aspects of the ultrafast response to laser excitation. A (non-exhaustive) overview is presented in Fig. 1.1.
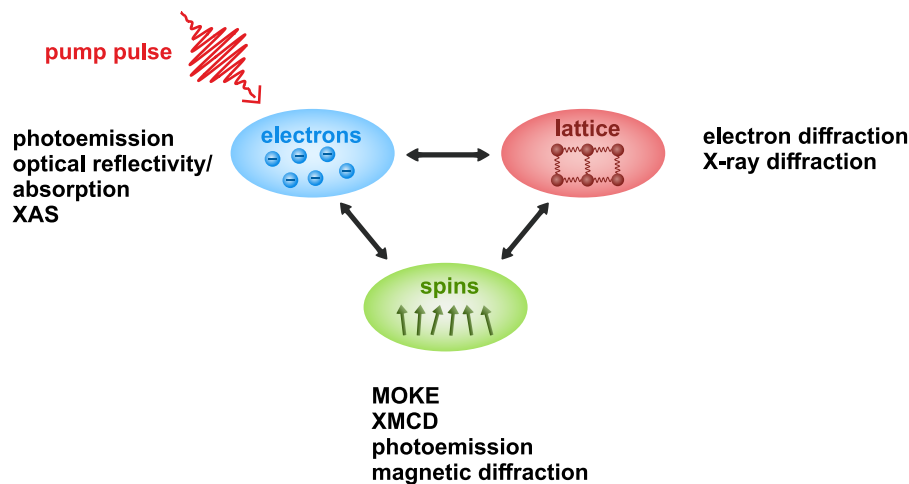
Figure 1.1: Schematic illustration of different degrees of freedom in a solid and probing techniques to access their responses to laser excitation (pump pulse). More details are described in the text.

Electronic degrees of freedom can for example be probed with time-resolved photoemission techniques, optical reflectivity or absorption measurements, and with X-ray absorption spectroscopy (XAS). The response of magnetic degrees of freedom can be investigated using the magneto-optical Kerr effect (MOKE), X-ray magnetic circular dichroism (XMCD), photoemission techniques, and magnetic X-ray diffraction. To access the lattice dynamics, the most direct techniques are time-resolved diffraction techniques, namely X-ray and electron diffraction. With any of these techniques, already a lot of information on the coupled non-equilibrium dynamics of electronic, magnetic, and lattice degrees of freedom can be obtained. Combining several probes to investigate a material is even more powerful: it allows to relate the dynamics of different subsystems with each other, thus yielding more comprehensive and complementary information on relaxation pathways and the underlying coupling strengths. Also the pump pulse is a tuning knob to gain further information: by tuning the photon wavelength, different electronic transitions can be excited. Different initial non-equilibrium states of the material result in different relaxation pathways, which can then be compared with each other. In the case of materials with a band gap, it is even possible to exclusively excite specific lattice or magnetic degrees of

freedom instead of electronic transitions. This can be achieved by pumping with low photon energies in the terahertz range.

In this thesis, the focus lies on time-resolved electron diffraction, which is introduced in detail in Chapter 2. Several materials of both technological and fundamental interest were studied: black phosphorus (Chapter 3), the elemental *3d* ferromagnets nickel, iron, and cobalt (Chapter 4), as well as the *4f* ferromagnets gadolinium and terbium (Chapter 5).

Black phosphorus is a layered material that can be exfoliated down to a monolayer (2D material). Its tunable band gap in the infrared range and high carrier mobility make it an important building block for 2D heterostructure devices. In addition, it has an extraordinary in-plane anisotropic structure, which is reflected in many macroscopic properties. In this work, it is uncovered how this peculiar structural anisotropy affects the material's response to laser excitation. A pronounced nonthermal behavior of the lattice is revealed, with consequences for the transient anisotropy of the atomic vibrations. Furthermore, tuning knobs to control the timescales of this nonthermal state are investigated.

An interesting aspect of the *3d* and *4f* ferromagnets studied here is their ultrafast demagnetization, whose underlying microscopic processes and their interplay are still a subject of investigation [Eic17; Dor19; Fri20; Guy22]. In this work, the ultrafast lattice responses of these ferromagnets are accessed directly with time-resolved diffraction and the microscopic energy flow between electronic, magnetic, and lattice degrees of freedom is analyzed. For the *3d* ferromagnets iron, cobalt, and nickel, experimental and theoretical results are combined to yield a quantitative description of the microscopic energy flow. The results reveal the substantial role of ultrafast demagnetization in the lattice dynamics and provide a quantitative model for the microscopic energy flow in elemental *3d* ferromagnets. Furthermore, novel insights into the strongly out-of-equilibrium, nonthermal response of the spin system are gained.

In contrast to the itinerant *3d* ferromagnets, the nature of the magnetic moment in elemental *4f* ferromagnets is predominantly localized, which affects the ultrafast relaxation pathways. In this work, the ultrafast lattice responses of gadolinium and terbium are examined both above and below their Curie temperatures. In addition, detailed temperature-dependent results for the lattice dynamics and time-resolved MOKE results are provided for terbium. It is found that several aspects of the experimental results do not agree with a thermal picture of ultrafast demagnetization. This work provides detailed experimental results on the ultrafast lattice dynamics, which are complementary to demagnetization measurements, and therefore serve as a basis for understanding the complex ultrafast responses of *4f* ferromagnets.

Before discussing the experimental details and the results, the next two sections give a brief overview of the microscopic couplings and their roles in the equilibration processes, which serves as a basis for understanding the experimentally measured ultrafast dynamics.

1.2   Microscopic couplings in solids

When analyzing the ultrafast response of a material to laser excitation, different coupling mechanisms need to be considered, which are briefly introduced in this section. They are presented in the order of to their (typical) interaction strength, however, it is important to note that all of these processes occur simultaneously and also influence each other.

First, when a visible laser is absorbed by a material, electrons are excited to states with higher energies. The initial population of excited states depends on the band structure of the

material as well as the photon energy and is strongly nonthermal, i.e. it cannot be described with a Fermi-Dirac distribution function. Following the creation of such a nonthermal distribution, the electronic system will relax back towards thermal equilibrium via electron-electron scattering. A schematic illustration of an electron-electron scattering event is presented in Fig. 1.2(a). In the lowest-order process, two electrons exchange energy and momentum with each other. For an electron in a certain state, the available scattering pathways depend on the band structure as well as on the occupation of other electronic states. As time progresses, multiple electron-electron scattering events transform the initial nonthermal distribution closer towards a Fermi-Dirac distribution. Throughout this work, this process is referred to as "electron thermalization" or "carrier thermalization", since it generally applies to both electrons and holes. Typically, carrier thermalization in metals is (approximately[1]) achieved on the order of tens to hundreds of femtoseconds [MR13; Nie14; Uls15]. In general, the thermalization time depends on the material, the pump laser wavelength, and the excitation density.

While electron-electron coupling can establish thermal equilibrium within the electronic system, restoring equilibrium between electrons and other subsystems requires other coupling mechanisms. In particular, equilibration between electrons and the lattice is governed by electron-phonon coupling, which is schematically depicted in Fig. 1.2(b). Essentially, the coupling between electrons and phonons is due to Coulomb interactions between the electrons and the ion cores. Phonons consist of periodic displacements of the ions and thus lead to a perturbation of their electrostatic potential. Therefore, phonons couple different Bloch states with each other. An electron can scatter from one Bloch state into another via the absorption or creation of a phonon, if energy and momentum conservation are fulfilled. In the case of a laser-excited material with a hot electronic distribution, on average, more phonons are emitted than absorbed, thus leading to a net energy relaxation of the electrons while the lattice gains energy. Typically, most of the energy transfer between electrons and phonons happens on sub- to few picosecond timescales [Wal16a; Wal17b; Zah21d].

The distribution of the additional phonons created by electron-phonon scattering depends on the matrix elements as well as on the available phase space (i.e. the band structures and occupation numbers). Particularly for semiconductors or insulators, which have profound phase-space constraints due to the band gap, electron-phonon scattering alone cannot establish thermal equilibrium within the lattice. This is achieved by direct phonon-phonon scattering, which is schematically illustrated in Fig. 1.2(c). Phonons are the vibrational eigenstates of a crystal with harmonic interatomic potential. In perfectly harmonic crystals, different phonons should therefore not (directly) interact. However, in reality, interatomic potentials differ from the harmonic approximation, in particular for high phonon occupation numbers (i.e. large atomic displacements). In this case, phonons are not vibrational eigenstates anymore, and coupling between different phonon modes occurs. The lowest-order processes involve three phonons, either a decay of one phonon into two (anharmonic decay) or the opposite process. Compared to electron-electron coupling and electron-phonon coupling, this interaction is typically the least efficient one. For many materials, it has been found that phonon populations remain nonthermal for tens of picoseconds after laser excitation [Tri10; Wal17b; Ste18; Zah20a; Sei21].

Particularly for magnetic materials, another essential degree of freedom is the spin. In many magnetic materials, an ultrafast reduction of the magnetization or even magnetization switching

---

[1]Other scattering processes, in particular electron-phonon scattering, lead to minor deviations from a Fermi-Dirac distribution also on longer timescales [WR19].
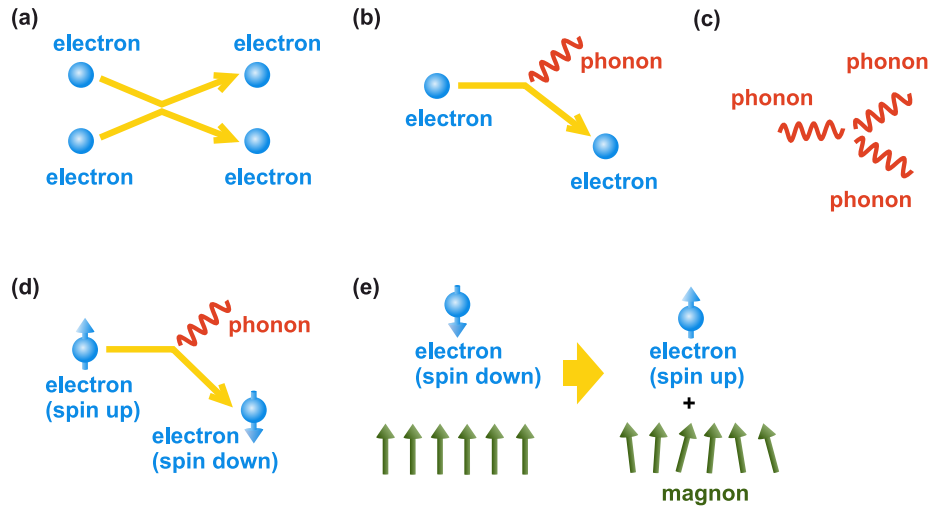
Figure 1.2: Schematic illustration of different scattering mechanisms in solids. (a) Electron-electron scattering. (b) Electron-phonon scattering. The phonon can either be emitted or absorbed in this process. (c) Phonon-phonon scattering. A phonon can decay into two lower-energy phonons (anharmonic decay), but also the opposite process is possible (phonon collision). (d) Elliott-Yafet spin-flip scattering. In the presence of spin-orbit coupling, scattering events with non-magnetic scatterers (e.g. phonons) can induce spin-flips. (e) Magnon emission via exchange scattering. Electrons can scatter from a minority to a majority state, accompanied by the emission of a magnon.

after laser excitation is observed [Bea96; KKR10], which raises questions about the microscopic coupling mechanisms governing these phenomena. There are several ways in which magnetic degrees of freedom can interact with other subsystems. One mechanism is Elliott-Yafet spin-flip scattering, which is illustrated in Fig. 1.2(d). The origin of this scattering mechanism is spin-orbit coupling, which leads to a mixing of spin-up and spin-down eigenstates. Therefore, a scattering event of an electron with a non-magnetic scattering center, e.g. a phonon, has a finite probability of flipping the electron's spin [Ell54]. The spin flip comes with a decrease of angular momentum in the spin system. Due to angular momentum conservation, the angular momentum needs to be transferred to the lattice.

A second mechanism that is discussed in the context of ultrafast magnetism is magnon emission via exchange scattering, which is illustrated in Fig. 1.2(e). A minority electron can flip its spin and generate a magnon. Such processes have been shown to have a significant contribution to the decay of excited electronic states in iron [Sch10], suggesting that ultrafast magnon generation plays a significant role in the response of ferromagnets to laser excitation. However, exchange scattering alone cannot change the magnetization of ferromagnets, since the total angular momentum of the spin system remains unchanged. In order to reduce the magnetization, angular momentum needs to be dissipated to other degrees of freedom. Recent experiments suggest that most of the angular momentum is dissipated to the lattice [Dor19; Tau22]. Furthermore, also direct coupling between lattice and spin subsystems can occur, mediated by magneto-crystalline anisotropy [Wie11] or by the distance-dependence of exchange coupling [MDW12]. Direct spin-lattice coupling is likely an important mechanism in the demagnetization of very localized magnetic moments, e.g. the $4f$ moments of rare-earth metals, which lack spin-flip or exchange-scattering channels [Wie11].

In addition to the local effects discussed so far in this section, it is also important to mention that non-local (i.e. transport) effects can occur. Non-local effects, for example super-diffusive spin transport [BCO10], can also contribute to the magnetization response to laser excitation. The role of such non-local effects in the laser-induced dynamics depends strongly on the sample geometry (e.g. sample thickness, substrate material) and can be minimized by using thin, freestanding samples. Furthermore, in the case of antiferromagnets and ferrimagnets, coupling between different sublattices can also change the magnetization [Thi17].

1.3 Relating non-equilibrium dynamics to coupling strengths – the two-temperature model and beyond

As described in the previous section, the relaxation pathway of a laser-excited material is determined by the interplay of different coupling strengths. To relate the experimentally observed non-equilibrium dynamics to the underlying microscopic couplings, a model is required. A very widely used model for the laser-induced dynamics is the two-temperature model (TTM), which was introduced by Kaganov et al. [KLT57] and was first applied to laser-excited materials by Anisimov et al. [AKP74]. Later, Allen derived the TTM equations from the time-dependent Boltzmann equations and related the electron-phonon coupling parameter in the TTM to the Eliashberg function (which stems from superconductivity theory) [All87].

The TTM only considers electronic and lattice degrees of freedom, i.e. it is applicable to non-magnetic materials. Both the electrons and the lattice are assumed to be always in internal thermal equilibrium, which means that they can be described with temperatures T_e and T_l, respectively. The interaction between the two subsystems is described with the electron-phonon coupling parameter G_{ep}. The time evolution of the electron and lattice temperatures is then given by the following coupled differential equations [AKP74; All87]:

$$c_l(T_l) \times \frac{dT_l}{dt} = G_{ep}(T_e) \times (T_e - T_l) \tag{1.1}$$

$$c_e(T_e) \times \frac{dT_e}{dt} = G_{ep}(T_e) \times (T_l - T_e) + P(t), \tag{1.2}$$

with c_l: lattice heat capacity, c_e: electron heat capacity, $P(t)$: source term (laser excitation).

Even though the TTM can describe experimental results in many cases, it does not always offer an accurate picture of the laser-induced dynamics. Already when Allen derived the TTM from the time-dependent Boltzmann equations, he noted: "The assumption that the distributions F [the electron distribution] and N [the phonon distribution] are always thermal is of course incorrect at some level, possibly only in detail or possibly more seriously" [All87]. To date, pump-probe experiments have revealed several examples of materials that cannot be described with a TTM [Cha14; Wal16a; Wal17b]. In particular, assuming a thermalized phonon distribution is often problematic, since phonon-phonon scattering is typically less efficient than electron-phonon scattering. In fact, also one of the materials presented in this work, black phosphorus, exhibits pronounced nonthermal phonon dynamics, which is presented in Chapter 3. Also for the electrons, calculations predict deviations from thermal behavior [WR19; WC20].

Consequently, depending on the material, a more sophisticated theoretical description than the TTM may be necessary. A more detailed modeling can be achieved with the time-dependent Boltzmann equation formalism [WR19; Sei21; Car21], which can describe the population changes

of electrons and phonons without relying on thermal distribution functions. However, such models are significantly more complex and thus come with a high computational cost. To capture the nonthermal dynamics of the material approximately with a less complex model, the TTM can be extended by differentiating between more subsystems [Wal16a].

Besides the limitation to thermal distributions, the TTM is also unable to describe changes in magnetic degrees of freedom following laser excitation, e.g. ultrafast demagnetization. To describe magnetization dynamics, the spin system was added phenomenologically by extending the TTM to a three-temperature model (3TM) [Bea96]. Analogously, also the 3TM is limited to thermal descriptions of the different subsystems. Depending on the material and the timescales considered, a more sophisticated model may be necessary. In fact, one such model is employed in this work, energy-conserving atomistic spin dynamics (ASD) simulations. This model can describe the coupled energy flow between electrons, spins, and phonons and has the major advantage that it is not limited to a thermal description of the spin system. Instead, the spin dynamics are directly simulated. Details about this model are presented in Chapter 4.

Chapter 2

Experiment and data analysis

A successful electron diffraction experiment comprises several aspects. Besides the experimental setup itself, other key components are the preparation of suitable samples as well as the extraction of the relevant information from the experimental data. This chapter aims to give an overview of these different aspects of the electron diffraction experiment.

2.1   Sample preparation

For electron diffraction experiments in transmission, thin samples (with thicknesses on the order of tens of nanometers) are necessary due to the strong interaction of electrons with matter. The required thickness depends on the electron energy, on the atomic number(s), and on the density of the material. Typically, for electron energies on the order of tens of keV, sample thicknesses well below $100\,\mathrm{nm}$ are necessary, which requires specialized techniques for sample preparation. This section describes sample preparation techniques for layered materials as well as for samples grown on single-crystalline salt crystals. For materials that can neither be exfoliated nor grown on salt or thin membranes, microtome cutting can be used to obtain thin samples.

2.1.1   Layered van der Waals materials

Many layered crystals, for example graphite and transition metal dichalcogenides (TMDCs), can be exfoliated to obtain thin multilayers and even monolayers (2D materials). This is typically possible when different layers of the material are held together only by van der Waals interactions. In this subsection, the preparation of freestanding thin-film multilayers of such layered materials is described. The technique is applicable to a wide range of layered van der Waals materials, provided that the material can sustain contact with water.

The sample preparation process is presented in Figure 2.1. It starts with a bulk crystal of the van der Waals material (here: graphite), shown in Fig. 2.1(a). First, to maximize the sample yield and to obtain fresh, smooth surfaces, the crystal is divided into several thinner crystal flakes. For this, a very sharp (ideally new) razor blade is employed to cut the crystal along its layers, as shown in Fig. 2.1(b). Smooth surfaces of the resulting flakes can be obtained with a low angle of the blade to the crystal surface and by applying very little force during the process. The resulting flakes are presented in Fig. 2.1(c). Next, a quadratic glass slide (around $2\mathrm{x}2\,\mathrm{cm}$ in size) is required. On this glass slide, a smaller rectangle of polydimethylsiloxane (PDMS) with a thickness of around $1\text{-}2\,\mathrm{mm}$ and a size of roughly $7\mathrm{x}7\,\mathrm{mm}$ is placed, as shown

in Fig. 2.1(d). The PDMS is not strictly necessary but improves the results. Next, one of the pre-thinned flakes is placed on the glass slide. For this, the flake is first attached to a piece of regular adhesive tape with a length of around 3 cm. The adhesive tape with the flake is then fixed to the glass slide with two other pieces of adhesive tape. Here, the side with the flake points away from the glass and the PDMS, since the van der Waals crystal needs to be accessible for exfoliation. The flake should be on top of the PDMS piece and the adhesive tape should be wrapped tightly around the glass slide to ensure that the flake is flat. The result is presented in Fig. 2.1(e). Next, a second glass slide is required. A small amount of a water-soluble thermoplastic mounting adhesive (here: Crystalbond 555-HMP) is placed on the glass slide, as shown in Fig. 2.1(f). The glass slide is then heated on a hot plate (temperature setting around 100° C) until the glue has melted, as presented in Fig. 2.1(g). Then, the glass slide with the glue is removed from the hot plate and a thin ring made of aluminum foil is placed around the glue acting as a spacer, shown in Fig. 2.1(h). The second glass slide with the crystal is now placed on top of the molten glue (see Fig. 2.1(i)). The molten glue should cover the crystal, as shown in Fig. 2.1(j). However, pressing the upper glass slide down should be avoided since a relatively thick (>1 mm) layer of glue is required for some of the further steps.

After the stack has cooled down and the glue has turned solid again, the two glass slides are separated, as shown in Fig. 2.1(k). A part of the flake now sticks to the glue. Sometimes, there are already suitable thin films on the glue, which can be identified with an optical microscope. Materials with a band gap in the visible range exhibit thickness-dependent colors, which can serve as a rough thickness estimation. A more precise thickness determination based on transmission measurements is explained below. If no suitable flakes are present, the material on the glue can be thinned further by exfoliation with adhesive tape, as presented in Fig. 2.1(l). Typically, the steps (e)-(l) need to be repeated several times until a suitable thin film is produced. To obtain large, thin samples, the quality of the pre-thinned flakes shown in Fig. 2.1(c) is an important factor.

Once a suitable film is identified with the optical microscope, as for example shown in Fig. 2.1(m), the next step is to transfer it to a transmission electron microscopy (TEM) grid. For this, the glue is cut with a scalpel until there is an isolated small piece of glue around the sample, as presented in Fig. 2.1(n). Since the glue is rather soft, the cutting needs to be performed with very little force, otherwise, the glue can bend and damage the sample. It is also possible to harden the glue by storing the sample in a desiccator for several hours before cutting it. Afterwards, the piece of glue with the flake is carefully detached from the glass with the scalpel and placed on the surface of a beaker filled with distilled water, with the thin film pointing upwards. This step is presented in Fig. 2.1(o). The water-soluble glue dissolves, which can be observed from the side of the beaker. Once the glue has completely dissolved, the flake is ready to be picked up. A TEM grid is grabbed with inverted tweezers and inserted into the water at a safe distance from the sample, as presented in Fig. 2.1(p). Here, inserting the grid at a steep angle to the surface avoids bending of the TEM grid due to the surface tension of water. Then, now with a shallow angle between the TEM grid and the water surface, the sample is slowly picked up with the grid, as shown in Fig. 2.1(q). If the sample is not at the desired position on the TEM grid, it is possible to place it back in the water, as long as it hasn't dried yet. When the sample is at the desired position, the TEM grid is left to dry on the tweezers. It is important to make sure that the inverted tweezers have dried completely before releasing the sample. A microscope image of the final, freestanding sample on the TEM grid is presented in

Fig. 2.1(r) (transmission) and Fig. 2.1(s) (reflection). Wrinkles are typically not avoidable but can be reduced by choosing a TEM grid with small windows (e.g. 600 bars per inch or more).
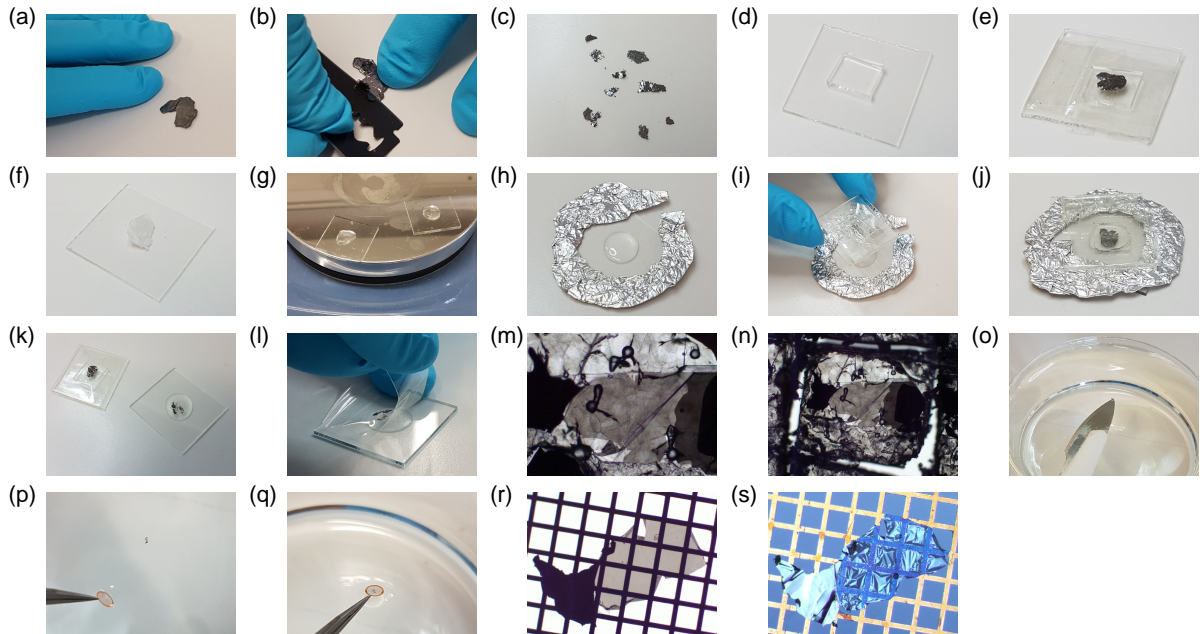
Figure 2.1: Sample preparation steps for van der Waals crystals, shown for graphite as an example. Details are described in the text.

After sample preparation, it is desirable to characterize the thickness of the freestanding sample. If the optical constants of the material are known, the thickness can be inferred from optical transmission measurements. Note that in most cases, multilayer calculations are necessary to relate thickness and transmission due to thin-film interference effects, especially in the case of non-metallic samples.

A simple method to measure the transmission of such small samples in certain wavelength ranges combines an optical microscope, a grayscale camera, and optical bandpass filters. An optical bandpass filter is inserted into the light path of the microscope. Then, a camera image of the sample under the microscope (with illumination only from below the sample) is recorded. Here, it is important to record both the sample as well as an area without the sample (background). The background mustn't be saturated in the camera image. In addition, it is important to set the gamma correction of the camera to 1 (no correction). If these conditions are fulfilled, the image pixel values are proportional to the light intensity. By comparing the sample region and a region without sample, the transmission in the range of the bandpass filter can be calculated[1]. A reliable calculation can be achieved by making a histogram of a region with both sample and background and then performing a fit with two peak functions (here: Gaussians). An example is presented in Fig. 2.2. The method was tested with two different neutral density[2] filters (NE03A and NE10A from Thorlabs) as "sample" and three different narrowband bandpass filters. For bandpass filters in the range from 406-422 nm and 773-812 nm and a halogen

---

[1]Here, it is assumed that the intensity of the light source varies little in the region of the bandpass filter, which is a good approximation for narrowband filters.

[2]Spectral variations of the optical density occur. The measured transmission was thus compared to the transmission data provided by the manufacturer.

(a)

(b)
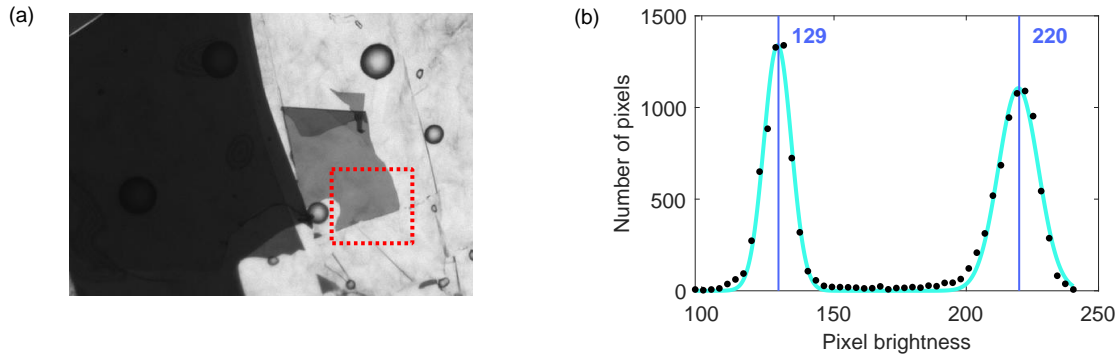
Figure 2.2: Transmission measurements of small thin-film samples with the optical microscope. (a) Grayscale image of a thin WSe$_2$ flake on glue, taken with a 773-812 nm bandpass filter. The dashed red rectangle marks the area that is used to determine the transmission of the thin flake in this wavelength range. The structure of the background, for example the bubbles, stems from the glue. The dark region on the left is a thicker flake. (b) Histogram of the area marked in (a). The x-axis shows the pixel brightness (values from 0 to 255). The y-axis shows the number of pixels with this value. The bin width of the histogram is around 3. The histogram shows two peaks. The brighter peak (brightness 220) corresponds to the substrate and the darker peak (brightness 129) corresponds to the WSe$_2$ flake. The light blue curve corresponds to the result of a fit with two Gaussians. From the brightness of the two peaks, the transmission in the range of the bandpass filter can be calculated as $T = 129/220 \approx 59\%$.

lamp, the precision was found to be better than 3 %; for a bandpass filter from 628-672 nm, the precision was only around 14 %. Note that the precision of this method depends on the spectrum of the microscope lamp, the transmission of the sample, and the spectral window of the bandpass filter. With the right combination of microscope lamp and bandpass filter, the method yields a fast and precise transmission measurement, even for very small samples. By using different bandpass filters, the transmission in different wavelength regions can be accessed. Combining the results of these transmission measurements with multilayer calculations based on the optical constants of the material then allows determining the thickness of the thin-film samples.

2.1.2   Thin films grown on salt

Many materials, for example many mono-elemental metals, can easily be deposited as thin films, especially if polycrystalline samples suffice. A standard sample preparation technique for electron transmission experiments is to use single-crystalline salt (NaCl) crystals as a substrate material for sample deposition [Dwy07]. The salt crystal can then be dissolved in water, leaving the thin-film sample floating on the water surface. This method was used to prepare the freestanding films of nickel, iron, cobalt, and platinum studied in this work, as well as some of the rare-earth metal films studied in Chapter 5.

Figure 2.3 shows different steps of this sample preparation method. First, the NaCl crystal is cut into smaller pieces that roughly correspond to the size of a TEM grid. This can be achieved by pressing a blade on an edge of the crystal, as shown in Fig. 2.3(a). The NaCl crystal usually breaks along a high-symmetry direction. The small piece of salt is grabbed with tweezers (shown in Fig. 2.3(b)) and slowly lowered into a beaker filled with distilled water, with the sample side pointing upwards. When the thin film reaches the water, it starts to detach

Figure 2.3: Preparation steps for samples grown on salt (NaCl) crystals. Details are described in the text.

from the salt and floats on the water surface (see Fig. 2.3(c)). The piece of salt is lowered further until the film fully detaches, as shown in Fig. 2.3(d). Then, the sample can be picked up with a TEM grid, analogous to the case of layered materials described in Sec. 2.1.1. As an example of a resulting sample, Fig. 2.3(e) shows a microscope image of a metal film on a TEM grid (recorded in reflection geometry).

While difficult to prepare, thin-film samples for transmission electron diffraction have advantages. Transport effects are less pronounced compared to many other techniques, due to the relatively low sample thicknesses, the absence of a substrate, and the bulk sensitivity of the technique. The latter also means that the sample surface, which can be oxidized or exhibit a different structure than the bulk, typically only has a small contribution to the total signal. This is for example relevant for the material discussed in Chapter 3, black phosphorus, which is air-sensitive. In addition, the strong interaction of electrons with matter can be an advantage, for example when 2D monolayers or materials with very light elements are studied. On the other hand, heat accumulation can be a problem and needs to be avoided with a sufficiently low repetition rate of the laser and a suitable size of the TEM grid (to enable sufficient heat dissipation away from the sample to the environment).

2.2 The femtosecond electron diffraction experiment

Time-resolved diffraction techniques allow resolving non-equilibrium changes in the structure of materials [Dwy06; Zew06; SM11; Mil14]. Both X-ray diffraction and electron diffraction have a time-resolved counterpart, each with its own advantages and disadvantages. X-rays do not interact with magnetic and electric fields, which adds flexibility for example when studying magnetic materials. In addition, the interaction of X-rays with matter is much weaker compared with electrons, allowing the study of thick samples. On the other hand, the Ewald sphere of X-rays is much smaller, which means that typically a smaller region of reciprocal space is accessible. In addition, despite recent progress [Bar06; Zam09; Sch19; Afs20], bright lab-based X-ray sources remain a challenge. In contrast, creating electron bunches in the lab is easily achieved using the photoelectric effect. A major challenge of electron diffraction is caused by the fact that electrons are charged particles. Coulomb repulsion therefore leads to a temporal broadening of the electron pulse over time (space charge broadening) [Siw02], which limits the time resolution of the experiment.

There are two main strategies to overcome this challenge. The first strategy is based on recompression of the electron pulse. This can be achieved with radio-frequency (RF) waves in a cavity [Oud10; Cha12], which accelerate or decelerate the electrons based on their positions in the pulse to compensate for the temporal broadening. This requires a certain space-charge-

induced broadening in the first place, i.e. a considerable propagation of the beam, and takes advantage of the broadening to recompress the beam. With this method, it is possible to recover a short pulse at one specific distance from the electron source, where the sample is then placed.

The second strategy is to minimize the propagation of the electron pulses, i.e. to minimize the distance between electron generation and sample [Dwy06; Ger15; WBE15]. Any temporal broadening after the sample does not degrade the time resolution, since the pump-probe measurement principle is based on probing the sample spectroscopically with the electron pulses and the detection is anyway time-integrated. This strategy is used here, employing the femtosecond electron diffraction (FED) setup developed by Lutz Waldecker et al. [WBE15] (with some modifications, including a new laser system and cryogenic cooling). In the following, details about the experiment are provided.

2.2.1   Laser and optical setup

Ultrashort laser pulses are obtained from a commercial titanium-sapphire (Ti:Sa) amplified laser system (Coherent Astrella). A Ti:Sa oscillator creates ultrashort pulses at a repetition rate of 80 MHz. The pulses are stretched in time and selected pulses are then amplified in a multipass amplifier cavity. Finally, the amplified pulses are recompressed. The resulting laser pulses have a temporal width of 40 fs FWHM, a central wavelength of 800 nm, a repetition rate of 4 kHz and a pulse energy of 1.5 mJ.

A schematic diagram of the optical setup is presented in Figure 2.4. After leaving the laser system, the ultrashort pulses are split into two parts: 90 % of the beam goes into a commercial two-stage optical parametric amplifier with additional frequency mixers (here: TOPAS-Prime+NirUVis from Light Conversion), which can convert the 800 nm-pulses to pulses with different central wavelengths ranging from 250 nm to 2.5 μm. These pulses are used for exciting the sample (pump). The wide tunability of the pump wavelength allows to vary the initial distribution of photo-excited electrons in the sample, and thus to study relaxation processes after different initial non-equilibrium conditions.

The beam coming out of this optical parametric amplifier is sent through a reflective neutral density (ND) filter to adjust its intensity. The reflected part of the beam is discarded on a beam dump. The transmitted part is collimated with a telescope, which also reduces the beam diameter by half. Finally, the beam is focused, enters the vacuum chamber, and is directed towards the sample. The reflection of the pump beam on the vacuum feedthrough is picked up with a D-shaped pickoff mirror and directed to a camera for alignment purposes and to estimate the beam spot size on the sample. For the latter, the camera is placed such that its distance from the feedthrough window is equal to the distance between the feedthrough window and the sample. In addition, there is the possibility to perform experiments with tilted samples, which is described in detail in Sec. 2.2.2. This requires pumping the samples from the side instead of from the back. For this pumping geometry, an additional mirror can be placed in the pump path, as illustrated with a dashed mirror.

The second part of the main beam (10 % of the laser output) is split again. Of these 10 %, 70 % can be employed as an alternative pump beam, when pump wavelengths of 800 nm or 400 nm are desired. This has the advantage of enhanced stability compared to the output of the TOPAS-Prime+NirUVis. For this case, an additional mirror can be placed in the pump path, as sketched in Fig. 2.4 with a dashed mirror.
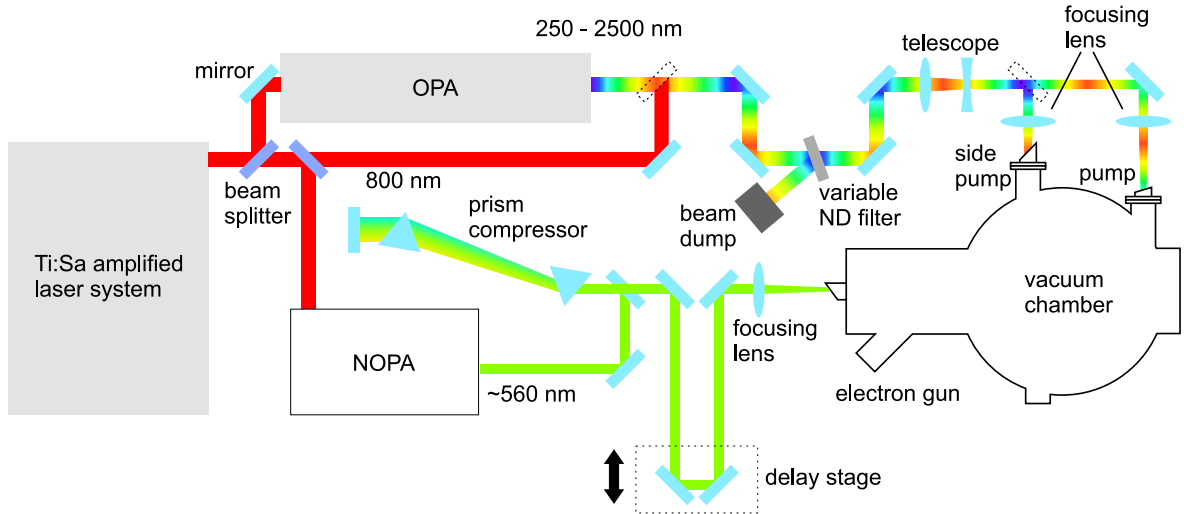
Figure 2.4: Optical setup for the pump-probe electron diffraction experiment. Details are described in the text.

The other 30%, i.e. 3% of the total laser output, are used to generate probe pulses (electron pulses) by photoemission from a gold cathode. In general, the wavelength of the probe pulses should be chosen according to the work function of the cathode material used for photoemission, because a large initial energy and momentum spread of the photoemitted electrons can affect the reciprocal-space resolution and the time resolution adversely. In this setup, two-photon photoemission on thin gold films is employed to create electrons. The work function of these films is around 4.4 eV, slightly smaller than bulk gold [Wal16b]. Therefore, for two-photon photoemission, photon wavelengths smaller than around 560 nm (corresponding to 2.2 eV photon energy) are required. Such photons are created with a home-built non-collinear optical parametric amplifier (NOPA), shown in Fig. 2.5.

First, the beam diameter is reduced by 50 % with a telescope. Next, the beam is split into two parts: the transmitted part (corresponding to around 150 mW) is focused and sent into a β-barium borate (BBO) crystal for second harmonic generation (SHG). In this non-linear process, two 800 nm-photons combine to one 400 nm-photon, as schematically shown in the box next to the BBO in Fig. 2.5. Afterwards, a second lens is used to refocus the beam, which now contains both 400 nm- and 800 nm-light. Two dichroic mirrors are employed to separate these two components. The transmitted 800 nm-light is discarded while the reflected 400 nm-light is directed towards a second BBO crystal for optical parametric amplification, which is schematically depicted in the box next to this BBO in Fig. 2.5.

For optical parametric amplification, in addition to the 400 nm-beam (pump), also photons with the desired wavelength of around 560 nm are required (signal). These are obtained by white-light continuum generation. For this, the part reflected on the beam splitter is used (around 2.5 mW). It is sent through a reflective, variable ND filter to adjust its intensity. In addition, an iris is used for fine adjustments of the intensity and for optimizing the beam shape. Next, the beam is focused and sent through a sapphire plate, in which various non-linear processes lead to the creation of a broad spectrum of wavelengths (supercontinuum or white-light continuum). The diverging white-light beam (shown in yellow) is refocused and the

remaining 800 nm-light is filtered out using a short-pass filter. The white light is then directed towards the BBO crystal, which is placed at the focal spot of the white-light beam.

In the BBO crystal, the white light gets amplified at the expense of 400 nm-light. This process is depicted in the box next to the BBO in Fig. 2.5. Due to its wide frequency range and because it has transmitted through a lens, the white light is chirped, with the lower-frequency components traveling ahead of the higher-frequency ones. Therefore, varying the arrival time of the 400 nm-pulses influences the amplified frequency range. In addition, the angle of the BBO crystal determines the phase-matching condition and thus influences the amplified frequency range as well. Both parameters are chosen such that the desired wavelength of around 560 nm is predominantly amplified[3].

The residual 400 nm-light is discarded on a beam dump. In addition, light with a frequency of around 1400 nm (idler) is produced together with the signal beam. The idler beam is also sent to the beam dump. The amplified green light is recollimated. Typical output powers of the NOPA are around 3 mW, corresponding to a pulse energy of 0.75 μJ.
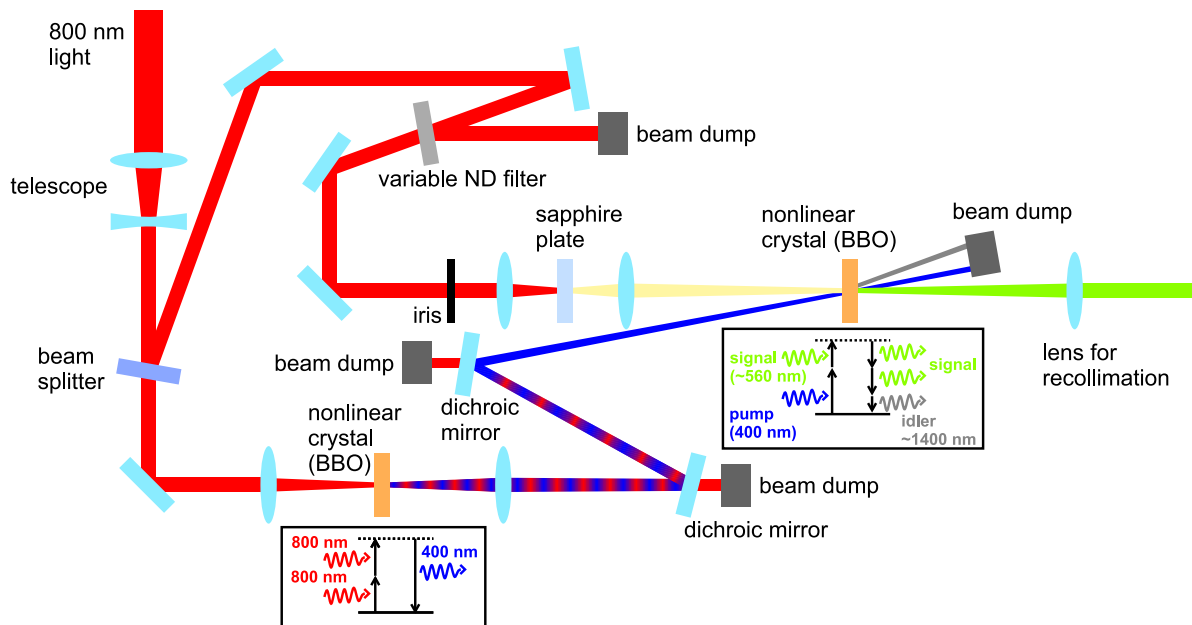
Figure 2.5: Sketch of the non-collinear optical parametric amplifier (NOPA) used to generate probe pulses with a wavelength of around 560 nm. Details are described in the text.

The pulses coming out of the NOPA are chirped, caused mostly by transmissive optical elements, for example the recollimation lens. This results in longer pulses and thus degrades the time resolution of the experiment. Therefore, the pulses are recompressed with a prism compressor, as sketched in Fig. 2.4. The first prism disperses the beam, which is then sent to a second prism, placed at a certain distance from the first one. Afterwards, the beam is reflected on a mirror and passes both prisms again. Spectral components of the beam with long wavelengths are deflected less by the prisms compared to short-wavelength components due to chromatic dispersion. Therefore, the propagation lengths in air and inside the second prism are

---

[3]In practice, when time resolution is not the limiting factor, slightly smaller wavelengths can be chosen to produce more electrons per pulse. Furthermore, the exact work function varies slightly between cathodes.

different for different wavelengths. By adjusting the distance between the two prisms and/or the position of the second prism perpendicular to the beam, the different propagation lengths can be chosen such that they compensate for the temporal chirp of the pulses.

Next, the probe pulses are sent to a retroreflector, which is mounted on a translation stage (delay stage). With this, the relative time delay between pump and probe pulses is controlled. Finally, the probe beam is focused and sent into the vacuum chamber for electron generation. The focusing lens can be moved along the beam direction, such that the spot size on the cathode can be adjusted. A small spot size increases coherence and electron flux but worsens time resolution. Therefore, the optimal spot size depends on the experiment. Similar to the pump beam, also the reflection of the probe beam on the vacuum feedthrough is picked up and sent to a camera for alignment and beam position stabilization.

2.2.2 Diffraction chamber
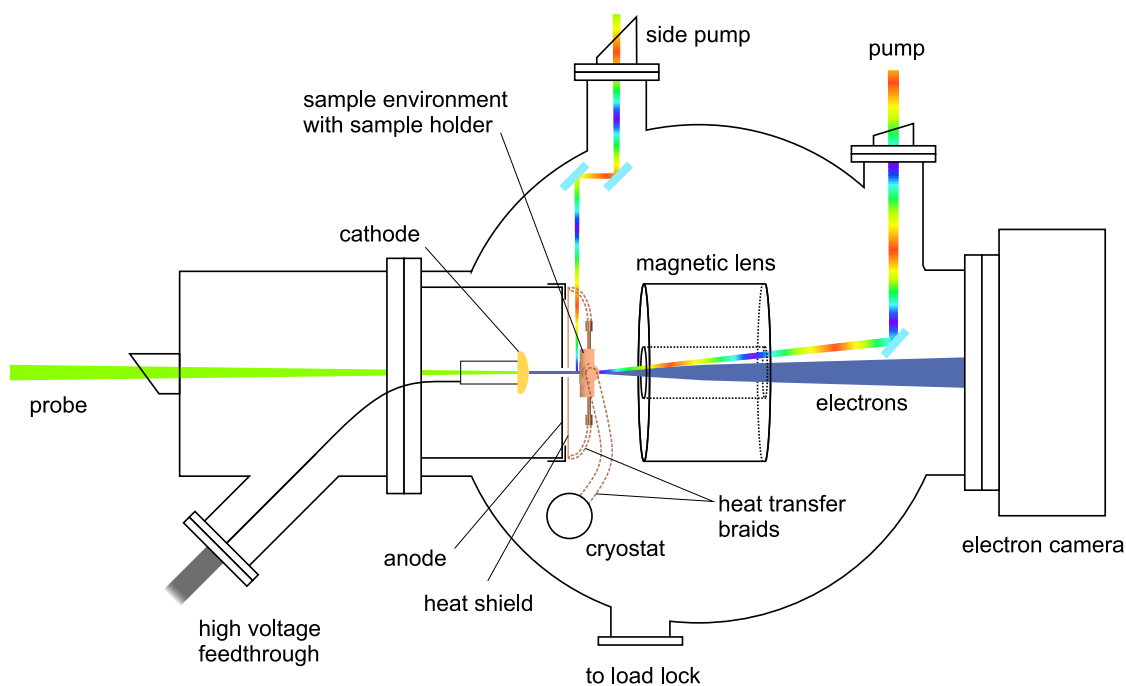
Figure 2.6: Sketch of the vacuum chamber and its most important components. Details are described in the text.

Figure 2.6 presents the most important components inside the vacuum chamber. As already discussed in the previous section, electrons are generated by photoemission and directed towards the sample. The transmitted beam is focused using a magnetic lens and diffraction patterns are recorded with an electron camera. For excitation, pump pulses are sent to the sample from the back (at an angle of around 6° relative to the electron beam). Alternatively, the pump beam can be sent in at an angle of 90° for experiments with tilted samples. In the following subsections, the different components inside the vacuum chamber are described in detail.

2.2.2.1   Electron generation

The generation of electron pulses occurs on the left side of the sketch presented in Fig. 2.6. The convergent probe beam enters the chamber and hits the cathode (shown in yellow) from the back side, leading to photoemission at the front surface. The cathode sits on a threaded tube, which is connected to the high voltage supply with a cable on the side. The threaded tube is mounted in the middle of a larger tube (housing) with a ceramic piece (not shown in Fig. 2.6). The housing is grounded, as well as the anode, which is mounted at a distance of around 10 mm from the cathode. The anode consists of a polished silicon wafer with a small hole of around $150\,\mu$m in the middle.

The cathode is on a large (negative) potential of 60-100 kV to accelerate the photoemitted electrons. To achieve such large potentials over a distance of only around 10 mm, the cathode is polished and has a mushroom-like shape, such that the field strengths are as low as possible everywhere [Wal16b]. A close-up view of the mounted cathode is presented in Fig. 2.7.
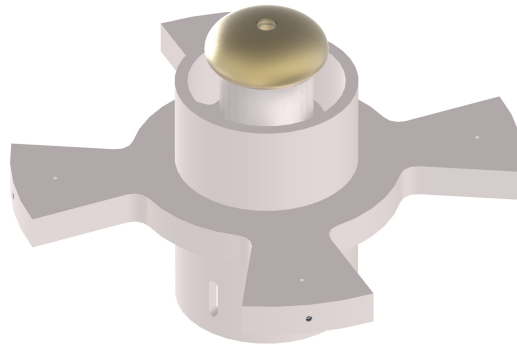
Figure 2.7: Close-up view of the mounted cathode. The sapphire window in the middle allows the beam to pass from the back and hit the thin gold film with which the cathode is coated. The cathode is screwed on a threaded steel tube, which is in turn mounted on electrically insulating ceramic pieces (shown in gray here). There is an additional piece inside the threaded tube, a metal ring with two holes, which serves as a connector to the high voltage cable.

The cathode is made of non-magnetic steel with a sapphire window in the center so that the probe beam can transmit to the front side. It is coated with 3 nm of chromium (for adhesion to the sapphire) and 25 nm of gold. Electrons are photoemitted from the surface of the gold film by the probe pulses. After exiting the anode through its hole, the high-energy electrons then pass through the sample, which is placed at a small distance from the anode (typically a few millimeters).

2.2.2.2   Sample environment and sample holders

The samples are mounted in a sample holder, which is inserted in a sample environment. The sample environment is presented in Fig. 2.8 (with a sample holder inserted). It consists of the main body and a cover plate, in between which the sample holder sits. It is possible to slide the sample holder in and out using a transfer stick, thus allowing easy sample exchange without breaking the vacuum of the main chamber. At the same time, good thermal contact

of the sample holder is required for efficient cryogenic cooling. Therefore, the sample holder is pressed onto the main body of the sample environment by two molybdenum springs mounted on the inside of the cover plate. To cool the sample, a heat transfer braid is attached from the top, using the copper plug also shown in Fig. 2.8. The heat transfer braid connects to a flow cryostat (Janis ST-400), as illustrated schematically in Fig. 2.6. In addition, a heat shield is attached to the gun housing at a small distance from the anode, which serves to reduce radiative heating of the samples. This shield is connected to the sample environment with two thinner heat transfer braids. Those braids connect via the two pieces on the side of the sample holder (see Fig. 2.8). The sample environment is mounted on stepper motors, which allow translations in all three directions. The copper braids are flexible enough to allow this motion of the sample environment. Furthermore, for temperature control, a small heater is inserted in the sample environment. It is tightly fitted into a hole in the main body, close to the sample holder (see Fig. 2.8). On the left side of the sample environment, a temperature sensor is mounted (not visible). The vicinity of the heater and the sensor to the samples allows precise and stable temperature control.
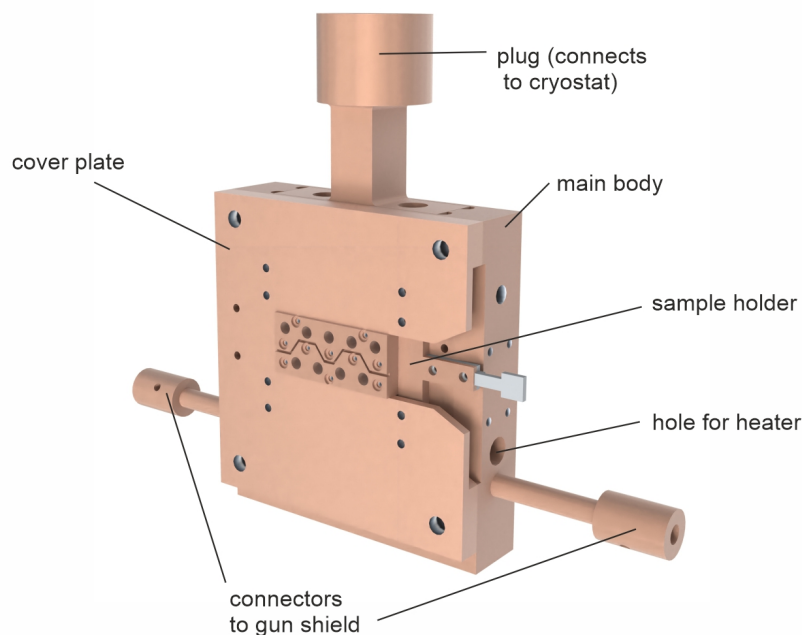
Figure 2.8: Sample environment with sample holder inserted. Here, the sample holder for normal geometry is shown. The two parts on both sides of the sample environment connect to the heat shield on the anode and the bigger plug at the top connects to the cryostat. Further details are described in the text.

A detailed view of the sample holders is presented in Fig. 2.9. There are two different options, depending on the experimental geometry. For normal incidence of the electron beam on the sample, the sample holder presented in Fig. 2.9(a) is used. The samples, which are typically either on TEM grids or on silicon nitride membranes, are placed into small indentations that match their size (diameter 3 mm). Up to nine samples can be mounted. To hold the samples in place and to ensure good thermal contact, covers are screwed on top. The covers are as thin as possible, such that the distance between anode and sample is minimized. Behind the

(a)   (b)
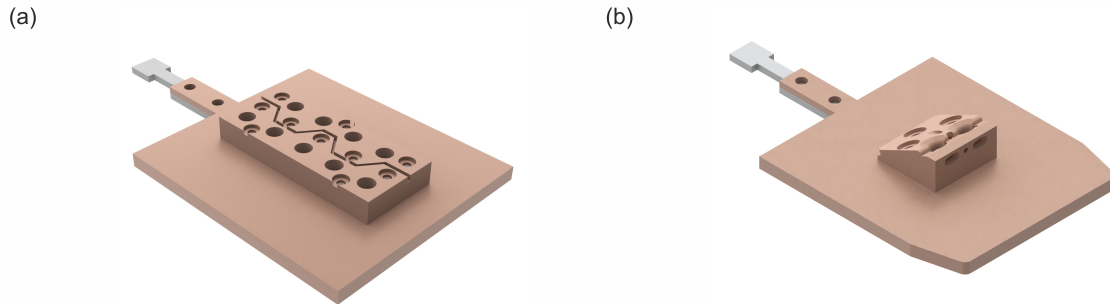
Figure 2.9: The two types of sample holders used in the electron diffraction setup. (a) Sample holder for experiments with normal incidence of the electron beam on the sample, which probe in-plane lattice dynamics. (b) Sample holder for experiments with the sample tilted by 26° to access out-of-plane lattice dynamic as well.

samples, there is a hole for electron transmission. It is smaller than the TEM grid size at first but widens to allow also diffracted parts of the beam to pass. The sample holders as well as the sample environment are made out of copper due to its high thermal conductivity. The pieces screwed on the side of the sample holders, which are required for sample transfer, are made out of aluminum. Aluminum is well-suited for this purpose since it deforms less easily compared to copper, is non-magnetic, and can resist shear strain.

When experiments at normal incidence are performed, the sample is pumped from the back of the sample holder, at an angle of about 6° relative to the electron beam. The reason for this is related to the finite spot sizes of pump and probe beams at the sample. If there are any variations in the time delay between pump and probe beam across the probed region, the time resolution worsens accordingly. For normal incidence of the electron beam, the time resolution is thus optimized when the pump beam has normal incidence as well. Therefore, the closest possible geometry to normal incidence is chosen.

In addition to normal geometry, samples can be tilted to access a different region of reciprocal space. In particular, this geometry allows studying out-of-plane dynamics of the sample. The sample holder for such experiments is presented in Fig. 2.9(b). The angle between sample and sample holder surface is 26°. This angle is chosen such that the time resolution is optimized for the pump beam arriving from the side (at 90° from the electron beam), based on the same considerations as described above for normal geometry[4]. Due to this geometry, only two samples can be mounted. The two large holes on the side ensure that the pump beam reaches the sample. The smaller hole in the middle is an alignment hole for the pump beam. There is an additional alignment hole for the electrons, which is normal to the sample holder surface and aligns with the center of the sample slots. The two alignment holes meet at the same distance from the sample holder surface as the center of mounted TEM grids. Also here, the samples are fixed with covers for good thermal contact. The rounded front edges of the sample holder are adapted from standard flag-style sample holders and facilitate sliding it into the sample environment. This design could also be employed for the normal-incidence sample holder in a future version.

---

[4]In the tilted case, the absolute arrival times are different for different parts of the probed region. Therefore, the optimal angle depends on the electron energy. Here, an electron energy of 74 keV was assumed, and the electron velocity was calculated taking into account relativistic effects.

2.2.2.3   Magnetic lens

After passing through the sample, the electron beam is focused with a magnetic lens. Here, a shrouded coil geometry is used [Lie55]. A schematic illustration of the magnetic lens is presented in Fig. 2.10. The housing, shown in gray, consists of magnetic steel with high iron content and
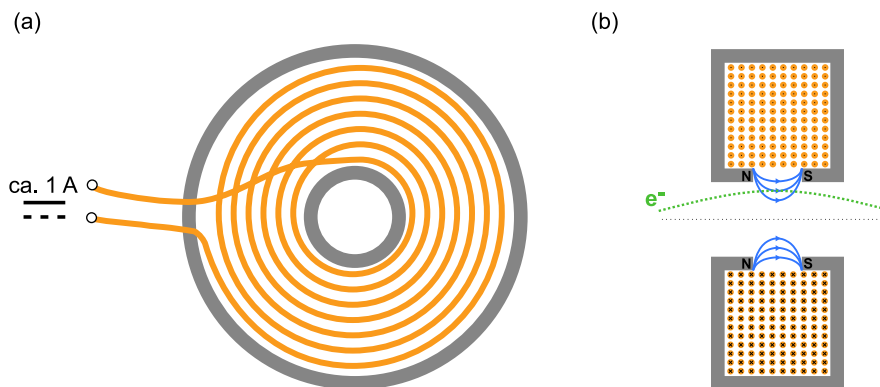
Figure 2.10: Schematic illustration of a shrouded coil magnetic lens. (a) Cross-section normal to the electron beam. (b) Cross-section parallel to the electron beam. The metal shield (shroud) is displayed in gray. Wires are displayed in orange. In (b), the direction of the electric current is indicated by dots/arrows on the wires. Magnetic field lines are sketched in blue, and an example of an approximate electron trajectory (without Lorentz-force-induced spiraling) is shown in dashed green. The dashed black line marks the electron-optical axis.

therefore shields magnetic fields efficiently. The electron beam passes through the hole in the middle. Around this hole, a wire is wrapped multiple times (several hundred windings), as shown in Fig. 2.10(a). A DC current of about 1 A is applied to create a magnetic field around the wire. The magnetic field is shielded by the housing and guided to a small gap located in the middle of the lens, as shown in Fig. 2.10(b). Electrons that pass straight through the center of the lens do not get deflected, since the field lines are parallel to their propagation direction. In contrast, electrons that do not travel along the electron-optical axis experience Lorentz forces. When the electron-optical axis of the magnetic lens is aligned with the electron beam, electrons that do not travel on this axis have a velocity component transverse to it. Furthermore, the Lorentz forces that they experience will also cause transverse velocity components. As a consequence of the transverse velocity components, these electrons experience Lorentz forces caused by magnetic field components *parallel* to the electron-optical axis, which act perpendicular to the electron-optical axis. Due to the inhomogeneity of the magnetic field, the electrons are deflected inwards in total (in addition to performing a spiraling motion). Therefore, the assembly acts as a positive lens for the electrons.

To record diffraction patterns, the current of the magnetic lens is adjusted such that the photoemission spot on the cathode is imaged on the electron detector. In addition, it is possible to record real-space images by increasing the current until the sample is imaged on the detector. The applied currents range from 1-1.5 A, depending on the imaging mode and the distances of sample, anode, and magnetic lens. Since such currents lead to significant resistance heating, the lens is cooled from the top with a cold finger. An additional copper ring around the lens ensures efficient heat transport from the lens to the cold finger. In addition, the magnetic lens

is mounted on a three-axis manipulator. This allows aligning the center of the lens to the electron beam. Furthermore, the size of the diffraction pattern can be changed by moving the lens parallel to the electron beam and adjusting the current (and thus the focal length of the electron lens) accordingly.

2.2.3   Detection

After passing through the magnetic lens and propagating for another $\sim 40\,\text{cm}$, the electrons are recorded with an electron detector. Here, a commercial electron camera is used (TVIPS TemCam F416). Electron detection is achieved with a phosphor screen (scintillator), which is fiber-coupled to a CMOS chip. A sketch of the detection method is presented in Fig. 2.11. The incoming electrons hit the phosphor and create photons, which are then guided towards the camera chip by optical fibers. It is thus an indirect detection method. To suppress thermal noise, the chip can be cooled to $0°\,\text{C}$. The detection method is sensitive not only to electrons but also to visible light. To avoid light on the detector, the phosphor screen is coated with $50\,\text{nm}$ of aluminum in addition to the standard coating provided by TVIPS. Nevertheless, contributions from light leakage on the detector are observed, likely due to inhomogeneities of the coating.
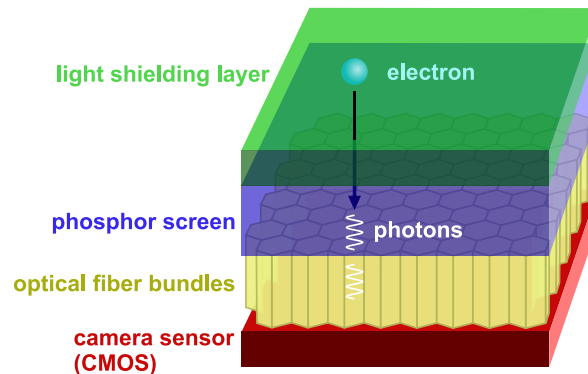
Figure 2.11: Schematic illustration of the electron detection method employed in the FED setup. The high-energy electrons transmit through the light-shielding layer (green) to the phosphor screen (blue), where they create multiple photons. Photons are then directed towards a camera sensor (red) with optical fibers, which are arranged in hexagonal bundles (yellow).

As an alternative to such indirect electron detectors, more recently also direct detection methods have become available, which collect secondary electrons created along the path of high-energy electrons through matter (see for example Ref. [FH07] for further details). A major advantage of this detection method is that a lot of noise sources are suppressed. In addition, the detector is not light-sensitive. On the other hand, recording multiple closely-spaced electron hits can be challenging, because the secondary charge can be shared between pixels [FH07; van20] and for some detectors also due to the way the digital signal is generated. Nevertheless, direct electron detectors offer an interesting alternative to indirect detection methods and are already successfully used for low-dose applications [Ves15; Gen16].

2.3 From diffraction patterns to the lattice dynamics

The electron diffraction experiment yields a series of diffraction images at different pump-probe delays, which are then analyzed to obtain the lattice response to laser excitation. This section provides an overview of different data analysis steps of time-resolved transmission electron diffraction data, both for polycrystalline samples and single crystals.

2.3.1 Processing of the diffraction images

In the first step of the data analysis, artifacts in the diffraction images should be removed. In general, artifacts depend on the detector and detection mode as well as on the electron lens(es). Here, the case of an integrating detection scheme is discussed (as opposed to electron counting). In this case, there is often a constant background contribution. This can easily be accounted for by subtracting the intensity of a "dark" image without electrons and pump laser. For light-sensitive electron detectors, depending on the pump wavelength and the quality of the light shield, there can also be a pump-induced background. This is more difficult to account for because it can change over time due to fluctuations or drifts of the pump beam. A mask can be applied to exclude regions with high laser background from the analysis.

Apart from background contributions, it should also be considered that typically not every pixel of the electron camera has exactly the same sensitivity. In particular, for the detector employed here, inhomogeneities arise due to the bundling of optical fibers (see Sec. 2.2.3). This can be accounted for with a flatfield correction. To record a flatfield directly, a homogeneous illumination with electrons is required, which is often difficult in home-built time-resolved electron diffraction setups. In the following, a method to obtain a high-quality flatfield from unfocused[5] polycrystalline or amorphous diffraction patterns is described.

If the diffraction pattern of the employed polycrystalline or amorphous material was perfectly circularly symmetric, all angular intensity variations would be due to different pixel sensitivities. Then, a flatfield could be obtained by dividing the diffraction pattern by its azimuthal average. However, in practice, this is typically not the case. For example, samples can have an in-plane preferred orientation caused by the substrate they were grown on (typically NaCl single crystals). In addition, there can be distortions in the diffraction image and the electron beam can be inhomogenous.

An example is presented in Fig. 2.12(a) and (b). Figure 2.12(a) shows an unfocused diffraction pattern of a polycrystalline nickel film. Figure 2.12(b) shows a flatfield obtained by dividing the diffraction pattern by its azimuthal average. Artifacts at the positions of the diffraction rings are clearly visible, highlighting that this simple comparison of the diffraction pattern to its azimuthal average is not sufficient to obtain a high-quality flatfield.

To solve the problem of a not perfectly circularly symmetric diffraction image, the image can be divided into sectors, with the zero-order beam at the center of the circle. This is illustrated in Fig. 2.12(c). Then, for each of the sectors, a flatfield of this sector is obtained by dividing the sector by the azimuthal average of this sector only. Here, the number of sectors needs to be significantly larger than the symmetry of the non-circularly symmetric features. While this eliminates the artifacts in the flatfield due to those features, it can introduce new artifacts at

---

[5]An unfocused diffraction pattern has fewer intensity variations in the radial direction compared to a focused one. Therefore, this improves the results, especially in the presence of lens aberrations, which distort the circular symmetry.
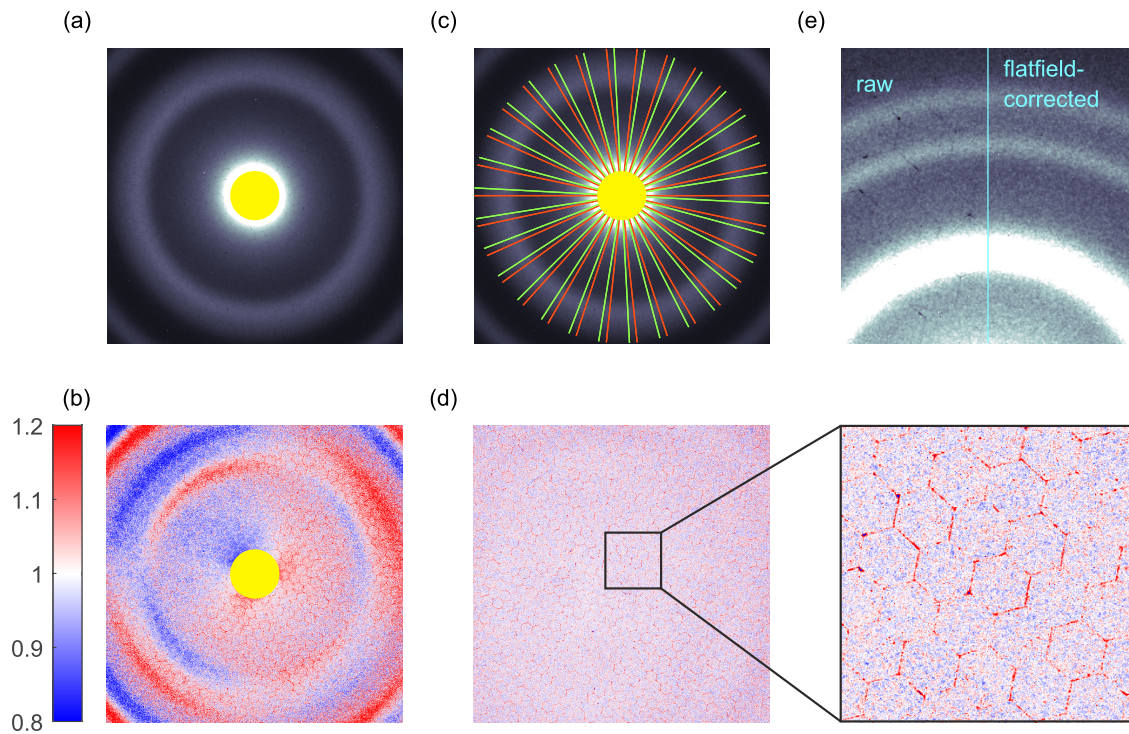
Figure 2.12: Flatfield determination based on unfocused diffraction patterns. (a) Unfocused diffraction pattern of nickel. The yellow circle marks the area that is not used for the flatfield calculation because it is too close to the zero-order beam. (b) Simple flatfield, obtained by comparing the diffraction pattern shown in Panel (a) to its azimuthal average. The flatfield contains artifacts, which are due to non-circularly symmetric features in the diffraction pattern. (c) Sectors used for an improved flatfield calculation. Here, the image is divided into 30 sectors, shown with red lines. A flatfield is calculated by comparing each sector to its azimuthal average. To avoid artifacts at the sector boundaries, the sectors are rotated multiple times. The green lines show an example of a rotation angle of $3°$. (d) Result of the improved flatfield calculation. Here, 30 sectors were used and they were rotated in steps of $1°$. 5 different diffraction patterns with different positions of the zero-order beam were used for this flatfield calculation. The improved flatfield clearly reveals the hexagonal structure of the detector while minimizing artifacts. Here, the correction factor is shown, which means that the red areas correspond to less sensitive regions of the detector. (e) Comparison of flatfield-corrected data to uncorrected data. Here, a diffraction pattern of polycrystalline cobalt is shown. The region shown here is the same as the enlarged region of Panel (d) shown below. The flatfield correction can remove the hexagonal structure from the experimental data.

the sector boundaries. This can be avoided by repeating the procedure multiple times, each time with a slightly more rotated sector distribution, as illustrated in Fig. 2.12(c). The resulting flatfields are then averaged.

Note that it is important to mask defective pixels, which would otherwise introduce artifacts in the flatfield. In addition, this procedure does not work very close to the zero-order beam. To obtain a flatfield of the whole detector area the electron beam can be displaced, for example with a permanent magnet, before repeating the flatfield procedure described above. Ideally, the displacement is repeated several times and the results are averaged. Finally, a high-quality

flatfield is obtained, as shown in Fig. 2.12(d). Here, the flatfield reveals the boundaries of the hexagonal fiber bundles which couple the phosphor screen to the camera sensor (see Sec. 2.2.3 for camera details). With the flatfield, this experimental artifact can be removed from the diffraction images, as demonstrated in Fig. 2.12(e).

After background subtraction and flatfield correction, the last image processing step is the normalization of the diffraction images to the electron flux. The electron flux can vary during a measurement, for example due to pointing or intensity drifts of the probe beam, or due to cathode degradation. A simple normalization method uses the total image intensity. Here, it is important to exclude problematic regions of the diffraction image, for example the zero-order beam (if saturated), beam stops, defective pixels, and regions outside the field of view. Note that this normalization method relies on good background subtraction. For single crystals, the normalization factor obtained in this way can often be further improved by subtracting a constant offset. Such an offset can be caused by a constant contribution to the image intensity due to defective pixels and/or residual background intensity. It can be obtained either by minimizing the correlation coefficient between normalized peak intensities and total image intensity, or by a linear fit to the (not normalized) average unpumped peak intensity as a function of total image intensity. An alternative to the normalization by the total image intensity is the normalization by the zero-order beam intensity. In the absence of an independent measure of the zero-order beam intensity (e.g. with a Faraday cup), the zero-order beam intensity can be extracted from the diffraction images. Due to the brightness of the zero-order beam, this scheme may require recording an additional low-exposure diffraction image right after every diffraction image in the data set to obtain the unsaturated zero-order beam intensity. When the probe delay is varied such as in the FED setup employed here, this normalization method can have advantages, particularly for measurements that contain a large range of pump-probe delays (up to tens or hundreds of picoseconds). However, it should be noted that for thicker samples, the zero-order beam can show a response to laser excitation due to higher-order scattering effects [Lig11]. This may lead to systematic errors if the zero-order beam is used for normalization.

2.3.2 Extraction of the lattice response to laser excitation

2.3.2.1 Signatures of the lattice response in diffraction

After the diffraction images have been corrected for experimental artifacts as described above, the lattice response to laser excitation can be extracted. There are several changes of the lattice that can be triggered by laser excitation. An overview is presented in Fig. 2.13.

First of all, electronic excitation of a material can launch coherent phonons, either by displacive excitation (DECP mechanism) [Zei92] or by impulsive stimulated Raman scattering (ISRS) [RJN87]. Coherent phonons lead to periodic changes of the structure factor and thus cause periodic intensity modulations of certain Bragg reflections [Wal17a]. These can be detected in time-resolved diffraction in case the time resolution of the experiment is smaller than the period of the coherent phonon [Wal16b]. Furthermore, the electronic excitation by the laser pulse causes a thermodynamic non-equilibrium between electronic and lattice degrees of freedom, which leads to energy flow to the lattice, i.e. the creation of phonons. These phonons are incoherent and therefore lead to an intensity reduction of the Bragg reflections (Debye-Waller effect, described for example in Refs. [WP75; Gia02; PDW11]). At the same time, the intensity
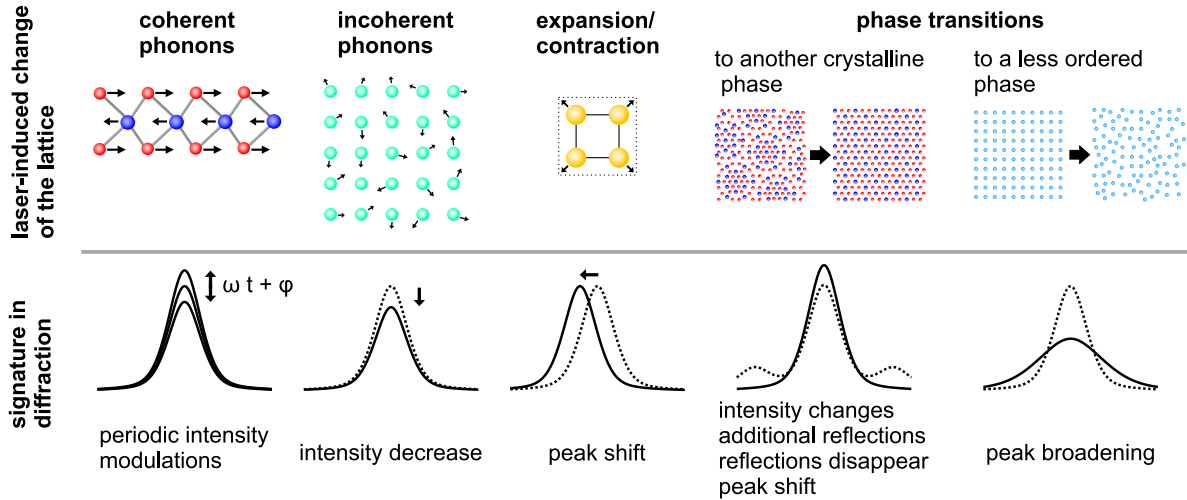
Figure 2.13: Overview of different lattice responses to laser excitation. The upper part illustrates possible laser-induced changes of the lattice. The lower part shows the corresponding signature in time-resolved diffraction.

of the background rises (diffuse scattering) [Tri10]. This decay of the Bragg reflection intensities due to incoherent phonons is the main observable employed in this work.

In addition, excitation of phonons typically increases the equilibrium interatomic distances due to the anharmonicity of the interatomic potential. In the case of femtosecond laser excitation, the sudden heating of the crystal thus typically launches a strain wave. In freestanding thin films, the strain wave reflects at both surfaces and results in a breathing motion of the film. The breathing motion corresponds to a modulation of the lattice constant and can therefore be observed as a periodic shift of the Bragg reflection positions. It is often observed even at normal incidence of the electron beam, which can be due to wrinkling of the freestanding thin film or to contributions from shear modes, as discussed in Ref. [Har09]. The period of the oscillation depends on the film thickness and the speed of sound and is typically on the order of several picoseconds. Note that in addition to lattice anharmonicities, also the electronic excitation [Nie06; Wan08] and magnetostrictive effects [Rep16; Koc17; Rei18; Pud19] can contribute to the total stress.

Finally, laser excitation can also drive structural phase transitions. These can be either from one crystalline phase to another, for example melting of a charge density wave [Eic10], or to a less ordered phase, e.g. (pre-)melting of the material [Ern09; Vas18]. The former leads to changes in the Bragg reflection intensities and positions according to the rearrangement within and/or changes of the unit cell, while the latter also leads to an increase of the Bragg reflection width due to the increased disorder.

The materials presented in this work do not exhibit structural phase transitions in the measured temperature range. Coherent phonons were not observed in any of the experiments. Therefore, in the remainder of this section, the focus lies on the analysis of intensity changes due to incoherent phonons.

The intensities of the Bragg reflections decrease with increasing phonon population. The reason for this intensity decrease is that incoherent phonons introduce disorder in the crystal lattice (dynamic disorder), as illustrated schematically in Fig. 2.13. The relationship between

the Bragg reflection intensities and the atomic displacements caused by phonons was first theoretically described by Peter Debye and Ivar Waller at the beginning of the 20th century [Deb13; Wal23]. The relevant quantity for describing the influence of incoherent phonons on the Bragg reflection intensities is the mean-squared atomic displacement (MSD), which is the result of all the phonon modes excited in the crystal. This description of the atomic displacements with MSDs is employed throughout this work. Note that by describing the effect of the time-dependent atomic motion on the diffraction patterns with MSDs, correlations between the atoms are neglected. This is an approximation because chemical bonds cause correlations between the movements of different atoms [Gia02]. Nevertheless, it is a reasonable description when many different phonon modes are excited incoherently [WP75; War90], which is the case for the experiments presented in this work.

Depending on the structure of the material, the MSD can also be anisotropic. A pronounced example of anisotropic MSD is discussed in Chapter 3, which presents the anisotropic structural dynamics of laser-excited black phosphorus. The general case can be described by the so-called anisotropic mean-squared displacement matrix or U-matrix [Tru96], which is a symmetric 3x3 matrix describing the MSD of an atom in all directions. The MSD in a certain direction $\hat{\boldsymbol{n}}$ is then given by:

$$\langle \mathbf{u}^2 \rangle_{\hat{\mathbf{n}}} = \hat{\boldsymbol{n}}^{\mathrm{T}} \mathbf{U} \hat{\boldsymbol{n}}. \tag{2.1}$$

Depending on the space group of the material and the Wyckoff position of the atom, there can be symmetry-related constraints for the U-matrix, which are tabulated in Ref. [WP75]. In addition, note that MSDs differ for symmetry-inequivalent atoms in the unit cell, i.e. in materials consisting of several elements or if the same element is located at different Wyckoff positions. In such cases, the MSD of each symmetry-inequivalent atom is described by a different U-matrix.

Depending on the crystal structure and the interatomic forces, the resulting MSD can be isotropic or anisotropic. Figure 2.14 shows several examples. The first example in Fig 2.14(a) shows the isotropic case, i.e. $U_{11} = U_{22} = U_{33}$ and all off-diagonal elements are zero. In contrast, Panels (c) and (d) depict examples of anisotropic cases. Note that anisotropic MSDs are not ellipsoids, but rather have a peanut-like shape. Alternatively, it is also possible to describe the atomic displacements in terms of thermal ellipsoids, which are surfaces that mark a certain probability of atomic displacement (typically 50 %) [Tru96].

To describe the effect of the MSD on the Bragg reflection intensities, the so-called temperature factor τ is employed. The structure factor F in the presence of atomic vibrations is then given by [PDW11]:

$$F(\mathbf{q}) = \sum_k f_k\, \tau_k \exp(i\mathbf{q} \cdot \mathbf{r}_k). \tag{2.2}$$

Here, f_k are the atomic form factors, $\mathbf{q}$ is the scattering vector ($q = 4\pi \sin(\theta)/\lambda$ with λ being the electron wavelength and θ being the Bragg angle), $\mathbf{r}_k$ stands for the positions of the individual atoms in the unit cell and the summation is performed over all atoms in the unit cell. The temperature factor is related to the U-matrix as follows [Gia02]:

$$\tau = \exp\{-\frac{1}{2}[U_{11}(ha^*)^2 + U_{22}(kb^*)^2 + U_{33}(lc^*)^2 +$$
$$+ 2U_{12}ha^*kb^* + 2U_{23}kb^*lc^* + 2U_{13}ha^*lc^*]\}. \tag{2.3}$$

Here, h, k, and l denote the Miller indices and a^*, b^*, and c^* denote the reciprocal lattice vectors of the crystal. In the isotropic case, $U_{11} = U_{22} = U_{33}$ and all non-diagonal elements
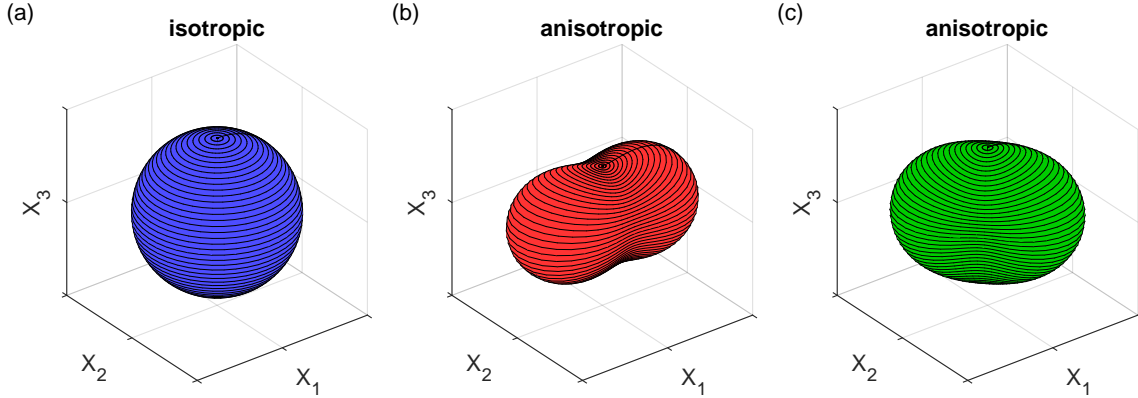
Figure 2.14: Examples of isotropic and anisotropic atomic MSDs. (a) Isotropic MSD, i.e. all diagonal elements of the U-matrix are equal and all non-diagonal elements are zero (see text for examples). (b) Example of an anisotropic MSD in which the diagonal elements are different (here: $U_{11} = 2\,U_{22} = 2\,U_{33}$). (c) Example of an anisotropic MSD in which the diagonal elements are the same, but a non-diagonal element is non-zero ($U_{12} = U_{21} = -0.15\,U_{11}$).

are zero. For example, this is the case for mono-atomic materials with face-centered cubic (fcc) or body-centered cubic (bcc) crystal structures, as shown in Table 2.1. For hexagonal close-packed (hcp) mono-atomic materials, assuming isotropic MSD is an approximation. Whether this approximation is reasonable depends on the unit cell dimensions, specifically on the ratio of the lattice constants c/a [WIO71; MD19]. For c/a smaller than or equal to ~1.63, isotropic MSD is a good approximation, which is the case for all materials studied in this work.

crystal structure	fcc	bcc	hcp
space group	225	229	194
Wyckoff position	4a	2a	2c
U-matrix constraints	$U_{11} = U_{22} = U_{33}$ $U_{12} = U_{13} = U_{23} = 0$	$U_{11} = U_{22} = U_{33}$ $U_{12} = U_{13} = U_{23} = 0$	$U_{11} = U_{22}$ $U_{13} = U_{23} = 0$
examples	Ni, Pt, Au, Cu	Fe, Cr	Co, Gd, Tb

Table 2.1: U-matrix constraints for three common crystal structures of mono-atomic materials, face-centered cubic (fcc), body-centered cubic (bcc), and hexagonal close-packed (hcp). The space groups and Wyckoff positions stem from the Inorganic Crystal Structure Database (ICSD) and U-matrix constraints were taken from Ref. [WP75]. Note that these are only valid for mono-atomic lattices with these crystal structures, typically simple elemental metals.

In the isotropic case, Eq. 2.3 can be further simplified to give:

$$\tau = \exp\{-\frac{1}{2} U_{11} \mathbf{q}^2\} = \exp\{-\frac{1}{2} \times \frac{1}{3} \langle \mathbf{u}^2 \rangle \, \mathbf{q}^2\}. \tag{2.4}$$

Here, $\langle \mathbf{u}^2 \rangle$ stands for the total MSD considering *all* directions, i.e the mean-squared distance of the atom from its equilibrium position. The factor 1/3 follows from the fact that the momentaneous displacement of the atom can be along any direction. The MSD in a certain direction corresponds to the time-average of the squared projection of the displacement in this partic-

ular direction, e.g. $U_{11} = \langle(\mathbf{u} \cdot \hat{\mathbf{x}}_1)^2\rangle$. Since the MSD is isotropic, $\langle(\mathbf{u} \cdot \hat{\mathbf{x}}_1)^2\rangle = \langle(\mathbf{u} \cdot \hat{\mathbf{x}}_2)^2\rangle = \langle(\mathbf{u} \cdot \hat{\mathbf{x}}_3)^2\rangle = \frac{1}{3}\langle\mathbf{u}^2\rangle$.

Finally, the intensities of the Bragg reflections are proportional to the *square* of the structure factor. Hence, for isotropic MSDs and if all atoms are symmetry-equivalent, the Bragg reflection intensities are given by:

$$I(\mathbf{q}) = I_0(\mathbf{q}) \exp\{-\frac{1}{3}\langle\mathbf{u}^2\rangle\,\mathbf{q}^2\} \tag{2.5}$$

Here, I_0 denotes the intensity of the Bragg reflection in the absence of lattice vibrations. In a time-resolved diffraction experiment, the focus lies on the relative changes of Bragg reflection intensities after excitation, which are related to transient MSD changes as follows:

$$\frac{I(t)}{I(t < 0)} = \exp\{-\frac{1}{3}\Delta\langle\mathbf{u}^2\rangle\,\mathbf{q}^2\} \tag{2.6}$$

Here, $\Delta\langle\mathbf{u}^2\rangle = \langle\mathbf{u}^2\rangle(t) - \langle\mathbf{u}^2\rangle(t < 0)$ is the transient MSD change. The next sections describe how to extract such MSD changes reliably from experimental data.

2.3.2.2 Data analysis for polycrystalline materials

For polycrystalline materials, the diffraction pattern consists of Debye-Scherrer rings, as shown in Fig. 2.15(a). In this case, after correcting for drifts of the zero-order beam, an azimuthal average is calculated (radial profile/RP), yielding one-dimensional data as presented in Fig. 2.15(b) (dashed red curve). There can be non-circularly-symmetric distortions in the image, caused for example by imperfect alignment of the magnetic lens. The distortions are typically stronger for higher scattering vectors and thus lead to a broadening of the outer diffraction rings in the RP. In such cases, the RP can be improved by taking sector-wise RPs, similar to the flatfielding procedure described in Sec. 2.3.1. One of the sector-wise RPs is chosen as reference and the distance axis of the others is corrected with a correction parameter γ:

$$r' = \left(\frac{r}{r_0}\right)^{\gamma} r_0. \tag{2.7}$$

Here, r is the original distance from the center, r' is the corrected distance, and r_0 is an arbitrary distance close to the first diffraction ring (here: the maximum of the first diffraction ring in the reference RP). For each sector-wise RP, γ is chosen such that the residuals to the reference RP are minimized. Only after this correction, the sector-wise RPs are averaged. The correction can significantly increase the sharpness of outer diffraction rings, as presented in Fig. 2.15(b) (green curve).

After calculating the RPs, the next step is to analyze their transient changes. Fig. 2.16 shows an example of time-resolved changes in platinum by presenting the RP before laser excitation and pump-induced changes of the RP at selected time delays. The amplitude of the diffraction rings decreases due to the Debye-Waller effect. At the same time, the intensity of the background rises. Due to the limited coherence of the electron beam[6], different peaks overlap, especially for higher scattering vectors. Disentangling the strong overlap of different peaks as well as the simultaneous dynamics of background and peaks are major challenges in

---

[6]The coherence can be improved by a tighter focus on the cathode. However, this comes with a cost of reduced time resolution and/or signal-to-noise ratio, since space charge effects increase when the electrons in the pulse are closer to each other.
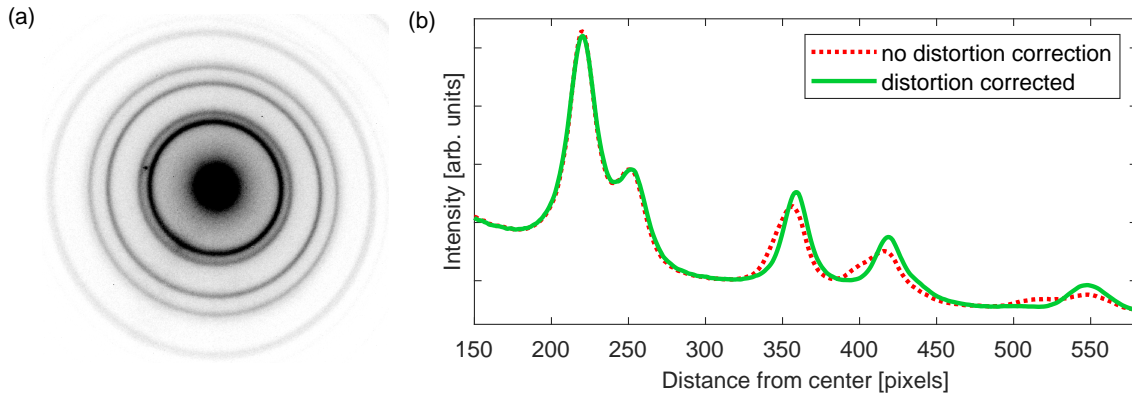
Figure 2.15: Diffraction from polycrystalline samples. (a) Diffraction pattern of a polycrystalline nickel film. This diffraction pattern is visibly distorted, likely due to misalignment of the magnetic lens. (b) Radial profile (RP) with and without distortion correction. The distortion-corrected RP was calculated based on 12 sector-wise RPs. Details of the distortion correction are described in the text.

the analysis of time-resolved data from polycrystalline samples. In this subsection, an approach to extract MSD dynamics reliably from time-resolved polycrystalline data is presented, which was published in Ref. [Zah21d]. The code of this fitting routine is publicly available [Zah21c].

In a conventional analysis of polycrystalline data, only the most prominent diffraction rings are considered, typically by performing a fit to the peaks in the RP and extracting time-dependent changes of the fit parameters. However, this leads to many time-dependent fit parameters. These often exceed the number of physical parameters of the lattice that change after laser excitation because some information is encoded in all reflections, namely lattice expansion and MSD rise. The strong overlap of different rings means that their fit parameters are correlated, which can lead to imprecise fit results. In addition, background subtraction is challenging, since there are only few regions in the RP without contributions from diffraction rings. For these reasons, inconsistencies between MSD rises and lattice expansions extracted from different rings are often observed.

An approach to minimize time-dependent fit parameters is to consider the full diffraction pattern and directly fit the "physical" lattice changes following laser excitation, instead of time-dependent parameters for individual rings. Such a global fitting approach requires prior knowledge about the expected lattice changes. Here, it is assumed that no phase transitions or coherent phonons are induced by the laser excitation, therefore only the MSD and the lattice constant change. In addition, only materials with one atom per unit cell are considered. The approach can however be extended to cover also more complex materials or heterostructures.

The global fitting routine consists of two steps: first, a fit is performed to the RP before laser excitation (static fit). Second, a fit is performed to time-dependent changes in the RP (dynamic fit), with the fit parameters limited to MSD change, expansion, and changes of the background. In the first step (static fit), it is important to obtain a very good description of the RP before laser excitation. For optimal signal-to-noise ratio of the experimental data, all RPs recorded before the arrival of the pump pulse are averaged. As an example, data recorded on platinum are discussed here. The average of all RPs before laser excitation is presented in Fig. 2.16(a) (blue curve). Since the crystal structure of the sample is known (platinum has an fcc crystal structure with a lattice constant of 3.924 Å [ESJ51]), the positions of the rings
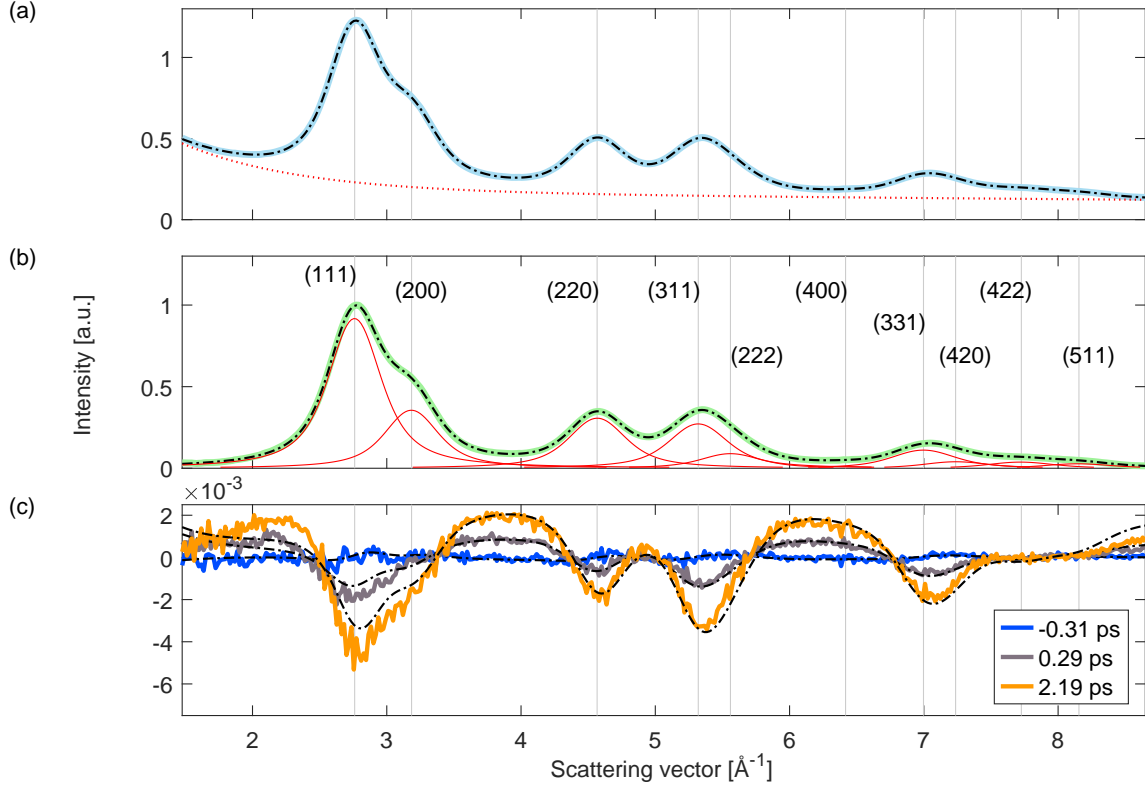
Figure 2.16: Azimuthally averaged diffraction pattern (radial profile, RP) of platinum and pump-induced changes. (a) RP of platinum before laser excitation. The solid blue curve represents experimental data and the dashed black curve is the result of the global fitting analysis. The background contribution (fit result) is shown as a dashed red curve. (b) RP after background subtraction. The green curve corresponds to the experimental data and the dashed black curve is the result of the global fit. The contributions from the individual Bragg reflections are displayed in red. (c) Time-resolved changes in the RP for selected time delays. The solid curves are experimental data and the black dashed curves correspond to the fit results. The curves represent differences compared to the RP before laser excitation. Note that the intensity units are the same in all three panels. In addition, the x-axis was converted from image pixels to scattering vectors using the result of the global fit. Adapted from Ref. [Zah21d].

in reciprocal space are known. Nevertheless, due to distortions of the diffraction pattern such as spherical aberrations of the magnetic lens, the relationship between the distance of a ring from the zero-order beam (ring radius) and the scattering vector is non-linear. Therefore, a distortion correction parameter γ is introduced as a fit parameter. In addition, the distance from the zero-order beam in pixels needs to be converted into scattering vector. Therefore, the radius of the first ring in pixels, r_1, is also a fit parameter. Including the distortion correction, the radii r_i of the other rings are then determined by:

$$r_i = \left(\frac{q_i}{q_1} \right)^{\gamma} r_1. \tag{2.8}$$

Here, q_i are the scattering vectors of the diffraction rings. In the absence of distortions, $\gamma = 1$ (no correction). For barrel distortions, which is the case here, γ is smaller than 1 (here: around 0.96). In the case of pincushion distortions, γ would be larger than 1. With Eq. 2.8, which is a phenomenological correction, the major part of the distortion can be accounted for. In

addition, to obtain a precise description of the static RP, individual radius correction factors f_i are required as fit parameters, which are constrained such that the radii cannot deviate by more than a few percent (here: 2%) from the radii given by Eq. 2.8. The constraint minimizes cross-talk of the positions of overlapping diffraction rings in the fit, which is particularly important for rings that are not clearly visible as distinct peaks in the RP, e.g. the (222) reflection.

The peaks in the RP are described as Lorentzians. The peak amplitudes are fit parameters. For perfectly polycrystalline samples, the amplitudes could also be obtained from structure factor calculations or literature. However, many thin-film samples grown on NaCl crystals have a preferred orientation, which changes the relative intensities of the diffraction rings. By fitting the peak amplitudes in the RP, the fitting procedure can be easily applied to samples both with and without preferred orientation.

The width of the Lorentzians in reciprocal space is one fit parameter, w_{reci}. The width of the rings in reciprocal space is thus the same for all peaks, which means that broadening due to finite crystallite sizes (Scherrer equation) is not considered. This is a reasonable approximation since the broadening in time-resolved electron diffraction experiments is typically dominated by the finite coherence of the electron pulses. Note that the width of the peaks in the RP, w_{i}, is slightly different for different peaks due to the non-linear relationship between pixels and scattering vectors (caused by distortions, see Eq. 2.8). In total, the fit function describing all rings in the observed range of reciprocal space is given by:

$$F(r) = \sum_{i=1}^{N} \frac{A_i}{\left(1 + \left(\frac{r - r_i f_i}{w_{\mathrm{i}}}\right)^2\right)} \ . \tag{2.9}$$

Here A_i are the amplitudes of the rings (fit parameters) and N is the number of diffraction rings in the observed range of reciprocal space.

In addition to the intensity from the rings, there is also a significant background intensity. This intensity arises from the tail of the zero-order beam, static disorder of the crystal, and diffuse scattering (dynamic disorder). Depending on the sample, further contributions can also come from the substrate or the surfaces of the thin film. The background is time-dependent, since diffuse scattering increases when more phonons are created. The intensity of the zero-order beam can also be time-dependent due to higher-order scattering effects [Lig11]. To describe the background intensity in the fit, a phenomenological function is used, which is chosen depending on the experimental conditions. For the measurement presented here, the following function was used:

$$B(r) = a \times \exp\{-r/b\} + c + d \times r. \tag{2.10}$$

The sum $F + B$ is then convolved with a Gaussian to account for the finite coherence of the electron pulses. In addition to the broadening due to the limited coherence, particularly the outer rings can be broadened further by distortions that are not circularly symmetric. Furthermore, the focusing of the magnetic lens can be slightly different for different diffraction orders [Wal16b]. To correct for such effects, an additional fit parameter δ is introduced, which distorts the distance axis linearly before the convolution:

$$r' = r\,(1 - \delta \frac{r - r_{\mathrm{start}}}{r_{\mathrm{end}} - r_{\mathrm{start}}}). \tag{2.11}$$

r_{start} and r_{end} are the radii of the beginning and the end of the fit range, respectively. δ is typically equal or larger than zero. The former corresponds to no correction and the latter

means that the width of the Gaussian (and therefore the broadening) effectively increases with scattering vector.

Regarding the width of the Gaussian for the convolution, it should be noted that this fit parameter strongly correlates with the width of the Lorentzians (w_{reci}), which is not surprising since both of them control the width of the peaks in the RP. This means that the fit result for these two parameters usually depends on the starting parameters. In order to nevertheless obtain reliable results, the global fitting routine includes a systematic variation of these two parameters. The combination that yields the least residuals is identified and used for the further steps. More information about the width optimization is available in Ref. [Zah21d].

The static fit result is presented in Fig. 2.16(a) as a dashed black curve. An excellent description of the experimental RP is achieved. Fig. 2.16(b) shows the experimental RP with the fit result for the background contribution subtracted (green curve) and the contributions of the individual rings (fit result, red curves). The dashed black curve corresponds to the result of the static fit, again highlighting the excellent agreement of fit result and experimental data. Such good agreement is necessary for the subsequent step of the fitting routine.

In the second step of the fitting routine (dynamic fit), time-dependent changes of the RP are analyzed. The results of the static fit are used to minimize time-dependent fit parameters. Therefore, only the following time-dependent changes are allowed:

- decreases of the diffraction ring intensities, corresponding to an increase of the MSD. Equation 2.6 is used here to describe the intensity changes, which is valid for mono-elemental materials with isotropic MSD. It is possible to extend the fitting to more complex materials, which would require introducing more than one MSD fit parameter as well as a structure factor calculation.

- expansion or contraction of the lattice, which changes the positions of all diffraction rings:

$$q_i(t) = \frac{q_{i,0}}{1 + \epsilon(t)} \,. \tag{2.12}$$

  Here, $q_{i,0}$ is the scattering vector before laser excitation.

- changes of the background parameters. The background increases, which is caused by an increase of diffuse scattering due to the additional phonons excited.

Since some background parameters are correlated, the fit result can sometimes be improved by constraining their maximum change from one delay to the next. However, care must be taken to ensure that the boundaries are wide enough to not alter the extracted MSD dynamics. The boundaries must be such that the time-dependent increase of the background can be adequately described for all delays.

The results of the dynamic fit are presented in Fig. 2.16(c) for three different pump-probe delays. Solid curves are experimental data and dashed black curves represent fit results. In general, good agreement with the experimental data is observed. It is noticeable that the fit result underestimates the time-dependent peak intensity changes for low scattering vectors while overestimating them for high scattering vectors. This is likely due to higher-order scattering effects beyond the kinematic limit, which "redistribute" intensity between diffraction orders (including the zero-order beam). Hence, these effects lead to deviations from the relationship of Eq. 2.6. For the example discussed here, platinum metal, higher-order scattering effects are
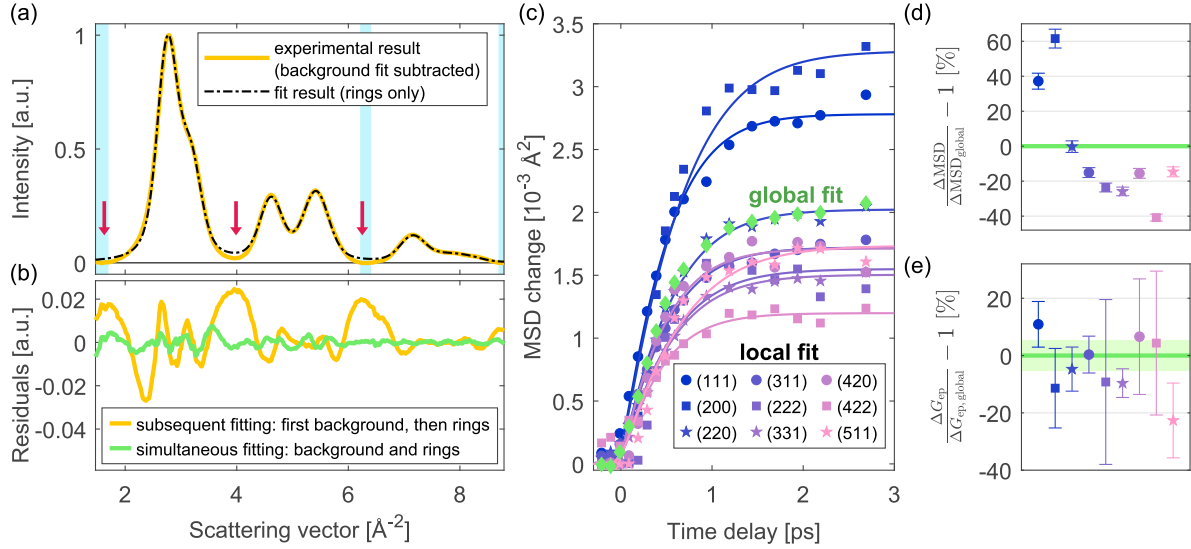
Figure 2.17: Comparison of the global fitting approach to other analysis methods. (a) Fit result for the case in which subsequent fits of background and diffraction rings are performed. Light blue areas mark the regions to which the background fit is performed. The solid yellow curve represents the experimental data after background subtraction and the dashed black curve represents the result of a fit of the diffraction rings (without background). The red arrows mark areas of particularly high disagreement between background and rings. (b) Residuals of the subsequent fit shown in (a) (yellow curve) and residuals of the global fitting routine, which fits rings and background simultaneously (green curve). (c) Result of a "local" fit of the MSD changes, i.e. the intensity change of each ring is a separate fit parameter. The result of the global fit is shown as green diamonds. Solid curves are fits with a two-temperature model (TTM). (d) Amplitude of the MSD changes of the individual peaks shown in (c), relative to the result of the global fit (green line). The values correspond to TTM results at $3\,\mathrm{ps}$. The error bars were calculated from the standard errors obtained from the TTM fits, assuming that the MSD is proportional the to temperature (high-temperature limit, see Sec. 2.3.2). The error bar of the global fit result falls within the line width. (g) Values for the electron-phonon coupling parameter G_{ep} extracted with a TTM from the local fits, relative to G_{ep} from the global fit (green line). The error bars correspond to standard errors obtained from the TTM fits. The standard error of the global fit is displayed as a shaded green area. Adapted from Ref. [Zah21d].

probably present in the RP due to its high atomic number and density. In such a case, if fits on individual diffraction rings were performed, different rings would yield different results for the amplitudes of the MSD changes. Since the global fitting routine extracts the MSD dynamics based on the full diffraction pattern, it is likely more accurate compared to "local" fits of individual diffraction rings in the presence of multiple scattering effects.

In addition, deviations of the fit result from the experimental data are observed at both ends of the fit range. These are likely due to the phenomenological background function. Furthermore, the results for the background are generally expected to be less precise at the ends of the fit range, because the comparison between experiment and fit ends there. However, for most of the fit range, both the background and the diffraction ring changes are well described by the fit result.

The global approach presented here has two main advantages, which are illustrated in Fig. 2.17. The first advantage is that the fit is performed to both diffraction rings and back-

ground simultaneously. An alternative approach is to first subtract a background and then perform a fit to the diffraction rings only. For example, the background can be subtracted by fitting a background function to user-defined "background regions", which is illustrated in Fig. 2.17(a). The light blue areas mark the background regions and the RP after background subtraction is shown as a yellow curve. The subsequent fit of the diffraction rings is shown as a dashed black curve. The main problem of this approach is that the background regions typically contain contributions from the diffraction rings as well (due to the limited coherence). The background is thus overestimated in the first step, leading to bad agreement between fit and experiment in the second step, when a fit is performed to the diffraction rings. Regions of high deviations are indicated by red arrows. An additional disadvantage is that the fit result for the background depends on the choice of background regions.

Figure 2.17(b) compares the residuals of this subsequent fitting approach (yellow curve) to the residuals of the static fit of the global fitting routine (green curve). The global fit exhibits much lower residuals and therefore achieves a better description of the static diffraction pattern. A good description of the static pattern is essential to obtain accurate results for the time-dependent quantities, in particular, the background subtraction has a significant influence on the amplitude of the MSD dynamics.

The second advantage is that the global fit results for the lattice dynamics are based on the full diffraction pattern instead of individual rings. Fig. 2.17(c) shows the results of a fit in which the intensities (and thus the MSD changes) of different rings are separate fit parameters ("local" fit). To ensure direct comparability to the global fit, the same fit function is used. Due to the significant overlap of diffraction rings, expansion is not considered[7] and all MSD changes are constrained to be non-negative. Different rings yield different results for the MSD changes, an ambiguous result since the same MSD change is encoded in all diffraction rings. Due to this ambiguity of the local fit, the final result for the MSD dynamics depends on which rings are considered in the analysis. In particular, the amplitude of the MSD rise differs significantly for different diffraction rings, as shown in Fig. 2.17(d). Similarly, also values for the electron-phonon coupling parameter G_{ep} extracted from a local fit can vary significantly, as presented in Fig. 2.17(e). In contrast, the global fit yields one result for the MSD change (and G_{ep}), which is based on all diffraction rings.

In summary, the global fitting routine presented here minimizes time-dependent fit parameters by performing a fit of physical quantities (MSD rise, expansion) to the full diffraction pattern. It can be applied in the absence of phase transitions and/or coherent phonons and removes ambiguities compared to other analysis approaches, yielding reliable results for the lattice dynamics. The approach described here can be directly applied to all materials with one atom per unit cell, and it could also be extended to describe more complex materials and heterostructures.

2.3.2.3   Data analysis for single crystals

For single crystals, for example exfoliated layered materials, Bragg reflections are observed as peaks in the diffraction pattern, as shown in Fig. 2.18(a). Here, the observed Bragg reflections depend on the orientation of the sample relative to the electron beam and can be determined

---

[7]Typically, expansion effects are small and whether or not expansion is considered in the fit has a negligible effect on the MSD dynamics.

with the Ewald sphere construction. For high-energy electron scattering, the Ewald sphere is almost flat on the length scales of the reciprocal lattice vectors. This is illustrated in Fig. 2.18(c). Therefore, many different Bragg reflections are observed at once, which is an advantage. For example, analyzing a large number of Bragg reflections can enable the separation of MSD changes of different atoms in the unit cell. An important point to keep in mind is that with increasing scattering vector, the Ewald sphere intersects the Bragg reflections in reciprocal space further from their centers, which can have implications for the observed dynamics [Win21].
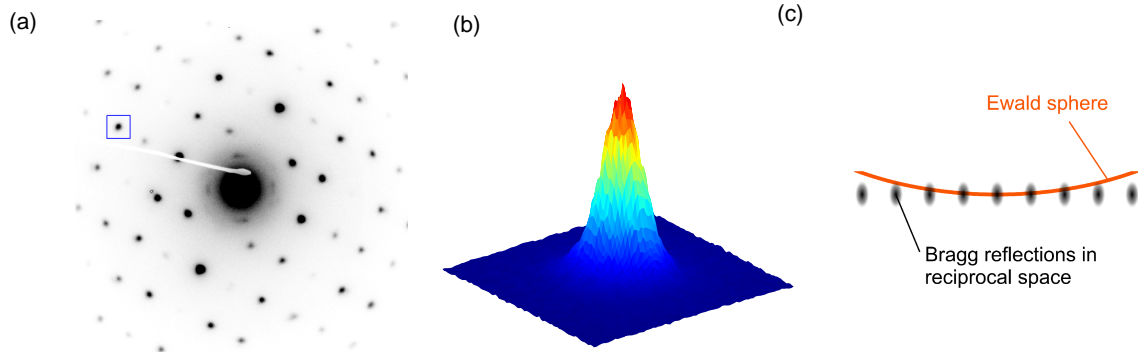
Figure 2.18: Diffraction from a single crystal. (a) Example diffraction pattern from a single crystal (here: black phosphorus). The white shadow is caused by a beam block for the zero-order beam. (b) Example of the shape of an observed Bragg reflection, marked in Panel (a) with a blue rectangle. (c) Schematic illustration of the Ewald sphere construction for high-energy electron diffraction. Here, the situation for normal incidence is presented. The Bragg reflections are sketched in black. The shape of the Bragg reflections in reciprocal space depends on the sample quality as well as on the thickness of the sample. The elongation of the Bragg reflections in the direction of the sample normal is caused by the small sample thickness of only tens of nanometers. Due to the large Ewald sphere in high-energy electron diffraction, many Bragg reflections are observed at once. With increasing scattering vector, the distance between the observed part of the reflection and its center increases.

To extract time-resolved changes in the diffraction patterns, fits to observed Bragg reflections are performed. The fit routine employed here was developed by Yoav William Windsor. For exfoliated high-quality crystals, the shape of the observed reflections is typically determined mostly by the electron beam properties, which depend on the spot size of the probe beam on the cathode. As an example of a typical shape of a reflection, Fig. 2.18(b) shows a close-up of the reflection marked in Fig. 2.18(a). A two-dimensional Pseudovoigt function is used as a fit function, which has enough free parameters to yield a good description of the observed reflections:

$$P(x,y) = a\left[(1-\eta)\exp\left(-\ln(2)\left(\left(\frac{x-x_0}{2s_x}\right)^2 + \left(\frac{y-y_0}{2s_y}\right)^2\right)\right) + \right.$$
$$\left. + \eta\left(\frac{1}{1 + \left(\frac{x-x_0}{2s_x}\right)^2 + \left(\frac{y-y_0}{2s_y}\right)^2}\right)\right]. \quad (2.13)$$

Furthermore, there is a free parameter for the rotation of the axes $\hat{x}$ and $\hat{y}$ with respect to the image axes.

In addition to the reflections themselves, there are also background contributions to the intensity in the region of the reflection, although much less compared to polycrystalline data. As in the case of polycrystalline materials, these contributions stem for example from the tail of the zero-order beam and from diffuse scattering caused by static and dynamic disorder. To take static and time-dependent background contributions into account, a tilted plane $T(x, y) = c_0 + c_1 x + c_2 y$ is added to the fit function. The fit is performed to a square area around the reflection, as shown in Fig. 2.18(a) and (b). Based on the fit results for the changes of the peak amplitudes a in Eq. 2.13, MSD dynamics can then be extracted, as described in Sec. 2.3.2.1. Furthermore, size changes of the unit cell (e.g. expansion) are reflected in changes of x_0 and y_0 as functions of pump-probe delay.

2.3.3   The relationship between MSD and lattice temperature

The last two sections described how to obtain the MSD dynamics from the diffraction patterns. If the lattice is in thermal equilibrium, the MSD can be directly converted into lattice temperature, provided that the phonon properties of the material are known. However, the assumption of a thermalized phonon distribution is often not justified on short timescales after laser excitation. Typically, direct phonon-phonon scattering is not efficient enough to establish thermal equilibrium of the phonons on sub- or few-ps timescales [ROM20]. In this case, how far from equilibrium the transient phonon population is depends on the details of electron-phonon scattering. In particular for materials with optical phonons, pronounced deviations from thermal equilibrium can occur. As an example, graphite has strongly-coupled optical phonons (SCOPs), which are excited much more efficiently by the photo-excited carriers [Cha14]. This leads to a pronounced transient nonthermal phonon distribution with these phonons being excited much more than in thermal equilibrium. In such cases, a lattice temperature is not defined. A similar behavior is also observed for black phosphorus, as described in Chapter 3. For simple metals, nonthermal phonon populations have been observed as well, e.g. in aluminum [Wal16a]. It is thus important to verify that the phonon distribution is actually thermal (or close to thermal) before converting MSD into lattice temperature.

For materials with only one atom per primitive unit cell, the conversion can be done using the phonon density of states (DOS) $g(\omega)$. The MSD as a function of temperature is then given by [PDW11]:

$$\langle \mathbf{u}^2 \rangle = \frac{\hbar}{2m} \int_0^\infty \coth\left(\frac{\hbar\omega}{2k_{\mathrm{B}}T}\right) \frac{g(\omega)}{\omega} d\omega. \qquad (2.14)$$

Here, m is the mass of the atom and ω is the phonon frequency. $g(\omega)$ is the DOS per atom, which means that its integral over all frequencies is equal to 3. Note that as the phonon frequency decreases, $g(\omega)$ goes to zero, but the term $\coth\left(\frac{\hbar\omega}{2k_{\mathrm{B}}T}\right)$ as well as $\frac{1}{\omega}$ diverge. In practice, it is thus not trivial to compute the integral of Eq. 2.14. Small errors of the phonon DOS in the low-frequency region can lead to very large errors of the MSD. In practice, the accuracy of the calculation can be improved by replacing the low-frequency region of the DOS with the result of a fit with a polynomial function that goes to zero at least quadratically. A quadratic dependence of the DOS on the frequency corresponds to a constant speed of sound (long-wavelength limit). Therefore, the leading term in the long-wavelength/low-frequency limit should be quadratic.
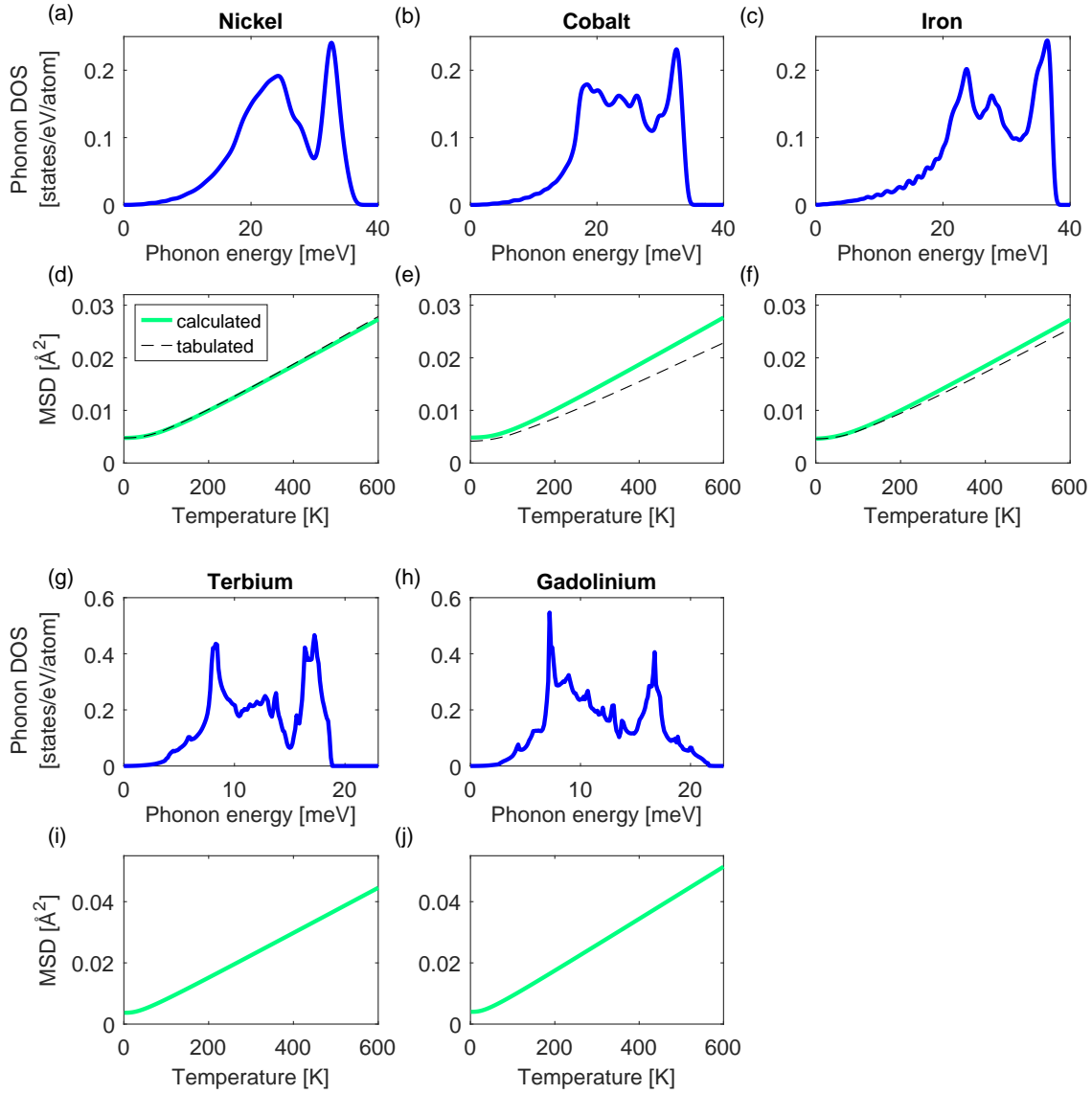
Figure 2.19: Phonon DOS and temperature-dependent MSDs of the ferromagnets studied in this work. (a) Phonon DOS of nickel obtained from a DFT calculation. (b) Same as (a), but for cobalt. (c) Same as (a), but for iron. (d) MSD as a function of temperature, calculated based on the phonon DOS shown in (a). For improved accuracy, the region $\hbar\omega < 5\,\mathrm{meV}$ was replaced by the result of a fit to the phonon DOS with the following function: $y(\hbar\omega) = a\,(\hbar\omega)^2 + b\,(\hbar\omega)^3$. For comparison, the dashed black curve shows the tabulated result from Ref. [PDW11]. (e) Same as (d), but for cobalt. In this case, the tabulated result from Ref. [PDW11] is an estimation based on the Debye model. (f) Same as (d), but for iron. (g) Phonon DOS of terbium, calculated with DFT+U. (h) Same as (g), but for gadolinium. (i) Debye-Waller factor of terbium, calculated from the phonon DOS shown in (g). The region below $\hbar\omega < 1\,\mathrm{meV}$ was replaced by the result of a fit with the abovementioned function for improved accuracy. (j), Same as (i), but for gadolinium. Details about the DFT and DFT+U calculations are provided in Sec. 2.4.

Figure 2.19 presents the phonon DOS of nickel, cobalt[8], iron, gadolinium[8], and terbium[8] as well as the calculated Debye-Waller factors. For iron, cobalt, and nickel, tabulated values from Ref. [PDW11] are also shown for comparison. For nickel and iron, the calculated Debye-Waller factors agree very well with the tabulated ones. For cobalt, the agreement is worse. However, this may be due to the literature result for cobalt being an estimation based on the Debye model.

In general, the MSD as a function of temperature exhibits a characteristic behavior: at low temperatures, the MSD is dominated by zero-point motion. At high temperatures ($\hbar\omega \ll 2k_{\mathrm{B}}T$ for all phonon modes), $\coth\left(\frac{\hbar\omega}{2\mathrm{k_B}T}\right) \approx \frac{2\mathrm{k_B}T}{\hbar\omega}$ and thus the MSD is proportional to the temperature. Note that for high temperatures and depending on the material, anharmonic effects can occur, which lead to deviations from a linear behavior [WP75].

Here, only the case of materials with one atom per primitive unit cell was discussed. For materials with more atoms per primitive unit cell, which have optical phonons, the phonon DOS is not sufficient to calculate the MSD. In this case, also the phonon polarization vectors are required, as described for example in Ref. [PDW11].

2.4   From DFT results to temperature models

Once the MSD/lattice temperature dynamics have been extracted, it is often insightful to compare the experimental results to theory. In this work, density functional theory (DFT) calculations were employed to obtain the electron-phonon coupling matrix elements as well as the electron and phonon DOS. For the $3d$ ferromagnets iron, cobalt, and nickel, DFT calculations were performed by Jan Vorberger and Tim Butcher. GGA-PBE pseudopotentials were employed in the calculation. An unshifted k-point grid of $32 \times 32 \times 32$ points and a q-point grid of $8 \times 8 \times 8$ points was used. The plane-wave energy cut-off was $40\,\mathrm{Ha}$ for iron and $50\,\mathrm{Ha}$ for cobalt and nickel. Further details are available in Refs. [Zah20c; Zah21a; Zah21b].

For the $4f$ ferromagnets terbium and gadolinium, DFT+U calculations[9] were employed, which were performed by Haichen Wang and Miguel Marques. DFT+U calculations were used here due to the strong electronic correlation effects in rare-earth metals [Söd14]. The calculations were performed with the DFT code *abinit*, using LDA-PAW pseudopotentials and an effective U of $6.0\,\mathrm{eV}$. An unshifted k-point grid of $12 \times 12 \times 12$ points and a q-point grid of $6 \times 6 \times 6$ points was used. The plane-wave energy cutoff was $25\,\mathrm{Ha}$ and the cutoff for the LDA-PAW pseudopotentials was $50\,\mathrm{Ha}$. The relaxed lattice constants were $a = 3.534\,\mathrm{\AA}$, $c = 5.641\,\mathrm{\AA}$ for gadolinium and $a = 3.415\,\mathrm{\AA}$, $c = 5.767\,\mathrm{\AA}$ for terbium.

Once the electron and phonon properties and the electron-phonon coupling matrix elements have been obtained from DFT, the next step is to combine them with a model for the dynamics of the material following laser excitation. In case the two-temperature model (TTM) is employed (see Eqs. 1.1 and 1.2), the electron-phonon coupling parameter G_{ep} as well as the electron and lattice heat capacities are required as inputs for the model. This section describes how these

---

[8]Note that cobalt, gadolinium, and terbium have a hexagonal close-packed (hcp) crystal structure with two atoms per primitive unit cell. However, they consist of only one element each and both sites are symmetry-equivalent. As discussed in Sec. 2.3.2, certain hcp metals can be well approximated as having isotropic MSD. This is the case for all materials here and it is thus a good approximation to treat them as materials with one atom per unit cell.

[9]The U stands for the on-site interaction parameter U in the Hubbard model, which allows to describe electronic correlations.

inputs can be calculated from the results of a DFT calculation. Only the case of metals is described here. For semiconductors and insulators, the situation is typically more complex and often a description with the TTM is insufficient, for example due to pronounced phase-space constraints for electron-electron and electron-phonon scattering. Code that performs the calculations described in the following (except Eq. 2.15) is publicly available [Zah22a].

For metals, it is convenient to describe the electron-phonon coupling using the (generalized) Eliashberg function $\alpha^2 F$, which is defined as follows [All87]:

$$\alpha^2 F(\epsilon, \epsilon', \omega) = \frac{2}{\hbar N_c^2 g_e(\mu)} \sum_{\mathbf{kk'}} |M_{\mathbf{kk'}}^{\mathbf{q}}|^2 \, \delta(\omega - \omega(\mathbf{q})) \, \delta(\epsilon - \epsilon(\mathbf{k})) \, \delta(\epsilon' - \epsilon(\mathbf{k'})). \tag{2.15}$$

Here, $\mathbf{k}$ and $\mathbf{k'}$ denote the initial and final momentum of the scattering electron, $\mathbf{q} = \mathbf{k'} - k$ is the wavevector of the phonon that takes part in the scattering process, and $M_{\mathbf{kk'}}^{\mathbf{q}}$ is the matrix element of the scattering process. $\epsilon(\mathbf{k})$ and $\epsilon(\mathbf{k'})$ are the respective electron energies and ω is the phonon frequency. N_c denotes the number of unit cells over which the summation is performed, g_e is the electronic DOS (normalized to the unit cell) and μ is the chemical potential. The chemical potential is temperature-dependent because the number of electrons per unit cell, N_e, is constant:

$$N_e = \int_{-\infty}^{\infty} g_e(\epsilon) \frac{1}{\exp\left(\frac{\epsilon - \mu(T)}{k_B T}\right) + 1} d\epsilon = \int_{-\infty}^{\epsilon_F} g_e(\epsilon) d\epsilon. \tag{2.16}$$

Here $\epsilon_F = \mu(0\,\mathrm{K})$ denotes the Fermi energy. In the case of spin-resolved DFT calculations, as performed for the ferromagnetic materials studied in this work, one can either assume a common chemical potential μ for both spin types or choose to calculate individual chemical potentials for each spin type. While the former reflects the equilibrium situation better, the latter is likely closer to the situation shortly after laser excitation. In this work, except for the visualization of Fig. 2.20, separate chemical potentials for each spin type were calculated. In practice, for the electron temperatures reached in the experiments, the differences compared to a common chemical potential are small.

To calculate the electron-phonon coupling parameter G_{ep} from the Eliashberg function, some approximations are typically made. First of all, based on Wang et al., the Eliashberg function can be approximated as follows [Wan94; Wal16a]:

$$\alpha^2 F(\epsilon, \epsilon', \omega) \approx \frac{g_e(\epsilon) g_e(\epsilon')}{g_e^2(\mu)} \, \alpha^2 F(\mu, \mu, \omega). \tag{2.17}$$

Furthermore, as the deviations of the chemical potential from the Fermi energy are small for the temperatures relevant here, the following approximation is made:

$$\alpha^2 F(\mu, \mu, \omega) \approx \alpha^2 F(\epsilon_F, \epsilon_F, \omega) = \alpha^2 F(\omega). \tag{2.18}$$

The approximation of Eq. 2.17 assumes that the matrix elements $M_{\mathbf{kk'}}^{\mathbf{q}}$ don't depend on $\mathbf{k}$ and $\mathbf{k'}$ for all states that take part in the electron-phonon relaxation process, which are the states around the chemical potential. This approximation is based on an argument of scale: in typical simple metals, such as the ferromagnets studied in this work, the highest-energy phonons have a frequency of several tens of meV (see Fig. 2.19). However, electronic properties are expected to change on larger energy scales, as for example evidenced by the energy scales on which the electronic DOS changes. Figure 2.20(a)-(c) present the electronic DOS for the $3d$ ferromagnets studied in this work together with the "phonon window", the typical range

in which electron-phonon scattering occurs. The comparison shows that in this range, the electronic DOS varies only very little, suggesting that the character of the states does not change significantly. Furthermore, Lin et al. made a direct quantitative comparison of G_{ep} with and without this approximation for aluminum and found only small differences [LZC08].
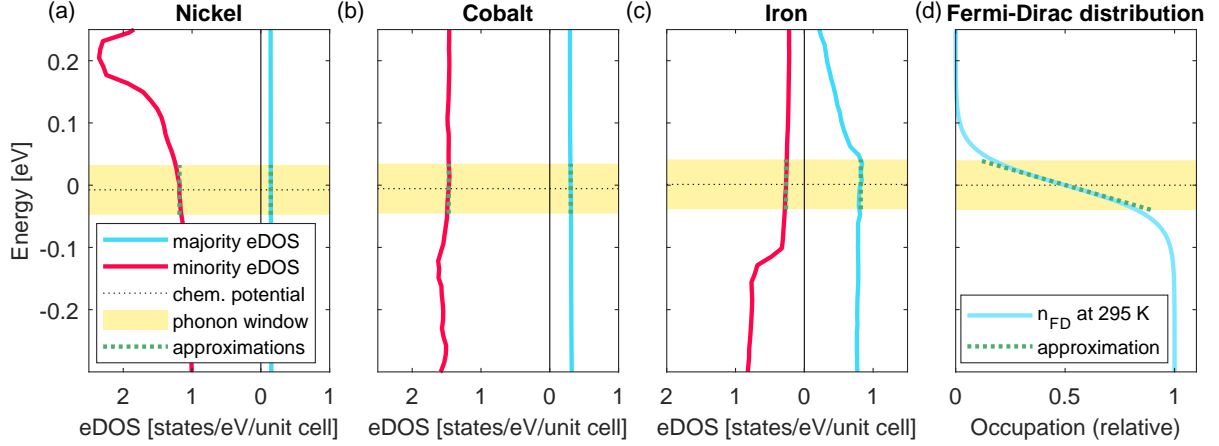
Figure 2.20: Approximations in the calculation of the electron-phonon coupling parameter G_{ep}. (a) Electronic DOS of ferromagnetic nickel, calculated with spin-resolved DFT. The chemical potential μ at room temperature (295 K) is shown as a dashed black line. The yellow areas visualize the "phonon window", the typical range for electron-phonon scattering. Here, an energy range from $\mu - \hbar\omega_{max}$ to $\mu + \hbar\omega_{max}$ is shown. This corresponds to the states that an electron at the chemical potential can scatter into with one electron-phonon scattering event. Note that in reality there are no sharp borders of the "phonon window" since electrons above and below the chemical potential also participate in electron-phonon scattering. For simplicity, $\hbar\omega_{max} = 40$ meV is assumed for all three materials, which is slightly larger than their maximum phonon frequencies (see Fig. 2.19). The approximations of Eq. 2.19 are shown as dashed green lines. (b) Same as (a), but for cobalt. (c) Same as (a), but for iron. (d) Fermi-Dirac distribution function n_{FD} at room temperature (295 K) together with the "phonon window". The dashed green line corresponds to the approximation of Eq. 2.20.

Similarly, based on the comparison of the electronic DOS with the "phonon window", the following approximation is made:

$$g_e(\mu + \hbar\omega) \approx g_e(\mu). \tag{2.19}$$

This approximation is visualized with the dashed green lines of Fig. 2.20(a)-(c). The approximation provides a very good description of the electronic DOS in the "phonon window" for all cases. Furthermore, the Fermi-Dirac distribution is approximated with a first-order Taylor expansion:

$$n_{FD}(\epsilon + \hbar\omega) \approx n_{FD}(\epsilon) + \frac{\partial n_{FD}}{\partial \epsilon}\hbar\omega. \tag{2.20}$$

This approximation is visualized in Fig. 2.20(d) for $\epsilon = \mu$, showing that it is reasonable for energies close to the chemical potential. With these approximations, the energy flow between electrons and phonons, Z, can then be described as [All87; LZC08; Wal16a]:

$$Z(T_e, T_l) = -\frac{2\pi}{g_e(\mu)} \int_0^\infty (\hbar\omega)^2 \, \alpha^2 F(\omega) \, [n_{BE}(\omega, T_e) - n_{BE}(\omega, T_l)] \, d\omega \times$$
$$\times \int_{-\infty}^\infty g_e^2(\epsilon) \frac{\partial n_{FD}(\epsilon, T_e, \mu)}{\partial \epsilon} d\epsilon. \tag{2.21}$$

Here, T_e and T_l are the temperatures of the electrons and the lattice, respectively. n_{BE} is the Bose-Einstein distribution function (with $\mu = 0$) and n_{FD} is the Fermi-Dirac distribution function. The electron-phonon coupling parameter is then given by:

$$G_{ep}(T_e, T_l) = \frac{Z(T_e, T_l)}{T_e - T_l}. \tag{2.22}$$

Note that Eqs. 2.21 and 2.22 calculate the energy transfer rate and electron-phonon coupling per unit cell, since also the electronic DOS is in units of states per unit cell here (see Eq. 2.16). The values per volume can be obtained by dividing by the unit cell volume. In the spin-resolved case, G_{ep} is calculated for each spin type separately, based on the Eliashberg function and electronic DOS of this spin type. Therefore, spin-flip scattering is not included.

As shown in Eqs. 2.21 and 2.22, G_{ep} depends on both the electron and the lattice temperatures. The dependence of G_{ep} on the lattice temperature is presented in Fig. 2.21 for the example of ferromagnetic iron.
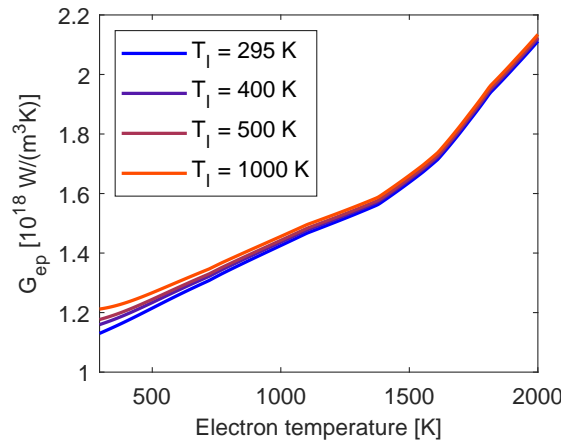
Figure 2.21: Electron-phonon coupling parameter G_{ep} of ferromagnetic iron for different lattice temperatures. Due to the weak dependence of G_{ep} on the lattice temperature, it is often a good approximation to consider only the dependence of G_{ep} on the electron temperature. The sum of majority and minority G_{ep} is presented.

Since G_{ep} changes relatively little over the range of lattice temperatures typically reached in electron diffraction experiments (for freestanding thin films and kHz repetition rates ~150-300 K lattice temperature rise), it is often a good approximation to neglect the dependence of G_{ep} on the lattice temperature in Eq. 2.21.

In addition to G_{ep}, also the electron and lattice heat capacities are necessary to perform a TTM. The electronic heat capacity, c_e, is given by:

$$c_e(T) = \left(\frac{\partial E_e}{\partial T}\right)_V = \frac{d}{dT}\left[\int_{-\infty}^{\infty} g_e(\epsilon) \frac{\epsilon}{\exp\left(\frac{\epsilon - \mu(T)}{k_B T}\right) + 1} d\epsilon\right]. \tag{2.23}$$

Here E_e denotes the energy of the electrons. For a free electron gas and with the approximation $\mu(T) \approx \epsilon_F$, the electronic heat capacity is proportional to the temperature (see for example Ref. [IL09]). In reality, significant deviations from a linear relationship can occur [LZC08], in particular for transition metals, which exhibit strong variations of the electronic DOS around the Fermi level (see also Fig. 2.22(d)).

Similarly to Eq. 2.23, the lattice heat capacity, c_l, can be calculated as:

$$c_l(T) = \left(\frac{\partial E_l}{\partial T}\right)_V = \frac{d}{dT}\left[\int_{-\infty}^{\infty} g_l(\epsilon)\frac{\epsilon}{\exp\left(\frac{\epsilon}{k_B T}\right) - 1}d\epsilon\right]. \tag{2.24}$$

Here E_l denotes the lattice energy and g_l denotes the phonon DOS. For high temperatures, c_l approaches the classical thermodynamic value of $3k_B$ per atom. A good estimate for the applicability of the high-temperature limit is the Debye temperature (see also Fig. 2.22(e)). For mono-elemental metals, which typically have rather low Debye temperatures, the high-temperature limit is often already a reasonable approximation at room temperature.

An overview of the DFT calculation results for the $3d$ ferromagnets iron, cobalt, and nickel is presented in Fig. 2.22. These results are the basis of the energy flow models presented in Chapter 4. The data are publicly available in Ref. [Zah22a]. Analogously, Fig. 2.23 presents an overview of the DFT+U calculation results for the $4f$ ferromagnets terbium and gadolinium.
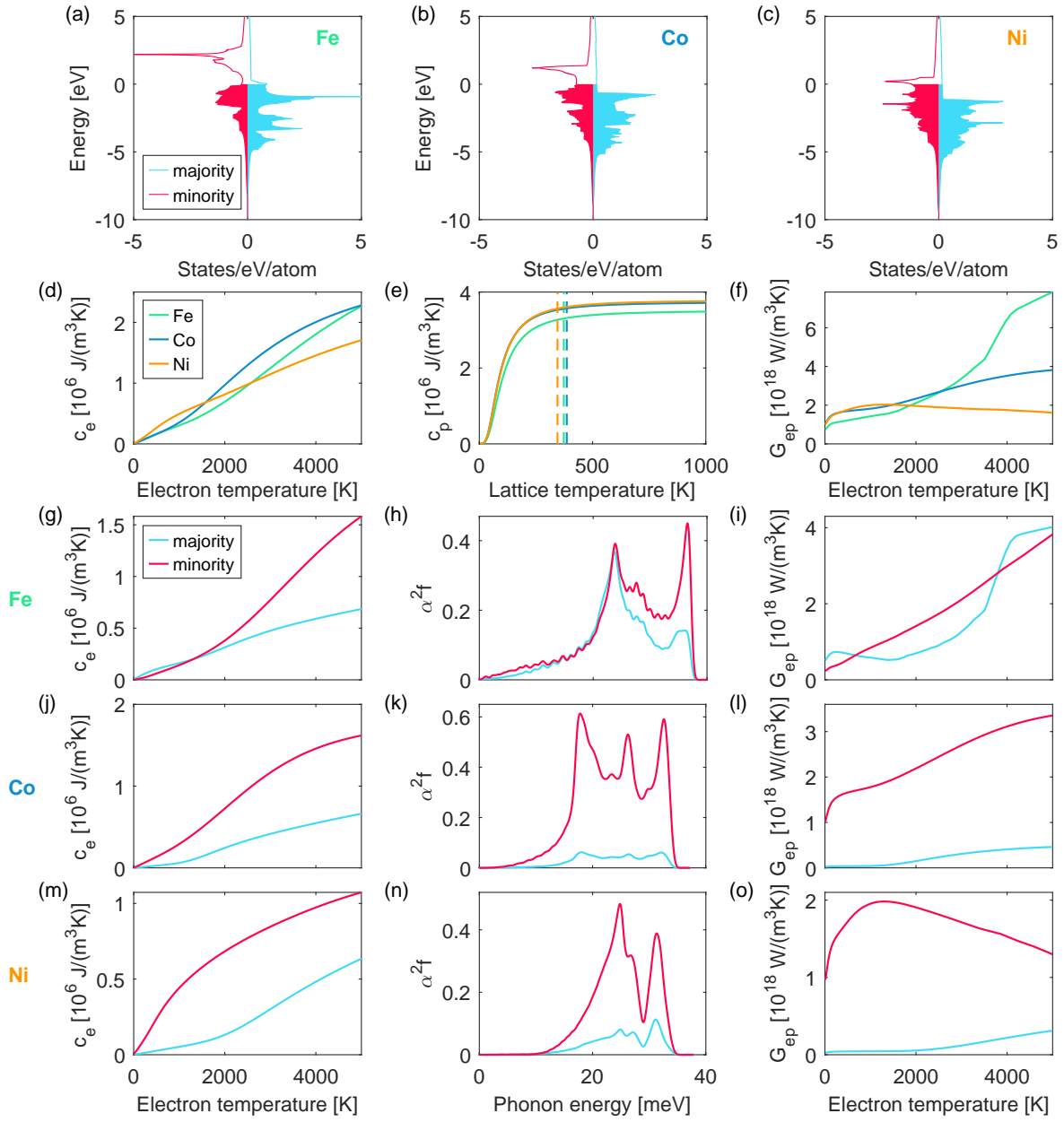
Figure 2.22: Results of spin-resolved DFT calculations for iron, cobalt, and nickel. (a) Spin-split electronic DOS for ferromagnetic iron. States below the Fermi level (here at 0 eV) are shown filled. (b) Same as (a), but for cobalt. (c) Same as (a) and (b), but for nickel. (d) Electronic heat capacities of iron, cobalt, and nickel. The sum of majority and minority contributions is presented. (e) Lattice heat capacities of iron, cobalt, and nickel calculated from the phonon DOS. Literature results for the Debye temperatures Θ_D from Ref. [HPL74] are presented as well (dashed lines). (f) Electron-phonon coupling parameters G_{ep} as functions of electron temperature, calculated for a lattice temperature of 295 K. The sum of majority and minority contributions is presented. (g) Contributions of majority and minority electrons to the electronic heat capacity of iron. (h) Majority and minority Eliashberg function of iron. (l) Majority and minority contributions to the electron-phonon coupling parameter G_{ep} of iron. (j)-(l) Same as (g)-(i), but for cobalt. (m)-(o) Same as (g)-(i), but for nickel. Details on the DFT calculations are described in the text.
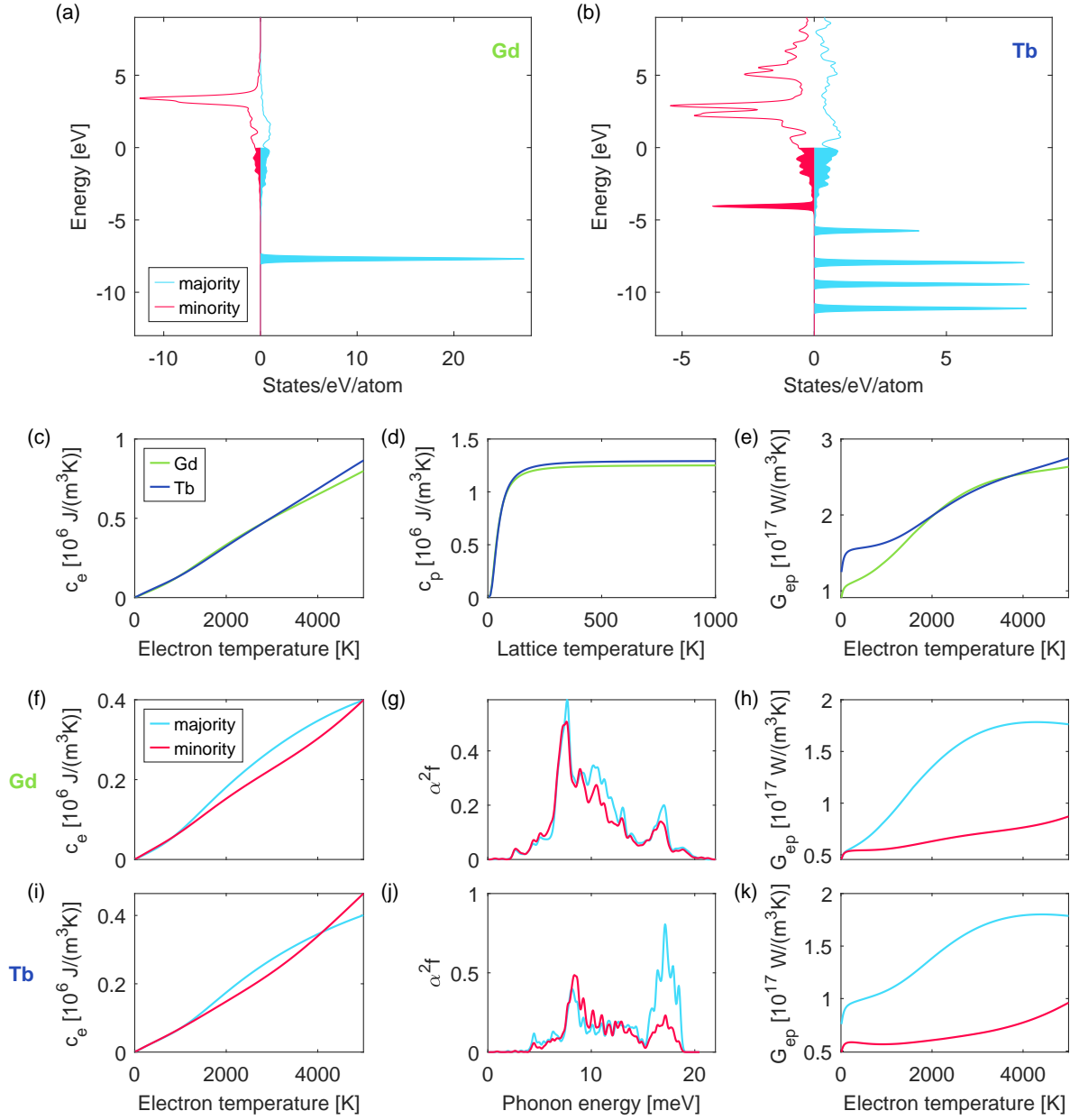
Figure 2.23: Results of spin-resolved DFT+U calculations for gadolinium and terbium. (a) Spin-split electronic DOS of ferromagnetic gadolinium. States below the Fermi level (here at $0\,\mathrm{eV}$) are shown filled. (b) Same as (a), but for terbium. (c) Electronic heat capacities of gadolinium (green) and terbium (blue). The sum of majority and minority electron heat capacity is presented. (d) Lattice heat capacities of gadolinium and terbium, calculated from the phonon DOS. (e) Electron-phonon coupling parameters G_{ep} for a lattice temperature of $295\,\mathrm{K}$. (f) Majority and minority contributions to the electronic heat capacity of gadolinium. (g) Majority and minority Eliashberg function of gadolinium. (h) Majority and minority contributions to G_{ep} of gadolinium. (i-k) Same as (f-h), but for terbium. Details on the DFT+U calculations are described in the text.

Chapter 3

Nonthermal lattice dynamics in black phosphorus

The first unambiguous production of graphene by Novoselov et al. [Nov04], which was achieved by mechanical exfoliation of a graphite crystal, triggered tremendous research interest in the field of 2D materials. Soon afterwards, also other layered van der Waals crystals were exfoliated down to the monolayer [Nov05]. Nowadays, a large number of different 2D materials with widely different properties are available [Xu13; GG13]. The continued research interest is based on several attractive properties of 2D materials. First of all, the fact that monolayers can be produced and are, for many materials, stable in ambient conditions offers the perspective of building very small and mechanically flexible devices. In addition, monolayers or few layers often exhibit properties that are different from their bulk counterparts. For example, the band gap of black phosphorus is thickness-dependent [Tra14; Li17]. Some transition metal dichalcogenides (TMDCs) exhibit transitions from indirect to direct band gap [Spl10; Zha13] and in addition, excitonic effects become more pronounced due to reduced screening in the out-of-plane direction [Che15; Wan18]. In some magnetic layered materials, the transition from bulk to monolayer changes the magnetic state, e.g. from antiferromagnet to ferromagnet [Hua17] or from paramagnet to ferromagnet [Bon18]. Finally, a major advantage of 2D materials is that combining them is very easy since the out-of-plane adhesion of different layers is caused by van der Waals interactions only. This means that any two materials can be combined to form heterostructures, regardless of the lattice constant mismatch [GG13]. In fact, the angle between the two crystals even offers an additional tuning knob to control the behavior of heterostructures, which has led for example to the discovery of superconducting "magic-angle" graphene [Cao18].

Due to the vast possibilities of combining different 2D materials, they are often compared to Lego bricks [GG13; Lay15]. To take full advantage of their possibilities, it is necessary to have different kinds of 2D materials with different properties available. While graphene offers high carrier mobility due to its Dirac cones, it lacks a band gap, which is disadvantageous for many applications. Semiconducting TMDCs have a band gap in the visible range, but significantly lower carrier mobility compared to graphene. Black phosphorus bridges the gap between these two classes of 2D materials because it has a tunable band gap in the infrared to visible range [Tra14; Li17] and high carrier mobility [Li14; XWJ14; Lon16]. Furthermore, its in-plane anisotropic structure offers yet another tuning knob for heterostructure devices.

Since any device operates in non-equilibrium conditions, microscopic insights into relaxation pathways and the underlying couplings in 2D materials are desired. Electron-phonon coupling is an important relaxation channel for excited carriers and a detailed understanding is thus relevant for applications in which hot carriers are excited or injected into the material. Phonon-phonon coupling influences properties such as thermal conductivity and is thus also an important factor for the functionality of heterostructure devices. The lattice sensitivity of time-resolved diffraction makes it an ideal tool to study both of these couplings.

This chapter presents time-resolved electron diffraction results on multilayer black phosphorus, which were obtained together with Patrick Hildebrandt and are partially discussed also in his bachelor thesis [Hil18]. The results presented in Sec. 3.3 were published in [Zah20a]. The experimental data of this section are publicly available [Zah20b]. Section 3.4 presents further, unpublished results also based on the analysis of Bragg reflections. Additional results of a project led by Hélène Seiler, which focused on the analysis of the diffuse scattering background, are presented in Sec. 3.5 and were published in Ref. [Sei21]. All DFT calculations presented in this chapter, which as the same as in Ref. [Sei21], were performed by Fabio Caruso (Christian-Albrechts-Universität zu Kiel) and Marios Zacharias (Cyprus University of Technology). The diffuse scattering intensity calculations presented in Sec. 3.5 were performed by Marios Zacharias.

3.1 Crystal structure, electronic and vibrational properties

The crystal structure of black phosphorus is presented in Fig. 3.1. The material exhibits in-plane anisotropy since it consists of puckered layers of phosphorus atoms. The two inequivalent high-symmetry directions in the layer plane are called the armchair and zigzag directions, respectively, as indicated in Fig. 3.1(b). The space group of bulk black phosphorus is 64 or *Cmce*, and all phosphorus atoms are symmetry-equivalent (Wyckoff positions 8f).
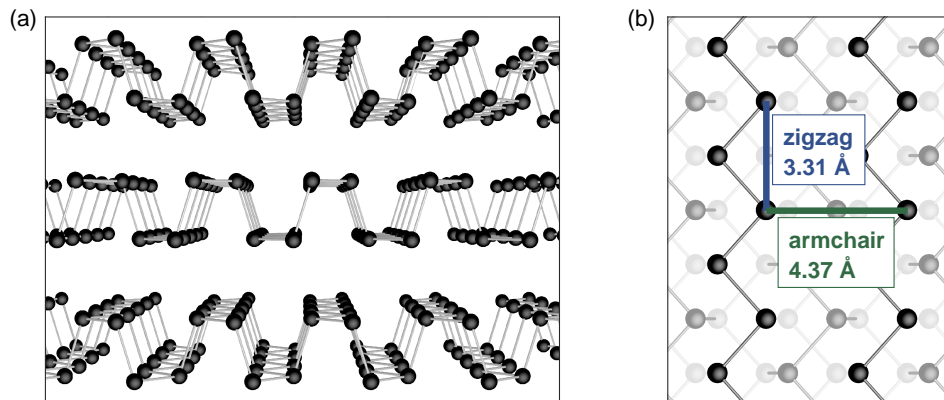
Figure 3.1: Anisotropic crystal structure of black phosphorus. (a) Side view of the crystal structure showing the van der Waals bonded layers as well as the puckered structure. (b) Top view of the crystal structure with the two inequivalent high-symmetry directions indicated. Adapted from Ref. [Zah20a].

The in-plane anisotropy of the atomic structure translates into anisotropy of the electronic and vibrational properties. These are presented in Fig. 3.2, which shows the electron and phonon band structures of bulk black phosphorus calculated with DFT. The anisotropy of the

band structures manifests in anisotropy of many macroscopic properties of black phosphorus, such as optical absorption [Tra14; Low14; XWJ14; Jia18] and in-plane thermal [Luo15; Lee15; Jan15; Sun17] and electrical [Qia14; Liu14; XWJ14; He15] conductivities.
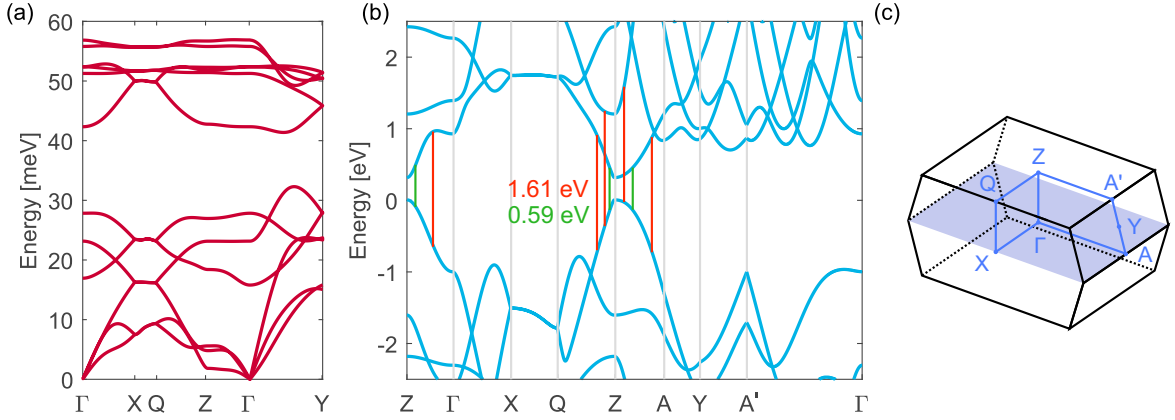
Figure 3.2: Vibrational and electronic properties of bulk black phosphorus. (a) Phonon band structure and (b) electronic band structure along high-symmetry directions, both calculated with DFT (calculations from Ref. [Sei21]). For the electronic band structure, a scissor shift was applied to the unoccupied bands to obtain the correct band gap of around 0.3 eV. Examples of optical transitions in the case of excitation with 0.59 eV and 1.61 eV photon energy are also presented. (c) Brillouin zone with high-symmetry points, following the convention used in Ref. [RPM18]. Adapted from Ref. [Sei21].

3.2 Electron diffraction experiments

A thin-film sample of black phosphorus was prepared as described in Sec. 2.1.1. A microscope image of the flake on a TEM grid is presented in Fig. 3.3(a). The measurements were conducted on the thinner, gray part of the flake. The thickness of this area was estimated to be 39 ± 5 nm, based on its transmission and the optical constants of black phosphorus reported in Ref. [Jia18]. The transmission diffraction pattern of the sample is presented in Fig. 3.3(b). Due to the crystal symmetry, only reflections (h0l) with even h and l are allowed [Hah16]. However, additional, "forbidden" reflections are visible, which may be due to stacking faults, multiple scattering, or structural deviations at the surface. Since black phosphorus is air-sensitive, it is likely that oxidation of the surface occurred during the preparation of the sample (in ambient conditions). To minimize degradation, the sample was stored in vacuum directly after preparation. Since the sample contains 74 ± 10 layers in total, a significant contribution of the surface to the measured lattice dynamics is not expected.

Due to the very anisotropic optical properties of black phosphorus, the pump polarization has a pronounced influence on the amount of energy that is absorbed by the sample. Therefore, it strongly influences the amplitude of the laser-induced dynamics in a pump-probe experiment. Before the experiment, the relative orientation between pump pulses and the crystal structure was identified by scanning the pump polarization. Figure 3.3(c) shows the intensities of the (400) and (004) reflections at 50 ps after laser excitation as functions of pump polarization angle. A sinusoidal modulation with a period of 180° is clearly observed, in agreement with reported optical properties [Jia18]. The polarization angles with the strongest reduction of Bragg

(a)

(c)

(b)
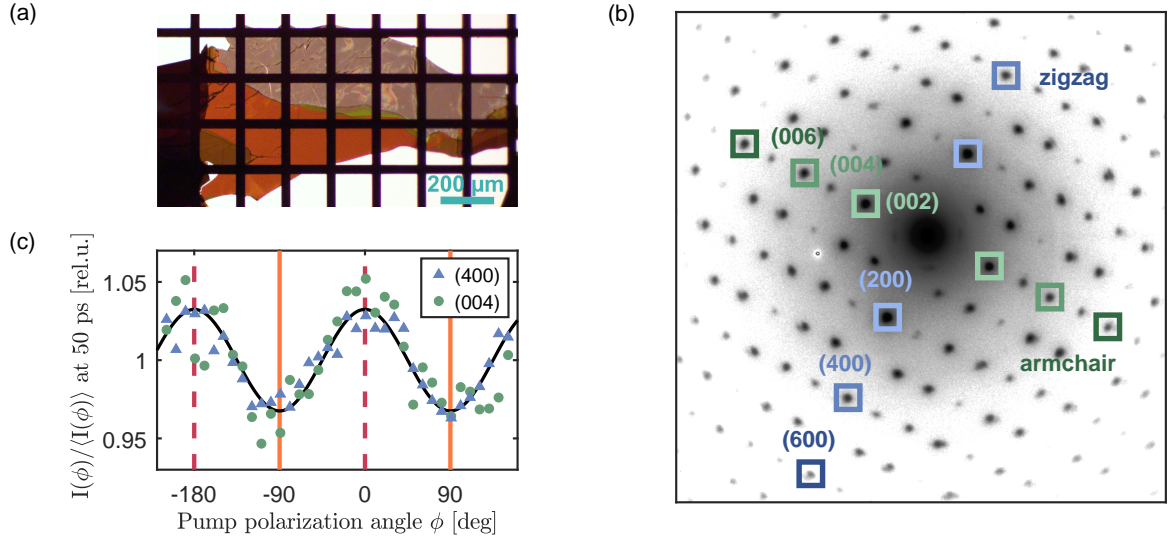
Figure 3.3: The black phosphorus sample, its diffraction pattern, and characterization of the crystal directions relative to the pump polarization. (a) Microscope image of the black phosphorus thin-film sample on a TEM grid. The flake consists of several areas with different colors, which are caused by thin-film interference. The upper, gray area is the thinnest one and was therefore used for measurements. (b) Transmission electron diffraction pattern of black phosphorus. The high-symmetry peaks along the armchair and zigzag directions are marked in green and blue, respectively. This panel was adapted from Ref. [Zah20a]. (c) Scan of the pump polarization angle to identify the high-symmetry directions. Images were recorded with a pump-probe delay of 50 ps, i.e. well after electron-phonon equilibration. The intensities of the (400) and (004) reflections are shown as functions of pump polarization angle, relative to their average intensity over the whole scan. The data are the average of Friedel pairs. Solid orange lines mark angles at which the polarization is along the armchair direction while dashed red lines mark angles at which the polarization is along the zigzag direction. Note that the minima of the experimental data correspond to the highest optical absorption because the signal consists of a *reduction* of the reflection intensities. The black curve is the result of a fit with a cosine function with a fixed period of 180°. The incident fluence of this measurement was $(9.8 \pm 1.4)\,\mathrm{mJ/cm^2}$ and the pump wavelength was 770 nm.

reflection intensities, marked with solid orange lines in Fig 3.3(c), correspond to polarization along the armchair direction. In contrast, the angles with the least signal, marked with dashed red lines, correspond to polarization along the zigzag direction.

3.3 Anisotropic MSD dynamics

Next, pump-probe delay scans were performed to study laser-induced changes of the lattice. Figure 3.4 presents results for the pump polarization along the armchair direction of the crystal and a pump wavelength of 770 nm (corresponding to a photon energy of 1.61 eV). The measurement was performed with an incident fluence of $9.8 \pm 1.4\,\mathrm{mJ/cm^2}$ and at a base temperature of 100 K.

Fig. 3.4(a) shows the intensity evolution of high-symmetry Bragg reflections in the armchair and zigzag directions. A two-step behavior is observed, with a sub-picosecond intensity drop and a pronounced second drop on longer timescales. In addition, significant differences between reflections along the armchair and zigzag directions are observed. In order to analyze
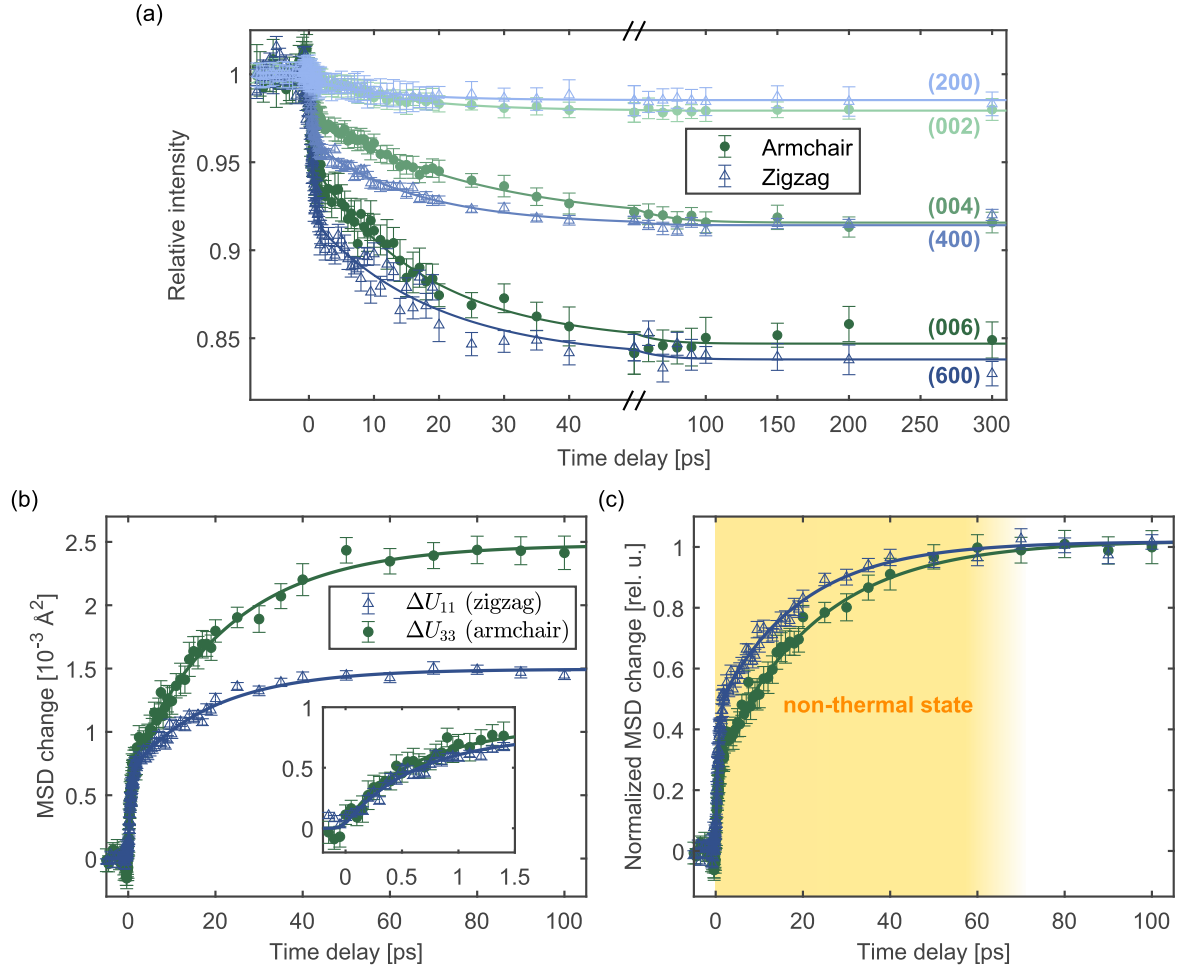
Figure 3.4: Evolution of Bragg reflection intensities and corresponding MSDs for high-symmetry reflections along the armchair and zigzag directions. (a) Relative changes of Bragg reflection intensities for Bragg peaks along the armchair (green dots) and zigzag directions (blue triangles). The intensities are the average of Friedel pairs, e.g. (002) and (00$\bar{2}$), since they exhibit the same dynamics. The data shown here are the average of several delay scans and the error bars correspond to the standard error of the mean. (b) MSD changes as functions of pump-probe delay in the armchair and zigzag directions. The weighted average of the results from the Bragg reflections shown in Panel (a) is presented. The inset shows a close-up of the dynamics at early time delays. (c) MSD dynamics normalized to the result of a bi-exponential fit at 100 ps. The yellow area marks the period during which the lattice is in a nonthermal state, evidenced by transient differences between the normalized MSD changes in the armchair and zigzag directions. Adapted from Ref. [Zah20a].

those changes in detail, the intensity changes are converted into MSD changes, as described in Sec. 2.3.2 for anisotropic materials. For Bragg reflections along the armchair direction, the relative intensity change is related to the MSD change as follows:

$$\frac{I(t)}{I_0} = \exp\{-[U_{33}(t) - U_{33}^0]\frac{4\pi^2}{c^2}l^2\}, \tag{3.1}$$

where I_0 denotes the intensity before laser excitation, U_{33}^0 is the MSD in the armchair direction before laser excitation, $c = 4.37\,\text{Å}$ is the lattice constant in the armchair direction [Aka89] and l corresponds to the Miller index of the Bragg reflection. Analogously, the relative intensity change for Bragg reflections along the zigzag direction is given by:

$$\frac{I(t)}{I_0} = \exp\{-[U_{11}(t) - U_{11}^0]\frac{4\pi^2}{a^2}h^2\}. \tag{3.2}$$

Here, $a = 3.31\,\text{Å}$ is the lattice constant in the zigzag direction [Aka89], h is the Miller index of the Bragg reflection and U_{11}^0 is the MSD in the zigzag direction before laser excitation. MSD changes were calculated for all Bragg reflections shown in Fig. 3.4(a) and their weighted average in the armchair and zigzag directions is presented in Fig. 3.4(b). The amplitude of the MSD rise is anisotropic, with a much larger rise in the armchair direction. This behavior is in qualitative agreement with diffraction results for the MSD in thermal equilibrium [Aka89] and indicates that the interatomic potential is anisotropic, with "softer" bonds in the armchair direction. Therefore, as the lattice temperature increases, the additional energy in the lattice causes a larger MSD increase in the armchair direction.

To analyze the time evolution of the MSDs quantitatively, a fit with the following bi-exponential function was performed:

$$y(t) = \left\{\theta(t - t_0)\left[A_1\left(1 - \exp\left\{-\frac{t - t_0}{\tau_1}\right\}\right) + A_2\left(1 - \exp\left\{-\frac{t - t_0}{\tau_2}\right\}\right)\right]\right\} * G(t). \tag{3.3}$$

Here, θ denotes the Heaviside step function and G(t) is a Gaussian with a width corresponding to the estimated time resolution of the experiment, here $150\,\text{fs}$ FWHM. The fit results for the armchair and zigzag MSDs are presented in Table 3.1.

	armchair	zigzag
A_1 $[10^{-3}\text{Å}^2]$	0.66 ± 0.03	0.68 ± 0.02
τ_1 [ps]	0.48 ± 0.05	0.58 ± 0.04
A_2 $[10^{-3}\text{Å}^2]$	1.84 ± 0.03	0.85 ± 0.03
τ_2 [ps]	22 ± 1	20 ± 2

Table 3.1: Results of a bi-exponential fit (Eq. 3.3) to the MSD dynamics after excitation with $770\,\text{nm}$ light polarized along the armchair direction, at a base temperature of $100\,\text{K}$. The errors correspond to $68.3\,\%$ confidence intervals of the fit.

The pronounced two-step behavior of the MSD dynamics indicates that the fast timescale is predominantly caused by electron-phonon equilibration while the slower timescale is mostly due to phonon-phonon equilibration. The time constant of the fast component, $\sim 0.5\,\text{ps}$, is consistent with time-resolved optical and photoemission results [Wan16; IYX17; Che19]. The amplitude of the fast component is similar for both directions. In contrast, the amplitude of the slower

component is significantly higher for the armchair direction. At a pump-probe delay of 100 ps, it can be assumed that the lattice is already close to a thermal state. Therefore, the distinct amplitude ratios A_1/A_2 indicate that directly after the initial electron-phonon equilibration, the lattice is in a nonthermal state, with a higher MSD in the zigzag direction compared to thermal equilibrium. Consequently, on average, electron-phonon coupling is stronger for phonon modes with a large atomic displacement in the zigzag direction. In addition, since the MSD rises further after the initial electron-phonon equilibration, it can be concluded that electron-phonon equilibration produces a larger number of high-energy phonons compared to thermal equilibrium. This conclusion is based on a combination of two effects. First, high-energy phonons decay into multiple low-energy phonons due to energy conservation. Second, on average, low-energy phonons produce a higher displacement per phonon compared to high-energy phonons [PDW11]. In summary, the initial electron-phonon equilibration leads to a strongly nonthermal state of the lattice with a relatively large number of high-energy (e.g. optical) phonons excited and a relatively large MSD in the zigzag direction.

On longer timescales, the nonthermal state of the lattice relaxes back to thermal equilibrium. This is visualized in Fig. 3.4(c), which shows the MSD rise in the armchair and zigzag directions normalized to the respective fit result at 100 ps. The differences between the armchair and zigzag directions persist up to ~60 ps, indicating that the lattice thermalizes on this timescale. The timescale is similar compared to results for WSe$_2$ [Wal17b] and graphite [Ste18].

In principle, both direct phonon-phonon scattering as well as electron-phonon scattering processes contribute to phonon thermalization. In the case of black phosphorus, the valence band maximum and the conduction band minimum are located at the Z-point of the Brillouin zone, as shown in Fig. 3.2(b). The excitation with 1.61 eV photon energy excites predominantly carriers in the Z-valley, as illustrated by vertical red lines in Fig. 3.2(b). Likewise, also an electron distribution that has thermalized via electron-electron scattering predominantly[1] occupies states in the Z-valley [Sei21]. There is only one Z-point in the Brillouin zone. Consequently, whether or not the excited carriers have thermalized, most of them can only relax within the Z-valley, thus predominantly emitting phonons with small momenta. Electron-phonon scattering alone is therefore unable to establish thermal equilibrium of the phonon system over the full Brillouin zone. Hence, it can be assumed that phonon thermalization is mostly achieved by direct phonon-phonon scattering (via anharmonicity of the interatomic potential).

Based on the experimental results for the MSD evolution in the armchair and zigzag directions shown in Fig. 3.4(b), it is possible to calculate the full in-plane MSD dynamics (see Eq. 2.1). Due to the symmetry of black phosphorus (space group 64 with phosphorus atoms sitting at Wyckoff positions 8f), the in-plane off-diagonal elements of the U-matrix, U_{13} and U_{31}, are zero [WP75]. Also U_{12} and U_{21} are zero due to symmetry, which however does not affect the in-plane MSD. The diagonal elements U_{11} and U_{33} correspond to the MSDs in the zigzag and armchair directions, respectively. For an arbitrary in-plane direction $\hat{\mathbf{n}} = (\cos(\phi), 0, \sin(\phi))^{\mathrm{T}}$, the MSD in this direction is thus given by:

$$\mathrm{MSD}(\phi) = \hat{\boldsymbol{n}}^{\mathrm{T}} \begin{pmatrix} U_{11} & 0 & 0 \\ 0 & U_{22} & U_{23} \\ 0 & U_{32} & U_{33} \end{pmatrix} \hat{\boldsymbol{n}} = U_{11} \cos^2\phi + U_{33} \sin^2\phi \qquad (3.4)$$

---

[1]In addition, depending on the electron temperature, there can be a smaller but non-negligible occupation of other low-energetic conduction band valleys as well [Sei21].

The total transient MSDs $U_{11}(t)$ and $U_{33}(t)$ are the sum of the MSD before laser excitation and the MSD rise induced by the excitation of additional phonons. From the time-resolved electron diffraction experiment, only MSD changes after laser excitation are obtained, but not the total MSDs. To estimate the MSDs before laser excitation, it was assumed that both before and after excitation, the MSDs are proportional to the lattice temperature, which corresponds to the high-temperature limit. In addition, the temperature rise induced by the laser pulse was estimated to be $270 \pm 50\,\text{K}$, based on the absorbed energy density of $380 \pm 70\,\text{J/cm}^3$ and the heat capacity of black phosphorus. Here, the heat capacity was approximated as consisting only of its dominant contribution, the lattice heat capacity, which was calculated from the phonon DOS [Mac18].

With these results, the time evolution of the full in-plane MSD can be visualized, which is presented in Fig. 3.5(a) for several pump-probe delays. Already before excitation, the MSD is anisotropic due to the anisotropic interatomic potential that favors atomic displacements in the armchair direction. After laser excitation, the total MSD increases due to the additional phonons that are excited. During phonon thermalization, the MSD increases further due to the increased population of lower-energy phonons.

In addition to the MSD increase, also the shape of the MSD changes. The transient shape change is visualized in Fig. 3.5(b), which shows the MSD curves of Fig. 3.5(a) normalized to their area. The nonthermal phonon occupation leads to a transiently larger MSD in the zigzag direction compared to equilibrium and thus a reduction of the MSD anisotropy. On longer timescales, the lattice thermalizes and the equilibrium anisotropy is restored, as visualized by the dashed curves.
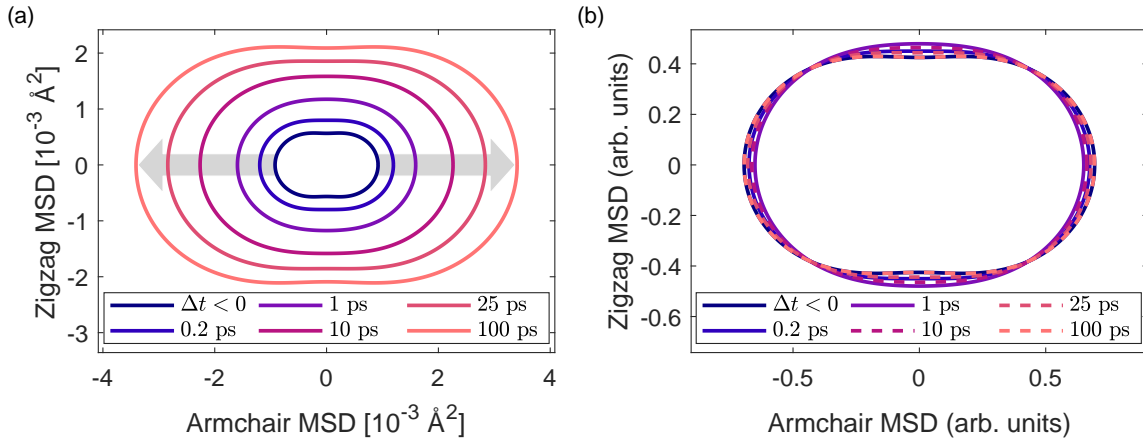
Figure 3.5: Evolution of the in-plane MSD after laser excitation. (a) MSD curves at different pump-probe delays, from before excitation (dark blue) up to 100 ps after the arrival of the laser pulse (bright red). In addition to the overall increase of the in-plane MSD, also its shape changes transiently. (b) MSD curves normalized to their area, highlighting shape changes to a transiently less anisotropic MSD with a relatively high displacement in the zigzag direction. Adapted from Ref. [Zah20a].

3.4   The influence of pump wavelength, pump polarization, absorbed energy density, and base temperature

So far, only experiments with the pump polarization in the armchair direction have been discussed. However, in general, details of the excitation (e.g. pump wavelength and polarization) can influence the observed lattice dynamics, in particular for semiconductors – their carrier thermalization is often less efficient compared to metals. First, the influence of the pump wavelength on the lattice dynamics is investigated. For this, in addition to the measurement with a pump photon wavelength of 770 nm already discussed in the previous section[2], also a measurement with a pump photon wavelength of 2100 nm was recorded. As illustrated in Fig. 3.2(b), with 2100 nm photon wavelength, only transitions close to the Z-point can be excited. With 770 nm, the excitation is also centered around the Z-point, but the excited carriers are on average energetically much further away from the band extrema. There is also a larger spread in the momenta of the excited carriers. The initial distribution of excited carriers differs significantly for the two wavelengths.

To avoid any influences of the absorbed energy density on the comparison, the pump laser power was adjusted to produce a similar amplitude of the MSD changes in both measurements. The comparison of the results is presented in Fig. 3.6. As shown in Fig. 3.6(a), the amplitudes of the pump-probe effect and thus the absorbed energy densities are very similar in both cases. Note that the slightly different amplitude ratios $\Delta U_{33}/\Delta U_{11}$ after thermalization are likely an experimental artifact caused by systematic errors because the differences persist up to at least 300 ps and the field of view varied slightly in the experiments. To compare the dynamics quantitatively, a bi-exponential fit with Eq. 3.3 was performed for each time trace and the MSD changes were normalized to the fit results at 100 ps.

Figure 3.6(b) presents the comparison of the normalized MSD changes in the armchair direction. Within the experimental precision, no differences are observed in the MSD dynamics. The same result is obtained for the zigzag direction, as presented in Fig. 3.6(c). No effects of the photon wavelength on the lattice dynamics are observed. Consequently, electron-phonon coupling leads to a very similar nonthermal phonon distribution in the two cases. This can be explained by efficient carrier thermalization, which would lead to similar carrier distributions in both cases before significant electron-phonon energy transfer occurs. Fast electron thermalization on timescales < 50 fs has been observed in another layered van der Waals material, graphite [Roh18]. Alternatively, a potential scenario is that the (nonthermal) carrier distributions couple to similar phonon modes in both cases. For both 770 nm and 2100 nm photon wavelengths, there are significant phase-space constraints for scattering of the excited carriers with phonons. In both cases, most of the energy relaxation of excited carriers occurs within the Z-valley, thus creating phonons close to Γ. However, in the limit of very weak carrier thermalization, the created phonons would be on average much closer to Γ for 2100 nm compared to 770 nm excitation wavelength. This would be expected to influence the MSD dynamics as well, which is not observed. Consequently, carrier thermalization in black phosphorus is likely rather efficient and thus leads to the observed independence of the dynamics on the photon wavelength.

---

[2]For the sake of comparison, a more robust normalization method was employed here (normalization by total image counts), which yielded good results for all measurements of this section. The differences are small compared to the MSD dynamics presented in Sec. 3.3, for which a different normalization method was employed.
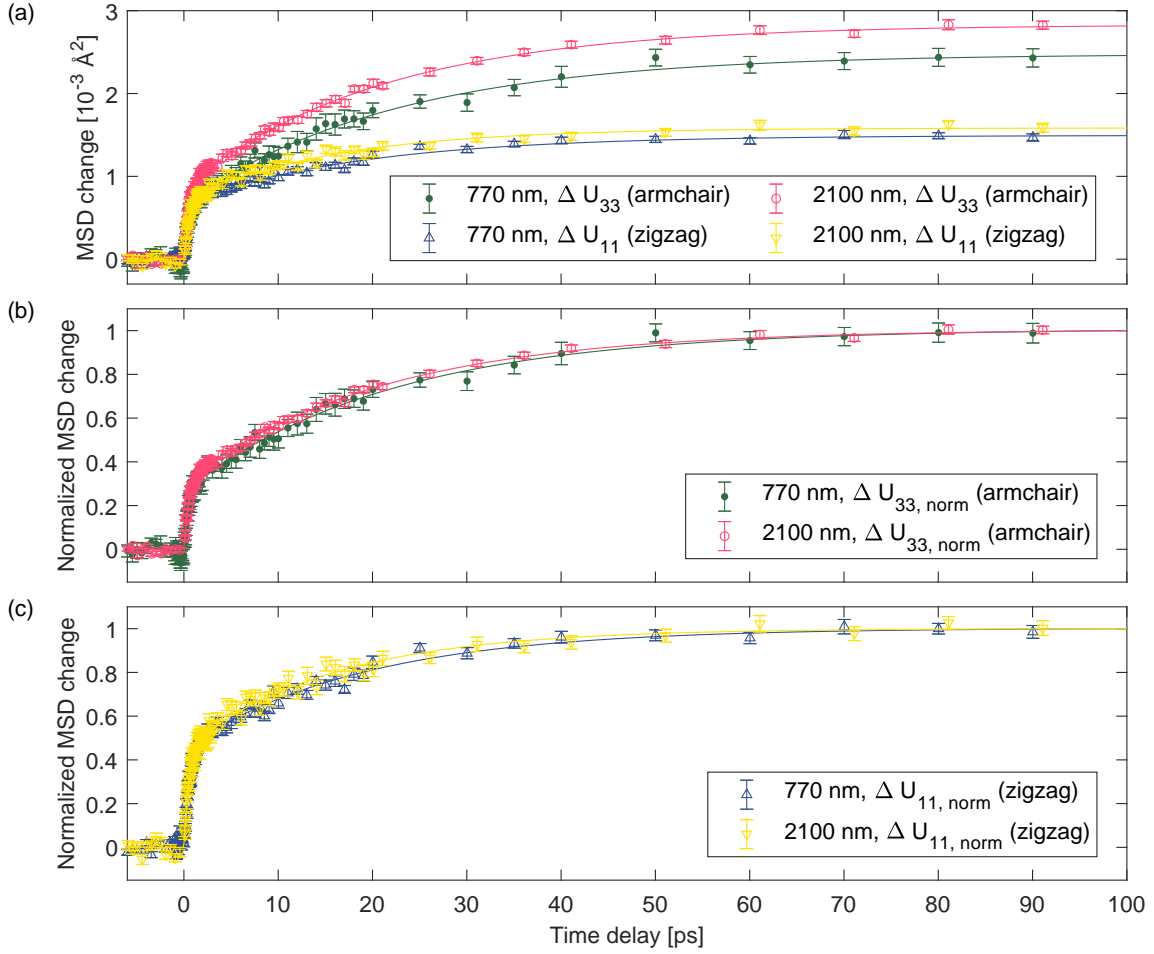
Figure 3.6: Influence of the pump wavelength on the observed MSD dynamics. Experiments with pump photon wavelengths of 2100 nm and 770 nm are compared. In both cases, the pump polarization was along the armchair direction. (a) MSD dynamics in the armchair and zigzag directions. (b) Normalized MSD dynamics in the armchair direction. All MSD changes were normalized to the results of a bi-exponential fit at 100 ps. (c) Same as (b), but for the MSD dynamics in the zigzag direction.

Next, the dependence on the polarization of the pump light is investigated. In general, changing the pump polarization changes the matrix elements of the electronic transitions, which means that different electronic states are initially excited. Depending on the efficiency of carrier thermalization, this can also influence the lattice dynamics. To study the polarization dependence of the lattice dynamics in black phosphorus, in addition to the experiment with polarization in the armchair direction discussed in Sec. 3.3, an experiment with polarization in the zigzag direction and otherwise unchanged excitation conditions was recorded.

The comparison is presented in Fig. 3.7. For zigzag polarization, the amplitude of the MSD rise is lower due to the anisotropic optical properties, as shown in Fig. 3.7(a). Based on the optical constants for zigzag polarization [Jia18], the absorbed energy density of this measurement was $140 \pm 30 \, \mathrm{J/cm^3}$, and thus a factor of ~ 2.6 lower than the experiment in the armchair direction. This factor is similar to the amplitude ratios of the MSD rises, ~ 2.8 for the MSD in the armchair direction and ~ 2.9 for the MSD in the zigzag direction. Note that absorbed energy density and MSD rise are not expected to be exactly proportional, but to a
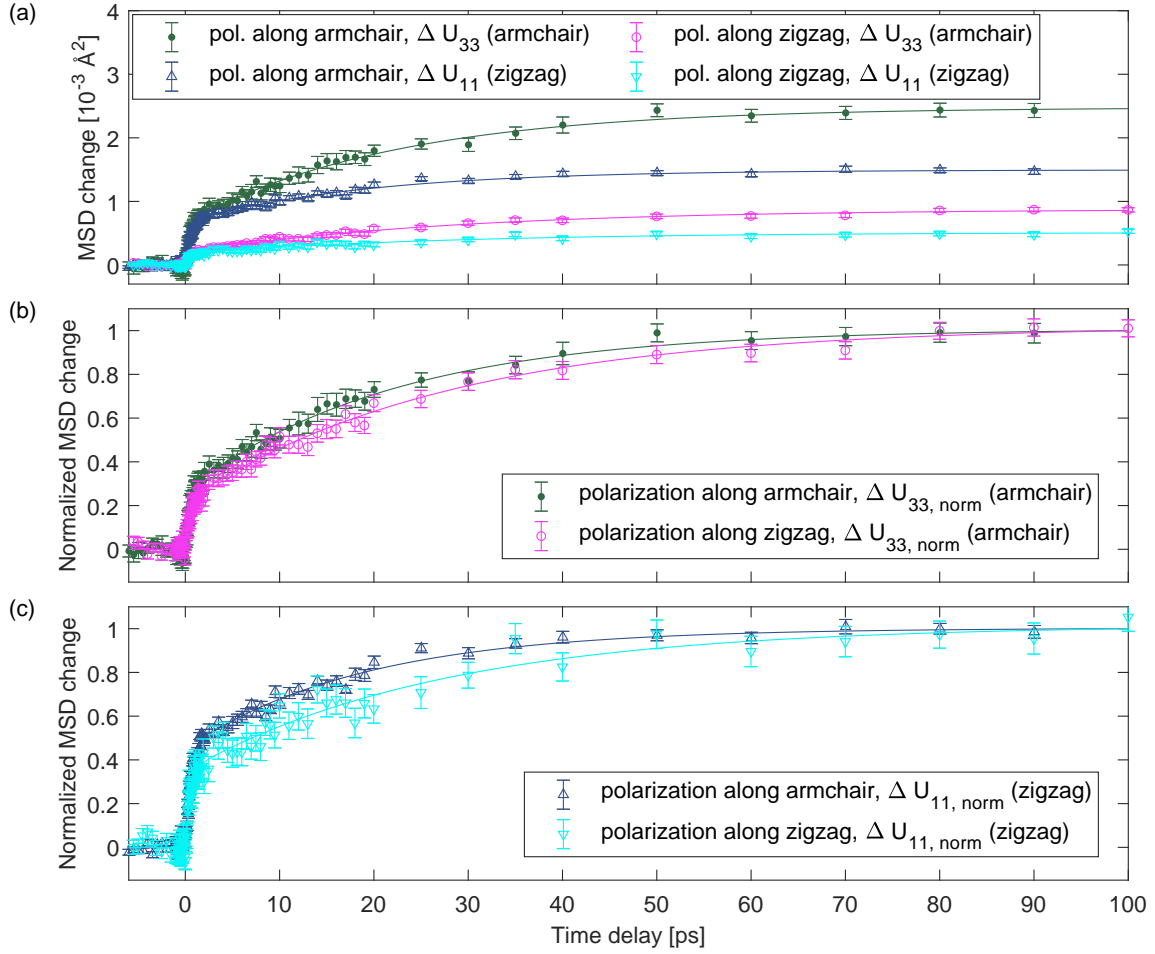
Figure 3.7: Influence of the pump polarization on the MSD dynamics. Measurements with pump polarization along the armchair and zigzag directions and otherwise unchanged excitation conditions are compared. The pump wavelength was $770\,\mathrm{nm}$ and the incident fluence was the same in both cases $(9.8 \pm 1.4\,\mathrm{mJ/cm^2})$. (a) MSD dynamics in the armchair and zigzag directions for both polarization directions. (b) MSD dynamics in the armchair direction for both polarization directions, normalized to the results of a bi-exponential fit (Eq. 3.3) at 100 ps. (c) Same as (b), but for the MSD dynamics in the zigzag direction.

good approximation. The exact relationship depends on the electron and lattice heat capacities and on whether the high-temperature limit is applicable for the MSD (see Sec. 2.3.3).

When comparing the normalized MSD dynamics for armchair and zigzag polarization, differences are observed, as presented in Fig. 3.7(b) for the MSD along the armchair direction and in Fig. 3.7(c) for the MSD along the zigzag direction. In both cases, the amplitude of the slow MSD rise (A_2) relative to the fast rise (A_1) is larger for zigzag polarization. In general, this behavior could be caused by the specific electronic states that are excited in each case (in combination with slow carrier thermalization), but it could also be due to the significantly different absorbed energy densities. Since the lattice dynamics of black phosphorus were found to be wavelength-independent, carrier thermalization is probably rather efficient, which means that the latter explanation for the observed differences between armchair and zigzag polarization is more likely.

To investigate effects of the absorbed energy density on the MSD dynamics, another measurement with 2100 nm pump wavelength was recorded, with a significantly lower absorbed energy density than the measurement of Fig. 3.6. Figure 3.8 compares results of bi-exponential fits with Eq. 3.3 for the two measurements with 2100 nm wavelength (shown in gray) and the two measurements with 770 nm wavelength and different polarization directions (shown in red). As a measure of the absorbed energy density, the sum of all MSD amplitudes is used, i.e. $A_{1,\text{armchair}} + A_{2,\text{armchair}} + A_{1,\text{zigzag}} + A_{2,\text{zigzag}}$. As presented in Fig. 3.8(a) and (d), the ratio of the amplitudes A_2/A_1 decreases with absorbed energy density for the MSDs in both the armchair and zigzag directions. For the fast time constant τ_1, no dependence on the absorbed energy density is observed. In contrast, the slow time constant τ_2 decreases with absorbed energy density. Since the same trends are observed for the two measurements with 2100 nm wavelength (both with polarization along the armchair direction) as well as the two measurements with 770 nm (with polarization along armchair and zigzag direction), it is likely that the observed differences for the two polarization directions are caused by the different absorbed energy densities. However, to fully exclude any effects of the pump polarization on the MSD dynamics, additional measurements are required. In particular, either matching the absorbed energy density for both polarization directions or recording measurements with several absorbed energy densities each would allow to better disentangle different contributions to the MSD dynamics.

Based on the experimental results presented in Fig. 3.8, it is likely that predominantly the slow component of the MSD dynamics depends on the absorbed energy density, since besides the amplitude ratio A_2/A_1 also τ_2 exhibits a dependence on the absorbed energy density. The slow component is mostly caused by phonon thermalization effects, as discussed in Sec. 3.3. Consequently, the experimental results point towards a dependence of the phonon thermalization on the absorbed energy density. There are two effects that can contribute to this. The first one is a population effect: for different absorbed energy densities, the final temperatures are different and thus also the final phonon populations, which are given by the Bose-Einstein distributions at the respective temperatures. Apart from more phonons being excited in total for high absorbed energy densities, also the relative population increase of different phonon frequencies is different, as illustrated in Fig. 3.9. For low absorbed energy densities, the additional phonons after excitation and phonon thermalization are shifted towards lower frequencies compared to high absorbed energy densities. Assuming that the energy and momentum distribution of the initially excited phonons doesn't depend on the absorbed energy density, phonon thermalization requires more redistribution towards lower frequencies for low absorbed energy densities. Redistribution to lower frequencies significantly enhances the MSD amplitude. Therefore, the effect could contribute to the higher relative amplitude of the slow component (A_2) and its larger time constant (τ_2) at low absorbed energy densities. However, in total, the differences are small, suggesting that it is not the only mechanism contributing to the observed behavior.

A second mechanism is an effect of the interaction itself: as discussed in Sec. 3.3, due to restrictive phase space constraints for electron-phonon scattering, phonon thermalization is predominantly achieved by direct phonon-phonon scattering (anharmonic decay and phonon-phonon collisions). In particular, anharmonic decay leads to the population of lower-frequency phonons at the expense of higher frequencies. The phonon-phonon scattering rates increase with increasing temperature [TM95; Sei21]. At low temperatures, the nuclei are located close to the interatomic potential and therefore the harmonic approximation is very good. As the temperature rises, the atomic MSD increases, and the average distance of the atoms from the
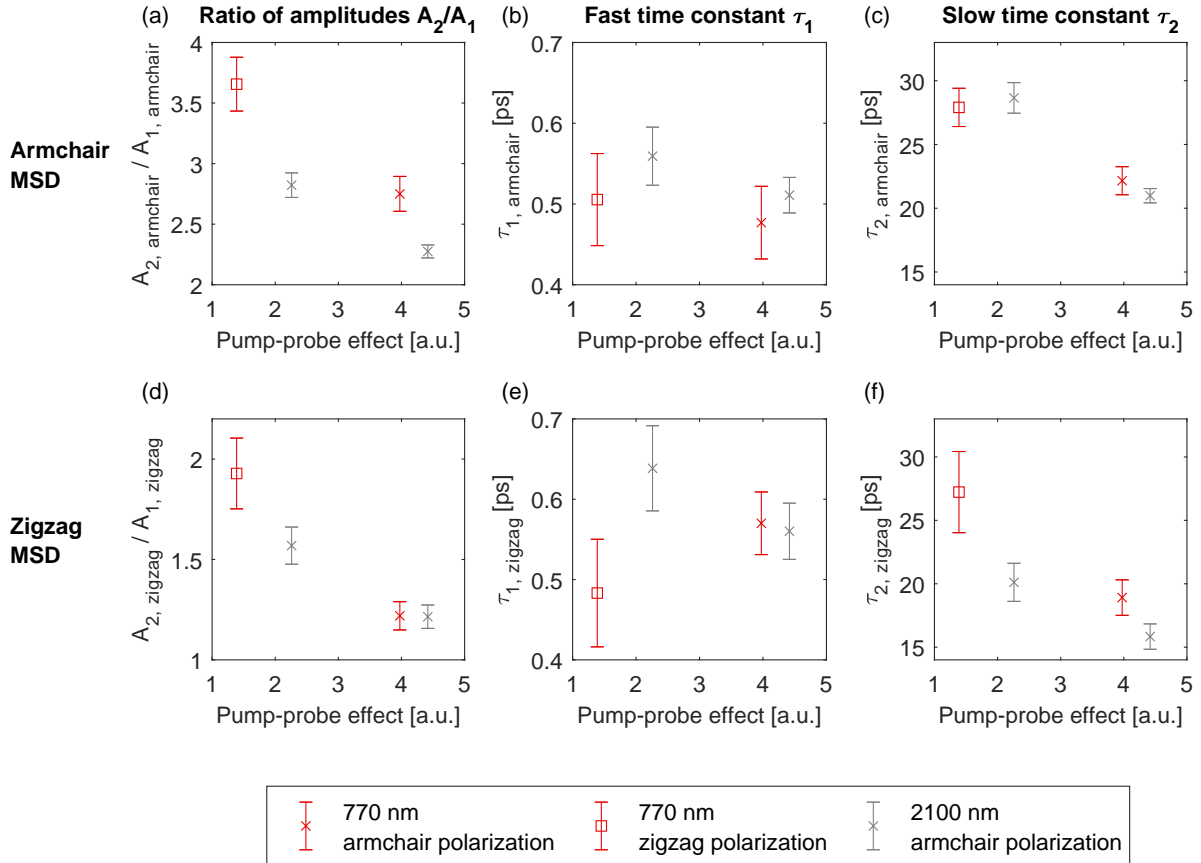
Figure 3.8: Dependence of the MSD dynamics on the absorbed energy density. Results of the bi-exponential fit with Eq. 3.3 are compared between different measurements. As a measure of the absorbed energy density, the total amplitude of the pump-probe effect is shown on the x-axes, calculated as $A_{1,\,\mathrm{armchair}} + A_{2,\,\mathrm{armchair}} + A_{1,\,\mathrm{zigzag}} + A_{2,\,\mathrm{zigzag}}$. The measurements presented here are the measurements previously shown in Figs. 3.6 and 3.7, plus a measurement at 2100 nm recorded with relatively low absorbed energy density. (a) Ratio of the amplitudes of the slow (A_2) and fast component (A_1) for the MSD along the armchair direction. (b) Time constant of the fast component for the MSD along the armchair direction. (c) Time constant of the slow component for the MSD along the armchair direction. (d) Same as (a), but for the MSD along the zigzag direction. (e) Same as (b), but for the MSD along the zigzag direction. (f) Same as (c), but for the MSD along the zigzag direction. The error bars correspond to 68.3 % confidence intervals obtained from the fit.

minimum of the interatomic potential increases as well. As a consequence, anharmonic effects play a larger role. In the case of laser excitation, additional phonons are created by electron-phonon and phonon-phonon scattering, thus enhancing anharmonic effects. The enhancement is larger for higher absorbed energy densities and therefore contributes to the observed decrease of τ_2 with absorbed energy density. It can also influence the amplitude ratios A_2/A_1 because separating the MSD dynamics in two different exponential contributions is an approximation. It is thus plausible that a change in phonon-phonon coupling strength can influence both amplitudes.

In order to further investigate the temperature-dependence of phonon-phonon scattering processes as well as population effects, there is an additional tuning knob available: the temperature of the material before laser excitation (base temperature). In addition to the measurement with 2100 nm photon wavelength and 100 K base temperature presented in Fig. 3.6, a measure-
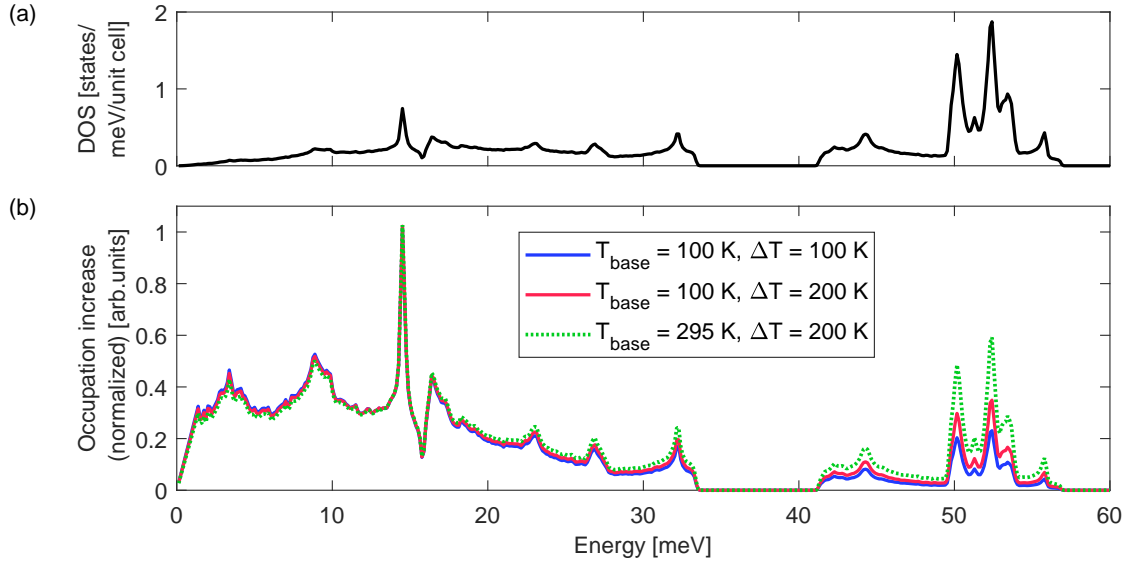
Figure 3.9: Phonon occupation increase after laser excitation and lattice thermalization for different experimental conditions. (a) Phonon DOS from the DFT calculations presented in Ref. [Sei21]. The number of states is given per conventional unit cell with 12 phosphorus atoms. (b) Normalized increase in phonon occupation for two different absorbed energy densities and base temperatures (T_{base}). The results were calculated based on the phonon DOS presented in (a) and the Bose-Einstein distributions at different temperatures. To compare the frequency distributions of the additional phonons, each curve was normalized to its integral.

ment at room temperature and otherwise unchanged experimental conditions was performed. The comparison of the two measurements is presented in Fig. 3.10. Panel (a) presents the direct comparison of the amplitudes of the MSD changes in both the armchair and zigzag directions. As expected, the amplitudes of the MSD changes are very similar for the two measurements, since the same incident pump fluence and polarization was employed in both cases. Note that as in Fig. 3.6, the slightly different amplitude ratios $\Delta U_{33}/\Delta U_{11}$ observed for the two base temperatures cannot be reliably interpreted, since they could also be caused by systematic errors. Figure 3.10(b) and (c) present a comparison of the normalized MSD changes for the armchair and zigzag directions, respectively. Pronounced differences are observed for the two base temperatures. First, for 295 K base temperature, the amplitude ratios A_2/A_1 are lower for both armchair and zigzag MSD. Second, the slow rise is significantly faster in the measurement at room temperature. Table 3.2 compares the fit results for all parameters of Eq. 3.3.

The most striking difference is observed for the time constant τ_2, which is by a factor of ~ 2 smaller in the room temperature measurement. This indicates that phonon thermalization is much more efficient compared to the measurement at 100 K. Since the incident laser fluence was the same and thus the absorbed energy densities were very similar[3], any effects of the absorbed energy density can be excluded as a cause of the different MSD dynamics. The significant reduction of τ_2 with increasing temperature is likely caused at least partially by the temperature dependence of anharmonic decay. This is in qualitative agreement with temperature-dependent

---

[3]Differences could occur due to temperature-dependent changes of the band structure, matrix elements, or equilibrium carrier occupation. Nevertheless, the resulting absorption differences are small, as evidenced by the very similar magnitude of the pump-probe effect in both cases (see Fig. 3.10(a)).
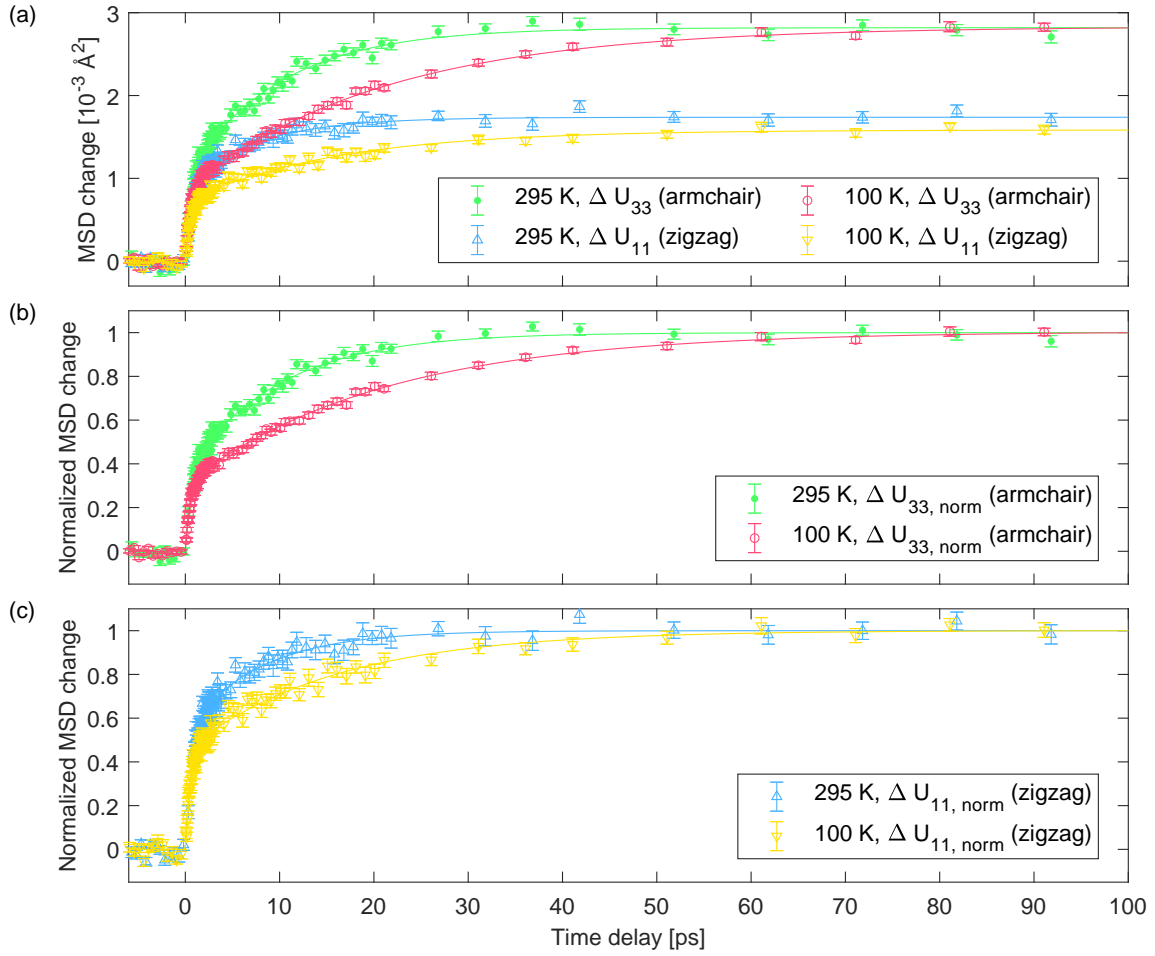
Figure 3.10: Dependence of the MSD dynamics on the temperature before laser excitation (base temperature). A measurement at a base temperature of 100 K is compared to one at 295 K. The pump wavelength was 2100 nm and the excitation conditions, in particular also the incident pump fluence, were the same in both measurements. (a) MSD dynamics along the armchair and zigzag directions for both base temperatures. (b) MSD dynamics along the armchair direction for both base temperatures, normalized to the results of the bi-exponential fit (Eq. 3.3) at 100 ps. (c) Same as (b), but for the MSD dynamics along the zigzag direction.

	100 K		295 K	
	armchair	zigzag	armchair	zigzag
$A_1 \ [10^{-3}\mathrm{\AA}^2]$	0.86 ± 0.02	0.72 ± 0.02	1.01 ± 0.04	0.94 ± 0.05
$\tau_1 \ [\mathrm{ps}]$	0.51 ± 0.03	0.56 ± 0.04	0.61 ± 0.06	0.75 ± 0.07
$A_2 \ [10^{-3}\mathrm{\AA}^2]$	1.97 ± 0.02	0.87 ± 0.03	1.81 ± 0.04	0.80 ± 0.05
$\tau_2 \ [\mathrm{ps}]$	21.0 ± 0.6	16 ± 1	9.8 ± 0.5	7.8 ± 0.9

Table 3.2: Results of a bi-exponential fit (Eq. 3.3) to the MSD dynamics after excitation with 2100 nm light polarized along the armchair direction, comparison between 100 K and 295 K base temperature. The errors correspond to 68.3 % confidence intervals of the fit.

measurements of (single-state) phonon lifetimes with Raman spectroscopy [Tri19], which revealed an increase of phonon linewidth with temperature for most Raman-active phonons. The result is also in agreement with the time-dependent Boltzmann calculations of Ref. [Sei21]. In addition to the temperature dependence of anharmonic decay, another (likely smaller) contribution to the reduction of τ_2 can stem from the different phonon population increases in both cases (as discussed previously and illustrated in Fig. 3.9(b)).

Regarding the amplitude components A_1 and A_2 of the MSD increase, there is a tendency that A_1 is higher for the measurement at $295\,\mathrm{K}$ compared to $100\,\mathrm{K}$, while the opposite is true for A_2. However, due to the vastly different time constants τ_2, these results cannot be interpreted unambiguously. Even though A_1 is dominated by electron-phonon scattering and A_2 is dominated by phonon-phonon scattering, as mentioned previously, there is no sharp separation between the two processes. Both electron-phonon scattering and phonon-phonon scattering processes happen simultaneously and also influence each other. Therefore, more efficient phonon-phonon scattering can influence not only τ_2, but also the results for A_1 and A_2.

3.5 Accessing transient momentum distributions with ultrafast diffuse scattering

The analysis presented in the previous two sections focused on the Bragg reflections. It revealed pronounced nonthermal phonon distributions on ultrafast timescales and could follow the redistribution of phonon energies towards Bose-Einstein statistics. However, based on the Bragg reflections alone it is not possible to learn which phonon modes are predominantly populated when the lattice is in a nonthermal state. Only the total effect of *all* additional phonons on the MSD can be measured. The atomic displacements caused by a certain phonon mode are described by its phonon polarization vector. It is important to note that the direction of atomic displacement is generally not the same as the momentum of the phonon mode. The MSD dynamics therefore do not enable access to the momentum distribution of the additional phonons. To access this information, the diffuse scattering background can be analyzed, which encodes information on the phonon momenta [Tri10; Wal17b; Ste18].

To visualize changes in the diffuse scattering background of black phosphorus, the diffraction pattern before laser excitation was subtracted from the diffraction patterns recorded after the arrival of the pump laser pulse. The resulting difference images are presented in Fig. 3.11(a)-(c) for the same measurement as in Sec. 3.3 and several pump-probe delays.

Following laser excitation, the Bragg reflections decrease (blue dots in Fig. 3.11), which was analyzed in detail in Sec. 3.3. In addition, the intensity of the diffuse scattering background increases (red areas in Fig. 3.11). With increasing pump probe delay, there are profound changes in the diffuse scattering background: at $2\,\mathrm{ps}$ pump-probe delay, the difference image exhibits vertical stripes. In contrast, at $10\,\mathrm{ps}$ delay, a diamond-shaped structure is visible, which is further intensified at $50\,\mathrm{ps}$ delay. These changes in the diffuse background directly show that the phonon distribution changes profoundly on timescales of tens of picoseconds, in agreement with the results of Sec. 3.3.

In order to gain detailed insights into the nonthermal phonon distributions, the experimental results were complemented by calculations based on the time-dependent Boltzmann formalism. Here, the electrons were assumed to be in internal thermal equilibrium, which is a reasonable
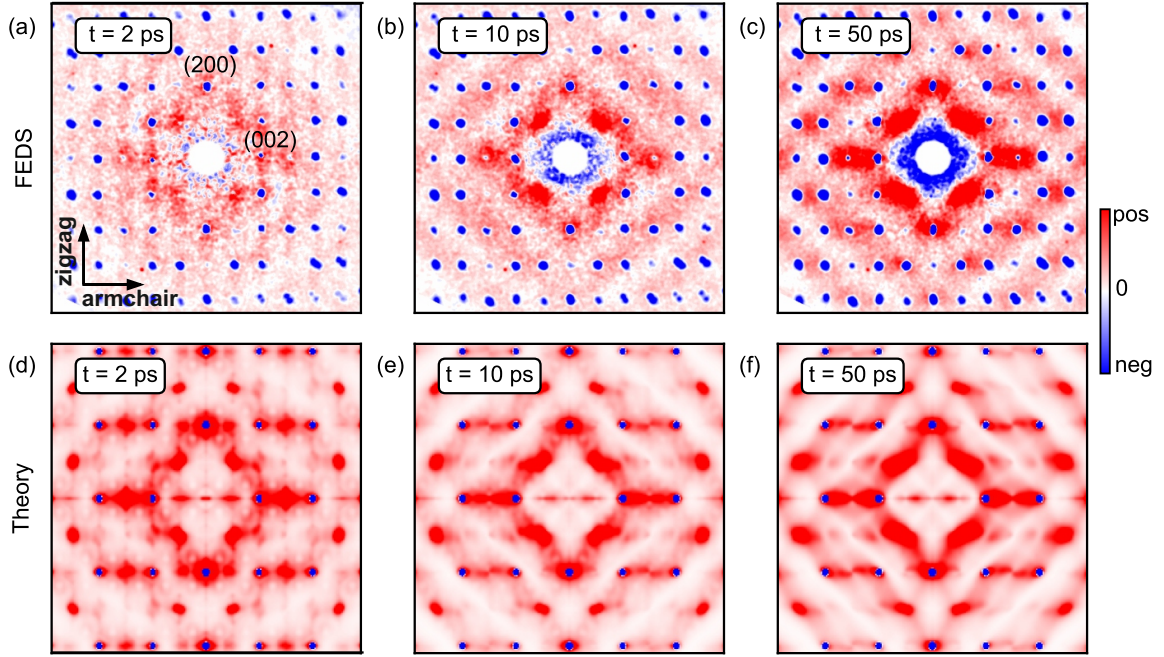
Figure 3.11: Experimental and theoretical diffuse scattering signals of black phosphorus. (a)-(c) Experimentally measured difference images (difference to pre-time-zero diffraction pattern) at several pump-probe delays. The data were two-fold symmetrized and normalized to a common number. Blue corresponds to an intensity decrease while red corresponds to an intensity increase. (d)-(f) Simulated difference images at the same pump-probe delays as in (a)-(c), calculated using the time-dependent Boltzmann equation formalism and the all-phonon structure factor [Zac21]. The data were normalized to a common number. Adapted from Ref. [Sei21].

approximation based on the results of Sec. 3.4. Both electron-phonon and phonon-phonon scattering processes are described using the time-dependent Boltzmann equation formalism [Car21]. Due to the complexity of the calculation, it was restricted to electron momenta in the Q-Z-A′ plane and phonon momenta in the X-Γ-A plane. Further details are available in Ref. [Sei21].

Figure 3.12 presents the calculation results. To visualize the nonthermal evolution of the phonons, the phonon occupation numbers were converted to temperatures (of the individual phonon modes). Fig. 3.12(a)-(e) present the momentum distribution of the additional phonons by showing the temperatures of phonon modes in the X-Γ-A plane at several pump-probe delays. To show the distribution of phonon energies as well, Fig. 3.12(f)-(h) present the phonon band structure with phonon temperatures at several pump-probe delays.

Shortly after laser excitation ($t = 100$ fs), only phonons around Γ are excited, as presented in Fig. 3.12(a). Figure 3.12(f) shows that these phonons are predominantly optical phonon modes. On intermediate timescales (500 fs to few ps), phonon modes along the Γ-A direction are preferentially populated (see Fig. 3.12(b) and (c)). This can be explained by the asymmetric shape of the electronic DOS around the Z-point and by electron-phonon scattering of highly excited electrons from the A- and Y-valleys to the Z-valley. Regarding the energies, it can be seen from Fig. 3.12(g) that optical modes are still populated significantly more than in thermal equilibrium. On timescales of tens of picoseconds, phonon thermalization across the
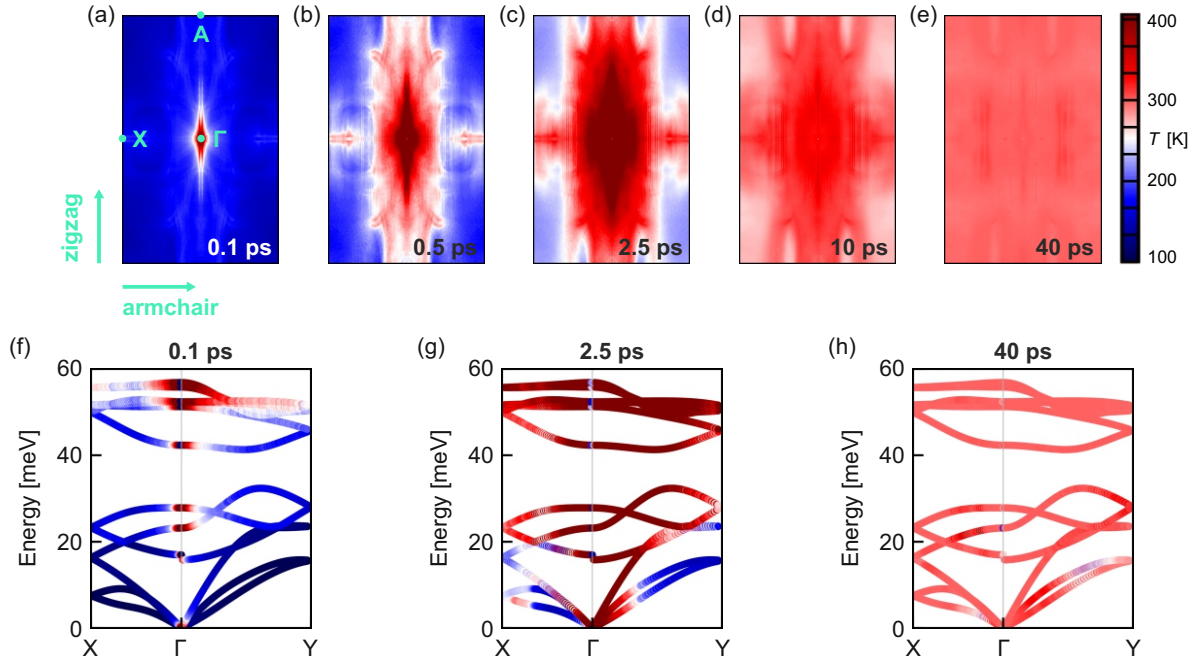
Figure 3.12: Calculated evolution of the non-equilibrium phonon population. For visualization purposes, temperatures of individual phonon modes are presented (instead of occupation numbers). (a)-(e) Phonon temperatures in the X-Γ-A plane at several pump-probe delays, showing the non-equilibrium distribution of phonons in momentum space. (f)-(h) Phonon band structure with temperatures of individual modes at several pump-probe delays, showing the non-equilibrium energy distribution in addition to the non-equilibrium momentum distribution. Adapted from Ref. [Sei21].

full Brillouin zone is achieved, as presented in Fig. 3.12(d), (e) and (h). These results are in qualitative[4] agreement with the conclusions drawn from the measured MSD dynamics (Sec. 3.3). In particular, the calculated initial creation of high-energy (optical) phonons and the subsequent thermalization of the lattice on timescales of tens of picoseconds agrees well with the measured two-step behavior of the MSD dynamics.

In order to relate the non-equilibrium calculations to the experimentally measured diffuse scattering signal, calculating the phonon structure factor (also called inelastic structure factor) is required. Here, the all-phonon structure factor was calculated as described in Ref. [Zac21]. The results for the transient changes in scattering intensity are presented in Fig. 3.11(d)-(f). The calculated images agree well with the experimental results. In particular, the faint vertical stripes at a pump-probe delay of 2 ps are reproduced, showing that the nonthermal phonon population on short timescales after laser excitation is well captured by the time-dependent Boltzmann calculations. Also on longer timescales, the calculation offers a good description of the experimental results. The emergence of a diamond-shaped structure in the difference images is well described, meaning that also the relaxation pathway of the lattice back to a thermal state is captured by the calculations.

---

[4]For a quantitative comparison, the MSD dynamics from theory could be calculated from the phonon occupation numbers, using the phonon energies and polarization vectors. In practice, problems arise at low phonon wavevectors, as discussed in Sec. 2.3.3. Therefore, a quantitative comparison is not presented here.

To summarize, the analysis of the diffuse scattering background and the time-dependent Boltzmann calculations confirm the results of the previous sections: following laser excitation, electron-phonon coupling leads to a highly nonthermal state of the lattice with predominantly high-energy phonons excited. On timescales of tens of picoseconds, thermal equilibrium of the lattice is restored. In addition, the results presented in this section yield information about the momenta of the transiently excited phonons, which is not accessible via a Bragg reflection analysis. The time-dependent Boltzmann calculations presented in Fig. 3.12 reveal yet another manifestation of the structural anisotropy of black phosphorus: the transient phonon distribution is highly anisotropic in momentum space, with momenta predominantly along the zigzag direction. In general, the results highlight the complexity of the ultrafast response of black phosphorus to laser excitation, which is dominated by phase-space constraints and thus exhibits strongly nonthermal phonon populations.

3.6 Summary and outlook

In summary, the lattice of black phosphorus exhibits a strongly nonthermal and anisotropic behavior following laser excitation. For all measurements reported here, the same qualitative behavior was observed. Energy transfer from the photo-excited electrons to the lattice within ~ 500 fs leads to a transient, nonthermal state of the lattice with a relatively high atomic displacement in the zigzag direction. Also the phonon momenta are predominantly along the zigzag direction in this non-thermal state. On a timescale of tens of picoseconds, the lattice relaxes back to a thermal state.

The details of the lattice response depend on the experimental conditions. The most striking differences were observed for different base temperatures. Increasing the base temperature from 100 K to 295 K leads to a twice faster lattice thermalization. Similar, but less pronounced effects were also observed with increasing absorbed energy density. These trends are likely caused predominantly by the temperature-dependence of direct phonon-phonon scattering. In contrast, a comparison of 770 nm and 2100 nm excitation wavelength revealed no differences in the MSD dynamics, suggesting efficient electron thermalization.

The results for the lattice dynamics of black phosphorus presented here are relevant for applications of black phosphorus in non-equilibrium conditions [She15; Sot15; Liu17]. In particular, the timescale of electron-phonon equilibration is a crucial factor for applications in which hot carriers are either excited or injected in black phosphorus. The details of electron-phonon coupling and phonon thermalization are relevant for heat management, which is essential for successful device miniaturization. In addition, the observed transient nonthermal state of the lattice could affect macroscopic properties such as thermal or electrical conductivities, which would influence the performance of devices operating far from thermal equilibrium. Finally, the observed dependence of phonon thermalization on the base temperature offers an additional tuning knob for either prolonging or shortening the nonthermal state of the lattice, depending on the desired application.

Beyond black phosphorus, anisotropic effects of nonthermal states are also expected for other anisotropic materials. In particular, all van der Waals crystals are anisotropic in the out-of-plane direction. Therefore, anisotropic MSD dynamics are expected after laser excitation or carrier injection, especially for semiconducting, insulating, and semimetallic van der Waals materials with pronounced phase-space constraints for electron-phonon scattering. Indeed, anisotropic

MSD dynamics have already been reported for monolayer WSe_2 [Tun19]. Such behaviors could influence not only the transient properties of the material itself but also transport across interfaces, e.g. across laterally stacked heterostructures. To study out-of-plane dynamics of van der Waals materials with time-resolved transmission electron diffraction, the side pumping geometry discussed in Sec. 2.2.2 could be employed.

Chapter 4

Lattice dynamics in $3d$ ferromagnets

In magnetic systems, besides the electron and phonon subsystem, also magnetic degrees of freedom play a role in the ultrafast response of the material to laser excitation. Before 1996, it was believed that spin order needs at least several tens of picoseconds to react to ultrafast electron or lattice temperature changes [Agr84; Vat90; VBM91]. Then, a groundbreaking experiment by Beaurepaire et al. showed that in the itinerant $3d$ ferromagnet nickel, laser excitation leads to a magnetization reduction on much faster timescales of only few hundreds of femtoseconds [Bea96]. This discovery opened up the perspective of magnetic data manipulation on femtosecond timescales and started the field of ultrafast magnetism. Since then, ultrafast demagnetization as well as magnetization switching have been observed in a large number of materials [KKR10], and a lot of work has been done to understand the phenomenon microscopically [Bea96; Kaz07; Bal08; Atx10; BCO10; Sch10; KKR10; Koo10; MR14; TP15; Car15; Eic17; Gor18; Dor19; Guy22]. Several mechanisms have been identified as potentially contributing to ultrafast demagnetization. Koopmans et al. attributed the effect to Elliott-Yafet spin-flip scattering and proposed the so-called microscopic three-temperature model (M3TM) to describe ultrafast magnetization dynamics [Koo10]. Battiato et al. elucidated the role of spin-dependent transport [BCO10], which significantly increases the demagnetization rate for materials on metallic substrates. More recently, also evidence for ultrafast magnon generation was reported [Sch10; Car15; Tur16; Eic17].

The lattice of $3d$ ferromagnets plays two important roles in laser-induced dynamics. First of all, it acts as a sink for angular momentum. Any change of the magnetization comes with an angular momentum change of the spin system, which needs to be compensated by other degrees of freedom. Two recent studies show experimental evidence that angular momentum is dissipated to the lattice [Dor19; Tau22].

In addition to its role as an angular momentum sink, the lattice also plays a significant role in the ultrafast energy flow due to its large heat capacity. Directly after excitation, the deposited energy is predominantly stored in the electron system. During thermalization of the electrons with the other two subsystems, a large portion of that energy flows to the lattice. This can be seen by comparing the heat capacities of electrons, spins, and the lattice, which are presented in Fig. 4.1(a) for nickel (black curves). Consequently, electron-phonon coupling has a strong influence on the electron dynamics, and thus indirectly also on the spin dynamics. On the other hand, also the spin heat capacity is high compared to the electron heat capacity,

which means that energy flow into and out of magnetic degrees of freedom has a strong influence on the electron dynamics as well, and can thus indirectly[1] influence the lattice dynamics.

Most models for ultrafast magnetization dynamics are compared mainly to experimental results for the spin dynamics. This approach does not necessarily lead to good agreement with the responses of the other two subsystems. For example, the three-temperature model (3TM) introduced by Beaurepaire et al. [Bea96], a phenomenological extension of the TTM, describes the spin dynamics of nickel very well. However, it yields a lattice response significantly slower than experimental results, as shown in Fig. 4.1(b). Also the comparison to electron temperature dynamics [Ten18] reveals significant discrepancies. The M3TM by Koopmans et al. [Koo10] yields good agreement to the experimentally measured electron-lattice equilibration time in nickel. However, the experimentally measured electron dynamics are not described well. Both models are based on electron and phonon heat capacities that differ significantly from literature results, as shown in Fig. 4.1(a). These discrepancies in the heat capacities contribute to the disagreement with experiments, particularly for the electron temperature dynamics. A model that is consistent with the responses of electron, phonon, and spin system is still missing.
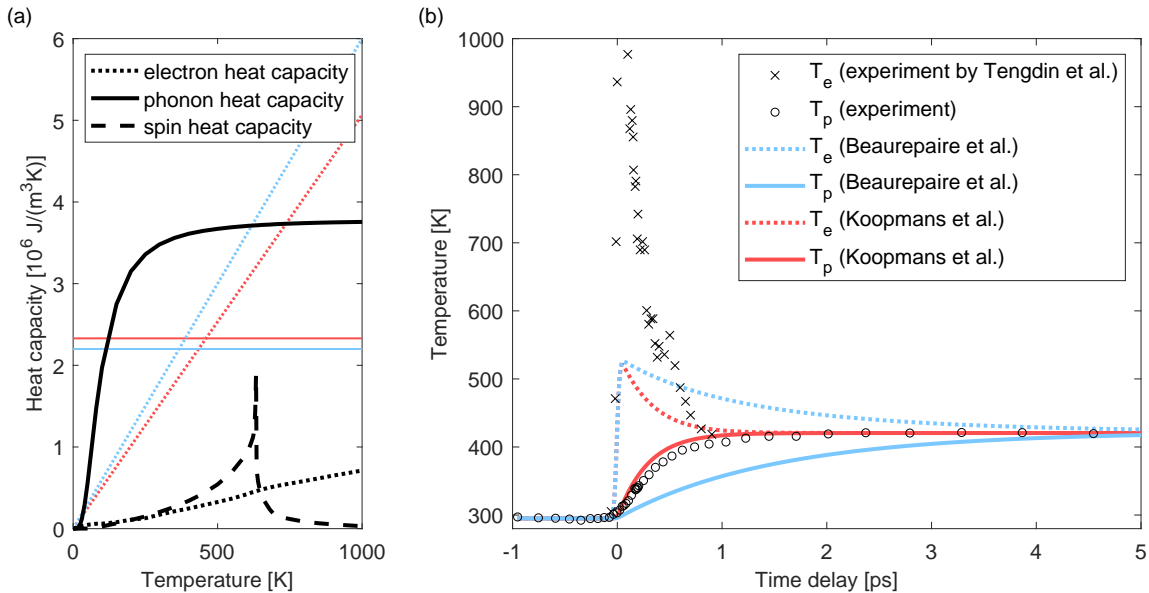
Figure 4.1: Experimental results for the heat capacity contributions and ultrafast electron and lattice responses of nickel. (a) Contributions of phonons, electrons, and spins to the heat capacity of nickel (black curves). The data are experimental results from Ref. [Mes81]. In addition, the values assumed in the 3TM by Beaurepaire et al. [Bea96] (blue curves) and in the M3TM by Koopmans et al. [Koo10] (red curves) are presented. Phonon heat capacities are shown as solid lines and electron heat capacities are shown as dotted lines. Since Ref. [Koo10] doesn't provide the Sommerfeld coefficient γ directly, γ and the resulting electronic heat capacity were calculated as in Ref. [Koo10], with the value of $3.86\,\frac{\mathrm{J}}{\mathrm{m}^3\mathrm{K}}$ for the total heat capacity at room temperature [Mes81]. (b) Experimentally measured electron and lattice responses and comparison to the 3TM by Beaurepaire et al. [Bea96] and the M3TM by Koopmans et al. [Koo10]. The experimentally measured electron temperature dynamics stem from Ref. [Ten18].

---

[1]In general, direct spin-lattice coupling can also contribute to the magnetization dynamics. For the elemental $3d$ ferromagnets iron, cobalt, and nickel, the fact that the demagnetization timescale is faster than the electron-lattice equilibration suggests that demagnetization is predominantly driven by electron-spin coupling.

For a description of the laser-induced dynamics that is consistent with the responses of all three subsystems, any model must be compared to experimental results for their responses to laser excitation. The magnetization responses of iron, cobalt, and nickel have been studied extensively using the magneto-optical Kerr effect (MOKE) [Car08; Koo10; Rot12; You18; Büh18; Gor20; Bor21; Uni21], X-ray magnetic circular dichroism (XMCD) [Sta07], and photoemission [Eic17; Ten18; Gor18; AW20; Büh20; Gor20]. In addition, optical and photoemission techniques have been applied to study the electronic responses [Caf05; Kam05; Car08; Ten18; AW20; Büh20; Gor20]. In contrast, information on the lattice responses is scarce. Time-resolved diffraction is only sensitive to the lattice and is thus the most direct way to study the lattice response. However, only few time-resolved diffraction studies of the femtosecond lattice responses of iron, cobalt, and nickel exist in literature [Wan08; Wan10; Rot19; Dur20]. In addition, values for the electron-phonon coupling parameters G_{ep} vary by several orders of magnitude [Bea96; Wel98; SMW03; Caf05; Big05; HKN07; LZC08; Koo10; MR13; PIM13; DVV14; Per16; Mig17; Ogi18; Ten18; MM20; ROM20; Uni21; LZC]. Those discrepancies reflect the difficulties of extracting G_{ep} from experimental data in the case of magnetic materials, since three different subsystems (instead of two for non-magnetic materials) contribute to the experimental observations.

This chapter presents electron diffraction results for all three $3d$ ferromagnets. To avoid a fit of G_{ep} to experimental data, spin-resolved DFT calculations are employed, the results of which were already presented in Sec. 2.4. Using the DFT results, different models for the microscopic energy flow between electrons, spins, and phonons are compared to the experimental results. First, the TTM and the 3TM are discussed, which are however not sufficient to consistently describe the responses of the materials to laser excitation. A better description of both the magnetization responses as well as the microscopic energy flow is achieved with energy-conserving atomistic spin dynamics (ASD) simulations.

The ASD simulations presented here were performed by Florian Jakobs and Unai Atxitia (Freie Universität Berlin) and the DFT calculations were performed by Jan Vorberger and Tim Butcher (Helmholtz-Zentrum Dresden-Rossendorf). The samples were grown by Dieter Engel (Max-Born-Institut). The time-resolved Faraday rotation measurement of iron, the results of which are presented in Fig. 4.11(b), was performed by Reza Rouzegar (Fritz-Haber-Institut). Most of the results presented in this chapter were published in Ref. [Zah21a] (nickel) and Ref. [Zah21b] (iron and cobalt). The experimental data are publicly available [Zah21e; Zah22b], as well as the DFT calculation results [Zah20c; Zah22a], and the ASD simulation results for iron and cobalt [Jak22].

4.1 Femtosecond electron diffraction results

The samples for the electron diffraction experiments were grown on NaCl crystals by magnetron sputter deposition, resulting in polycrystalline films. To protect the metal films from oxidation, 5 nm of amorphous Si_3N_4 was deposited before and after depositing the ferromagnet. The thickness of the ferromagnet was 20 nm in all cases. To obtain freestanding samples, the films were transferred onto TEM grids as described in Sec. 2.1.2. The films were not exposed to a magnetic field before the experiment. All measurements were conducted at room temperature (295 K).
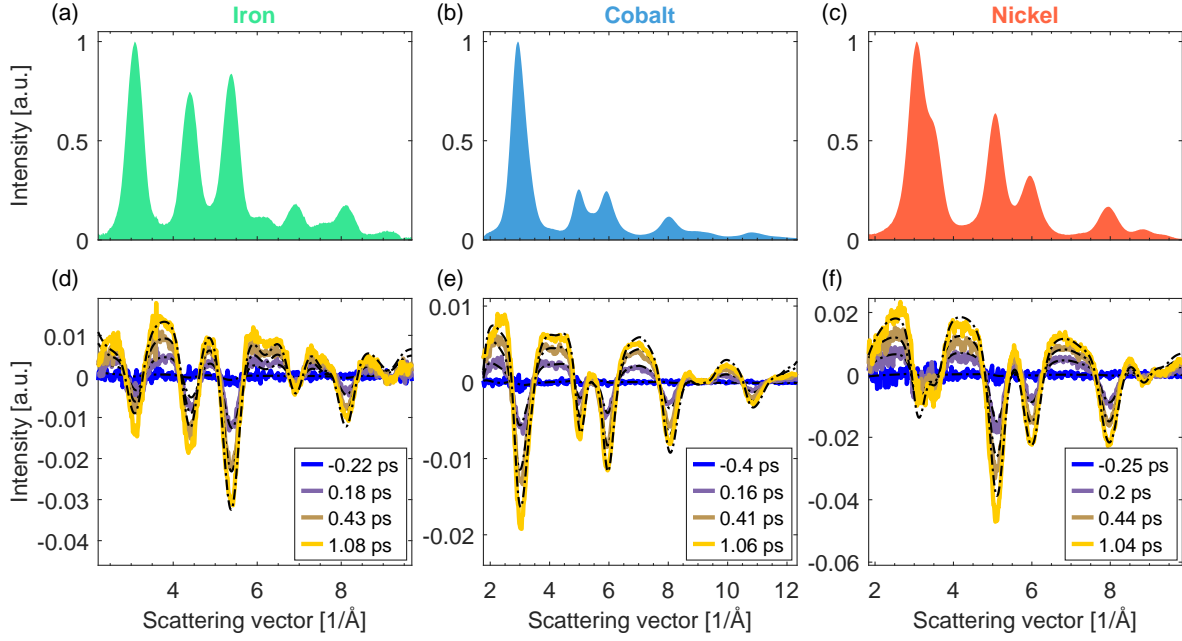
Figure 4.2: Azimuthally averaged diffraction patterns (radial profiles, RP's) of iron, cobalt, and nickel and their time-resolved changes following laser excitation. (a) RP of iron. For illustration purposes, the background (result from the static fit of the global fitting routine) was subtracted and the distance from the zero-order beam in pixels was converted to scattering vector. Here, the scattering vector is defined such that $q = 4\pi \sin(\theta)/\lambda$ with λ being the electron wavelength and θ the Bragg angle. (b) Same as (a), but for cobalt. (c) Same as (a), but for nickel. (d) Time-resolved changes in the RP of iron after laser excitation. The absorbed energy density was $540\,\mathrm{J/cm^3}$, calculated based on the final lattice temperature after electron-phonon equilibration and the total heat capacity from literature (literature results as in Fig. 4.7). The differences compared with the RP before laser excitation are presented. Solid curves correspond to experimental data, and dashed black curves are fit results of the global fitting routine described in Sec. 2.3.2 (dynamic fit). The scale of the intensity is the same as in (a). (e) Same as (d), but for cobalt. The absorbed energy density was $680\,\mathrm{J/cm^3}$. (f) Same as (d), but for nickel. The absorbed energy density was $1180\,\mathrm{J/cm^3}$. In all measurements presented here, the pump wavelength was $2300\,\mathrm{nm}$.

Figure 4.2 presents azimuthally averaged diffraction patterns (radial profiles, RPs) of all three materials. Nickel crystallizes into a face-centered cubic (fcc) crystal structure, iron exhibits a body-centered cubic (bcc) structure at room temperature and cobalt exhibits a hexagonal close-packed (hcp) structure. Examples of time-dependent changes in the RPs following laser excitation are also presented. To extract lattice dynamics from the RPs, the global fitting routine described in Sec. 2.3.2 was employed, which yields the MSD increase as a function of pump-probe delay. The resulting MSD dynamics were converted into lattice temperatures using the Debye-Waller factors presented in Sec. 2.4. Examples of MSD/lattice temperature dynamics in all three ferromagnets are presented in Fig. 4.3(a)-(c). In all cases, the MSD/temperature increase is well described by a single exponential function, convolved with a Gaussian to account for the time resolution of the experiment (~170 fs FWHM for the experiments on nickel and ~250 fs for the experiments on iron and cobalt, which were performed with a smaller probe beam size on the cathode). The time resolution was estimated based on the onset of the MSD/lattice temperature rise.
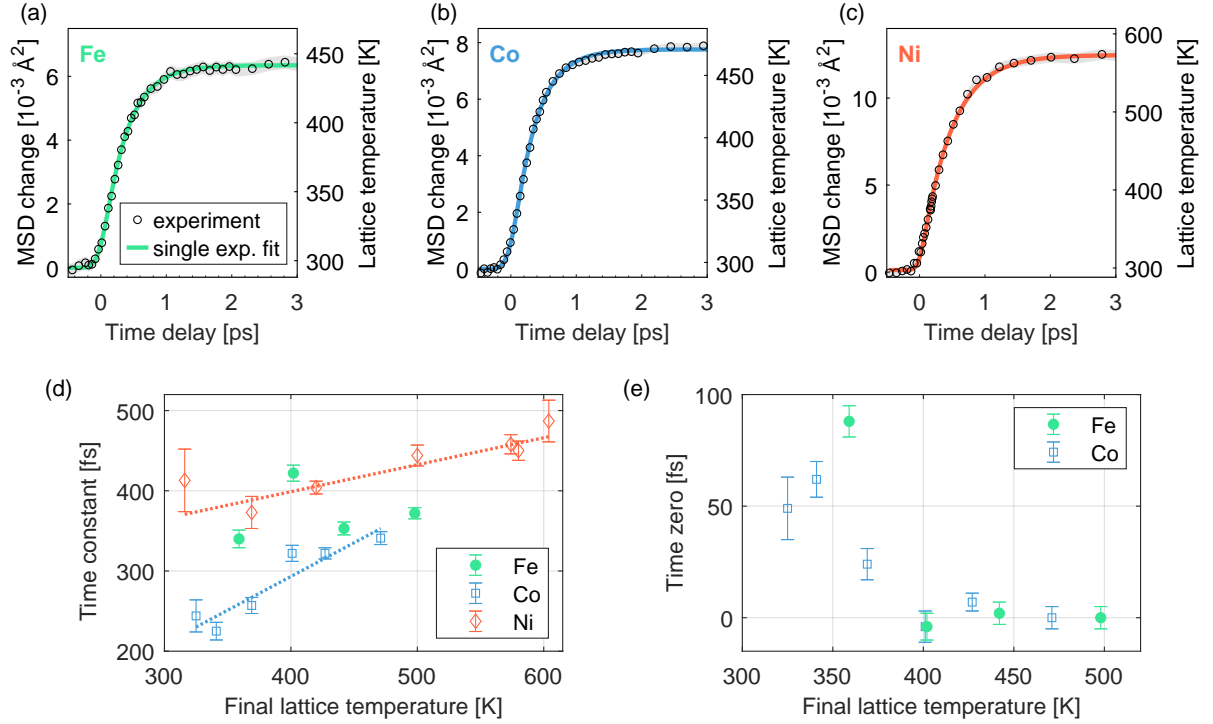
Figure 4.3: MSD changes following laser excitation of elemental $3d$ ferromagnets. (a) MSD rise in iron after excitation with a laser pulse. The absorbed energy density was $540\,\mathrm{J/cm^3}$ (the same measurements as in Fig. 4.2 are presented here). The black circles represent the experimental data and the gray shaded areas correspond to the standard errors of the experimental data obtained from the global fitting routine. The solid curve is the result of fit with a single exponential function, convolved with a Gaussian of $250\,\mathrm{fs}$ FWHM to account for the estimated time resolution of the experiment. (b) Same as (a), but for cobalt. The absorbed energy density was $680\,\mathrm{J/cm^3}$. (c) Same as (a), but for nickel. The absorbed energy density was $1180\,\mathrm{J/cm^3}$. In contrast to (a) and (b), the FWHM of the Gaussian was only $170\,\mathrm{fs}$ here, since the experiments on nickel were recorded with better time resolution. The pump wavelength was $2300\,\mathrm{nm}$ in all experiments presented here. The lattice temperatures on the right were calculated using the Debye-Waller factors (DWFs) presented in Sec. 2.4. For iron and cobalt, the DWFs calculated from DFT results were employed while for nickel, the tabulated DWF from Ref. [PDW11] was used, which is in good agreement with the DWF from DFT. All fits presented here were performed to the temperature dynamics. In practice, the difference between a fit to the temperature dynamics or the MSD dynamics is small, because the two quantities are essentially proportional at room temperature (see Sec. 2.4 for further details). (d) Fit results for the time constants of the single exponential function for all three materials and several fluences each. As a measure of fluence, the final lattice temperature after electron-phonon equilibration is used. For cobalt and nickel, the results of linear fits to the data are presented as well (dashed lines), since these two materials exhibit a clear increase of the time constant with increasing fluence. (e) Fit results for the onset of the single exponential function (time zero) for different fluences. The results are presented relative to the highest fluence because there is no absolute measure of time zero in the setup employed here. Only measurements on iron and cobalt are presented because the comparison is only possible when data for different fluences were recorded in the same measurement, which was not the case for nickel.

The results of the single exponential fits are presented in Fig. 4.3(d) and (e). The time constants, which are presented in Fig. 4.3(d), were found to be in the range of 200-500 fs for all three 3d ferromagnets, in agreement with some previous results from optical techniques [Kam05; Car08; Koo10]. Compared with previous electron diffraction results on nickel [Wan08], the time constants measured here are significantly smaller. For iron, the time constants measured here are similar compared with the electron diffraction results from Ref. [Rot19].

For nickel and cobalt, an increase of the time constant with increasing fluence was observed. In contrast, for iron, no clear fluence-dependence of the time constant was observed within the experimental accuracy. Generally, such an increase of the electron-lattice equilibration time with fluence is expected for most materials. It is caused by the increase of the electronic heat capacity with temperature (see for example Fig. 2.22(d)).

To analyze the fluence-dependence of the time constants for nickel and cobalt quantitatively, a linear fit was performed to the time constants as functions of final lattice temperature:

$$\tau(T_{\text{final}}) = a\,(T_{\text{final}} - 295\,\text{K}) + b \tag{4.1}$$

The results were $a = 0.84\pm0.17\,\frac{\text{fs}}{\text{K}}$, $b = 200\pm30\,\text{fs}$ for cobalt and $a = 0.34\pm0.06\,\frac{\text{fs}}{\text{K}}$, $b = 360\pm20\,\text{fs}$ for nickel and are shown in Fig. 4.3(d) as dashed lines.

In the case of iron and cobalt, all data presented in Fig 4.3(d) were recorded in the same measurement, which allows comparing not only the time constants but also the onsets of the lattice dynamics between different fluences. Figure 4.3(e) presents the fit results for the onset of the exponential function (time zero). Note that there is no absolute measure of the delay between the two pulses in the setup employed here. Therefore, time zero is shown relative to the highest fluence. For low fluences, time zero was found to be delayed compared with high fluences. It was verified that this behavior was not due to drifts during the data acquisition, by comparing delay scans acquired at different times during the measurement with the same fluence. Instead, the observation could be explained by carrier thermalization effects. A thermalized electron distribution (i.e. a Fermi-Dirac distribution) is expected to transfer energy to the lattice faster than a nonthermal one because electron thermalization increases the number of excited carriers that can scatter with phonons [WC20]. Electron thermalization is less efficient for lower excitation densities [MR13]. Therefore, when the lattice dynamics are phenomenologically described with a single exponential function, electron thermalization effects could cause such a delayed onset.

To study the influence of nonthermal electron distributions further, experiments with different excitation wavelengths were performed. The pump wavelength was varied significantly, from 2300 nm to 480 nm, to create significantly different initial electronic distributions. Due to the larger photon energy of 480 nm-light (2.58 eV compared to 0.54 eV for 2300 nm), electronic states with much higher energies are excited. Therefore, the initial electronic distribution following 480 nm-excitation is much further from the thermal case, in which excited carriers are predominantly found close to the chemical potential (within $\sim 2\,k_{\text{B}}T$). All measurements were analyzed using single exponential fits, as described above.

The resulting time constants are presented in Fig. 4.4. Within the experimental accuracy, no differences between the pump wavelengths were observed. This suggests that electron thermalization effects don't contribute significantly to the observed time constants of the lattice dynamics. This result, in combination with the delayed onset of the lattice dynamics for low fluences, suggests that predominantly thermalized electrons participate in electron-phonon
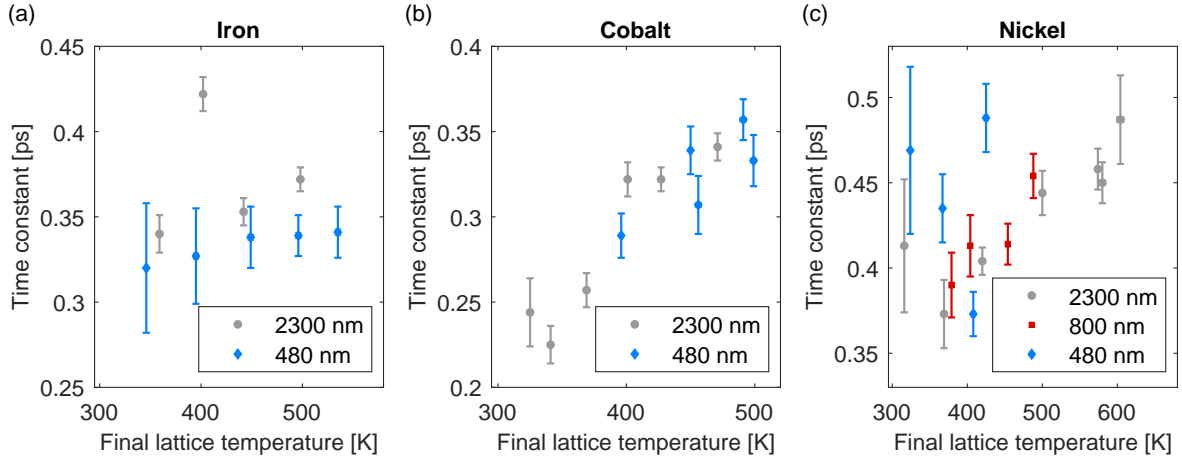
Figure 4.4: Comparison of experimental results for different pump wavelengths. (a) Time constants of the lattice temperature rise of iron for two different pump wavelengths, 2300 nm (gray dots) and 480 nm (blue diamonds) and different absorbed energy densities (corresponding to different final lattice temperatures after electron-phonon equilibration). The time constants were obtained from single exponential fits, as described in the text. The error bars are standard errors obtained from the fits. Due to different experimental conditions, the estimated time resolution of the two measurements was different, which was accounted for in the fits. For the measurements with 480 nm pump wavelength, 170 fs (FWHM) was employed, while for the measurements with 2300 nm pump wavelength, 250 fs (FWHM) was employed. (b) Same as (a), but for cobalt. (c) Same as (a), but for nickel. Here, additional measurements were performed for 800 nm pump wavelength. For all measurements shown in (c), the estimated time resolution was 170 fs FWHM. The values for the time resolution were estimated based on the onset of the lattice dynamics.

scattering. To investigate electron thermalization in greater detail, a probe that is sensitive to the electron system would be required, for example time-resolved photoemission. A recent photoemission study on iron reported electron thermalization within ~100 fs [Büh20].

4.2 Microscopic energy flow between electrons, spins, and phonons

Having analyzed the timescales of the lattice dynamics, the next step is to connect these observations to the microscopic couplings between electronic, magnetic, and lattice degrees of freedom. For this, a model of the ultrafast energy flow between those subsystems is required, which is the topic of this section. Throughout this work, the energy flow between different subsystems/degrees of freedom of a material is termed "microscopic energy flow". In all models presented here, the electron and phonon systems are assumed to be always in internal thermal equilibrium, characterized by an electron temperature T_e and a lattice temperature T_l, respectively. In addition, majority and minority electrons are always assumed to have the same temperature, based on experimental evidence of efficient coupling between them [Gor11].

4.2.1   Conventional two-temperature model

First, the experimental results are compared to the conventional two-temperature model (TTM), which was already introduced in Sec. 1.3. The TTM considers only lattice and electronic degrees of freedom. For a given absorbed energy density, the electron and lattice dynamics are determined by the electron-phonon coupling parameter G_{ep} and the heat capacities of electrons (c_e) and the lattice (c_l). Here, G_{ep}, c_e, and c_l were calculated based on spin-resolved DFT calculations, which was described in detail in Sec. 2.4. As already mentioned above, majority and minority electrons were described as one heat bath with a common temperature T_e, heat capacity $c_e = c_{e,majo} + c_{e,mino}$, and electron-phonon coupling parameter $G_{ep} = G_{ep,majo} + G_{ep,mino}$. This is a reasonable assumption based on photoemission measurements of majority and minority electron lifetimes, which suggest efficient scattering between electrons with opposite spin [Gor11]. The excitation density in the TTM was determined based on the lattice temperature in the range of $1.5 - 3\,\mathrm{ps}$ (for nickel) or $1.5 - 4\,\mathrm{ps}$ (for iron and cobalt), thus after electron-lattice equilibration (see also Fig. 4.3). The arrival time of the laser pulse (time zero) was determined from the single exponential fits described in the previous section. Consequently, there are no fit parameters in this TTM.

Figure 4.5 compares the TTM predictions to experimental results for the lattice dynamics. For all three materials, the TTM predictions for the lattice response are significantly faster compared to the experimental results for all fluences. Therefore, the TTM is insufficient to describe the lattice dynamics of iron, cobalt, and nickel quantitatively.
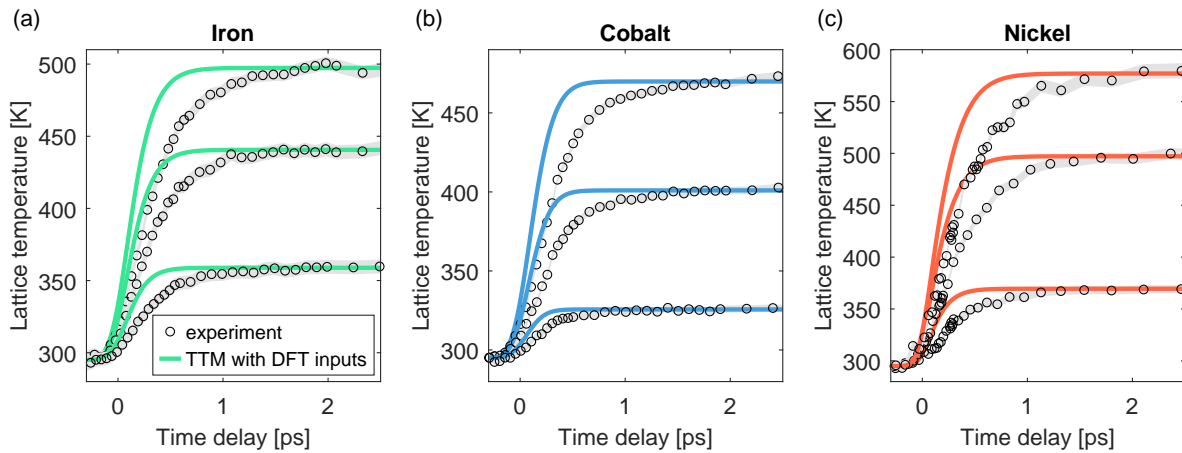
Figure 4.5: Comparison between the experimental results and the conventional TTM based on DFT calculations. For each material, three different fluences are presented. Black circles correspond to experimental data and solid curves show the TTM predictions. Gray shaded areas correspond to the standard errors of the experimental data.

A major disadvantage of applying the TTM to magnetic materials is that magnetic degrees of freedom are not accounted for. However, all three elemental $3d$ ferromagnets exhibit ultrafast demagnetization on timescales of hundreds of femtoseconds [Bea96; Car08; Koo10]. These timescales are similar compared with the timescales of electron-lattice equilibration (see Fig. 4.3). Since magnetic degrees of freedom provide a significant contribution to the heat capacity (see Fig. 4.1(a) for the example of nickel), magnetization dynamics are expected to play a role also in the microscopic energy flow on femtosecond timescales. Consequently, it is not surprising

that the TTM cannot describe the response of a ferromagnet to laser excitation. Instead, a model that considers energy flow into and out of magnetic degrees of freedom is required.

4.2.2 Three-temperature model

The simplest model that considers the spin system is the three-temperature model (3TM), which is a phenomenological extension of the TTM introduced by Beaurepaire et al. [Bea96]. In this model, the spin system is described based on its properties in thermal equilibrium, namely the spin heat capacity $c_s(T)$ and the magnetization $M(T)$. Analogously to G_{ep}, two additional coupling parameters G_{es} and G_{sp} are introduced to describe the electron-spin and the spin-phonon coupling, respectively. The evolution of the material after laser excitation is then given by the following three coupled differential equations [Bea96]:

$$c_e \frac{dT_e}{dt} = G_{ep}(T_l - T_e) + G_{es}(T_s - T_e) + P(t), \tag{4.2}$$

$$c_l \frac{dT_l}{dt} = G_{ep}(T_e - T_l) + G_{sp}(T_s - T_l), \tag{4.3}$$

$$c_s \frac{dT_s}{dt} = G_{es}(T_e - T_s) + G_{sp}(T_l - T_s). \tag{4.4}$$

T_s denotes the temperature of the spin system and c_s is the spin heat capacity. After solving the differential equations numerically, the magnetization dynamics are calculated as $M(T_s)$, using the equilibrium relationship between magnetization and temperature.

Here, G_{ep}, c_e, and c_l were taken from the DFT calculations and thus only G_{es} and G_{sl} were fit parameters. For the spin heat capacities, the experimental results presented in Fig. 4.7 were employed (dashed black curves). Time zero was not a fit parameter, but was instead determined from the single exponential fits described in Sec. 4.1, as for the TTM. The absorbed energy density was determined from the lattice dynamics in the range $1.5 - 3\,$ps (after electron-phonon equilibration).

Fig. 4.6 presents 3TM results for all three ferromagnets. The lattice dynamics are reasonably well described by the fit results, as shown in Fig. 4.6(a)-(c). A comparison to the TTM results shows that the inclusion of the spin system leads to significantly slower lattice dynamics. This is a combined effect of energy flow into the spin system and out of the spin system. Due to efficient electron-spin coupling in the elemental $3d$ ferromagnets, the spin system transiently absorbs more energy than after equilibration of all subsystems. During remagnetization, this energy is released. A significant portion of this energy goes to the lattice, which has a much larger heat capacity than the electrons (by a factor of ~37 for cobalt, ~32 for iron and ~23 for nickel at room temperature). For this reason, the lattice dynamics are strongly influenced by the magnetization dynamics. The comparison between TTM and 3TM shows that as anticipated based on its significant contribution to the heat capacity, it is essential to consider the spin system in any description of the microscopic energy flow on ultrafast timescales.

Nevertheless, when calculating the 3TM results for the magnetization responses, significant deviations from experimental results are observed. The 3TM fits result in very strong spin-electron coupling constants (on the order of $10^{20}\,\frac{W}{m^3K}$), which leads to spin temperatures that follow the electron temperature almost instantly. In addition, the 3TM fits predict a strongly fluence-dependent spin-lattice coupling, especially for iron. These parameters do not lead to
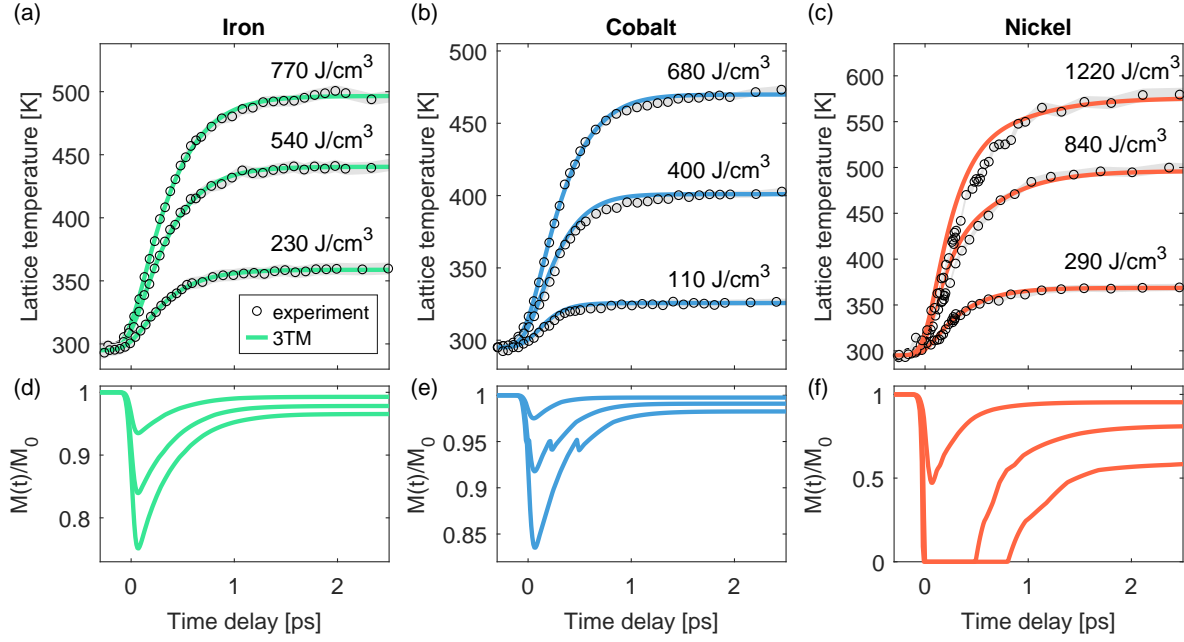
Figure 4.6: Results of 3TM fits to the lattice temperature dynamics. (a) 3TM fit results for the lattice temperature (solid curves) and experimental data (black circles) for iron at three different fluences. The gray shaded areas represent the standard errors of the experimental data. The absorbed energy densities in the 3TM were determined based on the lattice temperatures in the range from $1.5 - 3$ ps. (b) Same as (a), but for cobalt. (c) Same as (a), but for nickel. (d) Magnetization response calculated from the 3TM fit results shown in (a), using the temperature-dependent magnetization reported in Ref. [CG71]. The magnetization is normalized to its value before laser excitation (M_0). (e) Same as (d), but for cobalt, calculated from the 3TM fit results shown in (b). Here, the magnetization dynamics were calculated based on the experimental results from Ref. [MS51]. Note that the small jumps/drops in the magnetization dynamics close to time zero and after few hundred picoseconds stem from the data of Ref. [MS51], in which a slight increase of the magnetization upon the structural phase transition of cobalt at ~ 704 K was observed. Here, they are artifacts, since the lattice temperature did not rise beyond the transition temperature (see Panel (b)) and thus the phase transition did not occur. (f) Same as (d), but for nickel, calculated from the 3TM fit results presented in (c). Here, the temperature-dependent magnetization stems from Ref. [CG71].

realistic magnetization dynamics, as presented in Fig. 4.6(d)-(f). The discrepancies are most pronounced for nickel, which has the lowest Curie temperature and thus demagnetizes most for a given laser fluence. Also for iron and cobalt, both the demagnetization as well as the magnetization recovery are significantly faster compared with experimental results [Car08; Bor21].

These findings are analogous to the 3TM and M3TM results presented in Fig. 4.1, but from the lattice perspective: very good agreement to one subsystem is achieved. However, significant discrepancies to the responses of the other two subsystems remain. Therefore, no consistent description of the full laser-induced response of the material is achieved. While the agreement of the 3TM to all of the different subsystems could be improved by considering the responses of several subsystems in the fit, another significant shortcoming is inherent to the model: the spin system is described based on its properties in thermal equilibrium. This assumption is questionable on short timescales after laser excitation, and there is indeed theoretical and experimental

evidence for a nonthermal behavior of the spin system [Kaz07; Car08; Ten18]. Therefore, in the following, a model that can describe also nonthermal states of the spin system is employed.

4.2.3 Energy-conserving atomistic spin dynamics simulations

4.2.3.1 Model

In the next step, instead of relying on a thermal description of the spin system, its behavior is simulated directly using atomistic spin dynamics (ASD) simulations [Now07; Eva14]. In this model, the spin system is described with a classical Heisenberg Hamiltonian:

$$\mathcal{H} = -\sum_{i<j} J_{ij} \mathbf{S}_i \cdot \mathbf{S}_j - \sum_i d_z S_z^2. \tag{4.5}$$

Here, $\mathbf{S}_i$ are unit vectors, each of them representing a local magnetic moment at site i. J_{ij} is the Heisenberg exchange constant, which couples neighboring spins. The second term describes on-site anisotropy, here with the easy axis in the z-direction and constant anisotropy energy.

The time evolution of the individual spins $\mathbf{S}_i$ is described with the stochastic Landau-Lifshitz-Gilbert (LLG) equation:

$$\frac{(1+\alpha^2)\mu_s}{\gamma} \frac{\partial \mathbf{S}_i}{\partial t} = -(\mathbf{S}_i \times \mathbf{H}_i) - \alpha (\mathbf{S}_i \times (\mathbf{S}_i \times \mathbf{H}_i)). \tag{4.6}$$

Here, $\gamma = 1.76 \cdot 10^{11} \frac{1}{\text{Ts}}$ is the gyromagnetic ratio, and μ_s is the atomic magnetic moment (both spin and orbital contributions). α is the damping and $\mathbf{H}_i$ is the effective field that acts on the spin $\mathbf{S}_i$. The first term of Eq. 4.6 describes precession around $\mathbf{H}_i$ while the second term describes relaxation of the spins towards the direction of $\mathbf{H}_i$. In the *stochastic* LLG equation, $\mathbf{H}_i$ has an additional field-like noise term $\boldsymbol{\zeta}_i$:

$$\mathbf{H}_i = -\frac{\partial \mathcal{H}}{\partial \mathbf{S}_i} + \boldsymbol{\zeta}_i(t). \tag{4.7}$$

This noise term has white-noise properties [Atx09]:

$$\langle \boldsymbol{\zeta}_i(t) \rangle = 0 \quad \text{and} \quad \langle \boldsymbol{\zeta}_i(0)\boldsymbol{\zeta}_j(t) \rangle = 2\alpha k_B T_e \mu_s \delta_{ij}\delta(t)/\gamma. \tag{4.8}$$

The amplitude of the noise depends on the electronic temperature T_e, thus introducing temperature effects to the LLG equation. The coupling strength between electrons and spins is governed by the damping α, which determines how efficiently the spins react to the stochastic field. Direct spin-phonon coupling is not considered. To simulate the laser-induced spin dynamics as well as the equilibrium behavior with temperature, the stochastic LLG equation is solved numerically for system sizes of several million spins. Using such large systems minimizes boundary effects and allows to extract macroscopic parameters from the simulations. A simple cubic lattice structure was used in all simulations. Different lattice structures were tested and were found to have no significant influence on the results.

In order to quantitatively reproduce the equilibrium behavior of the spin system with temperature, the rescaled temperature model is employed [EAC15], which modifies the electron temperature as follows:

$$T_{\text{sim}} = T_c \left(\frac{T_e}{T_c}\right)^\beta. \tag{4.9}$$
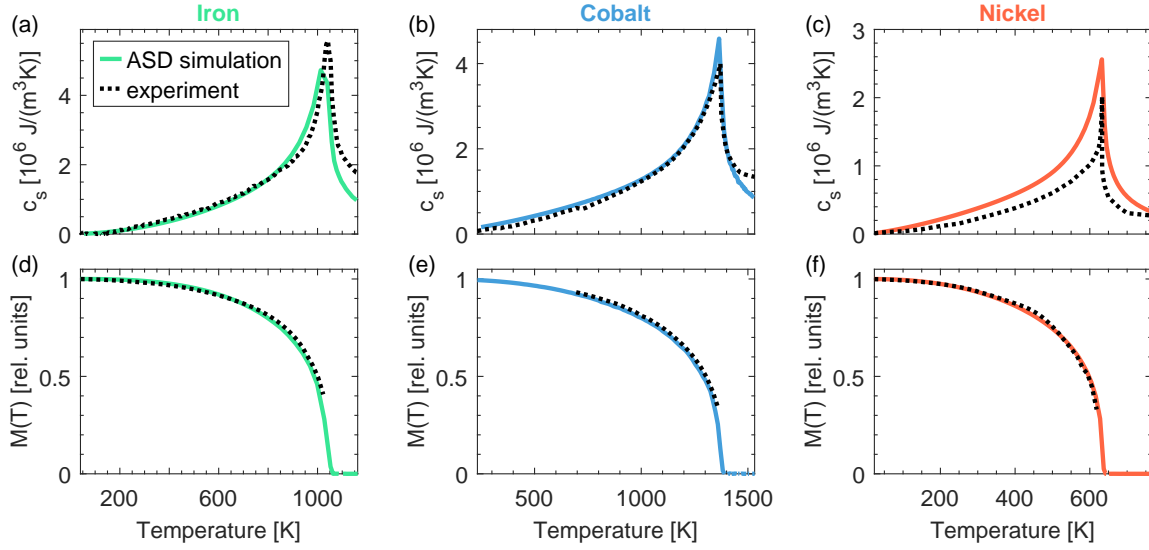
Figure 4.7: Equilibrium properties of the spin system, comparison between ASD simulations and experiment. (a) Spin heat capacity of iron. The solid curve is the ASD simulation result. The dashed black curve is based on experimental results for the total heat capacity of iron [Thu98]. The spin contribution was calculated following Ref. [Mes81]. First, a dilation correction was applied to obtain the heat capacity at constant volume, using the expansion coefficient from Ref. [Lid03]. Then, the DFT results for the contributions of electronic and lattice degrees of freedom were subtracted to obtain the spin heat capacity. (b) Same as (a), but for cobalt. Here, the experimental result was calculated as for iron, also based on Refs. [Thu98; Lid03]. (c) Same as (a), but for nickel. Here, the spin heat capacity was calculated based on the result for the combined heat capacity of electrons and spins (c_es) from Ref. [Mes81]. To obtain the spin heat capacity, the electron heat capacity from DFT was subtracted from c_es. (d) Temperature-dependent magnetization of iron, comparison between ASD simulation result (solid curve) and experiment (dashed black curve). The magnetization relative to its value at $0\,\mathrm{K}$ is presented. (e) Same as (d), but for cobalt. (f) Same as (d), but for nickel. For all three materials, the experimental results for the temperature-dependent magnetization were taken from Ref. [CG71].

Here, β is a material-dependent parameter and T_c is the Curie temperature of the material. With this correction, a good description of the temperature-dependent equilibrium magnetization and spin heat capacity can be achieved, as shown in Fig. 4.7 for all three materials. For nickel, the spin heat capacity is overestimated by the simulations, which is likely due to the small magnetic moment of nickel in combination with the classical nature of the ASD simulations. Table 4.1 summarizes all parameters used in the ASD simulations. They are partially based on Ref. [Eva14].

Conventionally, spin simulations do not consider energy flow into and out of the spin system [EAC15] and are therefore not energy-conserving. Instead, typically a TTM is solved and the resulting electron temperature dynamics are used to simulate the spin dynamics. However, here the goal was to describe also the microscopic energy flow, not only the spin dynamics. In this case, the ASD simulations need to be energy-conserving, which was implemented here following the approach of Ref. [Wie15]. The energy content of the spin system, $\mathcal{H}\{\mathbf{S}_i(t)\}$, was monitored at each time step of the simulation. The change of spin energy in the time step Δt

Table 4.1: ASD simulation parameters for iron, cobalt, and nickel.

	Fe		Unit	Co		Unit	Ni		Unit
J	4.8	$\times 10^{-21}$	J	6.324	$\times 10^{-21}$	J	2.986	$\times 10^{-21}$	J
d_z	0.5	$\times 10^{-23}$	J	0.67	$\times 10^{-23}$	J	0.5	$\times 10^{-23}$	J
μ_s	2.2		μ_B	1.72		μ_B	0.616		μ_B
α	0.005			0.01			0.01		
β	0.339			0.340			2.322		

was then calculated as follows:

$$\Delta E_s = \frac{s^2}{s(s+1)}(\mathcal{H}\{\mathbf{S}_i(t+\Delta t)\} - \mathcal{H}\{\mathbf{S}_i(t)\}). \tag{4.10}$$

Here, s is the spin quantum number. The factor $s^2/[s(s+1)]$ accounts for the fact that the spins are quantized in reality ($s \approx \frac{1}{2}$ for nickel, $s \approx \frac{3}{2}$ for cobalt, and $s \approx 2$ for iron), but described with a classical Heisenberg Hamiltonian. In such a classical description, the spins are not quantized, which corresponds to the limit $s \to \infty$. In general, the relationship between the Heisenberg exchange constant J and the Curie temperature T_c depends on s. For a simple cubic system with only nearest-neighbor interaction as employed here, J relates to T_c as follows [Whi07]:

$$J = \frac{s^2}{s(s+1)} \frac{1}{2} k_B T_c. \tag{4.11}$$

The value of J directly relates to the spin energy content E_s (see Eq. 4.5). Consequently, to obtain a good description of E_s and the correct Curie temperature within the classical model, the factor $s^2/[s(s+1)]$ needs to be considered in Eq. 4.10.

Finally, to make the ASD simulations energy-conserving, the TTM equation for the electron temperature (Eq. 1.2) was modified to take into account the spin energy change ΔE_s:

$$c_e \frac{\Delta T_e}{\Delta t} = G_{ep}(T_l - T_e) + P(t) - \frac{\Delta E_s}{\Delta t}. \tag{4.12}$$

With this modification, ASD simulations are able to describe the microscopic energy flow, in addition to the non-equilibrium spin dynamics.

4.2.3.2 Results and comparison with the experiment

Figure 4.8 presents ASD simulation results for iron and a comparison to the experimentally measured lattice dynamics (Panels (a)-(d)). For low and moderate absorbed energy densities, the ASD simulations yield an excellent description of the experimental results for the lattice dynamics. Similar to the 3TM, energy flow into and out of the spin system has a profound impact on the lattice dynamics, as the comparison to the TTM results (dashed curves in Fig. 4.8) reveals. For very high absorbed energy densities, there are discrepancies between experiments and simulations. This can be due to several reasons and will be discussed below. In addition to the lattice dynamics, the ASD simulations also yield a realistic description of the magnetization dynamics, shown in Fig. 4.8(e). The electron temperature dynamics predicted by the ASD simulations are presented in Fig. 4.8(f).

Figure 4.8: ASD simulation results for iron and comparison to the experimentally measured lattice responses. (a)-(d) Simulation results and experimentally measured lattice dynamics for several absorbed energy densities. The solid curves are ASD simulation results and the black circles are experimental data. The gray shaded areas represent the standard errors of the experimental data. For comparison, also results of the conventional TTM are presented (dashed curves). The displayed absorbed energy densities are from the ASD simulations and were determined based on the measured final lattice temperature. (e) ASD simulation results for the magnetization dynamics for the same absorbed energy densities as in Panels (a)-(d). The magnetization is normalized to its value before laser excitation (M_0). (f) ASD simulation results for the electron temperature dynamics, again for the same absorbed energy densities as in Panels (a)-(d). Adapted from Ref. [Zah21b].

Fig. 4.9 presents analogous results for cobalt. Excellent agreement between ASD simulation results and measured lattice dynamics is achieved for all absorbed energy densities. Also here, the differences between the TTM results and the ASD simulation results are large, corroborating the important role of energy flow to and from magnetic degrees of freedom in the lattice dynamics. The corresponding magnetization dynamics and electron temperature dynamics obtained from the simulations are presented in Fig. 4.9(e) and (f), respectively.

Figure 4.10 presents analogous results for nickel. As in the case of iron, for low and moderate absorbed energy densities, excellent agreement between ASD simulation results and experimentally measured lattice dynamics is achieved. For very high absorbed energy densities, discrepancies are observed, which will be discussed below. The simulation results for the magnetization dynamics are presented in Fig. 4.10(e). In the case of nickel, the differences between the results of the 3TM fits (see previous section) and the ASD simulations are most apparent, due to its rather low Curie temperature and magnetic moment. The ASD simulations yield a much more realistic description of the magnetization dynamics for all absorbed energy densities. The electron temperature dynamics from the simulations are presented in Fig. 4.10(f).

In summary, for all three elemental 3*d* ferromagnets, a clear trend is observed: the TTM, which doesn't consider magnetic degrees of freedom, is unable to describe the experimentally
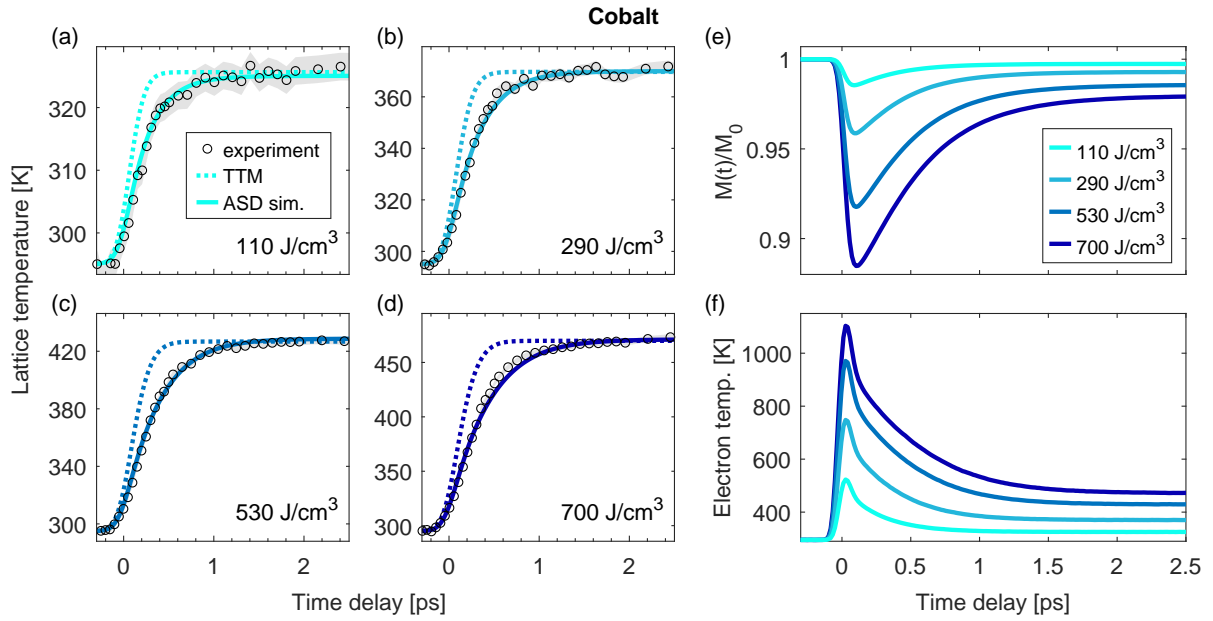
Figure 4.9: ASD simulation results for cobalt and comparison to experimental results. (a)-(d) Simulation results for the lattice dynamics (solid curves) and experimentally measured lattice temperatures (black circles) for a wide range of absorbed energy densities. Gray shaded areas correspond to the standard errors of the experimental data. Dashed curves correspond to TTM results. The displayed absorbed energy densities are from the ASD simulations. (e) Simulation results for the magnetization dynamics for the same absorbed energy densities as in (a)-(d). (f) Simulation results for the electron temperature dynamics, again for the same absorbed energy densities. Adapted from Ref. [Zah21b].

observed lattice dynamics. In contrast, when those degrees of freedom are considered using energy-conserving ASD simulations, excellent agreement is achieved for low and moderate absorbed energy densities. This demonstrates unambiguously that energy flow into and out of the spin system has a profound impact on the lattice dynamics, and has to be considered in any description of the microscopic energy flow.

So far, the comparison between experiments and models has focused on lattice dynamics. To go beyond the description of one subsystem and obtain a consistent model for the laser-induced dynamics of electrons, spins, and phonons, it is necessary to compare the simulations with experimental data for the other two subsystems as well. Figure 4.11 presents such a comparison with available experimental data for the electron and magnetization dynamics. The magnetization dynamics of iron from the simulations are presented in Fig. 4.11(a) alongside experimental results [Car08; Bor21]. For the magnetization dynamics, a variety of measurements exists in literature [Kam02; Car08; Car15; Raz17; Büh18; Zha20; Bor21]. However, the results differ significantly, even when only measurements on insulating substrates are considered. The two examples in Fig. 4.11(a) were both recorded on relatively thin films on an insulating substrate. Despite resulting in a similar final reduction of the magnetization, the measurements differ significantly, in particular regarding the amplitude of the initial magnetization reduction and the magnetization recovery. While there are significant discrepancies of the ASD simulations compared with the results from Borchert et al. [Bor21], good agreement is observed with the results from Carpene et al. [Car08].

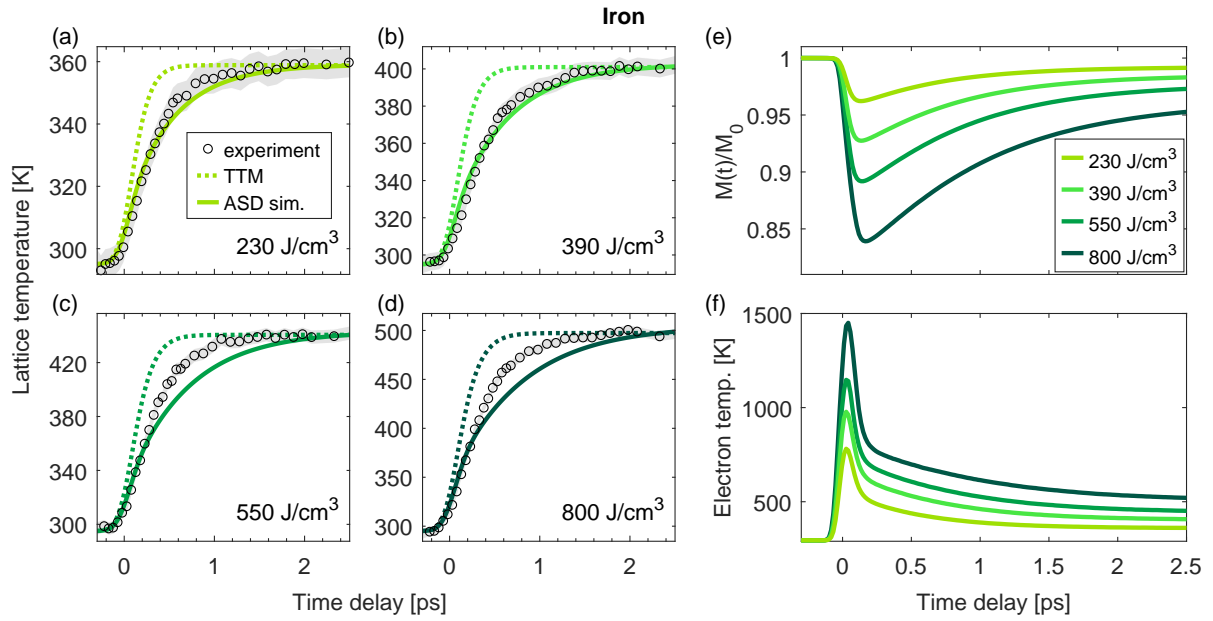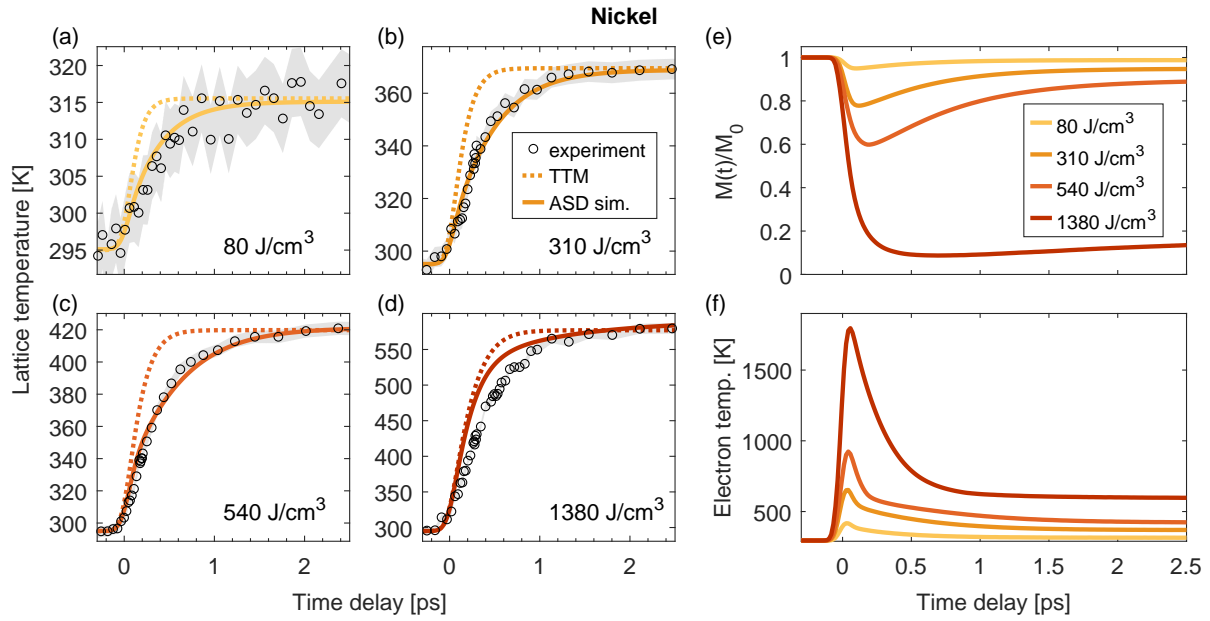Figure 4.10: ASD simulation results for nickel and comparison to the experimentally measured lattice responses. (a)-(d) Simulation results for the lattice temperature dynamics (solid curves) alongside experimental results (black circles) for a wide range of absorbed energy densities. The standard errors of the experimental data are shown as solid gray areas. Dashed curves show TTM results for comparison. The displayed absorbed energy densities are from the ASD simulations. (e) Simulation results for the magnetization dynamics for the same absorbed energy densities as in (a)-(d). (f) Simulation results for the electron temperature dynamics, again for the same absorbed energy densities. Panels (a)-(e) are adapted from Ref. [Zah21a].

Due to the pronounced disagreement of different literature results for iron, a measurement of the magnetization dynamics on the same iron film as employed in the electron diffraction experiments was performed. For this measurement, the film was not freestanding, but on a glass substrate, which ensured that the film was flat. A magnetic field was applied in the sample plane. The sample was excited with 800 nm-light at normal incidence. The incident fluence was $0.1\,\mathrm{mJ/cm^2}$, corresponding to an absorbed energy density of $\sim 30\,\mathrm{J/cm^3}$. The magnetization response was probed in transmission with another 800 nm-pulse, which was directed to the sample at an angle of 135° relative to the pump pulse. The change in Kerr ellipticity was recorded as a function of pump-probe delay. The result is presented in Fig. 4.11(b) (pink dots). The static Kerr ellipticity was not recorded and it was therefore not possible to determine the amplitude of the magnetization reduction. The magnetization is thus given in arbitrary units (right axis). For comparison, the ASD simulation result with the same absorbed energy density is also shown (solid curve and left axis). Good agreement between experiment and simulation is observed, in particular regarding the initial drop and recovery of the magnetization. The result suggests that at least for such low fluences, the ASD simulations yield a good description of the magnetization dynamics in the sample.

Next, the simulated electron temperature dynamics of iron are compared with experimental results. Only measurements with rather high absorbed energy densities exist in literature [Büh20; Gor20]. For such high absorbed energy densities, discrepancies are observed be-
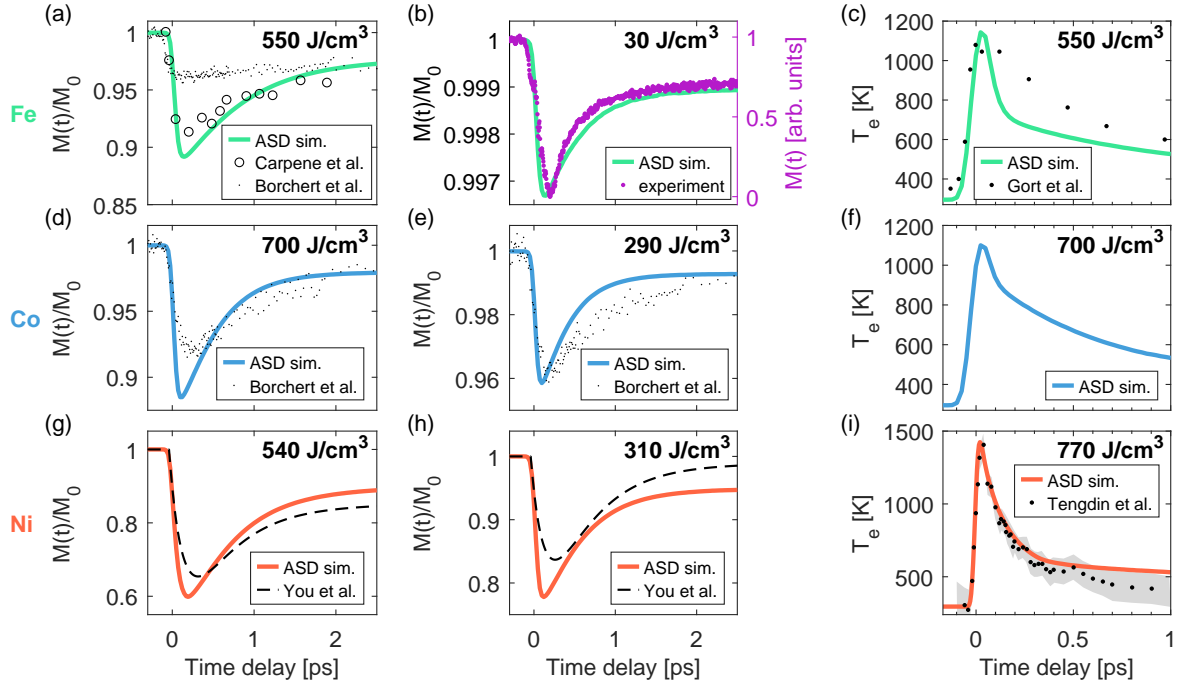
Figure 4.11: Comparison of ASD simulations with experimental data for spin and electron dynamics. (a) Simulated magnetization dynamics of iron (solid curve) and two different experimental results. Data with similar magnetization reduction at long delays are compared. The hollow circles represent results from Carpene et al. [Car08], recorded on a 7 nm-thick film of iron on magnesium oxide (MgO) with an incident fluence of $3\,\mathrm{mJ/cm^2}$. The small black dots correspond to data from Borchert et al. [Bor21] (absorbed fluence $1.5\,\mathrm{mJ/cm^2}$), recorded on a 15 nm-thick film of iron sputtered on a glass wafer and capped with 2 nm of tantalum. (b) Simulation results for a very low absorbed energy density of $30\,\mathrm{J/cm^3}$ alongside experimental results for the same absorbed energy density. The experimental data were measured on the same iron film as in the electron diffraction experiments, with the only difference being that the film was on a glass substrate here. Note the different y-axes for experiment and simulation – a quantitative determination of the normalized magnetization $M(t)/M_0$ was not possible in this experiment. (c) Simulation result for the electron temperature dynamics of iron alongside experimental results from Ref. [Gor20]. (d) Simulation result for the magnetization dynamics of cobalt and experimental results from Borchert et al. [Bor21] with an absorbed fluence of $1.83\,\mathrm{mJ/cm^2}$ (sample geometry as in (a)). Also here, data with similar magnetization reduction at long delays are compared. (e) Same as (c), but for a lower absorbed energy density (absorbed fluence of $0.89\,\mathrm{mJ/cm^2}$ in the experiment). (f) Simulation result for the electron temperature dynamics of cobalt. (g) Simulation result for the magnetization dynamics of nickel. The dashed black curve shows experimental results from You et al. [You18], which stem from a layer decomposition of data recorded on a 400 nm-thick nickel film. In contrast to (a),(b),(d), and (e), here the absorbed energy densities of experiment and simulation are matched. (h) Same as (e), but for a lower absorbed energy density. (f) Simulation result for the electron temperature dynamics and comparison to experimental results from Tengdin et al. [Ten18] (black dots). The gray shaded area indicates the errors of the experimental data. To match the experimental conditions, the pump pulse in the simulation was shorter here (30 fs FWHM). The absorbed energy density in the simulation was adjusted to match the electron temperature directly after excitation. All absorbed energy densities shown in this figure are from the ASD simulations.

tween ASD simulations and experiments, as shown in Fig. 4.11(c). This finding is consistent with the discrepancies observed for the lattice dynamics (see Fig. 4.8(d)), and suggests that for high absorbed energy densities, the ASD simulations cannot describe the microscopic energy flow in iron accurately. This can be due to several reasons, which will be discussed after inspecting the results for the other two materials.

For cobalt, the simulated magnetization dynamics are compared with experimental data in Fig. 4.11(d)-(e). The experimental results stem from Borchert et al. [Bor21] (black dots). ASD simulation results are shown as solid curves. Qualitatively, the experimental results are well described by the simulation. The initial drop of the magnetization is slightly faster in the simulations compared with the experiments. The magnetization recovery is also faster in the simulations. The amplitude of the initial magnetization drop relative to the magnetization at long time delays is well described. Note that also for cobalt, there is some spread in the experimental results for the magnetization dynamics [Koo10; Bor21; Uni21], albeit less pronounced compared to iron.

Regarding the electron temperature dynamics of cobalt, to the best of my knowledge, no experimental data are available in literature. For the sake of comparison to the other two materials, the simulated electron temperature dynamics for a similar absorbed energy density of $700\,\mathrm{J/cm^3}$ are presented in Fig. 4.11(f).

For nickel, the magnetization dynamics from the simulations are compared to experimental data from Ref. [You18]. The authors decomposed the data into the magnetization response of different layers and parameterized the relationship between absorbed energy density and magnetization dynamics. This allows a quantitative comparison to the ASD simulations for the same absorbed energy density. The comparison is presented in Fig. 4.11(g) and (h) for two different absorbed energy densities. Generally, the amplitude of the magnetization reduction is well described. The magnetization reduction in the simulations is faster compared to the experiment. The magnetization recovery is similar in the simulations compared to the experiment. The deviations of the final magnetization after equilibration of the system could be caused by the decomposition procedure of Ref. [You18]. The procedure did not consider transport effects, which play a role particularly on longer timescales.

A comparison between the electron temperature dynamics from the simulations and experimental data from Ref. [Ten18] is presented in Fig. 4.11(i). Here, the absorbed energy density of the ASD simulations was adjusted to match the maximum electron temperature reached in the experiment. The ASD simulations yield an excellent description of the experimental data. On longer timescales, the experimentally measured electron temperature continues to decrease further, which is not adequately described by the simulations. This is likely caused by transport effects, which are not included in the simulations. The experimental technique is sensitive to the surface and the sample was a relatively thick film with $400\,\mathrm{nm}$ thickness.

Comparing simulation results and experiments for all three ferromagnets, two common trends can be identified. First, the initial demagnetization is faster in the simulations compared to the experiments. This can be related to the idealized case assumed in the simulations: the excitation is assumed to be homogeneous, and in addition defects or domain walls are not considered. Furthermore, the description of the electron-spin interaction is phenomenological, which can lead to deviations particularly on short timescales after laser excitation. Also on the experimental side, extracting the magnetization dynamics directly after laser excitation can be challenging. In particular, the MOKE signal, which is widely used to measure magnetization

dynamics, can be influenced by state filling effects [Raz17]. Regarding photoemission, experiments have shown that shortly after laser excitation, the loss of spin polarization is not uniform across all electron energies [Gor18; Gor20]. For these reasons, results obtained with different experimental techniques or – in the case of photoemission – results based on different regions of the band structure can differ on short timescales after laser excitation. This has been directly demonstrated for the example of iron [Gor20].

The second common trend in all three $3d$ ferromagnets is that the agreement between simulations and experimentally measured lattice dynamics decreases as the absorbed energy density increases, particularly for iron and nickel. There can be several reasons for this behavior. First of all, the DFT calculations are ground-state calculations, which are therefore generally expected to be most accurate for small perturbations from equilibrium, i.e. for low absorbed energy densities. For higher absorbed energy densities, significant changes of the band structure can occur, in particular a reduction of the exchange splitting [Ten18]. This would change the electronic heat capacity and the electron-phonon coupling, thus influencing the electron-lattice equilibration. In addition, nonthermal phonon populations, which cannot be described by the model, could contribute to the observed lattice dynamics. Accounting for such effects could lower the optimal value for the damping parameter α (i.e. weaker electron-spin coupling). Finally, also the description of electron-spin coupling in general with the stochastic LLG equation could contribute to the observed discrepancies. First, the damping parameter α is constant for all absorbed energy densities and throughout the simulations. However, α could in reality depend on parameters that change after laser excitation, such as the electron temperature. Second, angular momentum dissipation is not considered in the description of electron-spin coupling. Particularly for high absorbed energy densities, a significant amount of angular momentum needs to be dissipated, which could constitute a bottleneck for magnetization reduction. Due to the associated energy flow into and out of the spin system, this would be directly reflected in the evolution of electron and lattice temperatures.

For low and moderate absorbed energy densities, the ASD simulations yield excellent agreement with experiments for all three elemental $3d$ ferromagnets. This is in remarkable contrast to the conventional TTM, which fails to describe lattice dynamics at all absorbed energy densities in all materials. These results highlight the prominent role of the spin system in the ultrafast energy flow dynamics: energy flow into and out of the spin system has a large effect on lattice dynamics as well as on electron dynamics. Note that it is the combined effect of both energy flow into *and* out of the spin system which causes the lattice dynamics to slow down. These results show that in general, an accurate description of the full laser-induced dynamics in ferromagnets can only be obtained when the transient energy content of the spin system is considered.

4.2.3.3 Microscopic energy flow

Based on the ASD simulation results, it is now possible to analyze the energy flow between electronic, magnetic, and lattice degrees of freedom in detail. Figure 4.12(a)-(c) presents the distribution of the additional energy after laser excitation between the three different subsystems as a function of pump-probe delay for all three materials. Following laser excitation, the additional energy in the system stays constant (black curves in Fig. 4.12(a)-(c)) and is merely redistributed between electron, spin, and lattice subsystems. The laser pulse only excites the
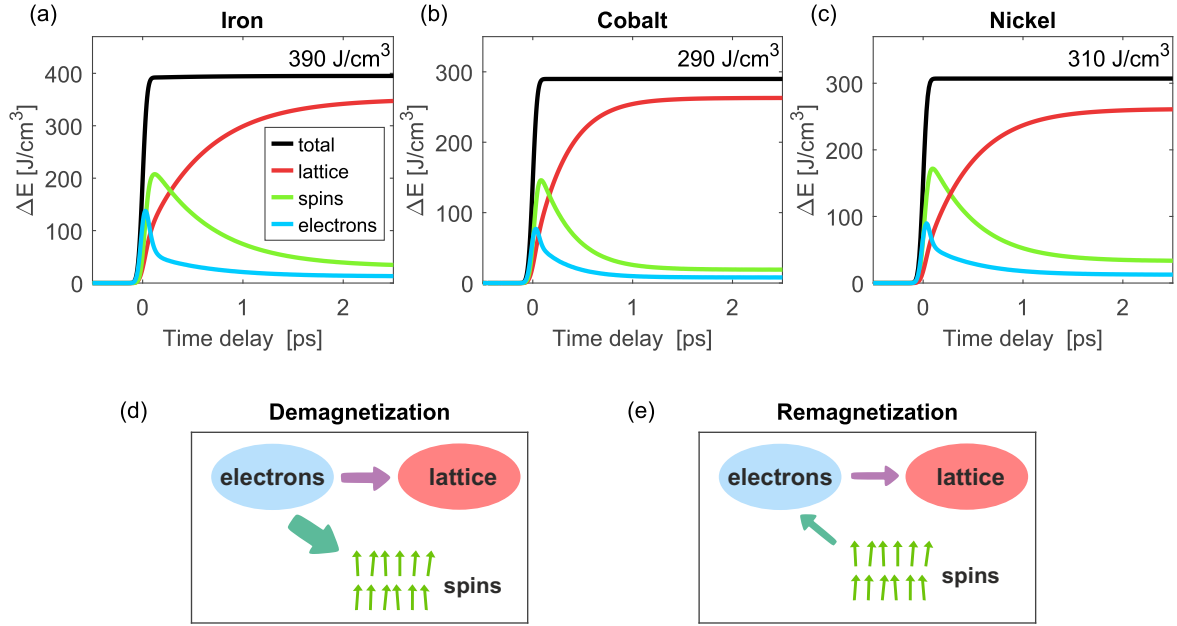
Figure 4.12: Microscopic energy flow between electrons, spins, and the lattice according to the ASD simulations. (a) Distribution of the additional energy deposited by the pump pulse between electronic (blue), magnetic (green), and lattice degrees of freedom (red) for iron. The total additional energy is shown in black. (b) Same as (a), but for cobalt. (c) Same as (a), but for nickel. (d) Schematic illustration of the three different subsystems and the microscopic energy flow between them during the demagnetization. (e) Same as (d), but for the period in which the magnetization recovers (remagnetization). Adapted from Refs. [Zah21a; Zah21b].

electrons (blue curves), which induces non-equilibrium between the three subsystems and thus initiates energy flow between them. Already shortly after excitation, the spin system (green curves) contains more of the additional energy than the electron system. This directly visualizes the important role of the spin system in the ultrafast energy flow dynamics, showing that the spin system is the dominant heat sink on short timescales after laser excitation. At the same time, also the lattice gains additional energy due to electron-phonon coupling, but at a much lower rate compared to the spin system. A schematic illustration of the energy flow processes during this period is presented in Fig. 4.12(d). Energy flows from the electrons to the spins as well as to the lattice, but with different rates. The additional energy in the spin system causes a reduction of the magnetization.

Eventually, due to the continuous drain of energy from the electrons to the lattice, the spin energy reaches a maximum and energy starts flowing back out of the spin system. Interestingly, the maximum of the spin energy does not coincide exactly with the magnetization minimum, particularly when the magnetization is strongly reduced. The minimum magnetization is reached slightly later than the maximum spin energy. For example, in nickel the delay is ~50 fs for an absorbed energy density of 1380 J/cm^3. This discrepancy indicates a nonthermal behavior of the spin system, which will be discussed in detail below.

A schematic illustration of the energy flow processes during remagnetization is presented in Fig. 4.12(e). Energy flows back from the spin system to the electrons. In addition, energy is drained from the electrons to the lattice, such that in total, the electrons lose further energy,

albeit at a much lower rate than during the demagnetization. Consequently, there is a net energy flow from the spin system to the lattice. Note that this energy flow is entirely indirect via the electrons since direct spin-lattice coupling is not included in the simulations. Finally, thermal equilibrium is established, with the energy being distributed according to the heat capacities of the different subsystems.

4.2.3.4   Nonthermal spin system

The main motivation for employing ASD simulations was that the spins are simulated directly, which allows to describe also nonthermal states of the spin system. Now, with ASD simulation results for both quasi-static heating and laser-induced dynamics, it is possible to analyze the nonthermal behavior of the spin system in detail. The quantities of particular interest are the spin energy and the magnetization: the spin energy determines the energy drain from the electrons and thus has a strong influence on the other two subsystems, while the magnetization is the quantity that is typically measured. In thermal equilibrium, the two quantities have a defined relationship $E_s(M)$, which can be calculated for example from the temperature-dependent spin heat capacity and magnetization. Here, the relationships $E_s(M)$ for all three materials were directly extracted from ASD simulations of quasi-static heating (see also Fig. 4.7). The results are presented in Fig. 4.13(a)-(c).

In non-equilibrium situations, such as after laser excitation, the equilibrium relationship $E_s(M)$ does not necessarily hold. Since ASD simulations of laser-induced dynamics yield both E_s and M as functions of pump-probe delay, it is possible to analyze for which time delays the equilibrium relationship is not fulfilled, which indicates a nonthermal spin system. To do so, the magnetization from the non-equilibrium simulations, $M(t)$, is converted into spin energy using the equilibrium relationship:

$$E_{s,\,thermal}(t) = E_s(M(t)) \tag{4.13}$$

This quantity is then compared to the actual spin energy in the simulations, $E_s(t)$. The comparison is presented in Fig. 4.13(d)-(f) for all three materials and the same absorbed energy densities as in Figs. 4.8, 4.9, and 4.10, respectively. The corresponding magnetization dynamics are presented in Fig. 4.13(g)-(i). On short timescales after laser excitation, the two curves $E_s(t)$ and $E_{s,\,thermal}(t)$ differ significantly, which indicates that the spin system is not in a thermal state. Since $E_{s,\,thermal}(t)$ is below $E_s(t)$, this nonthermal state is characterized by a relatively large amount of spin energy compared with its magnetization.

Generally, the relationship between spin energy and magnetization depends on which spin-waves/magnons are excited in the system. This is illustrated in Fig. 4.14 for the most simple case of a linear Heisenberg chain. A spin-wave with a very small wavevector leaves neighboring spins close to parallel, while spin-waves with larger wavevectors lead to more canting of neighboring spins. Based on the Heisenberg Hamiltonian (first term of Eq. 4.5), canting neighboring spins costs energy. The smaller the periodicity of the spin-wave (i.e. the larger the wavevector), the more energy it costs. The energetically least favorable spin-wave has a periodicity of two unit cells, canting all neighboring spins away from each other. This energy cost is directly reflected in the spin-wave dispersion, which is presented in Fig. 4.14(c). The energy cost of exiting one magnon is $\hbar\omega$ and each excited magnon leads to the same magnetization reduction because every magnon has spin 1 (see for example Ref. [Kit05]). The energy cost of exciting a magnon
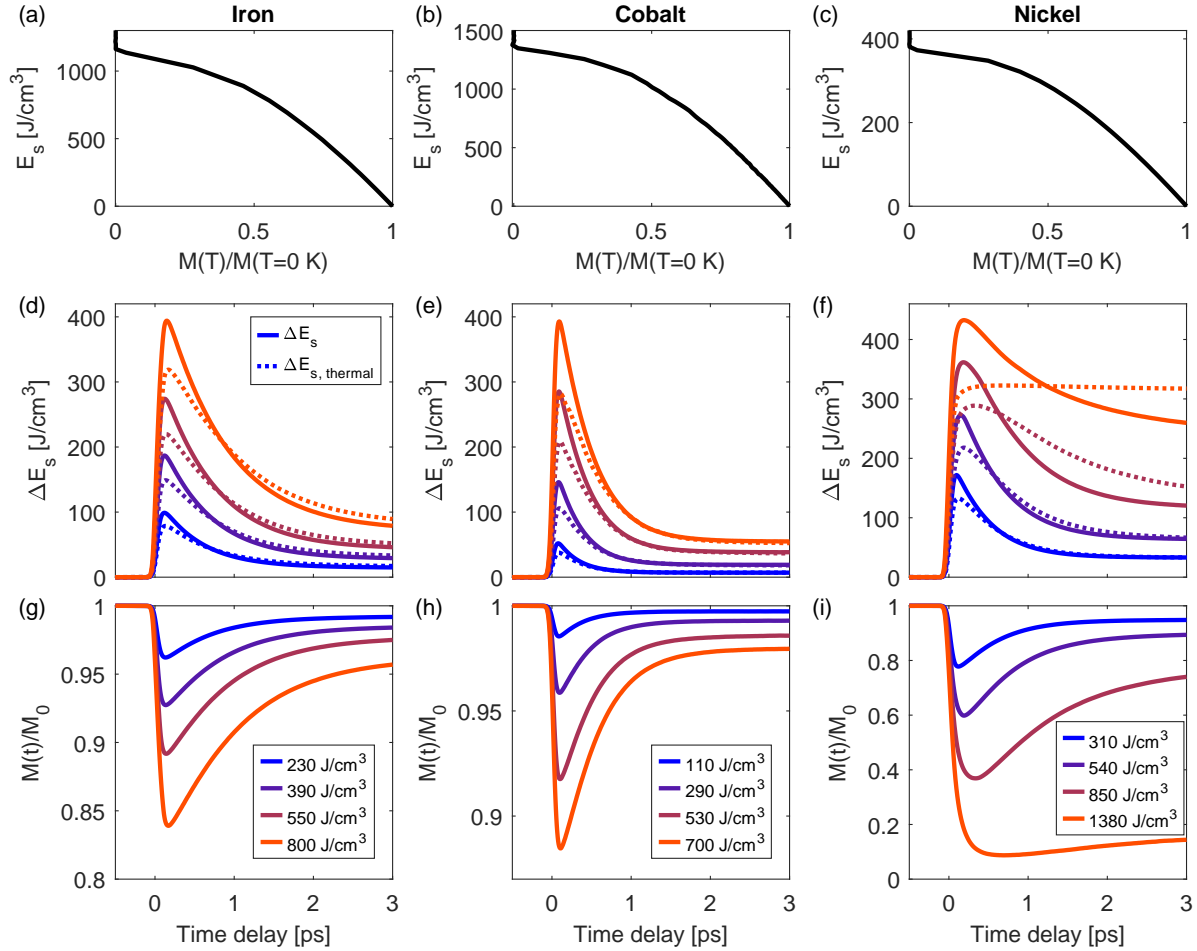
Figure 4.13: Identification of nonthermal states of the spin system in the ASD simulations by comparing magnetization with spin energy. (a) Equilibrium relationship between spin energy and magnetization for iron, obtained from an ASD simulation of quasi-static heating. The magnetization is given relative to its value at 0 K. (b) Same as (a), but for cobalt. (c) Same as (a), but for nickel. (d) Additional energy in the spin system as a function of pump-probe delay (solid curves) and the (hypothetical) energy content of a thermalized spin system (dashed curves) for iron. The absorbed energy densities correspond to the ones shown in Fig. 4.8. The dashed curves were calculated using the magnetization dynamics from the ASD simulations (see Panel (g)), assuming the equilibrium relationship shown in Panel (a). (e) Same as (d), but for cobalt. Note that the very small differences in (d) and (e) that persist on timescales larger than ~2.5 ps are numerical artifacts. They could originate from the finite time steps in the non-equilibrium simulations or the larger α employed in the simulations of quasi-static heating. (f) Same as (d), but for nickel. (g) Magnetization dynamics from the ASD simulations for iron. (h) Same as (g), but for cobalt. (i) Same as (g), but for nickel. Panels (d)-(i) are adapted from Refs. [Zah21a; Zah21b].

increases up to $q = \frac{\pi}{a}$, which corresponds to a real-space period of two unit cells, and decreases again. Consequently, the energy cost of a certain amount of magnetization reduction depends on the excited spin-waves/magnons. It is highest for intermediate wavevectors close to half of the Brillouin zone, which cant neighboring spins away from each other.

In the three-dimensional case of the (classical) ASD simulations, the fact that $E_{s,thermal}$ is below E_s for the first tens to hundreds of femtoseconds thus indicates that predominantly high-energy spin-waves with significant canting of neighboring spins are present on short timescales after laser excitation. This behavior is expected due to the local nature of the electron-spin interaction in the ASD simulations (the stochastic noise in the s-LLG equation has no correlation between different atomic sites, see Eq. 4.8).

Such a nonthermal distribution of spin excitations is analogous to nonthermal phonon distributions, but for the spin system instead of the lattice: for example, in the case of black phosphorus presented in Chapter 3, the coupling of electrons predominantly to high-energy phonons leads to a situation in which the lattice absorbs a significant amount of energy, but the atomic displacements are comparatively small. The equilibrium relationship between lattice energy content and atomic displacements is not applicable on short timescales after laser excitation. Similarly, here, a relatively large number of high-energy spin excitations is present, deviating from thermal equilibrium. Therefore, the equilibrium relationship between magnetization and spin energy is not applicable on short timescales after laser excitation.

On longer timescales, the behavior of the spin system depends on the demagnetization amplitude: when the magnetization is reduced by less than $\sim 50\,\%$, the spin system thermalizes on a timescale of several hundred femtoseconds. In contrast, when the magnetization is reduced more, the spin system remains in a nonthermal state for several picoseconds or longer. For the
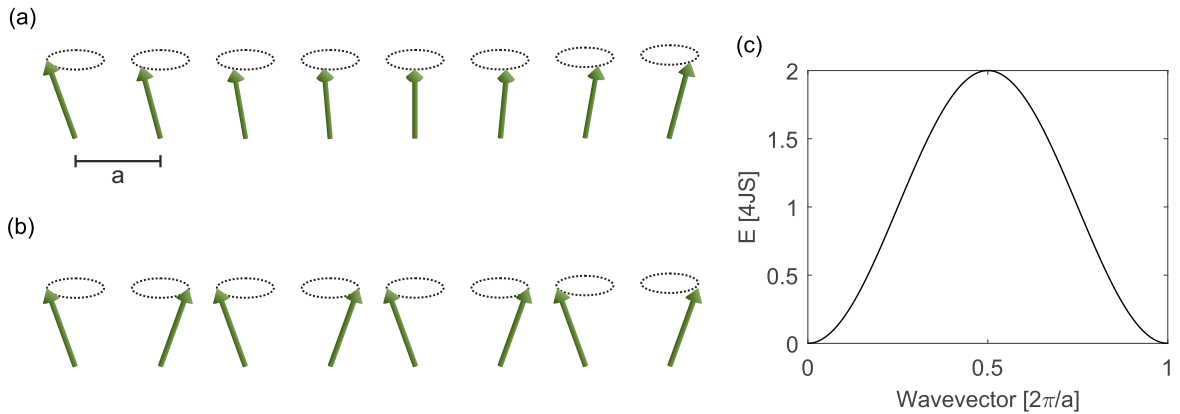
Figure 4.14: Schematic illustration of spin-waves with different wavevectors, using the example of a linear Heisenberg chain. (a) Sketch of a spin-wave with a long wavevector ($\pi/(8a)$). Neighboring spins are nearly parallel. (b) Sketch of a spin-wave with a wavevector of π/a, corresponding to a period of two unit cells. Neighboring spins are canted significantly away from each other. (c) Spin-wave dispersion of a linear Heisenberg chain with only nearest-neighbor interaction (see for example Ref. [Kit05]): $\hbar\omega = 4JS(1 - \cos(qa))$, with J being the exchange constant, S being the magnitude of the spin (here: not normalized to 1), q being the spin-wave/magnon wavevector and a being the real-space lattice constant of the one-dimensional chain. $E = \hbar\omega$ is presented in units of $4JS$. Note that this equation for the spin-wave dispersion is valid only for low spin temperatures, i.e. $S_z \approx S$.

absorbed energy densities shown in Fig. 4.13 (which correspond to those of the femtosecond electron diffraction experiments), this is the case only for nickel, which has the lowest Curie temperature and the lowest magnetic moment of the three materials. In such cases, on longer timescales, the relationship between E_s and M reverses. While the spin energy has already reduced significantly and is approaching its equilibrium value, the magnetization recovery lags behind and requires much longer timescales. This behavior can be attributed to domain formation and has also been observed in spin simulations by Kazantseva et al. [Kaz07].

To visualize this behavior, a simulation was performed for iron using a very high absorbed energy density as well as a significantly increased damping of $\alpha = 0.1$. Increasing α has the advantage that the spin system gets disordered significantly more following laser excitation because increasing α effectively increases the coupling of spins and electrons. At the same time, the system finally relaxes back to a state with a temperature far away from the Curie temperature. This combination makes the visualization clearer. Qualitatively, the same effects are observed for lower values of α as well. Furthermore, a small spin volume of only $100 \times 100 \times 100$ spins was used in the simulation, also for visualization purposes.

Figure 4.15 shows the time evolution of E_s and $E_{s,\text{thermal}}$, the corresponding magnetization dynamics, and a direct visualization of the spin system at different times during the non-equilibrium dynamics. The spin components along the z- and x-direction are visualized. The spin component along the y-direction behaves analogously to the one along the x-direction due to symmetry. Before laser excitation, the magnetization is in the z-direction. During and directly after the arrival of the laser pulse at $t_1 = 0\,\text{ps}$, there is significant short-range disorder in the system, meaning that neighboring spins are significantly canted with respect to each other. This costs a lot of energy and is responsible for the high spin energy content compared to a thermalized spin system. On longer timescales, domains form, which is already visible at $t_2 = 0.75\,\text{ps}$. At this point, the characteristics of the nonthermal state have reversed. Now, the spin energy is relatively low compared to the magnetization. This is a direct effect of domain formation: within one domain, neighboring spins are parallel, which is the energetically most favorable alignment. Only the domain boundaries come with an energy cost compared to the ground state. Therefore, the total spin energy in the system is rather low. The different domains are however aligned in different directions, which leads to a low macroscopic magnetization. As time passes, the domains become larger and more spins align along the z-direction, as shown for the examples of $t_3 = 1.5\,\text{ps}$, $t_4 = 4.5\,\text{ps}$, and $t_5 = 9\,\text{ps}$. This leads to a recovery of the magnetization. Finally, thermal equilibrium of the spin system is reestablished.

Consequently, the ASD simulation results predict a nonthermal spin system on short time-scales after laser excitation for all absorbed energy densities and a prolonged nonthermal state of the spin system for large magnetization reductions (i.e. high absorbed energy densities). Therefore, according to the ASD simulations, a thermal description of the spin system such as in the 3TM is not adequate, particularly for high absorbed energy densities.

It should however be noted that the description of the electron-spin interaction in the simulations is phenomenological, which raises the question of whether the initial spin excitations are described correctly. While the simulations cannot account for the details of electron-magnon scattering, a phase space argument suggests that indeed a higher number of intermediate-wavevector magnons compared to thermal equilibrium are excited: due to the typical energies of magnons and since electrons are fermions, the electronic states involved in electron-magnon scattering are all close to the Fermi surface. Most of the transitions from one electronic state
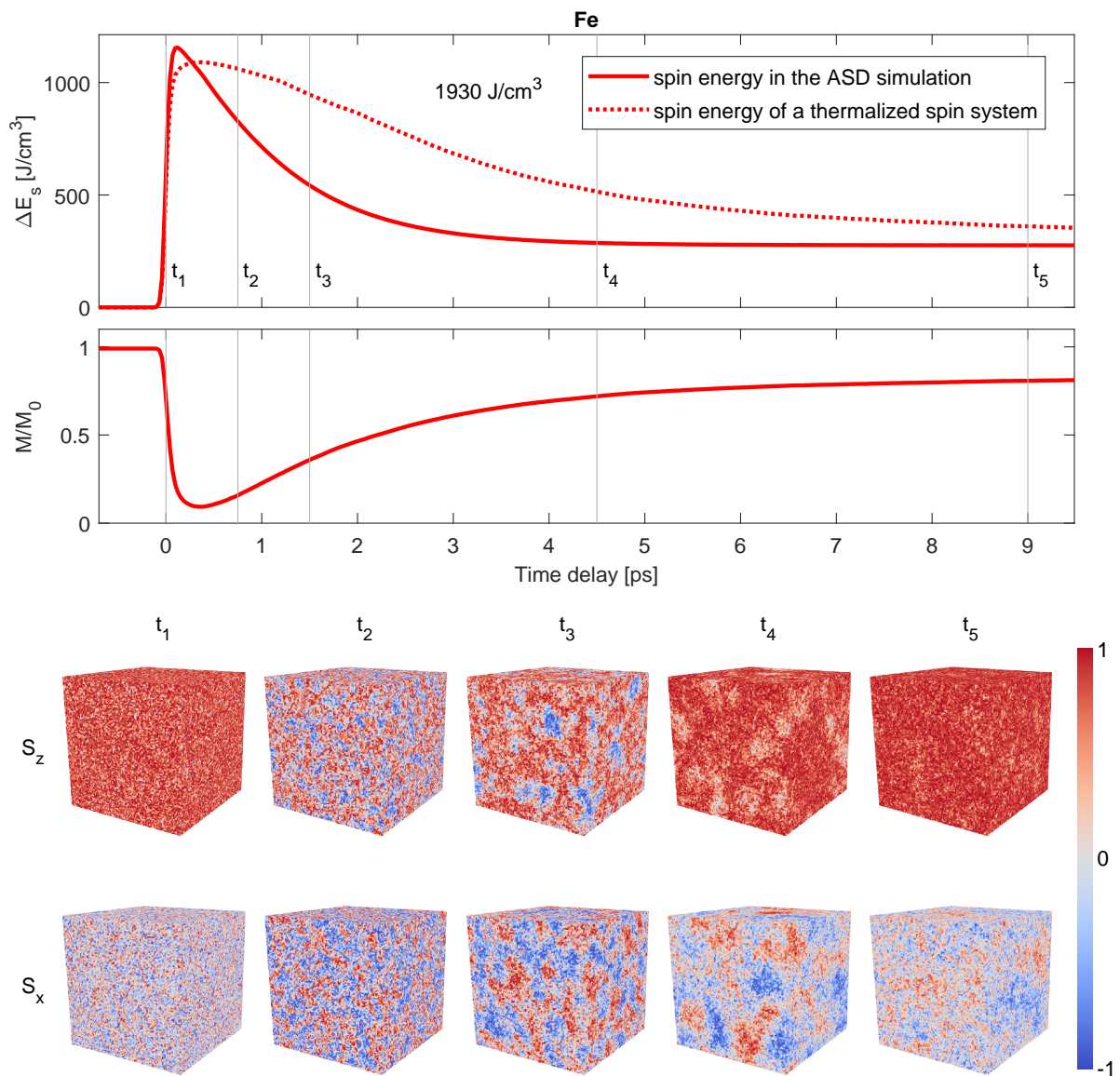
Figure 4.15: Visualization of nonthermal spin dynamics at high absorbed energy densities. The ASD simulation was performed on iron with an absorbed energy density of $1930\,\mathrm{J/cm^3}$ and assuming a high α-value of 0.1. The upper panel shows the evolution of the additional spin energy content ΔE_s (solid curve) as well as the hypothetical additional spin energy content of a thermalized spin system (dashed curve), calculated from the magnetization dynamics (shown directly below). The lower part of the figure directly visualizes the alignment of individual spins for selected pump-probe delays $t_1 - t_5$ (indicated in the upper panels). The spins are normalized such that $s_\mathrm{x}^2 + s_\mathrm{y}^2 + s_\mathrm{z}^2 = 1$. Only the surface of the cube of $100 \times 100 \times 100$ spins is visible, but it was verified that the inside of the cube exhibits analogous behavior. Adapted from Ref. [Zah21b].

.

to another on the Fermi surface involve intermediate changes of the electron wavevector, rather than very low or very high ones. Due to momentum conservation, the wavevector change of the electron needs to be compensated by the magnon wavevector. Hence, it is likely that a large number of magnons with intermediate wavevectors will be created. On the other hand, a thermalized distribution of magnons follows Bose-Einstein statistics[2] and thus contains mostly magnons with low wavevectors. This suggests that the ASD simulations are able to qualitatively describe the non-equilibrium magnon distribution after excitation, with a higher number of intermediate-wavevector magnons compared to thermal equilibrium. To improve the description of the initial magnon distribution further, the electron-spin coupling would need to be described on a more microscopic level, beyond the phenomenological description with the stochastic term of the LLG equation in combination with the damping α.

4.3   Summary and conclusions

In this chapter, the ultrafast lattice dynamics of the elemental 3*d* ferromagnets iron, cobalt, and nickel were studied with femtosecond electron diffraction. For all three materials, laser-induced lattice heating occurs on timescales of hundreds of femtoseconds, which are similar timescales compared with the magnetization dynamics. To analyze the ultrafast energy flow between electrons, spins, and phonons in detail, spin-resolved DFT calculations were combined with different energy flow models. The comparison of conventional TTM, 3TM, and energy-conserving ASD simulations with the experimental data revealed the prominent role of the spin system in the microscopic energy flow: for all three 3*d* ferromagnets, energy flow into and out of the spin system has a profound impact on the lattice dynamics. The spin system is the dominant energy sink directly after laser excitation and subsequently emits energy again during remagnetization, which causes a pronounced slowdown of the lattice dynamics. A description of the microscopic energy flow and the non-equilibrium magnetization dynamics was obtained using energy-conserving ASD simulations. For all three materials, the simulations yielded excellent agreement to the experimentally measured lattice dynamics at low and moderate absorbed energy densities. Furthermore, also the magnetization dynamics are well described by the simulations. These results are an important step towards a model of ultrafast demagnetization that is consistent with the responses of magnetic, electronic, and lattice degrees of freedom. They reveal the prominent role of the spin system, which needs to be considered in any model for the microscopic energy flow.

In addition, the ASD simulations predict a nonthermal behavior of the spin system. This manifests in a disparate evolution of spin energy content and magnetization. In particular, for large magnetization reductions (more than $\sim 50\,\%$), the simulations predict a prolonged nonthermal state that can last several picoseconds. This has implications for the interpretation of experimentally measured magnetization dynamics, suggesting that the absence of a magnetization recovery on picosecond timescales does not necessarily mean that the material has thermalized. In general, the ASD simulations predict that particularly for high absorbed energy densities, the 3TM does not offer an accurate description of the laser-induced dynamics.

---

[2]Since the ASD simulations are classical, the thermalized spin system in the simulations exhibits a Boltzmann distribution of magnons instead of a Bose-Einstein distribution. In addition, magnon/spin-wave frequencies are generally temperature-dependent due to magnon-magnon interactions. This does not alter the qualitative discussion presented here.

By directly simulating the spin system, energy-conserving ASD simulations go a step beyond the thermal description employed in the 3TM. In a future model, also the electron and phonon system could be treated in greater detail, without relying on the approximation of internal thermal equilibrium of those two subsystems. In particular for cobalt, which has optical phonons, nonthermal phonon dynamics could play a role [ROM20]. On the experimental side, microscopic effects could be better disentangled from transport and absorption profile effects by measuring the dynamics of all subsystems on identical samples. Such measurements would also enable a quantitative comparison of the responses of different subsystems as functions of absorbed energy density.

Nevertheless, the comparison to available experimental data already shows that energy-conserving ASD simulations are able to provide a quantitative description of the ultrafast energy flow in the elemental $3d$ ferromagnets. This is relevant both for the fundamental understanding of ultrafast demagnetization as well as for applications of these materials in heterostructure devices. Any application in non-equilibrium conditions will benefit from quantitative knowledge of the relaxation timescales and of the associated couplings and energy flow dynamics. Beyond the elemental $3d$ ferromagnets, a qualitatively similar influence of spin dynamics on the other two subsystems can also be expected for other magnetic materials, e.g. other itinerant ferromagnets, localized ferromagnets, ferrimagnets, and antiferromagnets. In the next chapter, the energy flow on ultrafast timescales will be studied for another class of magnetic materials, elemental $4f$ ferromagnets.

Chapter 5

Lattice dynamics in $4f$ ferromagnets

In contrast to the itinerant ferromagnetism in $3d$ transition metals, the major part of the magnetic moment of $4f$ ferromagnets is localized to the atomic site, with the corresponding electronic states located far below the Fermi level. Only a minor contribution to the magnetic moment that stems from $5d$ states is similarly delocalized as in itinerant ferromagnets. This has implications for the way that magnetic degrees of freedom can interact with electrons and the lattice. In particular, the $4f$ moments can neither interact via spin flips due to Elliott-Yafet scattering nor via magnon emission (see Sec. 1.2), since there are no unoccupied electronic states with the opposite spin available at energies in the vicinity of the $4f$ levels. A comparison of the electronic DOS of a $3d$ and a $4f$ metal is presented in Fig. 5.1 for the examples of cobalt and terbium.
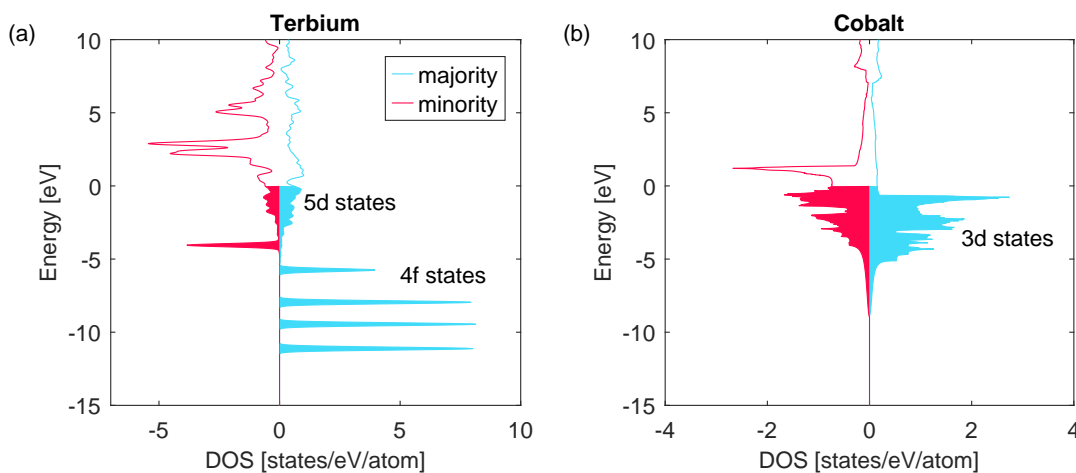
Figure 5.1: Comparison of the DOS of a $3d$ and a $4f$ ferromagnet. (a) Electronic DOS of the $4f$ ferromagnet terbium, obtained from DFT+U calculations (see Sec. 2.4 for details). States below the Fermi level (here located at $0\,\mathrm{eV}$) are shown as filled. The difference in occupation numbers between majority and minority states corresponds to the magnetic moment. From the comparison of occupied majority and minority states, it can be seen that most of the magnetic moment originates from the occupied majority $4f$ states, which lie far below the Fermi level. The fact that these states are very narrow in energy indicates that they are very localized. (b) Electronic DOS of the $3d$ ferromagnet cobalt, obtained from DFT calculations (see Sec. 2.4). Here, the magnetic moment stems entirely from the $3d$ states, which are more delocalized (and therefore broader in energy) compared to the $4f$ states of terbium and are located close to the Fermi level.

Elemental $4f$ metals exhibit ultrafast demagnetization following excitation with a laser pulse [Mel08; Koo10; Wie11; Fri15; Thi17; Fri20]. The demagnetization timescales can vary significantly for different $4f$ ferromagnets [Wie11; Fri20]. In addition, experiments have revealed that the magnetization dynamics of the (small) contribution of the $5d$ states to the magnetic moment can exhibit different dynamics compared with the (dominant) contribution of the $4f$ moments [Fri15; Fri20].

Due to the lack of spin-flip or exchange scattering channels for the localized $4f$ moments, direct spin-lattice interactions often play an important role in the laser-induced dynamics of $4f$ ferromagnets [Wie11; Esc14]. Hence, direct observation of the lattice dynamics is desired for a microscopic understanding of the timescales observed in the magnetization dynamics. In addition, the magnetic moment of the elemental $4f$ ferromagnets is typically much larger than those of the elemental $3d$ ferromagnets. For example, terbium has a magnetic moment of $9.34\,\mu_\mathrm{B}$ per atom [Fri20], while nickel has only $0.62\,\mu_\mathrm{B}$ per atom [DHM68]. As a consequence, the magnetic contribution to the heat capacity is substantial, much larger than in the case of $3d$ ferromagnets (compare for example Fig. 4.1(a) with Fig. 5.6(a) and (b)). This implies a significant energy cost of demagnetization. Therefore, a significant influence of the magnetization dynamics on the electron and lattice dynamics can be expected.

At the same time, $4f$ ferromagnets are also a significantly more complex material class compared with the elemental $3d$ ferromagnets: first of all, the presence of two different types of magnetic moment ($4f$ and $5d$ spins) adds complexity to the ultrafast response, because more subsystems interact with each other. Furthermore, different experimental techniques are required to probe these different aspects of the magnetization dynamics. In addition, electronic correlation effects play a larger role in rare-earth metals [Söd14]. As a result, regular DFT calculations struggle to describe $4f$ ferromagnets accurately, which adds complexity to their theoretical description. Finally, additional technical challenges arise: unlike the elemental $3d$ ferromagnets, the Curie temperatures of elemental $4f$ ferromagnets lie below or around room temperature and accessing the ferromagnetic phase thus often requires cryogenic cooling. In addition, rapid degradation in air or water occurs, which makes sample preparation for transmission electron diffraction challenging. Compared with the $3d$ ferromagnets studied in the previous chapter, $4f$ ferromagnets are a step up in complexity, and thus an interesting case for applying and expanding the microscopic energy flow concepts previously discussed for the $3d$ ferromagnets.

This chapter presents femtosecond electron diffraction results for two commonly studied $4f$ ferromagnets, terbium and gadolinium. It is particularly interesting to study these two materials together because they exhibit very different spin-lattice coupling strengths [Liu21] and demagnetization dynamics [Wie11], while otherwise being similar. Here, ultrafast diffraction experiments were performed on terbium and gadolinium films, both above and below their Curie temperatures. In addition, a detailed temperature-dependent study of the lattice dynamics was performed for terbium. These results were complemented by measurements of the magnetization dynamics of terbium with time-resolved MOKE, which were recorded on the same sample to maximize comparability. The MOKE measurements, which are presented in Sec. 5.3, were taken together with Felix Steinbach and Martin Borchert, employing a MOKE setup at the Max-Born-Institut [Bor21]. The samples were grown by Dieter Engel (Max-Born-Institut). The SQUID measurements presented in this chapter were performed by Evangelos Papaioannou and Camillo Ballani (Martin-Luther Universität Halle-Wittenberg). Haichen Wang and Miguel Marques

(Martin-Luther Universität Halle-Wittenberg) performed DFT+U calculations on terbium and gadolinium (see also Sec. 2.4) which were the basis of the 3TM results presented in Fig. 5.6 and served to calculate Debye-Waller-factors for the conversion of MSD to temperature.

5.1 Sample preparation and characterization

The elemental $4f$ metals oxidize easily in air and in water, which makes the preparation of thin, free-standing samples challenging. All samples employed in this work were magnetron-sputtered thin films. To protect the metal films from oxidation, a silicon nitride film was deposited both before and after deposition of the $4f$ metal. Compared to the $3d$ metal samples, a significantly thicker silicon nitride film was necessary to avoid oxidation. The samples employed in the first experiments on terbium and gadolinium (presented in Sec. 5.2.1) were 40 nm-thick metal films, sandwiched between 15 nm-thick layers of silicon nitride. The films were grown on salt (NaCl) crystals and transferred using the standard floating technique (see Sec. 2.1.2). The amount of time that the film was in contact with water was minimized by picking it up directly after detachment from the salt crystal and by accelerating the drying process with nitrogen flow. At the edges of the samples, degradation due to the contact with water was observed, as shown in Fig. 5.2 for the example of a terbium film. There were also large areas without any visible alterations of the films (see for example green arrows in Fig. 5.2), which were employed for the measurements presented in Sec. 5.2.1.
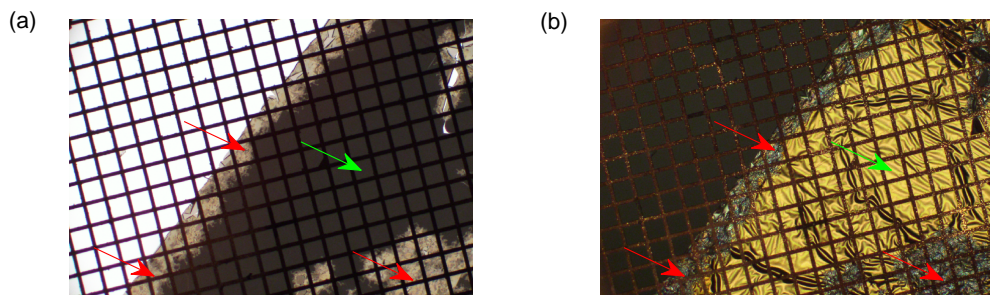
Figure 5.2: Microscope images of a terbium sample obtained with the standard floating technique. (a) Transmission microscope image of the sample on the TEM grid. The brighter areas of the sample (red arrows), which are predominantly located at edges, have degraded. The darker area in the middle (green arrow) did not exhibit any visible changes upon transfer to the TEM grid. (b) Reflection microscope image of the same sample. The degraded parts appear dull in reflection and are clearly separable from the shiny, unaltered parts of the sample.

For the detailed temperature-dependent measurements on terbium presented in Sec. 5.2.2, the sample geometry and preparation were optimized further. To minimize oxidation, the contact of the film with water was avoided altogether by directly growing the samples on commercially available silicon nitride membranes (10 nm thickness). To avoid oxidation from contaminants on the surface of the silicon nitride membranes, 2 nm of silicon nitride were deposited before the deposition of terbium. In addition, the terbium thickness was decreased to 20 nm to reduce multiple scattering effects. Finally, the surface of the terbium film was protected with
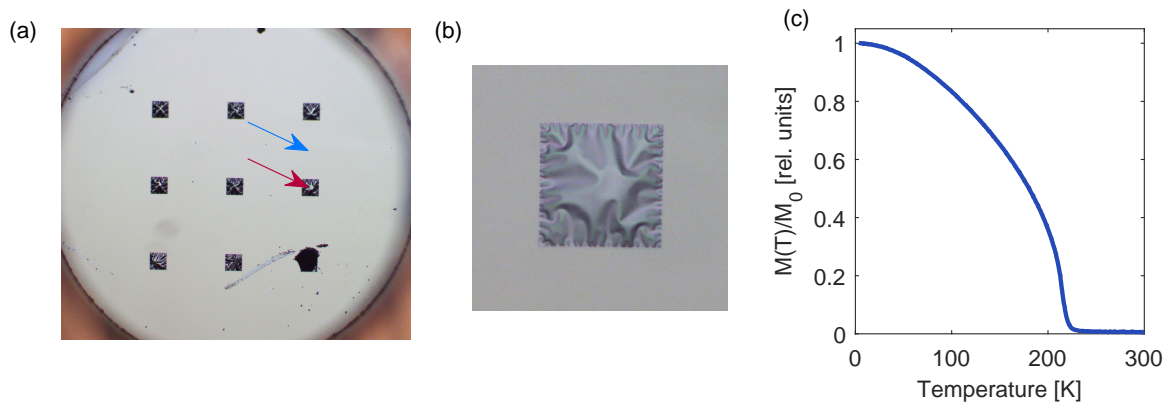
Figure 5.3: Microscope images and temperature-dependent magnetization curve of the terbium films evaporated on silicon nitride membranes. (a) Microscope image in reflection of the terbium sample employed in the diffraction measurements presented in Sec. 5.2.2 and the MOKE measurements presented in Sec. 5.3. The red arrow indicates the silicon nitride window on which the electron diffraction experiments were performed. The MOKE experiments (in reflection) were performed on an area with silicon substrate, indicated by the blue arrow. (b) Close-up view of the silicon nitride window employed in the electron diffraction experiments. (c) Temperature-dependent magnetization of the terbium films obtained from SQUID measurements. The measurements were performed on another, identical sample that was produced simultaneously with the sample in Panel (a).

another silicon nitride layer. The thickness of this layer was chosen to be 12 nm such that a symmetric sample geometry was obtained.

The terbium samples grown directly on silicon nitride membranes were characterized using a superconducting quantum interference device (SQUID). The result is presented in Fig. 5.3(c). The measured temperature dependence of the magnetization agrees with the Curie temperature of terbium from literature, 221 K [Coe10].

Both terbium and gadolinium exhibit an hcp structure at room temperature. Compared to the 3d ferromagnet cobalt, which also crystallizes into an hcp structure, the elemental 4f metals have significantly larger lattice constants (and thus smaller scattering vectors). The terbium film grown on salt exhibited different relative peak intensities compared with the terbium film grown directly on silicon nitride (see Figs. 5.4 and 5.7 of the following section). This indicates a different preferred orientation of the two samples, which was likely caused by the different substrates and is not expected to have any effect on the MSD dynamics studied here.

5.2   Femtosecond electron diffraction results

5.2.1   Terbium and gadolinium above and below their Curie temperatures

Femtosecond electron diffraction experiments on gadolinium and terbium were conducted at two base temperatures each, one above and one below the Curie temperature, and with several fluences. For gadolinium, which has a Curie temperature around room temperature (at 293 K [Coe10]) the sample was heated to 332 K for measurements in the paramagnetic phase. Measurements in the ferromagnetic phase were performed at 140 K. For terbium, which has a Curie temperature of 221 K [Coe10], measurements in the ferromagnetic phase were also performed at 140 K. Measurements in the paramagnetic phase were performed at room temper-

ature (295 K). The employed excitation wavelength was 2300 nm in all measurements. Table 5.1 presents an overview of the employed incident fluences and the corresponding absorbed fluences and absorbed energy densities. The absorptance of the samples at 2300 nm and 6° angle of incidence (measured from the sample normal) was calculated to be 44 % for terbium and 43 % for gadolinium, based on multilayer calculations [Win98] and optical constants from Refs. [Ahm82; Luk15; APS19]. For terbium, only the lowest three fluences were applied, because higher fluences caused permanent sample damage.

inc. fluence $[\mathrm{mJ/cm^2}]$	1.1 ± 0.4	1.7 ± 0.4	2.6 ± 0.6	3.1 ± 0.6	3.9 ± 0.8
abs. fluence (Gd) $[\mathrm{mJ/cm^2}]$	0.5 ± 0.2	0.7 ± 0.2	1.1 ± 0.3	1.3 ± 0.3	1.7 ± 0.4
abs. energy density (Gd) $[\mathrm{J/cm^3}]$	120 ± 50	180 ± 50	280 ± 70	330 ± 70	420 ± 90
abs. fluence (Tb) $[\mathrm{mJ/cm^2}]$	0.5 ± 0.2	0.8 ± 0.2	1.2 ± 0.3	–	–
abs. energy density (Tb) $[\mathrm{J/cm^3}]$	120 ± 50	190 ± 50	290 ± 70	–	–

Table 5.1: Incident (inc.) fluences, absorbed (abs.) fluences and absorbed energy densities for the experiments on gadolinium and terbium presented in Sec. 5.2.1. The incident fluences were calculated using Eq. 4 of Ref. [Har06]. Absorbed fluences and energy densities were determined based on multilayer calculations (see text for details).

The obtained diffraction patterns were analyzed with the global fitting routine presented in Sec. 2.3.2. Figure 5.4 presents radial profiles for both materials and examples of laser-induced changes of the radial profiles at several pump-probe delays. The results of the global fitting routine are presented as dashed black curves. Figure 5.5(a)-(d) presents results for the MSD dynamics of gadolinium and terbium above and below their Curie temperatures. In all cases, the MSD rises on a few-picosecond timescale following laser excitation. On longer timescales, a decrease is observed, which is likely caused by cooling of the probed area due to heat transport (laterally and to the silicon nitride layers). To analyze the dynamics of the MSD rise quantitatively, single exponential fits were performed, analogously to the fits employed in the previous chapter. Here, the fit range was from -5 to 12 ps and the estimated time resolution was 250 fs (FWHM).

Figure 5.5(e) presents fit results for the time constants for both materials and several fluences each. For both materials, time constants on the order of 1 ps are observed. The lattice dynamics of gadolinium are found to be around 15-25 % faster compared with terbium. Interestingly, this finding is in contrast to the DFT+U calculations presented in Sec. 2.4, which predict a larger electron-phonon coupling parameter for terbium (~38 % larger than gadolinium at 295 K) while the electronic and lattice heat capacities are nearly identical (see Fig. 2.23). From the DFT+U results, a faster lattice temperature rise of terbium compared to gadolinium would therefore be expected (not considering any contributions from the spin dynamics). This is opposite to the experimental results.

In addition, both materials exhibit an increase of the time constant with fluence. This is likely caused by the increase of the electronic heat capacity with electron temperature. The same effect was also observed for cobalt and nickel (see Fig. 4.4 of the previous chapter). In the case of gadolinium and terbium, the electronic heat capacity is rather small and thus the electron temperature increases significantly after laser excitation. This means that also the
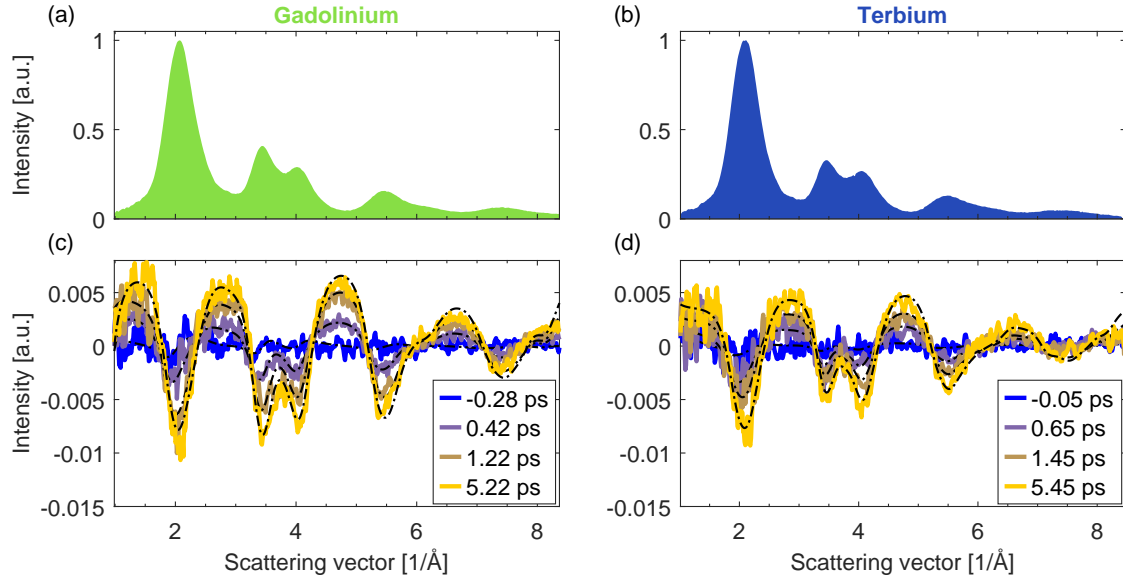
Figure 5.4: Diffraction patterns of gadolinium and terbium and laser-induced changes. (a) Radial profile of a diffraction pattern of gadolinium. The background (result from the global fitting routine) was subtracted and pixels were converted to scattering vectors for illustration purposes. (b) Same as (a), but for terbium. (c) Laser-induced changes in the radial profile of gadolinium at several pump-probe delays. Here, the sample was excited with a photon wavelength of 2300 nm and an incident fluence of $2.6 \pm 0.6 \, \mathrm{mJ/cm^2}$, corresponding to an absorbed energy density of $280 \pm 70 \, \mathrm{J/cm^3}$. The solid curves correspond to experimental data and the dashed black curves are the results of the global fitting routine. The intensity units are the same as in (a) such that both panels can be quantitatively compared. (d) Same as (c), but for terbium. The pump wavelength was 2300 nm and the incident fluence was $2.6 \pm 0.6 \, \mathrm{mJ/cm^2}$, corresponding to an absorbed energy density of $290 \pm 70 \, \mathrm{J/cm^3}$. The base temperature was 140 K in both cases.

electronic heat capacity increases significantly for high fluences and consequently a significant fluence-dependence of the time constant is expected.

Regarding the amplitudes of the MSD/temperature rise, gadolinium exhibits the same amplitudes for both 140 K and 332 K (see Fig. 5.5(e)). For terbium, slight differences were observed between 140 K and 295 K. However, this behavior was not reproduced in the detailed temperature-dependent study on terbium presented in Sec. 5.2.2. Therefore, these differences are likely an experimental artifact. Results on dysprosium suggest that the optical properties of elemental 4f metals do not exhibit significant changes with temperature [Rep16].

In order to quantify the recovery dynamics (i.e. the cooling of the lattice), linear fits were performed to the MSD data at pump-probe delays larger than 30 ps. Linear instead of bi-exponential fits were chosen here because the measured delay range is not large enough to resolve the time constant of the recovery. Bi-exponential fits (of the rise and decay) resulted in vastly different time constants for the recovery and large errors.

The negative of the slope from the linear fit corresponds to the recovery rate (in $\mathrm{\AA^2/ps}$). For a quantitative comparison of different fluences, the obtained slope of the linear function was divided by the amplitude of the MSD rise. This yields the recovery rate relative to the total amplitude of the rise (in 1/ps). Calculating such a relative recovery rate has the advantage
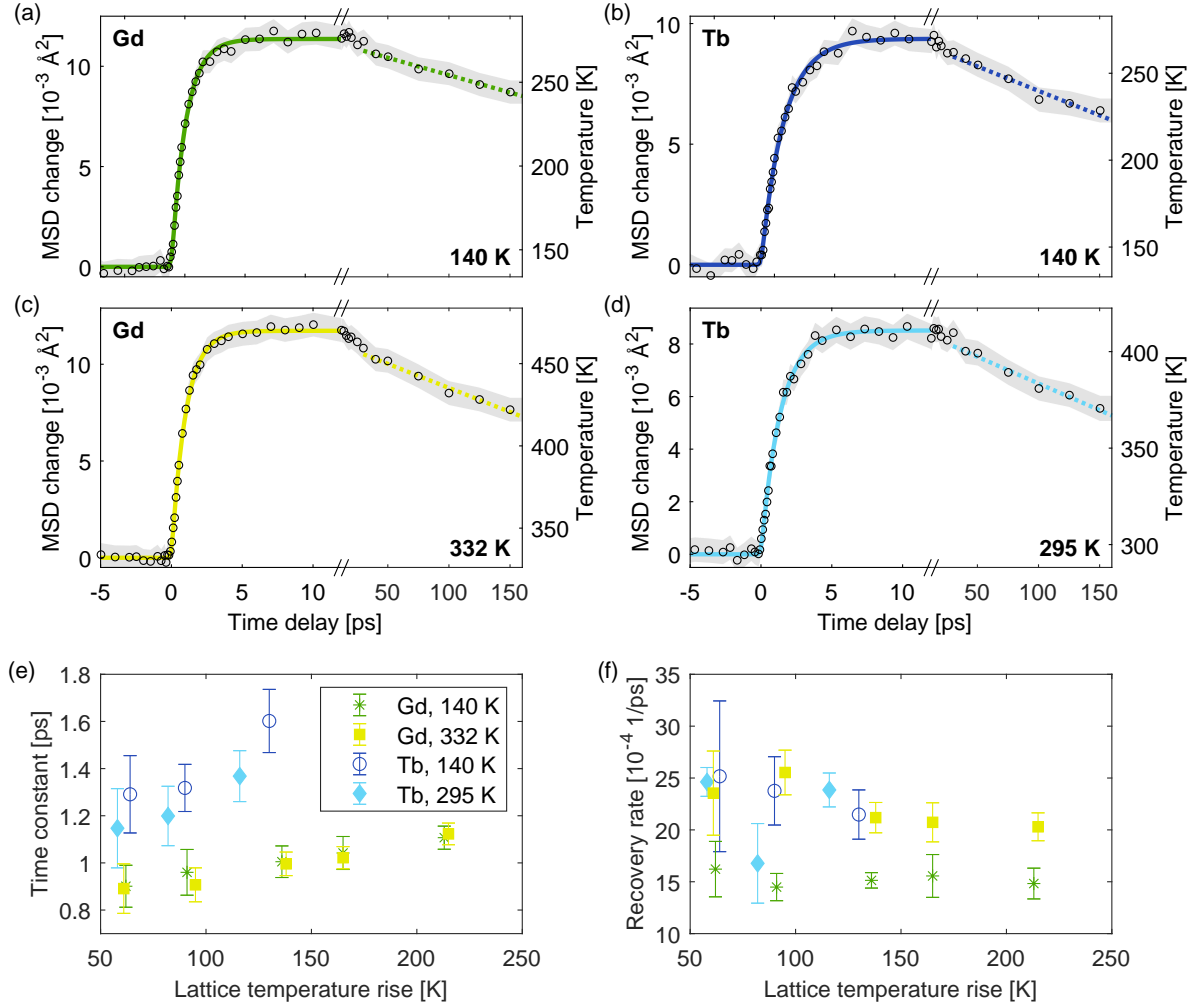
Figure 5.5: Comparison of the MSD dynamics in gadolinium and terbium above and below their Curie temperatures. (a) MSD/lattice temperature dynamics of gadolinium at 140 K, i.e. below the Curie temperature. Black circles are experimental data and the solid curve shows the results of a single exponential fit to the lattice temperature dynamics in the range from -5 to 12 ps. The dashed line corresponds to a linear fit in the range above 30 ps to analyze the recovery. Gray shaded areas correspond to the standard errors of the experimental data obtained from the global fitting routine. The conversion between MSD changes and temperature was done using the calculated Debye-Waller factors presented in Sec. 2.4. (b) Same as (a), but for terbium, also recorded at 140 K. (c) Same as (a), but for paramagnetic gadolinium, recorded at 332 K. (d) Same as (b), but for paramagnetic terbium, recorded at 295 K. (e) Fit results for the time constants of the lattice temperature rise in both materials (see solid curves in (a)-(d)). Results for different fluences are presented, corresponding to different lattice temperature rises. (f) Fit results for the recovery. Here, the negative of the slope of the linear fit is presented (dashed lines in Panels (a)-(d)), divided by the amplitude of the lattice temperature rise from the single exponential fit. This yields the relative recovery rate. All error bars in Panels (e) and (f) are standard errors obtained from the fits. The fluences and absorbed energy densities of all measurements presented here are summarized in Table 5.1.

that the value doesn't depend on the amplitude anymore and results at different fluences can therefore be directly compared.

The results are presented in Fig. 5.5(f). Generally, the relative recovery rate does not depend significantly on the fluence. For terbium, no differences are observed between 140 K and 295 K base temperatures within the experimental accuracy. For gadolinium, the recovery rate increases at high temperatures. This is likely related to the heat capacity of the silicon nitride layers, which is significantly higher at 332 K compared to 140 K [ZH04]. At the same time, the heat capacity of gadolinium is almost the same at 140 K and 332 K. Consequently, at 332 K, more energy flows from gadolinium to the silicon nitride layers when thermal equilibrium throughout all sample layers is established.

Interestingly, the comparison of experiments in the paramagnetic and ferromagnetic phase reveals no differences on picosecond timescales. No clear signatures of the magnetization dynamics are observed in the lattice dynamics, neither for gadolinium nor for terbium. This is surprising, since the substantial spin heat capacities suggest that the magnetization dynamics should have a pronounced influence on the lattice dynamics.

For detailed insights into the expected behavior, it is necessary to consider the spin heat capacities as well as the demagnetization timescales. It is known from literature that the main contribution to the magnetic moment, the 4f spins, behave quite differently in gadolinium and terbium: the 4f spins of gadolinium demagnetize on timescales of several picoseconds, while the 4f demagnetization in terbium is generally faster than in gadolinium and occurs on sub- to few-picosecond timescales [Wie11; Fri20]. Experimental studies have also shown that the demagnetization dynamics are fluence-dependent [Wie10] as well as base-temperature-dependent [Sul12].

To compare the magnetization dynamics to the lattice dynamics, quantitative information on the spin heat capacities is required. Fig. 5.6(a) and (b) present a decomposition of the heat capacities of gadolinium and terbium into the contributions from the different subsystems. The decomposition directly shows the importance of the spin heat capacity in both materials. As most of the magnetic moment stems from the 4f spins, they also account for most of the spin heat capacity. Consequently, based on energy flow arguments, a substantial influence of the 4f magnetization dynamics on the lattice dynamics would be expected, regarding both timescales and amplitudes. In particular, assuming thermal behavior of all subsystems (internally), it would be expected that the timescales of the 4f magnetization dynamics are reflected in the lattice dynamics.

One model that describes ultrafast dynamics under the assumption of internal thermal equilibrium in all subsystems is the three-temperature model (3TM). In the following, a 3TM is employed for terbium to show directly that the experimental results presented here, combined with magnetization dynamics from Ref. [Wie11], do not agree with such a thermal description. 4f and 5d spins are treated as one subsystem here, because in terbium, they were found to exhibit the same dynamics [Fri20]. Following the conclusions of Ref. [Wie11], the spin-phonon coupling parameter in the 3TM here was enhanced by the presence of hot electrons, by introducing a phenomenological fit parameter p:

$$G_{\mathrm{sp}}(T_{\mathrm{e}}) = G_{\mathrm{sp},0} \times \left(\frac{T_{\mathrm{e}}}{T_{\mathrm{l}}}\right)^{p}. \tag{5.1}$$
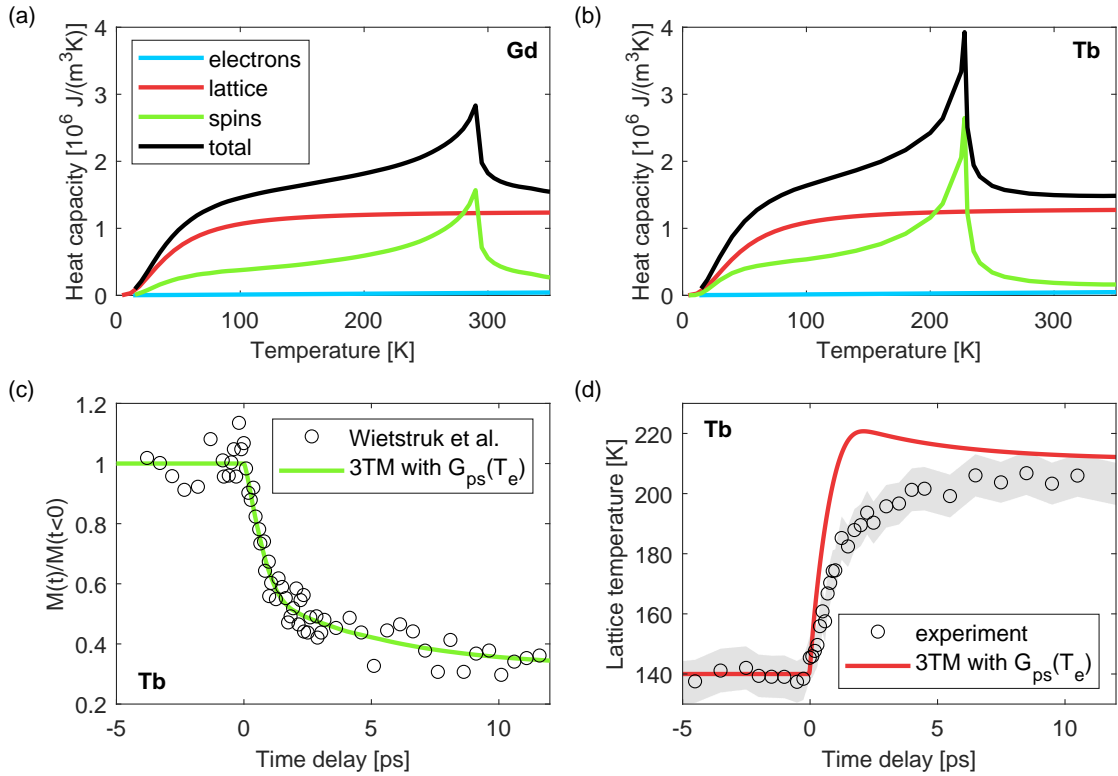
Figure 5.6: Heat capacities and three-temperature model (3TM) results. (a) Decomposition of the experimental heat capacity of gadolinium (literature result from Ref. [GSS54]). The electron and lattice contributions stem from DFT+U calculations (see Sec. 2.4 for details). The magnetic contribution was obtained by subtracting the electronic and lattice contributions from the total heat capacity. The dilation correction (the difference between heat capacity at constant volume and heat capacity at constant pressure) was not taken into account here, but it is typically a rather small correction in this temperature range [Mes81]. (b) Same as (a), but for terbium (experimental data from Ref. [JSS57]). For both materials, the magnetic contribution exhibits a pronounced negative curvature at low temperatures, which is generally not expected for the magnetic heat capacity (see for example Fig. 4.7 for comparison). The observation could stem from a residual contribution of the lattice, for example caused by potential systematic errors in the temperature of the experimental data. (c) Experimental data of the $4f$ magnetization dynamics from Ref. [Wie11] (black circles) together with 3TM results (green curve). In this particular 3TM, electron-spin coupling was not included and the phonon-spin coupling was temperature-dependent: $G_{sp}(T_e) = G_{sp,0} \times (T_e/T_l)^p$. A fit was performed to the experimental data from Ref. [Wie11]. The 3TM fit results were: absorbed energy density: $155 \pm 6 \, \text{J/cm}^3$, $G_{sp,0} = (7 \pm 6) \times 10^{16} \, \text{W/(m}^3\text{K)}$, $G_{ep} = (1.3 \pm 0.3) \times 10^{17} \, \text{W/(m}^3\text{K)}$, $p = 1.9 \pm 0.5$. Within the error bars, the result for G_{ep} agrees with the DFT+U results ($\sim 1.55 \times 10^{17} \, \text{W/(m}^3\text{K)}$ at room temperature, see Fig. 2.23). (d) 3TM prediction for the lattice dynamics (red curve). For comparison, experimental data with a similar final lattice temperature are presented. The absorbed energy density in the experiment was $120 \pm 50 \, \text{J/cm}^3$. Beyond the slightly different amplitudes, significant differences in the qualitative behavior exist between 3TM prediction and experimental data.

Direct electron-spin coupling was not included. With such a 3TM, the magnetization dynamics from Ref. [Wie11] can be well described, as presented in Fig. 5.6(c). However, when comparing the lattice response predicted by the 3TM to an experimental result with a similar lattice temperature rise, significant deviations between experiment and 3TM are observed. In particular, the second, few-picosecond drop of the magnetization (see Fig. 5.6(c)) leads to a temperature drop of the lattice in the 3TM, which is not observed experimentally. Generally, in a thermal description such as the 3TM, demagnetization that occurs after electron-lattice equilibration is always accompanied by energy drain from the lattice – a direct consequence of energy conservation. Note that for gadolinium, an even larger effect than for terbium would be expected, since the slow, few-picosecond component in the 4f demagnetization is more pronounced in gadolinium [Wie11]. However, such an influence of the magnetization dynamics on the lattice is observed neither for terbium nor for gadolinium.

In conclusion, the measurements on terbium and gadolinium above and below the Curie temperature show no clear signatures of the magnetization dynamics, which is in contrast to expectations based on energy flow considerations and assuming thermal equilibrium within the different subsystems. In the next section, this will be investigated further for the case of terbium.

5.2.2   Temperature-dependent measurements on terbium

To expand the comparison of ferromagnetic and paramagnetic phases presented in the previous section, detailed temperature-dependent experiments were performed on terbium. For these measurements, samples with optimized geometry and preparation method were employed (see Sec. 5.1). A diffraction pattern of the optimized terbium sample is presented in Fig. 5.7(a).
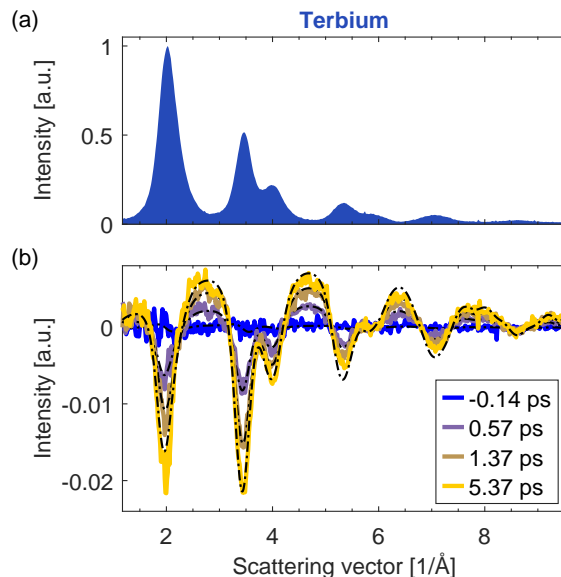
Figure 5.7: Diffraction pattern of the terbium sample employed in the measurements of Sec. 5.2.2 and laser-induced changes. (a) Radial profile of a diffraction pattern (background-subtracted and pixels converted to scattering vectors). (b) Time-resolved changes in the radial profile following laser excitation. The pump wavelength was 2300 nm and the incident fluence was $2.3 \pm 0.4 \, \mathrm{mJ/cm^2}$, corresponding to an absorbed energy density of $580 \pm 100 \, \mathrm{J/cm^3}$.

Measurements were performed at a variety of different base temperatures from 100 K to room temperature (295 K), keeping all other experimental conditions constant. Fig. 5.7(b) presents an example of time-dependent changes in the diffraction pattern. As in the previous section, the pump wavelength was 2300 nm. The incident fluence here was around 2.3 ± 0.4 mJ/cm^2. According to multilayer calculations [Win98] based on the optical constants of Refs. [Ahm82; Luk15], the absorptance of the sample at 2300 nm and $6°$ angle of incidence is 50 %. The resulting absorbed fluence and energy density are presented in Table 5.2. Both the absorptance as well as the relationship between absorbed fluence and absorbed energy density are different here compared to Sec. 5.2.1 due to the different sample thicknesses. Note that in the experiments of this section, in contrast to the previous section, the measured temperature rises were significantly smaller than expected from the calculated absorbed energy densities (by 35-45 %, based on the heat capacity of terbium [GSS54]). This could be due to uncertainties in the absorptance calculation, e.g. due to surface roughness or uncertainties in the optical constants, which were not considered here. Deviations of the sample thickness and losses on mirrors could also contribute to the observed discrepancies.

The results for the MSD dynamics are presented in Fig. 5.8(a). Very similar lattice dynamics are observed for all base temperatures, without any clear signatures of the magnetic phase transition around 221 K [Coe10]. To analyze the lattice dynamics quantitatively, bi-exponential fits were performed. The fit function was the same as for the bi-exponential fits in Chapter 3. To account for the time resolution, the bi-exponential function was convolved with a Gaussian with a FWHM of 250 fs. The results for the time constants and amplitudes are presented in Fig. 5.8(b)-(f).

The time constants of the lattice temperature rise (τ_1), presented in Fig. 5.8(e), are found to be around 1.1-1.5 ps, which is similar to the results presented in Sec. 5.2.1. Compared to those previous measurements, the lattice temperature rise is higher here despite the similar fluence. This can be explained by the different sample thicknesses. A minor increase of τ_1 with base temperature is observed. Fig. 5.8(f) presents the time constants of the recovery (τ_2). Here, no dependence on the base temperature is observed within the experimental accuracy. Fig. 5.8(b) shows the amplitudes of the initial MSD rise (A_1). It increases slightly with increasing base temperature. The amplitude of the recovery (A_2), shown in Fig. 5.8(c), also increases in magnitude (note the negative sign in Fig. 5.8(c)). Comparing the two amplitudes by taking their ratio (Fig. 5.8(d)), it is found that the relative magnitude of the recovery increases with base temperature. As already discussed in Sec. 5.2.1, this is likely related to the heat capacity of the silicon nitride layers. The heat capacity of silicon nitride increases significantly in the measured temperature range [ZH04]. Therefore, the total amount of energy that flows from the laser-excited metal to the silicon nitride layers increases with base temperature.

inc. fluence [mJ/cm^2]	2.3 ± 0.4
abs. fluence [mJ/cm^2]	1.2 ± 0.2
abs. energy density [J/cm^3]	580 ± 100

Table 5.2: Incident and absorbed fluence as well as absorbed energy density for the experiments presented in Sec. 5.2.2. All quantities were calculated analogously to Table 5.1.
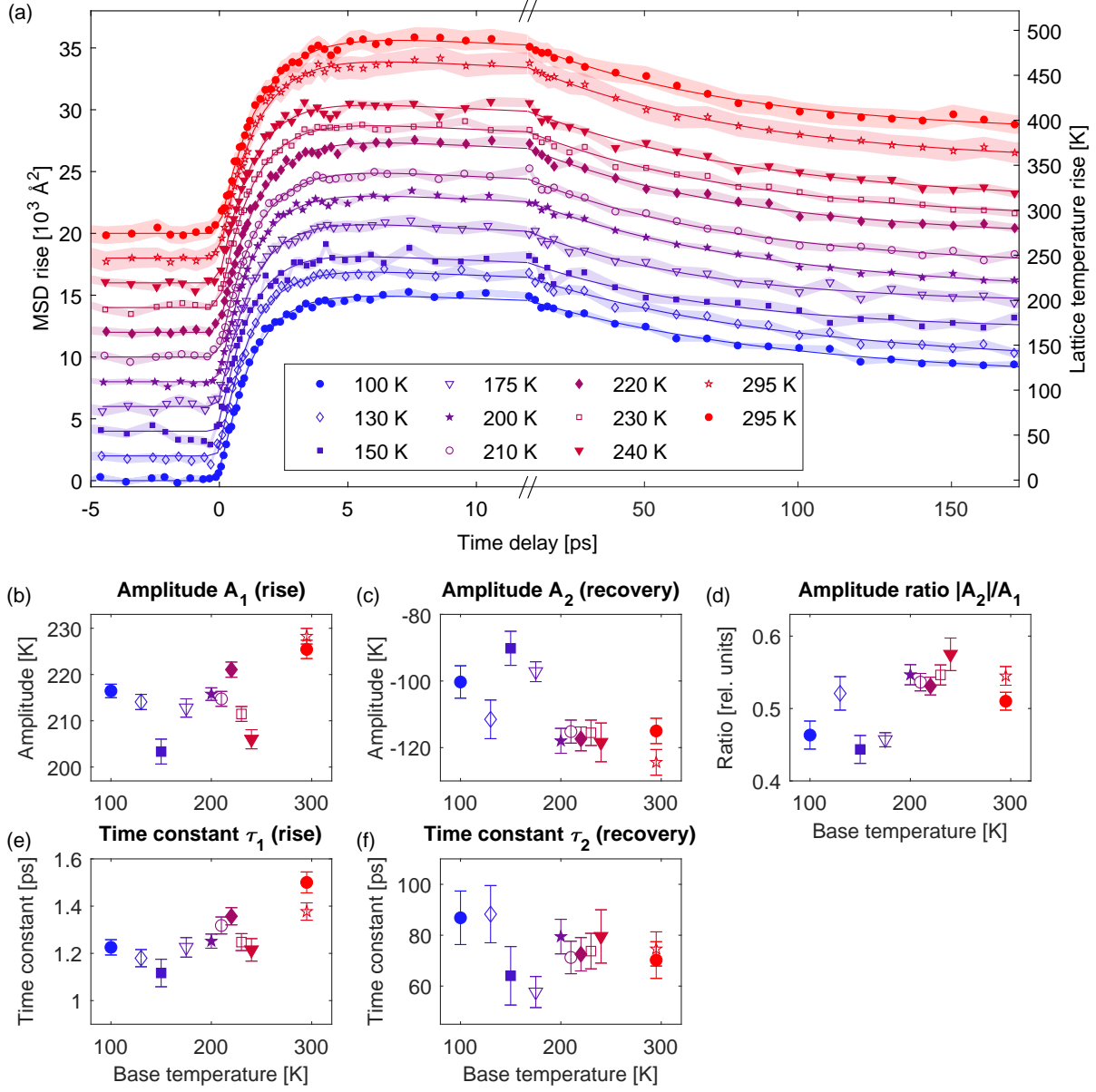
Figure 5.8: Lattice dynamics in terbium at different base temperatures. (a) MSD dynamics at different base temperatures. For clarity, the different curves are offset by $2\,\text{Å}$ per curve. Symbols represent experimental data and solid curves show the results of bi-exponential fits to the temperature dynamics. The shaded error bars represent the standard errors of the experimental data obtained from the global fitting routine. (b) Fit results for the amplitude of the lattice temperature rise (A_1). (c) Fit results for the amplitude of the recovery (A_2). (d) Ratio of the amplitudes $|A_2|/A_1$, which is a measure of the relative amplitude of the recovery. (e) Fit results for the time constant of the lattice temperature rise (τ_1). (f) Fit results for the time constant of the recovery (τ_2). Error bars in (b),(c),(e), and (f) are standard errors obtained from the bi-exponential fits. Error bars in (d) were calculated from the errors of A_1 and A_2.

In summary, the temperature-dependent measurements on terbium confirm the result of the previous section: clear signatures of the magnetization dynamics in the lattice dynamics are not observed. This is a surprising result because such signatures would be expected based on energy flow considerations, as discussed in Sec. 5.2.1. One reason for these discrepancies could be a nonthermal behavior of the spin system. For example, if the $4f$ spins demagnetized significantly less compared to a thermal scenario, less energy would flow to the spin system, resulting in less signatures in the lattice dynamics. An alternative explanation is that the measured area of the sample could have been in a non-ferromagnetic phase, either permanently or laser-induced. From SQUID measurements of the magnetic moment of two identical samples, it can be estimated that more than $50\,\%$ of the film is ferromagnetic. A more precise calculation is not possible, mostly because the area covered by the film can only be approximated. Therefore, it cannot be excluded that non-ferromagnetic areas exist. If such areas existed but were distributed evenly, e.g. as a non-magnetic layer close to the interface, then demagnetization signatures in the lattice dynamics would still be expected, albeit weaker. However, if such areas were distributed unevenly, predominantly at the measured area (see Fig. 5.3), it would lead to the absence of demagnetization signatures in the experimental data. To investigate this possibility further, a local probe of the magnetization would be required, for example using a Faraday microscope.

Alternatively, if the ground state of the system was not restored before the arrival time of the next pump pulse (i.e. within $250\,\mu$s), in particular if the ferromagnetic order was not restored, this would also explain the observations. It should be noted that in contrast to typical measurements of the magnetization dynamics, there was no magnetic field applied in the electron diffraction experiments. Therefore, upon cooling of the sample following laser excitation, a multi-domain state likely forms. If these domains comprise a large number of spins, no significant influence on the total spin energy and thus the microscopic energy flow is expected. However, in case the *local* re-ordering of the spin system – in particular the $4f$ spins – is not completed within $250\,\mu$s and significant short-range order remains, this would influence the microscopic energy flow dynamics when the next pulse arrives. To clarify if the absence of a magnetic field can delay the recovery of magnetic order, the magnetization recovery could be measured as a function of magnetic field strength or even without any magnetic field applied (on a single-domain sample).

5.3   Magnetization dynamics of terbium

Next, to gain insights into the magnetization dynamics of the sample and to compare them to the lattice dynamics, time-resolved (tr) magneto-optical Kerr effect (MOKE) measurements were performed on the terbium sample. With MOKE measurements in the visible wavelength range as employed here, the magnetization of the $5d$ states can be probed, because those states can be excited with visible photon energies (see also Fig. 5.1(a)). Here, the longitudinal MOKE geometry was employed, which means that the sample is magnetized in-plane and the plane of incidence of the probe beam is parallel to the magnetization. To magnetize the sample, a magnetic field of ~$280\,$mT was applied. The sample was pumped with $800\,$nm-light and probed with $400\,$nm-light. The angle of incidence of the probe beam was $26°$ with respect to the surface normal. Kerr rotation as a function of pump-probe delay was measured using a Wollaston prism and balanced photodiodes. A mechanical chopper in combination with

a boxcar integrator was employed to measure Kerr rotation with and without laser excitation almost simultaneously (pumped and unpumped signal). More details on the experimental setup are available in Ref. [Bor21].

The output voltage from the balanced photodetector is proportional to the intensity difference between s- and p-polarized light and is thus a sensitive measure of the polarization rotation of the probe beam. To minimize non-magnetic contributions to the signal, the magnetic field was alternated. The normalized magneto-optical contrast was then calculated as follows: first, low-frequency noise was determined as the difference of the unpumped signal from its average. The result was subtracted from the pumped signal. Next, the noise-corrected pumped signals for both magnetic field directions were subtracted. Finally, the resulting curve was normalized to the average of all data points before the arrival of the pump pulse, yielding the normalized MOKE signal.

Measurements were recorded with several different pump fluences. Table 5.3 presents the incident fluences as well as the corresponding absorbed fluences and energy densities. The absorptance of the sample was obtained via multilayer calculations [Win98], using the optical constants from Refs. [Ahm82; Luk15]. The result for the absorptance of the sample at 800 nm was 49 % for 26° incidence. Based on these calculations, an incident fluence of 2.5 mJ/cm^2 in the MOKE experiments corresponds to a very similar absorbed energy density compared with the diffraction experiments of Sec. 5.2.2. Consequently, those results can directly be compared with each other.

incident fluence [mJ/cm^2]	0.7	1.4	2.5	3.8	5.5	6.9
absorbed fluence [mJ/cm^2]	0.3	0.7	1.2	1.8	2.7	3.4
absorbed energy density [J/cm^3]	170	340	620	920	1340	1680

Table 5.3: Fluences and energy densities of the MOKE experiments. The incident fluences were calculated using Eq. 4 of Ref. [Har06]. The estimated error of the incident fluences is ~20 %.

The experimental tr-MOKE results for all fluences of Table 5.3 are presented in Fig. 5.9(a). For most fluences, a clear two-step decay of the MOKE signal is observed. The timescales are strongly fluence-dependent. To analyze the experimental results quantitatively, bi-exponential fits were performed in the range from -5 to 35 ps. The fit function was the same as in Chapter 3, and the time resolution was assumed to be 55 fs FWHM, based on Ref. [Bor21]. Since no systematic fluence-dependence of time zero was observed, the bi-exponential fit was repeated with time zero constrained to the average. The results for the amplitudes and time constants are presented in Fig. 5.9(b), (c), (e), and (f). The summed amplitudes, which correspond to the total drop of the MOKE signal, are presented in Fig. 5.9(d). The amplitude of the fast drop (A_1) increases linearly with fluence. In contrast, the amplitude of the second drop (A_2) first increases with fluence but stagnates at ~3 mJ/cm^2 incident fluence and decreases again. Note that the large error bars of the data at the highest fluence of 6.9 mJ/cm^2 indicate that for this fluence, the MOKE signal dynamics are better described by a single exponential instead of a bi-exponential drop.

Interestingly, as the fluence increases, the magneto-optical contrast is not completely quenched. Instead, it saturates at ~46 % of its pre-time zero value, which can be directly seen from the curves of Fig. 5.9(a) as well as from the summed amplitudes presented in Fig. 5.9(d). This puzzling behavior could have several reasons, which will be discussed in the following.
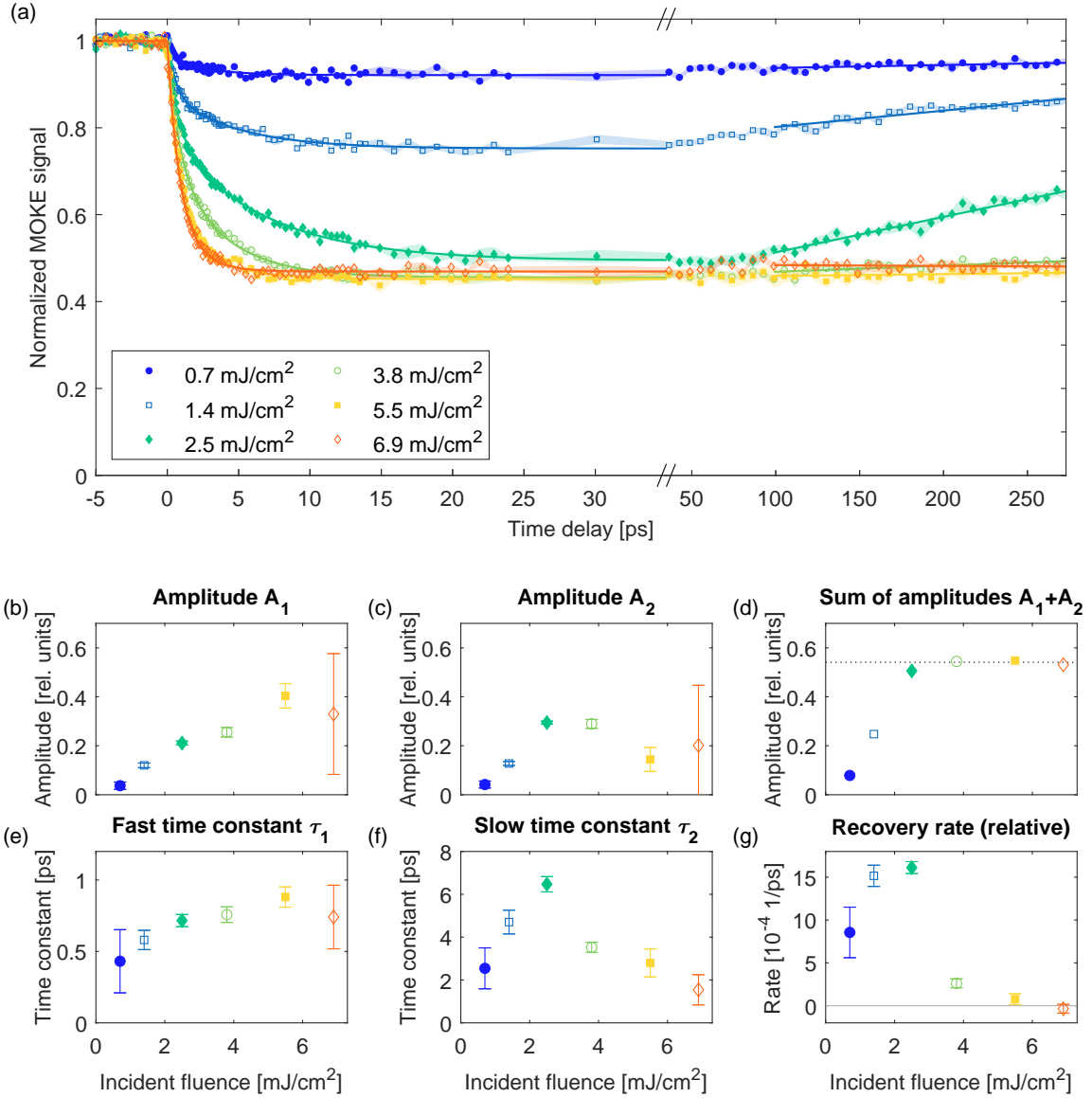
Figure 5.9: Time-resolved MOKE results for different incident fluences at a base temperature of 150 K. (a) Normalized MOKE signal as a function of pump-probe delay. Markers correspond to experimental data and shaded areas indicate their standard errors, calculated as the standard error of the average of several pump-probe scans. Solid curves on the left (delay range -5 to 35 ps) correspond to bi-exponential fit results. Solid lines on the right correspond to the results of linear fits to the recovery. (b) Amplitudes of the fast MOKE signal drop (A_1) from the bi-exponential fits as functions of incident fluence. (c) Amplitudes of the second, slower drop (A_2). (d) Sum of both amplitudes ($A_1 + A_2$). (e) Time constants of the fast MOKE signal drop (τ_1). (f) Time constants of the slow MOKE signal drop (τ_2). (g) Relative recovery rates, obtained from linear fits to the recovery in the range > 100 ps. The slope obtained from the linear fit was divided by the total amplitude of the MOKE signal decrease, $A_1 + A_2$. The error bars in (b), (c), and (e)-(g) correspond to the standard errors obtained from the fits.

In general, several scenarios can lead to such a saturation effect. First of all, a situation can arise in which some probed areas of the sample are not pumped. This can occur when the penetration depth of the probe beam is significantly larger than the penetration depth of the pump beam, or if the spot size of the pump beam is smaller than the spot size of the probe beam. The resulting MOKE signal, which is the average of the probed regions, would then contain contributions from unpumped regions. However, in the case here, there are two arguments against this scenario. First, the spot size diameter of the pump pulse on the sample was ∼9 times larger than that of the probe pulse. Second, the sample was a thin film with only 20 nm thickness, surrounded by insulating layers. The sample thickness is comparable to the penetration depth of 800 nm-light, which is around 27 nm based on Ref. [Ahm82]. It is therefore expected that the ferromagnetic layer can be heated completely by the pump pulse (and subsequent electron transport processes). Consequently, this first scenario is unlikely here.

Second, the saturation could be an intrinsic behavior of the sample, for example a bottleneck in angular momentum dissipation that hinders further demagnetization. However, magnetization dynamics of terbium were measured for several fluences in Ref. [Wie10] with time-resolved x-ray magnetic circular dichroism (XMCD) and complete demagnetization of the sample was observed. More recent, unpublished XMCD results by Gleich et al. [Gle] confirm this result. The main difference between MOKE and XMCD is that an XMCD experiment probes the 4f magnetism, while (visible) MOKE is sensitive to the 5d magnetism. Therefore, the XMCD and MOKE results would only be consistent if the 5d and the 4f magnetism behaved differently. However, the opposite has been reported for terbium [Fri20]. In addition, the 5d magnetization and the 4f magnetization would be expected to equilibrate eventually, either through indirect or direct coupling. The tr-MOKE data show no indication of such an equilibration. Therefore, this second scenario cannot explain the observations either.

Third, it is possible that the observed saturation of the magneto-optical contrast stems from the measurement technique. For example, it was pointed out by Cheskis et al. for the 3d ferromagnet nickel that in principle it is possible to obtain a situation in which the Stoner gap has fully collapsed, but the magneto-optical contrast is not suppressed completely [Che05]. In this scenario, the two spin types have vastly different temperatures, which causes different band filling effects for majority and minority optical transitions, thus leading to magneto-optical contrast. However, this scenario requires essentially no equilibration between majority and minority electrons, which is a questionable assumption on timescales of several hundreds of picoseconds. Another possibility is a contribution to the signal that does not stem from the magnetization and is not influenced by the pump pulse, but switches with the magnetic field. This would also explain the observations. However, it is unclear where such a contribution would come from.

In conclusion, the origin of the saturation of the MOKE signal remains an open question at this point. To elucidate its cause, further measurements are necessary. For example, different MOKE geometries and probe wavelengths could be employed to investigate influences of the measurement technique. Varying the pump wavelength and the base temperature could yield insights into contributions from the intrinsic sample behavior. In addition, an XMCD or extreme ultraviolet (XUV) MOKE experiment on the same sample would allow a direct comparison to the 4f spin dynamics. Understanding the origin of the saturation effect is required to quantitatively extract magnetization dynamics from the experimental results, in particular to obtain quantitative demagnetization amplitudes.

Having analyzed the amplitudes in detail, the timescales of the MOKE signal decrease are examined next. The time constants obtained from the bi-exponential fits are presented in Fig. 5.9(e) and (f). The fast time constant τ_1 increases linearly with fluence. In contrast, the second time constant τ_2 first increases significantly up to an incident fluence of $\sim 2.5\,\mathrm{mJ/cm^2}$ and then decreases again. The amplitude of the second drop A_2 behaves very similarly.

Interestingly, neither of the two time constants τ_1 or τ_2 corresponds to the observed time-scales of lattice heating (~ 1.1-$1.6\,\mathrm{ps}$, see Figs. 5.5 and 5.8) – τ_1 is a bit faster and τ_2 is much slower. Due to the saturation effects discussed above, at this point, it is not possible to say with certainty whether the MOKE dynamics include a contribution from measurement-related effects. Nevertheless, given that electron thermalization typically occurs on the timescale of tens to hundreds of femtoseconds and the lattice heating occurs on timescales of ~ 1.1-$1.6\,\mathrm{ps}$ (see Figs. 5.5 and 5.8), it is unlikely that the dynamics associated with the slower time constant τ_2 are influenced by measurement-related effects such as band filling or any lattice-related effect. Therefore, it can be assumed that τ_2 reflects magnetization dynamics of the $5d$ spins.

In addition to the bi-exponential fits to the dynamics at early times, the recovery occurring at later times was also analyzed. For this, linear fits to the data in the range $> 100\,\mathrm{ps}$ were performed, analogously to the linear fits employed in Sec. 5.2.1. Also here, the recovery rate was divided by the amplitude of the decrease, in this case the sum $A_1 + A_2$. The resulting relative recovery rate allows a direct comparison between different fluences. The results are presented in Fig. 5.9(g). First, the relative recovery rate increases with fluence, before it drops sharply at an incident fluence between $2.5\,\mathrm{mJ/cm^2}$ and $3.8\,\mathrm{mJ/cm^2}$ and reaches zero (no recovery) at fluences of $5.5\,\mathrm{mJ/cm^2}$ and above. This can either be due to heating of the sample well above the Curie temperature, or to an effect of transient domain formation, as discussed in Sec. 4.2.3.4 for the $3d$ ferromagnets. A comparison to the lattice temperature results presented in Sec. 5.2.2 indicates that the sample – at least its lattice – heats up beyond the Curie temperature for the higher fluences. In fact, already an incident fluence of $2.5\,\mathrm{mJ/cm^2}$ is expected to correspond to heating well beyond the Curie temperature (compare absorbed energy densities given in Tables 5.2 and 5.3). However, it should be noted that fluence determination in pump-probe experiments is often difficult and can thus be imprecise. Additional uncertainty stems from the different wavelengths employed in the MOKE and diffraction experiments, which requires optical constants from literature for the comparison. It is thus likely that the observed recovery for $2.5\,\mathrm{mJ/cm^2}$ is due to these sources of error. Fluences of $3.8\,\mathrm{mJ/cm^2}$ and above likely correspond to heating above the Curie temperature.

In addition to varying the pump fluence, varying the base temperature can provide further insights. In particular, such measurements enable a direct comparison with the temperature-dependent lattice dynamics presented in Sec. 5.2.2. Therefore, tr-MOKE measurements were performed at four different base temperatures, with an incident fluence of $2.5\,\mathrm{mJ/cm^2}$. This fluence was chosen to obtain a similar absorbed energy density as in the diffraction experiments (see Tables 5.2 and 5.3). The measurement results are presented in Fig. 5.10.

The base temperature visibly affects both the total amplitude as well as the timescales. Analogous to the fluence-dependent measurements, bi-exponential fits were performed. The results are presented in Fig. 5.10(b)-(f). Both the amplitudes and the timescales are base-temperature-dependent. The amplitude of the fast component A_1, presented in Fig. 5.10(b), decreases with increasing base temperature. In contrast, the amplitude of the slow component A_2, presented in Fig. 5.10(c), first increases with base temperature but decreases again close
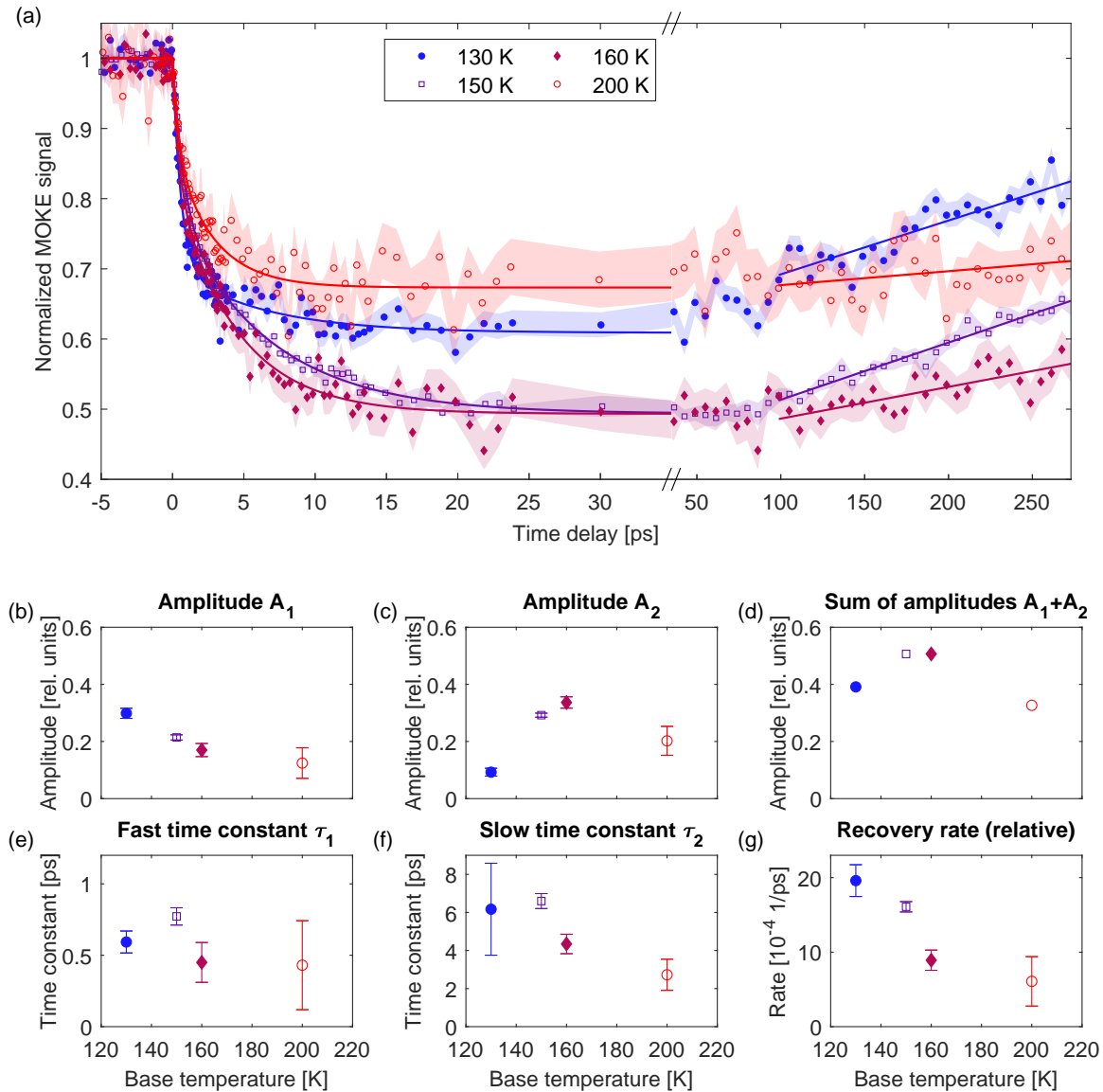
Figure 5.10: Time-resolved MOKE results for different base temperatures. (a) Normalized MOKE signal as a function of pump-probe delay. Markers correspond to experimental data and shaded areas are standard errors of the experimental data. For the data recorded at 150 K, the errors were calculated as the standard error of the average of several scans. For the other temperatures, only one scan was recorded. In this case, the errors were taken to be the same for all points of the scan and were calculated from the standard error of the data before the arrival of the pump laser pulse. The solid curves on the left (delay range -5 to 35 ps) correspond to bi-exponential fit results. The solid lines on the right correspond to the results of linear fits to the recovery dynamics. (b) Amplitudes of the fast MOKE signal drop A_1 (bi-exponential fit results) as functions of base temperature. (c) Amplitudes of the slow MOKE signal drop A_2. (d) Summed amplitudes $A_1 + A_2$. (e) Fast time constants τ_1. (f) Slow time constants τ_2. (g) Relative recovery rates obtained from linear fits to the recovery (delay range > 100 ps). To obtain the relative rate, the fit result for the slope was divided by the total amplitude of the MOKE signal decrease, $A_1 + A_2$. All errors in (b),(c), and (e)-(g) correspond to standard errors from the fits.

to the Curie temperature. The same holds for the total MOKE signal decrease (sum of both amplitudes), presented in Fig. 5.10(d). Regarding the time constant of the fast drop τ_1, no dependence on base temperature is observed, as presented in Fig. 5.10(e). In contrast, the time constant of the slow drop τ_2 decreases as the base temperature increases, as presented in Fig. 5.10(f).

Interestingly, also the relative recovery rate depends on the base temperature. As the base temperature increases, the recovery becomes slower. This is in stark contrast to the lattice dynamics, which show an *increase* of the recovery rate[1]. To be precise, such a direct comparison of the recovery rates requires considering that the magnetization $M(T)$ is non-linear in temperature (see Fig. 5.3(c)). For temperatures below the Curie temperature T_C, $M(T)$ is a concave function. Therefore, the relative magnetization change per temperature change, $|\Delta M|/[M(T_{\text{base}})\Delta T]$, increases with base temperature (T_{base}) as long as $\Delta T + T_{\text{base}} < T_C$. This condition is fulfilled because the observation of a magnetization recovery implies spin temperatures below T_C. In a thermal situation, the recovery rate of the magnetization would thus be expected to increase with base temperature, like the recovery rate of the lattice. This is in contrast to the experimental results. Consequently, the non-linearity of $M(T)$ cannot explain the observations. Instead, the slow-down of the MOKE signal recovery as the base temperature approaches T_C is an indication of a nonthermal behavior of the spin system. Possibly, a similar situation as discussed for the 3d ferromagnets could arise (see Sec. 4.2.3.4): following laser excitation, different magnetic domains could transiently form, which would delay the recovery of the macroscopic magnetization. In such cases, the magnetization recovery is decoupled from the lattice cooling. Instead, it depends on how fast the different domains align with each other. It is likely that this realignment would take longer close to T_C, with the system being already close to the transition to a disordered state. Such a scenario could therefore explain the decrease of the recovery rate with temperature.

In general, the strong temperature dependence of the tr-MOKE signal implies that any comparison to literature should consider the base temperature. The only fluence-dependent demagnetization of terbium in literature [Wie10] was measured at 90 K, which limits the comparability. Qualitatively, the XMCD results of Ref. [Wie10] exhibit the same fluence-dependent behavior as here, with a two-step behavior for low and intermediate fluences that becomes faster and turns into a one-step reduction for high fluences. The timescales as functions of fluence are even quantitatively similar but the absolute values of the fluences differ significantly. This may be explained by the different base temperatures and the different sample geometries. Another experiment on terbium, which employed photoemission, showed a one-step demagnetization of both 4f and 5d spins on similar timescales of 400 fs and 300 fs, respectively [Fri20]. These findings differ significantly from the XMCD results of Refs. [Wie10; Wie11]. Also the tr-MOKE results presented in this work exhibit generally slower dynamics than observed in Ref. [Fri20] (see Figs. 5.9 and 5.10). However, since only one fluence is presented in Ref. [Fri20], a detailed comparison to those results requires a better understanding of the saturation effect in the tr-MOKE signal first.

In summary, the tr-MOKE measurements on terbium yield strongly fluence-dependent and base-temperature-dependent results. In addition, a saturation of the MOKE signal decrease with increasing laser fluence was observed, the origin of which is unclear. Further studies of this

---

[1]The recovery amplitude increases (see Fig. 5.8(c)), note the negative sign) together with a base-temperature-independent recovery timescale (Fig. 5.8(f)). This corresponds to an increase of the recovery rate.

saturation effect are necessary in order to be able to quantitatively relate the tr-MOKE results to the magnetization dynamics of the sample. For example, different MOKE geometries or a different technique like XMCD could be employed, and the saturation effect could be studied for different base temperatures. Despite this open question, the data presented here already yield valuable insights into the non-equilibrium dynamics of the material: for most fluences, a two-step behavior is observed, with a slow timescale on the order of few picoseconds that has no corresponding timescale in the lattice dynamics. This points towards a decoupling of (total) spin energy and $5d$ magnetization on ultrafast timescales, since any significant energy change in the spin system is expected to leave a trace in the lattice temperature dynamics. Such decoupling is only possible for nonthermal states of the spin system. To confirm this supposition, fluence-dependent measurements of both lattice and magnetization dynamics could be employed. Another indication of nonthermal $5d$ spins comes from the recovery of the MOKE signal: it slows down with increasing base temperature, which is opposite to the base-temperature-dependence of the lattice recovery.

5.4   Towards a quantitative understanding of the microscopic energy flow

In the last two sections, experimental results at different base temperatures were presented and deviations from expectations based on a thermal picture of the ultrafast dynamics (e.g. a 3TM) were identified. To investigate these deviations further, a direct comparison of the experimentally measured amplitudes with thermal equilibrium can be made, without assuming any model for the dynamics. This comparison employs the equilibrium relationships between spin energy, temperature, and magnetization. Figure 5.11(a) and (b) present the temperature-dependent heat capacity and magnetization of terbium, respectively. From the heat capacity presented in Fig. 5.11(a), the temperature rise as a function of absorbed energy density can be calculated by integrating the heat capacity curve. As an example, the yellow shaded area corresponds to an absorbed energy density of $200 \, \mathrm{J/cm^3}$ at a base temperature of $100 \, \mathrm{K}$. In this case, after equilibration between all subsystems, the sample temperature is expected to be around $200 \, \mathrm{K}$. Figure 5.11(c) presents the expected temperature rise of the sample as a function of base temperature for several absorbed energy densities. For a constant absorbed energy density, the temperature rise depends strongly on the base temperature. Signatures of the Curie temperature at ~$220 \, \mathrm{K}$ are clearly present. The details depend on the absorbed energy density, however, what is common to all temperatures are pronounced amplitude differences below the Curie temperature and a flattening of the temperature-dependence above. Based on results on dysprosium from Ref. [Rep16], it is reasonable to assume that the absorption of the sample is (approximately) temperature-independent. In this case, the absorbed energy density would be constant for different base temperatures. Pronounced amplitude changes with temperature would then be expected in the lattice dynamics. However, the comparison with the experimental results of Sec. 5.2.2, presented in Fig. 5.11(e), shows that this is not the case. The final lattice temperature rise stays nearly constant as a function of base temperature. The comparison thus reveals discrepancies from the thermal behavior of ferromagnetic terbium.

Analogous predictions based on thermal equilibrium can also be made for the demagnetization amplitude. For this, the calculated temperature rise ΔT can be converted into mag-
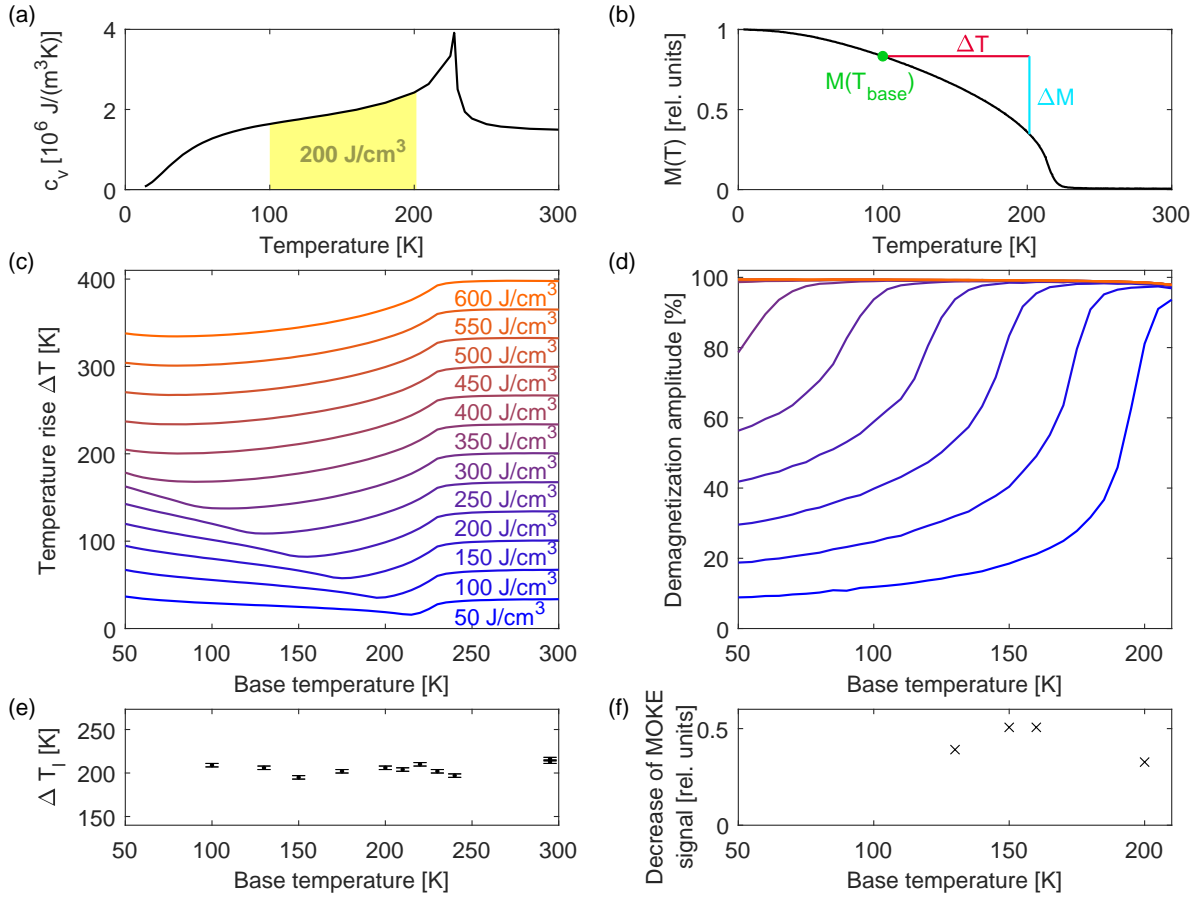
Figure 5.11: Expected trends in the base-temperature dependent measurements, based on equilibrium properties of terbium. (a) Heat capacity of terbium from Ref. [JSS57], which was employed to calculate the temperature rise corresponding to a certain absorbed energy density. As an example, the yellow shaded area represents an absorbed energy density of $200\,\mathrm{J/cm^3}$, starting from a base temperature of $100\,\mathrm{K}$. (b) Temperature-dependent magnetization curve of the terbium samples measured with a SQUID (also shown in Fig. 5.3(c)). Continuing the example of Panel (a), the green dot marks the equilibrium magnetization at $100\,\mathrm{K}$ and the red line shows the temperature rise ΔT for an absorbed energy density of $200\,\mathrm{J/cm^3}$. The blue line shows the corresponding magnetization decrease ΔM. (c) Expected temperature rise (after equilibration of all subsystems) as a function of base temperature. Curves for several absorbed energy densities are presented. The data were calculated using the heat capacity of Panel (a). (d) Expected demagnetization amplitude (after equilibration of all subsystems) as a function of base temperature. Curves for the same absorbed energy densities as in Panel (c) are presented. The demagnetization amplitude relative to the equilibrium value ($\Delta M/M(T_{\mathrm{base}})$) was calculated from the magnetization curve presented in Panel (b) and the calculated temperature rise ΔT from Panel (c). (e) Experimental results for the lattice temperature rise at different base temperatures. The data points correspond to the final lattice temperature rise (before the recovery sets in) and were obtained from single exponential fits in the range from -5 to 12 ps. The temperature scale is the same as in Panel (c) to facilitate the comparison. (f) Amplitude of the MOKE signal decrease (relative units) as a function of base temperature. The data presented here correspond to the sum of the two amplitudes A_1 and A_2 from the bi-exponential fits described in Sec. 5.3 (also presented in Fig. 5.10(d)).

netization reduction ΔM, employing the temperature-dependent magnetization curve. This is illustrated in Fig. 5.11(b). Finally, the relative demagnetization amplitude can be calculated as $\Delta M/M(T_{\text{base}})$. The results as functions of base temperature are presented in Fig. 5.11(d). The absorbed energy densities are the same as in Fig. 5.11(c). Based on this calculation, the demagnetization amplitude is expected to rise strongly as the base temperature approaches the Curie temperature. However, in the experiment, the base-temperature-dependent MOKE signal behaves differently. This is presented in Fig. 5.11(f), which shows the relative amplitude of the MOKE signal reduction as a function of base temperature. In particular, the measurement at 200 K, which is closest to the Curie temperature, exhibits the smallest amplitude. Assuming that the observed saturation effect is temperature-independent, this result disagrees with the thermal equilibrium case.

In summary, the measurements presented in this chapter yielded several results that are at odds with a thermal picture of the ultrafast energy flow. First of all, no clear signatures of the magnetization dynamics were observed in the lattice dynamics, neither in the measurements on terbium and gadolinium in Sec. 5.2.1 nor in the detailed base-temperature-dependent measurements on terbium in Sec. 5.2.2. Second, the amplitudes of both lattice dynamics and MOKE signal do not agree with the expectations based on equilibrium relationships either. Third, the recovery rate of the magnetization decreases close to the Curie temperature, opposite to the lattice behavior. These results point towards rather complex, nonthermal energy flow on ultrafast timescales. In fact, signatures of nonthermal behavior have been reported in literature for other elemental 4f metals: transient strain analyses of laser-excited gadolinium [Koc17] and dysprosium [Rep16] showed a long-lasting non-equilibrium between spin and phonon subsystems, with initially relatively low temperatures of the spin system. In addition, the cooling of the spin system in dysprosium was found to be delayed for base temperatures close to the magnetic transition [Rep16], which is in agreement with the base-temperature dependence of the MOKE signal recovery observed in this work (Fig. 5.10(g)). Furthermore, another experiment on dysprosium observed a mismatch between absorbed energy and demagnetization amplitude [Thi17], which is also indicative of a long-lasting non-equilibrium between different subsystems.

A detailed microscopic understanding of such complex nonthermal behaviors requires experiments on all subsystems and with several experimental conditions (e.g. temperatures and fluences). This work provides a detailed view on the ultrafast lattice dynamics in gadolinium and terbium, complemented by measurements that probe the 5d magnetization of terbium. In the future, the results for the lattice could be expanded by recording a larger experimental dataset, systematically varying both base temperature and fluence. For better comparability with other experiments, these experiments should ideally be performed with 800 nm pump wavelength. At the same time, tracking the optical absorption as a function of base temperature would be beneficial, for example by simultaneously recording transmission and absorption as functions of temperature. This would allow determining absorbed energy densities more precisely to eliminate any effects of absorption variations on the measured amplitudes. In addition, the equilibrium magnetization could be probed locally to quantitatively determine the magnetization of the areas that are measured in diffraction experiments, for example using Faraday rotation. Furthermore, the tr-MOKE experiments could be expanded, e.g. by recording fluence-dependent measurements at a number of base temperatures. Moreover, the origin of the saturation observed in the MOKE experiments needs to be investigated in order to gain detailed, quantitative results for the 5d spin dynamics. Finally, further insights into the ultra-

fast responses of 4f magnets could also be gained by time-resolved diffraction experiments on single-crystalline samples, especially in view of strong phonon-magnon hybridization observed in terbium, but not in gadolinium [Liu21]. Such experiments could yield detailed information on transient phonon populations and their connection to magnetic degrees of freedom. Likely, only a systematic combination of different probing methods and different experimental conditions will enable a quantitative understanding of the energy flow dynamics and allow to fully disentangle the microscopic mechanisms behind the complex ultrafast responses of 4f ferromagnets.

Chapter 6

Summary and outlook

In this work, femtosecond electron diffraction was employed to reveal ultrafast lattice dynamics in several material classes: the layered semiconductor black phosphorus, the itinerant ferromagnets iron, cobalt, nickel, and the localized (Heisenberg) ferromagnets gadolinium and terbium.

Black phosphorus, despite consisting of only one element, features a rather complex crystal structure (4 atoms per primitive unit cell) and thus has a large number of optical phonon branches (9). Its ultrafast lattice dynamics are governed by strong coupling of electrons to those optical phonons, in combination with pronounced phase-space constraints imposed primarily by the electronic structure. Following laser excitation, these characteristics of the material lead to a long-lasting nonthermal state of the lattice. Due to the in-plane anisotropic structure of black phosphorus, the transient nonthermal phonon population manifests not only in the overall MSD dynamics but also in a different evolution of the armchair and zigzag MSDs: the anisotropy between the armchair and zigzag MSDs is transiently reduced. On a timescale of tens of picoseconds, thermal equilibrium of the lattice is restored via phonon-phonon scattering. The observed transient nonthermal state of the lattice can be expected to manifest also in transient changes of other properties, e.g. thermal or electrical conductivities, or thermal coupling across interfaces. Therefore, the results presented in this work are directly relevant for applications of black phosphorus in non-equilibrium conditions, e.g. as saturable absorber [Sot15], in photocatalysis [She15], and in functional van der Waals heterostructures [Liu17].

In ferromagnets, besides the electron and lattice subsystems, also the magnetic order plays a role in the ultrafast dynamics of the material. In this work, the interplay between these different subsystems on ultrafast timescales was studied, in particular the relationship between lattice and spin dynamics. Experiments were performed for two different classes of magnetic materials: the itinerant $3d$ ferromagnets iron, cobalt, and nickel, as well as the $4f$ ferromagnets terbium and gadolinium, whose magnetic moments are much more localized.

In the elemental $3d$ ferromagnets, which demagnetize on timescales of few hundred femtoseconds at most, magnetization dynamics are governed by electron-spin coupling [Bea96]. In this work, the ultrafast lattice response to laser excitation was investigated using femtosecond diffraction. In order to gain insights into the microscopic energy flow, experimental results were combined with DFT calculations and several energy flow models. In particular, energy-conserving ASD simulations were employed to describe the coupled energy flow between electrons, spins, and phonons, allowing to directly simulate non-equilibrium (including nonthermal) states of the spin system. The direct comparison between a conventional TTM and energy-conserving ASD simulations revealed that the lattice is very sensitive to the spin dynamics: energy flow into and

out of the spin system slows down the ultrafast lattice response profoundly. The cause lies in the energy cost of demagnetization: as the spins demagnetize, energy is drained from the electrons. In contrast, when the magnetization recovers, energy is again released from the spin system and eventually mostly transferred to the lattice. It was shown here that energy-conserving ASD simulations provide a quantitative description of this microscopic energy flow: they yield a very good description of experimental data, in particular excellent agreement with the ultrafast lattice responses measured in this work. In addition, the ASD simulations revealed that the spin system is not always in a thermal state, which has the consequence that magnetization and spin energy are not related anymore by their equilibrium relationship – they decouple. In particular, for strong demagnetization (more than $\sim 50\,\%$), nonthermal behavior of the spins was found to persist on picosecond timescales. This means that a thermal model like the 3TM is then not applicable.

The results of this work highlight the importance of considering the energy content of the spin system in *any* model of ultrafast demagnetization. Here, quantitative agreement to experimental results was achieved with energy-conserving ASD simulations, demonstrating that such simulations offer a general and consistent description of the microscopic energy flow in all elemental $3d$ ferromagnets. The general conclusions on the ultrafast energy flow are expected to hold for other magnetic materials as well, including ferrimagnets and antiferromagnets. Furthermore, the results presented here serve as a basis for the quantitative description of more complex heterostructures containing iron, cobalt, or nickel, e.g. spintronic multilayer structures.

For the $4f$ ferromagnets terbium and gadolinium, detailed time-resolved diffraction results were provided in this work. Lattice dynamics were studied as a function of fluence and base temperature, with a particular focus on terbium, for which a detailed base-temperature dependence of the lattice dynamics was presented. Furthermore, the results for the lattice dynamics were complemented by time-resolved MOKE experiments on terbium, which can probe $5d$ magnetization dynamics. In the measurements presented in this work, several indications of a complex nonthermal response to laser excitation were identified: first of all, neither timescales nor amplitudes of the ultrafast lattice heating showed any clear signatures of the magnetization dynamics, despite the large magnetic heat capacities of both materials. Second, the temperature-dependent MOKE results for terbium also point towards a nonthermal response, as evidenced both by the recovery rates and by the amplitudes of the MOKE signal. This work provides detailed results for the ultrafast lattice responses of terbium and gadolinium and thus contributes information that cannot be obtained e.g. by magnetization-sensitive techniques. Therefore, the results presented here are an important step towards a full understanding of the complex ultrafast responses of $4f$ ferromagnets to laser excitation, which requires detailed experimental knowledge of all subsystems.

Based on this work on the elemental $3d$ and $4f$ ferromagnets, future studies could investigate the ultrafast lattice response and its connection to the magnetization dynamics in other technologically relevant magnetic materials. One emerging class of magnetic materials with interesting properties is magnetic layered van der Waals materials, for example CrI_3, $CrGeTe_3$, Fe_3GeTe_2, $FePS_3$, and $Cr_2Ge_2Te_6$. In some of these materials, magnetic order can even survive down to the monolayer limit [Lee16; Hua17; Fei18]. Naturally, such magnetic 2D materials are an important addition to the set of building blocks for van der Waals heterostructures. Some of these magnetic 2D materials have been shown to exhibit pronounced spin-lattice coupling, for example CrI_3 [WLY18] and $Cr_2Ge_2Te_6$ [Tia16]. This suggests that in any application involving

the manipulation of magnetic degrees of freedom, the lattice response needs to be considered as well, and lattice degrees of freedom may even be used to control magnetic order. Hence, a detailed understanding of the coupling between those two subsystems is required, which can be achieved with femtosecond electron diffraction studies. In general, the coupling of the lattice to other degrees of freedom is of interest also for another reason: successful device design requires thermal management. It is necessary to understand how fast and in which layers of a heterostructure heat is created following the excitation/injection of hot carriers, which is information that femtosecond electron diffraction can provide.

In addition to exploring ultrafast dynamics of novel 2D magnets, femtosecond electron diffraction is also a suitable tool to investigate spintronic heterostructures. Often, transfer and/or coupling processes across interfaces are employed to achieve the desired functionalities of such heterostructures, e.g. magnetic switching [Man14a], spin-current detection [Sai06], or production of terahertz radiation [Sei16]. Femtosecond electron diffraction allows to track the microscopic lattice energy content of different constituent materials quantitatively. In particular, it is possible to determine whether carriers are transferred between layers because they invariably heat up the respective layer via electron-phonon scattering. Time-resolved diffraction can thus provide important complementary insights for a better understanding of the microscopic processes in such heterostructures. The detailed experimental results on elemental $3d$ and $4f$ ferromagnets presented in this work provide a basis for understanding more complex structures containing these materials because a comparison to these results allows to better disentangle intra- and interlayer coupling processes in heterostructures.

On the instrumentation side, future developments could include broadening the available spectrum of excitation wavelengths to the terahertz (THz) range. THz light offers the possibility to directly and coherently excite specific phonon [Rin07; Man14b; Man15; Mäh18] or magnon modes [Kam11; Kub14]. It can thus create very different initial non-equilibrium states compared to excitation with visible wavelengths, especially for materials with a band gap (in which the THz excitation cannot excite any electronic transitions). This offers the possibility of directly studying e.g. the interplay of lattice and magnetic degrees of freedom [Mäh18], anharmonic coupling between different phonon modes [Man15], and the influence of specific phonon modes on the electronic structure [Rin07]. Time-resolved diffraction is an important tool to investigate THz-induced dynamics since it allows to directly and quantitatively resolve the evolution of the structural changes induced by THz excitation [Man14b].

In addition to the tunability of the excitation conditions, also the probe is an important tuning knob. Additional information on a sample's ultrafast response can be gained by combining different probes in one experiment, e.g. by adding an optical probe to the diffraction setup. In view of the difficulty of reproducing the exact same excitation conditions in different experiments, probing several quantities in the same experiment would allow a much more precise comparison and thus a more detailed understanding of the coupled dynamics of different subsystems. Perspectively, looking at different aspects of the sample's response (i.e. using different probes), in combination with inducing different non-equilibrium dynamics (i.e. using different excitation conditions), will allow disentangling the complex non-equilibrium response of solids further, enabling ever deeper insights into the fundamental coupling mechanisms that govern many of their properties.

Bibliography

[Afs20]   M. Afshari, P. Krumey, D. Menn, M. Nicoul, F. Brinks, A. Tarasevitch, and K. Sokolowski-Tinten, *Time-resolved diffraction with an optimized short pulse laser plasma X-ray source*, Struct. Dyn. **7**, 014301 (2020).

[Agr84]   M. B. Agranat, S. I. Ashitkov, A. B. Granovskii, and G. I. Rukman, *Interaction of picosecond laser pulses with the electron, spin, and phonon subsystem of nickel*, Sov. phys. JETP **59**, 804–806 (1984).

[Ahm82]   N. Ahmed-Mokhtar, J. Pétrakian, R. Philip, R. Fraisse, and B. Lazarides, *Comparative study of magneto-optical resonance in heavy rare earth metals*, Thin Solid Films **88**, 177–188 (1982).

[Aka89]   T. Akai, S. Endo, Y. Akahama, K. Koto, and Y. Marljyama, *The crystal structure and oriented transformation of black phosphorus under high pressure*, High Press. Res. **1**, 115–130 (1989).

[AKP74]   S. I. Anisimov, B. L. Kapeliovich, and T. L. Perel'man, *Electron emission from metal surfaces exposed to ultrashort laser pulses*, Sov. phys. JETP **39**, 375–377 (1974).

[All87]   P. B. Allen, *Theory of thermal relaxation of electrons in metals*, Phys. Rev. Lett. **59**, 1460–1463 (1987).

[APS19]   L. A. Akashev, N. A. Popov, and V. G. Shevchenko, *Optical Properties of Gadolinium in the Condensed State*, High Temp. **57**, 49–53 (2019).

[Atx09]   U. Atxitia, O. Chubykalo-Fesenko, R. W. Chantrell, U. Nowak, and A. Rebei, *Ultrafast Spin Dynamics: The Effect of Colored Noise*, Phys. Rev. Lett. **102**, 057203 (2009).

[Atx10]   U. Atxitia, O. Chubykalo-Fesenko, J. Walowski, A. Mann, and M. Münzenberg, *Evidence for thermal mechanisms in laser-induced femtosecond spin dynamics*, Phys. Rev. B **81**, 174401 (2010).

[AW20]   B. Andres and M. Weinelt, *Spin-resolved electronic structure of 3d transition metals during ultrafast demagnetization*, J. Magn. Magn. Mater. **501**, 166475 (2020).

[Bal08]   T. Balashov, A. F. Takács, M. Däne, A. Ernst, P. Bruno, and W. Wulfhekel, *Inelastic electron-magnon interaction and spin transfer torque*, Phys. Rev. B **78**, 174404 (2008).

[Bar06]   M. Bargheer, N. Zhavoronkov, M. Woerner, and T. Elsaesser, *Recent Progress in Ultrafast X-ray Diffraction*, ChemPhysChem **7**, 783–792 (2006).

[BCO10]   M. Battiato, K. Carva, and P. M. Oppeneer, *Superdiffusive Spin Transport as a Mechanism of Ultrafast Demagnetization*, Phys. Rev. Lett. **105**, 027203 (2010).

[Bea96] E. Beaurepaire, J.-C. Merle, A. Daunois, and J.-Y. Bigot, *Ultrafast Spin Dynamics in Ferromagnetic Nickel*, Phys. Rev. Lett. **76**, 4250–4253 (1996).

[Big05] J.-Y. Bigot, M. Vomir, L. Andrade, and E. Beaurepaire, *Ultrafast magnetization dynamics in ferromagnetic cobalt: The role of the anisotropy*, Chem. Phys. **318**, 137–146 (2005).

[Bon18] M. Bonilla, S. Kolekar, Y. Ma, H. C. Diaz, V. Kalappattil, R. Das, T. Eggers, H. R. Gutierrez, M.-H. Phan, and M. Batzill, *Strong room-temperature ferromagnetism in VSe_2 monolayers on van der Waals substrates*, Nat. Nanotechnol. **13**, 289–293 (2018).

[Bor21] M. Borchert, C. von Korff Schmising, D. Schick, D. Engel, S. Sharma, S. Shallcross, and S. Eisebitt, *Uncovering the role of the density of states in controlling ultrafast spin dynamics*, arXiv:2008.12612 (2021).

[Büh18] K. Bühlmann, R. Gort, G. Salvatella, S. Däster, A. Fognini, T. Bähler, C. Dornes, C. A. F. Vaz, A. Vaterlaus, and Y. Acremann, *Ultrafast demagnetization in iron: Separating effects by their nonlinearity*, Struct. Dyn. **5**, 044502 (2018).

[Büh20] K. Bühlmann, G. Saerens, A. Vaterlaus, and Y. Acremann, *Detection of femtosecond spin voltage pulses in a thin iron film*, Struct. Dyn. **7**, 065101 (2020).

[Caf05] A. P. Caffrey, P. E. Hopkins, J. M. Klopf, and P. M. Norris, *Thin Film Non-Noble Transition Metal Thermophysical Properties*, Microscale Thermophys. Eng. **9**, 365–377 (2005).

[Cao18] Y. Cao, V. Fatemi, S. Fang, K. Watanabe, T. Taniguchi, E. Kaxiras, and P. Jarillo-Herrero, *Unconventional superconductivity in magic-angle graphene superlattices*, Nature **556**, 43–50 (2018).

[Car08] E. Carpene, E. Mancini, C. Dallera, M. Brenna, E. Puppin, and S. De Silvestri, *Dynamics of electron-magnon interaction and ultrafast demagnetization in thin iron films*, Phys. Rev. B **78**, 174422 (2008).

[Car15] E. Carpene, H. Hedayat, F. Boschini, and C. Dallera, *Ultrafast demagnetization of metals: Collapsed exchange versus collective excitations*, Phys. Rev. B **91**, 174414 (2015).

[Car21] F. Caruso, *Nonequilibrium Lattice Dynamics in Monolayer MoS_2*, J. Phys. Chem. Lett. **12**, 1734–1740 (2021).

[CG71] J. Crangle and G. M. Goodman, *The Magnetization of Pure Iron and Nickel*, Proc. Math. Phys. Eng. Sci. **321**, 477–491 (1971).

[Cha12] R. P. Chatelain, V. R. Morrison, C. Godbout, and B. J. Siwick, *Ultrafast electron diffraction with radio-frequency compressed electron pulses*, Appl. Phys. Lett. **101**, 081901 (2012).

[Cha14] R. P. Chatelain, V. R. Morrison, B. L. M. Klarenaar, and B. J. Siwick, *Coherent and Incoherent Electron-Phonon Coupling in Graphite Observed with Radio-Frequency Compressed Ultrafast Electron Diffraction*, Phys. Rev. Lett. **113**, 235502 (2014).

[Che05] D. Cheskis, A. Porat, L. Szapiro, O. Potashnik, and S. Bar-Ad, *Saturation of the ultrafast laser-induced demagnetization in nickel*, Phys. Rev. B **72**, 014437 (2005).

[Che15]   A. Chernikov, C. Ruppert, H. M. Hill, A. F. Rigosi, and T. F. Heinz, *Population inversion and giant bandgap renormalization in atomically thin WS$_2$ layers*, Nat. Photonics **9**, 466–470 (2015).

[Che19]   Z. Chen, J. Dong, E. Papalazarou, M. Marsi, C. Giorgetti, Z. Zhang, B. Tian, J.-P. Rueff, A. Taleb-Ibrahimi, and L. Perfetti, *Band Gap Renormalization, Carrier Multiplication, and Stark Broadening in Photoexcited Black Phosphorus*, Nano Lett. **19**, 488–493 (2019).

[Coe10]   J. M. D. Coey, *Magnetism and Magnetic Materials*, Cambridge University Press (2010).

[Deb13]   P. Debye, *Interferenz von Röntgenstrahlen und Wärmebewegung*, Ann. Phys. **348**, 49–92 (1913).

[DHM68]   H. Danan, A. Herr, and A. J. P. Meyer, *New Determinations of the Saturation Magnetization of Nickel and Iron*, J. Appl. Phys. **39**, 669–670 (1968).

[Dor19]   C. Dornes, Y. Acremann, M. Savoini, M. Kubli, M. J. Neugebauer, E. Abreu, L. Huber, G. Lantz, C. A. F. Vaz, H. Lemke, E. M. Bothschafter, M. Porer, V. Esposito, L. Rettig, M. Buzzi, A. Alberca, Y. W. Windsor, P. Beaud, U. Staub, D. Zhu, S. Song, J. M. Glownia, and S. L. Johnson, *The ultrafast Einstein-de Haas effect*, Nature **565**, 209–212 (2019).

[Dur20]   D. Durham, K. Siddiqui, F. Ji, J. G. Navarro, P. Musumeci, R. Kaindl, A. Minor, and D. Filippetto, *Relativistic Ultrafast Electron Diffraction of Nanomaterials*, Microsc. Microanal. **26**, 676–677 (2020).

[DVV14]   M. Dvornik, A. Vansteenkiste, and B. Van Waeyenberge, *Thermodynamically self-consistent non-stochastic micromagnetic model for the ferromagnetic state*, Appl. Phys. Lett. **105**, 162411 (2014).

[Dwy06]   J. R. Dwyer, C. T. Hebeisen, R. Ernstorfer, M. Harb, V. B. Deyirmenjian, R. E. Jordan, and R. Dwayne Miller, *Femtosecond electron diffraction: 'making the molecular movie'*, Philos. Trans. R. Soc. A **364**, 741–778 (2006).

[Dwy07]   J. R. Dwyer, R. E. Jordan, C. T. Hebeisen, M. Harb, R. Ernstorfer, T. Dartigalongue, and R. J. D. Miller, *Experimental basics for femtosecond electron diffraction studies*, J. Mod. Opt. **54**, 923–942 (2007).

[EAC15]   R. F. L. Evans, U. Atxitia, and R. W. Chantrell, *Quantitative simulation of temperature-dependent magnetization dynamics and equilibrium properties of elemental ferromagnets*, Phys. Rev. B **91**, 144425 (2015).

[Eic10]   M. Eichberger, H. Schäfer, M. Krumova, M. Beyer, J. Demsar, H. Berger, G. Moriena, G. Sciaini, and R. J. D. Miller, *Snapshots of cooperative atomic motions in the optical suppression of charge density waves*, Nature **468**, 799–802 (2010).

[Eic17]   S. Eich, M. Plötzing, M. Rollinger, S. Emmerich, R. Adam, C. Chen, H. C. Kapteyn, M. M. Murnane, L. Plucinski, D. Steil, B. Stadtmüller, M. Cinchetti, M. Aeschlimann, C. M. Schneider, and S. Mathias, *Band structure evolution during the ultrafast ferromagnetic-paramagnetic phase transition in cobalt*, Sci. Adv. **3**, e1602094 (2017).

[Ell54]   R. J. Elliott, *Theory of the Effect of Spin-Orbit Coupling on Magnetic Resonance in Some Semiconductors*, Phys. Rev. **96**, 266–279 (1954).

[Ern09]   R. Ernstorfer, M. Harb, C. T. Hebeisen, G. Sciaini, T. Dartigalongue, and R. J. D. Miller, *The Formation of Warm Dense Matter: Experimental Evidence for Electronic Bond Hardening in Gold*, Science **323**, 1033–1037 (2009).

[Esc14]   A. Eschenlohr, M. Sultan, A. Melnikov, N. Bergeard, J. Wieczorek, T. Kachel, C. Stamm, and U. Bovensiepen, *Role of spin-lattice coupling in the ultrafast demagnetization of* $Gd_{1-x}Tb_x$ *alloys*, Phys. Rev. B **89**, 214423 (2014).

[ESJ51]   J. W. Edwards, R. Speiser, and H. L. Johnston, *High Temperature Structure and Thermal Expansion of Some Metals as Determined by X-Ray Diffraction Data. I. Platinum, Tantalum, Niobium, and Molybdenum*, J. Appl. Phys. **22**, 424–428 (1951).

[Eva14]   R. F. L. Evans, W. J. Fan, P. Chureemart, T. A. Ostler, M. O. A. Ellis, and R. W. Chantrell, *Atomistic spin model simulations of magnetic nanomaterials*, J. Phys. Condens. Matter **26**, 103202 (2014).

[Fei18]   Z. Fei, B. Huang, P. Malinowski, W. Wang, T. Song, J. Sanchez, W. Yao, D. Xiao, X. Zhu, A. F. May, W. Wu, D. H. Cobden, J.-H. Chu, and X. Xu, *Two-dimensional itinerant ferromagnetism in atomically thin* Fe_3GeTe_2, Nat. Mater. **17**, 778–782 (2018).

[FH07]   A. Faruqi and R. Henderson, *Electronic detectors for electron microscopy*, Curr. Opin. Struct. Biol. **17**, 549–555 (2007).

[Fri15]   B. Frietsch, J. Bowlan, R. Carley, M. Teichmann, S. Wienholdt, D. Hinzke, U. Nowak, K. Carva, P. M. Oppeneer, and M. Weinelt, *Disparate ultrafast dynamics of itinerant and localized magnetic moments in gadolinium metal*, Nat. Commun. **6**, 8262 (2015).

[Fri20]   B. Frietsch, A. Donges, R. Carley, M. Teichmann, J. Bowlan, K. Döbrich, K. Carva, D. Legut, P. M. Oppeneer, U. Nowak, and M. Weinelt, *The role of ultrafast magnon generation in the magnetization dynamics of rare-earth metals*, Sci. Adv. **6**, eabb1601 (2020).

[Gen16]   E. van Genderen, M. T. B. Clabbers, P. P. Das, A. Stewart, I. Nederlof, K. C. Barentsen, Q. Portillo, N. S. Pannu, S. Nicolopoulos, T. Gruene, and J. P. Abrahams, *Ab initio structure determination of nanocrystals of organic pharmaceutical compounds by electron diffraction at room temperature using a Timepix quantum area direct electron detector*, Act. Cryst. A **72**, 236–242 (2016).

[Ger15]   C. Gerbig, A. Senftleben, S. Morgenstern, C. Sarpe, and T. Baumert, *Spatio-temporal resolution studies on a highly compact ultrafast electron diffractometer*, New J. Phys. **17**, 043050 (2015).

[GG13]   A. K. Geim and I. V. Grigorieva, *Van der Waals heterostructures*, Nature **499**, 419–425 (2013).

[Gia02]   C. Giacovazzo, H. L. Monaco, G. Artioli, D. Viterbo, G. Ferraris, G. Gilli, G. Zanotti, and M. Catti, *Fundamentals of Crystallography*, Oxford University Press (2002).

[Gle]   M. Gleich, M. Weinelt, et al., unpublished.

[Gor11]   A. Goris, K. M. Döbrich, I. Panzer, A. B. Schmidt, M. Donath, and M. Weinelt, *Role of Spin-Flip Exchange Scattering for Hot-Electron Lifetimes in Cobalt*, Phys. Rev. Lett. **107**, 026601 (2011).

[Gor18]   R. Gort, K. Bühlmann, S. Däster, G. Salvatella, N. Hartmann, Y. Zemp, S. Holenstein, C. Stieger, A. Fognini, T. U. Michlmayr, T. Bähler, A. Vaterlaus, and Y. Acremann, *Early Stages of Ultrafast Spin Dynamics in a 3d Ferromagnet*, Phys. Rev. Lett. **121**, 087206 (2018).

[Gor20]   R. Gort, K. Bühlmann, G. Saerens, S. Däster, A. Vaterlaus, and Y. Acremann, *Ultrafast magnetism: The magneto-optical Kerr effect and conduction electrons*, Appl. Phys. Lett. **116**, 112404 (2020).

[GSS54]   M. Griffel, R. E. Skochdopole, and F. H. Spedding, *The Heat Capacity of Gadolinium from 15 to 355° K*, Phys. Rev. **93**, 657–661 (1954).

[Guy22]   L. L. Guyader, D. J. Higley, M. Pancaldi, T. Liu, Z. Chen, T. Chase, P. W. Granitzka, G. Coslovich, A. A. Lutman, G. L. Dakovski, W. F. Schlotter, P. Shafer, E. Arenholz, O. Hellwig, M. L. M. Lalieu, B. Koopmans, A. H. Reid, S. Bonetti, J. Stöhr, and H. A. Dürr, *State-resolved ultrafast charge and spin dynamics in [Co/Pd] multilayers*, Appl. Phys. Lett. **120**, 032401 (2022).

[Hah16]   T. Hahn, ed., *International Tables for Crystallography Volume A: Space-group symmetry*, Second online edition (2016).

[Har06]   M. Harb, R. Ernstorfer, T. Dartigalongue, C. T. Hebeisen, R. E. Jordan, and R. J. D. Miller, *Carrier Relaxation and Lattice Heating Dynamics in Silicon Revealed by Femtosecond Electron Diffraction*, J. Phys. Chem. B **110**, 25308–25313 (2006).

[Har09]   M. Harb, W. Peng, G. Sciaini, C. T. Hebeisen, R. Ernstorfer, M. A. Eriksson, M. G. Lagally, S. G. Kruglik, and R. J. D. Miller, *Excitation of longitudinal and transverse coherent acoustic phonons in nanometer free-standing films of (001) Si*, Phys. Rev. B **79**, 094301 (2009).

[He15]   J. He, D. He, Y. Wang, Q. Cui, M. Z. Bellus, H.-Y. Chiu, and H. Zhao, *Exceptional and Anisotropic Transport Properties of Photocarriers in Black Phosphorus*, ACS Nano **9**, 6436–6442 (2015).

[Hil18]   P.-N. Hildebrandt, *Gitterdynamik von schwarzem Phosphor untersucht mit zeitaufgelöster Elektronenbeugung*, bachelor thesis (2018).

[HKN07]   P. E. Hopkins, J. M. Klopf, and P. M. Norris, *Influence of interband transitions on electron-phonon coupling measurements in Ni films*, Appl. Opt. **46**, 2076–2083 (2007).

[HPL74]   C. Y. Ho, R. W. Powell, and P. E. Liley, *Thermal conductivity of the elements: a comprehensive review*, J. Phys. Chem. Ref. Data **3**, Supplement No. 1 (1974).

[Hua17]   B. Huang, G. Clark, E. Navarro-Moratalla, D. R. Klein, R. Cheng, K. L. Seyler, D. Zhong, E. Schmidgall, M. A. McGuire, D. H. Cobden, W. Yao, D. Xiao, P. Jarillo-Herrero, and X. Xu, *Layer-dependent ferromagnetism in a van der Waals crystal down to the monolayer limit*, Nature **546**, 270–273 (2017).

[IL09]   H. Ibach and H. Lüth, *Solid-state physics*, 4th ed., Springer, Berlin, Heidelberg (2009).

[IYX17]   V. Iyer, P. Ye, and X. Xu, *Mid-infrared ultrafast carrier dynamics in thin film black phosphorus*, 2D Mater. **4**, 021032 (2017).

[Jak22]   F. Jakobs, D. Zahn, T. A. Butcher, J. Vorberger, R. Ernstorfer, and U. Atxitia, *Atomistic spin dynamics simulations of iron and cobalt*, Zenodo, https://doi.org/10.5281/zenodo.5845847 (2022).

[Jan15]   H. Jang, J. D. Wood, C. R. Ryder, M. C. Hersam, and D. G. Cahill, *Anisotropic Thermal Conductivity of Exfoliated Black Phosphorus*, Adv. Mater. **27**, 8017–8022 (2015).

[Jia18]   H. Jiang, H. Shi, X. Sun, and B. Gao, *Optical Anisotropy of Few-Layer Black Phosphorus Visualized by Scanning Polarization Modulation Microscopy*, ACS Photonics **5**, 2509–2515 (2018).

[JSS57]   L. D. Jennings, R. M. Stanton, and F. H. Spedding, *Heat Capacity of Terbium from 15 to 350° K*, J. Chem. Phys. **27**, 909–913 (1957).

[Kam02]   T. Kampfrath, R. G. Ulbrich, F. Leuenberger, M. Münzenberg, B. Sass, and W. Felsch, *Ultrafast magneto-optical response of iron thin films*, Phys. Rev. B **65**, 104429 (2002).

[Kam05]   M. van Kampen, J. T. Kohlhepp, W. J. M. de Jonge, B. Koopmans, and R. Coehoorn, *Sub-picosecond electron and phonon dynamics in nickel*, J. Phys. Condens. Matter **17**, 6823 (2005).

[Kam11]   T. Kampfrath, A. Sell, G. Klatt, A. Pashkin, S. Mährlein, T. Dekorsy, M. Wolf, M. Fiebig, A. Leitenstorfer, and R. Huber, *Coherent terahertz control of antiferromagnetic spin waves*, Nat. Photonics **5**, 31–34 (2011).

[Kaz07]   N. Kazantseva, U. Nowak, R. W. Chantrell, J. Hohlfeld, and A. Rebei, *Slow recovery of the magnetisation after a sub-picosecond heat pulse*, EPL **81**, 27004 (2007).

[Kit05]   C. Kittel, *Introduction to Solid State Physics*, ed. by S. Johnson, 8th ed., John Wiley & Sons (2005).

[KKR10]   A. Kirilyuk, A. V. Kimel, and T. Rasing, *Ultrafast optical manipulation of magnetic order*, Rev. Mod. Phys. **82**, 2731–2784 (2010).

[KLT57]   M. I. Kaganov, I. M. Lifshitz, and L. V. Tanatarov, *Relaxations between electrons and the crystalline lattice*, Sov. phys. JETP **4**, 173–178 (1957).

[Koc17]   A. Koc, M. Reinhardt, A. von Reppert, M. Rössle, W. Leitenberger, M. Gleich, M. Weinelt, F. Zamponi, and M. Bargheer, *Grueneisen-approach for the experimental determination of transient spin and phonon energies from ultrafast x-ray diffraction data: gadolinium*, J. Phys. Condens. Matter **29**, 264001 (2017).

[Koo10]   B. Koopmans, G. Malinowski, F. D. Longa, D. Steiauf, M. Fähnle, T. Roth, M. Cinchetti, and M. Aeschlimann, *Explaining the paradoxical diversity of ultrafast laser-induced demagnetization*, Nat. Mater. **9**, 259–265 (2010).

[Kub14]   T. Kubacka, J. A. Johnson, M. C. Hoffmann, C. Vicario, S. de Jong, P. Beaud, S. Grübel, S.-W. Huang, L. Huber, L. Patthey, Y.-D. Chuang, J. J. Turner, G. L. Dakovski, W.-S. Lee, M. P. Minitti, W. Schlotter, R. G. Moore, C. P. Hauri, S. M. Koohpayeh, V. Scagnoli, G. Ingold, S. L. Johnson, and U. Staub, *Large-Amplitude Spin Dynamics Driven by a THz Pulse in Resonance with an Electromagnon*, Science **343**, 1333–1336 (2014).

[Lay15]   G. L. Lay, E. Salomon, T. Angot, and M. E. Dávila, *Increasing the lego of 2D electronics materials: silicene and germanene, graphene's new synthetic cousins*, Proc. SPIE **9467**, Micro- and Nanotechnology Sensors, Systems, and Applications VII, 139–143 (2015).

[Lee15]   S. Lee, F. Yang, J. Suh, S. Yang, Y. Lee, G. Li, H. Sung Choe, A. Suslu, Y. Chen, C. Ko, J. Park, K. Liu, J. Li, K. Hippalgaonkar, J. J. Urban, S. Tongay, and J. Wu, *Anisotropic in-plane thermal conductivity of black phosphorus nanoribbons at temperatures higher than 100 K*, Nat. Commun. **6**, 8573 (2015).

[Lee16]   J.-U. Lee, S. Lee, J. H. Ryoo, S. Kang, T. Y. Kim, P. Kim, C.-H. Park, J.-G. Park, and H. Cheong, *Ising-Type Magnetic Ordering in Atomically Thin FePS$_3$*, Nano Lett. **16**, 7433–7438 (2016).

[Li14]   L. Li, Y. Yu, G. J. Ye, Q. Ge, X. Ou, H. Wu, D. Feng, X. H. Chen, and Y. Zhang, *Black phosphorus field-effect transistors*, Nat. Nanotechnol. **9**, 372–377 (2014).

[Li17]   L. Li, J. Kim, C. Jin, G. J. Ye, D. Y. Qiu, F. H. da Jornada, Z. Shi, L. Chen, Z. Zhang, F. Yang, K. Watanabe, T. Taniguchi, W. Ren, S. G. Louie, X. H. Chen, Y. Zhang, and F. Wang, *Direct observation of the layer-dependent electronic structure in phosphorene*, Nat. Nanotechnol. **12**, 21–25 (2017).

[Lid03]   D. R. Lide, ed., *CRC Handbook of Chemistry and Physics*, 84th ed., CRC Press (2003).

[Lie55]   G. Liebmann, *A Unified Representation of Magnetic Electron Lens Properties*, Proc. Phys. Soc. B **68**, 737–745 (1955).

[Lig11]   M. Ligges, I. Rajković, C. Streubühr, T. Brazda, P. Zhou, O. Posth, C. Hassel, G. Dumpich, and D. von der Linde, *Transient (000)-order attenuation effects in ultrafast transmission electron diffraction*, J. Appl. Phys. **109**, 063519 (2011).

[Liu14]   H. Liu, A. T. Neal, Z. Zhu, Z. Luo, X. Xu, D. Tománek, and P. D. Ye, *Phosphorene: An Unexplored 2D Semiconductor with a High Hole Mobility*, ACS Nano **8**, 4033–4041 (2014).

[Liu17]   Y. Liu, B. N. Shivananju, Y. Wang, Y. Zhang, W. Yu, S. Xiao, T. Sun, W. Ma, H. Mu, S. Lin, H. Zhang, Y. Lu, C.-W. Qiu, S. Li, and Q. Bao, *Highly Efficient and Air-Stable Infrared Photodetector Based on 2D Layered Graphene–Black Phosphorus Heterostructure*, ACS Appl. Mater. Interfaces **9**, 36137–36145 (2017).

[Liu21]   B. Liu, H. Xiao, G. Siemann, J. Weber, B. Andres, W. Bronsch, P. M. Oppeneer, and M. Weinelt, *Signature of magnon polarons in electron relaxation on terbium revealed by comparison with gadolinium*, Phys. Rev. B **104**, 024434 (2021).

[Lon16]   G. Long, D. Maryenko, J. Shen, S. Xu, J. Hou, Z. Wu, W. K. Wong, T. Han, J. Lin, Y. Cai, R. Lortz, and N. Wang, *Achieving Ultrahigh Carrier Mobility in Two-Dimensional Hole Gas of Black Phosphorus*, Nano Lett. **16**, 7768–7773 (2016).

[Low14]   T. Low, A. S. Rodin, A. Carvalho, Y. Jiang, H. Wang, F. Xia, and A. H. Castro Neto, *Tunable optical properties of multilayer black phosphorus thin films*, Phys. Rev. B **90**, 075434 (2014).

[Luk15]   K. Luke, Y. Okawachi, M. R. E. Lamont, A. L. Gaeta, and M. Lipson, *Broadband mid-infrared frequency comb generation in a Si_3N_4 microresonator*, Opt. Lett. **40**, 4823–4826 (2015).

[Luo15]   Z. Luo, J. Maassen, Y. Deng, Y. Du, R. P. Garrelts, M. S. Lundstrom, P. D. Ye, and X. Xu, *Anisotropic in-plane thermal conductivity observed in few-layer black phosphorus*, Nat. Commun. **6**, 8572 (2015).

[LZC]   Z. Lin, L. V. Zhigilei, and V. Celli, *Electron-Phonon Coupling and Electron Heat Capacity in Metals at High Electron Temperatures*, retrieved from https://faculty.virginia.edu/CompMat/electron-phonon-coupling (following the approach of Z. Lin, L. V. Zhigilei, and V. Celli, Phys. Rev. B 77, 075133, 2008).

[LZC08]   Z. Lin, L. V. Zhigilei, and V. Celli, *Electron-phonon coupling and electron heat capacity of metals under conditions of strong electron-phonon nonequilibrium*, Phys. Rev. B **77**, 075133 (2008).

[Mac18]   Y. Machida, A. Subedi, K. Akiba, A. Miyake, M. Tokunaga, Y. Akahama, K. Izawa, and K. Behnia, *Observation of Poiseuille flow of phonons in black phosphorus*, Sci. Adv. **4**, eaat3374 (2018).

[Mäh18]   S. F. Mährlein, I. Radu, P. Maldonado, A. Paarmann, M. Gensch, A. M. Kalashnikova, R. V. Pisarev, M. Wolf, P. M. Oppeneer, J. Barker, and T. Kampfrath, *Dissecting spin-phonon equilibration in ferrimagnetic insulators by ultrafast lattice excitation*, Sci. Adv. **4**, eaar5164 (2018).

[Man14a]   S. Mangin, M. Gottwald, C.-H. Lambert, D. Steil, V. Uhlíř, L. Pang, M. Hehn, S. Alebrand, M. Cinchetti, G. Malinowski, Y. Fainman, M. Aeschlimann, and E. E. Fullerton, *Engineered materials for all-optical helicity-dependent magnetic switching*, Nat. Mater. **13**, 286–292 (2014).

[Man14b]   R. Mankowsky, A. Subedi, M. Först, S. O. Mariager, M. Chollet, H. T. Lemke, J. S. Robinson, J. M. Glownia, M. P. Minitti, A. Frano, M. Fechner, N. A. Spaldin, T. Loew, B. Keimer, A. Georges, and A. Cavalleri, *Nonlinear lattice dynamics as a basis for enhanced superconductivity in $YBa_2Cu_3O_{6.5}$*, Nature **516**, 71–73 (2014).

[Man15]   R. Mankowsky, M. Först, T. Loew, J. Porras, B. Keimer, and A. Cavalleri, *Coherent modulation of the $YBa_2Cu_3O_{6+x}$ atomic structure by displacive stimulated ionic Raman scattering*, Phys. Rev. B **91**, 094308 (2015).

[MD19]   C. Malica and A. Dal Corso, *Temperature-dependent atomic B factor: an ab initio calculation*, Act. Cryst. A **75**, 624–632 (2019).

[MDW12]   P.-W. Ma, S. L. Dudarev, and C. H. Woo, *Spin-lattice-electron dynamics simulations of magnetic materials*, Phys. Rev. B **85**, 184301 (2012).

[Mel08]   A. Melnikov, H. Prima-Garcia, M. Lisowski, T. Gießel, R. Weber, R. Schmidt, C. Gahl, N. M. Bulgakova, U. Bovensiepen, and M. Weinelt, *Nonequilibrium Magnetization Dynamics of Gadolinium Studied by Magnetic Linear Dichroism in Time-Resolved 4f Core-Level Photoemission*, Phys. Rev. Lett. **100**, 107202 (2008).

[Mes81]   P. J. Meschter, J. W. Wright, C. R. Brooks, and T. G. Kollie, *Physical contributions to the heat capacity of nickel*, J. Phys. Chem. Solids **42**, 861–871 (1981).

[Mig17]   K. P. Migdal, N. A. Inogamov, Y. V. Petrov, and V. V. Zhakhovsky, *Two-temperature equations of state for d-band metals irradiated by femtosecond laser pulses*, arXiv:1702.00825 (2017).

[Mil14]   R. J. D. Miller, *Femtosecond Crystallography with Ultrabright Electrons and X-rays: Capturing Chemistry in Action*, Science **343**, 1108–1116 (2014).

[MM20]   N. Medvedev and I. Milov, *Electron-phonon coupling in metals at high electronic temperatures*, Phys. Rev. B **102**, 064302 (2020).

[MR13]   B. Y. Mueller and B. Rethfeld, *Relaxation dynamics in laser-excited metals under nonequilibrium conditions*, Phys. Rev. B **87**, 035139 (2013).

[MR14]   B. Y. Mueller and B. Rethfeld, *Thermodynamic μT model of ultrafast magnetization dynamics*, Phys. Rev. B **90**, 144420 (2014).

[MS51]   H. P. Myers and W. Sucksmith, *The spontaneous magnetization of cobalt*, Proc. Math. Phys. Eng. Sci. **207**, 427–446 (1951).

[Nie06]   S. Nie, X. Wang, H. Park, R. Clinite, and J. Cao, *Measurement of the Electronic Grüneisen Constant Using Femtosecond Electron Diffraction*, Phys. Rev. Lett. **96**, 025901 (2006).

[Nie14]   Z. Nie, R. Long, L. Sun, C.-C. Huang, J. Zhang, Q. Xiong, D. W. Hewak, Z. Shen, O. V. Prezhdo, and Z.-H. Loh, *Ultrafast Carrier Thermalization and Cooling Dynamics in Few-Layer MoS_2*, ACS Nano **8**, 10931–10940 (2014).

[Nov04]   K. S. Novoselov, A. K. Geim, S. V. Morozov, D. Jiang, Y. Zhang, S. V. Dubonos, I. V. Grigorieva, and A. A. Firsov, *Electric Field Effect in Atomically Thin Carbon Films*, Science **306**, 666–669 (2004).

[Nov05]   K. S. Novoselov, D. Jiang, F. Schedin, T. J. Booth, V. V. Khotkevich, S. V. Morozov, and A. K. Geim, *Two-dimensional atomic crystals*, Proc. Natl. Acad. Sci. U.S.A. **102**, 10451–10453 (2005).

[Now07]   U. Nowak, *Classical Spin Models*, in: ed. by H. Kronmueller and S. Parkin, John Wiley & Sons, *Handbook of Magnetism and Advanced Magnetic Materials*.

[Ogi18]   T. Ogitsu, A. Fernandez-Pañella, S. Hamel, A. A. Correa, D. Prendergast, C. D. Pemmaraju, and Y. Ping, *Ab initio modeling of nonequilibrium electron-ion dynamics of iron in the warm dense matter regime*, Phys. Rev. B **97**, 214203 (2018).

[Oud10]   T. van Oudheusden, P. L. E. M. Pasmans, S. B. van der Geer, M. J. de Loos, M. J. van der Wiel, and O. J. Luiten, *Compression of Subrelativistic Space-Charge-Dominated Electron Bunches for Single-Shot Femtosecond Electron Diffraction*, Phys. Rev. Lett. **105**, 264801 (2010).

[PDW11]   L. Peng, S. Dudarev, and M. Whelan, *High Energy Electron Diffraction and Microscopy*, Oxford Science Publications (2011).

[Per16]   A. I. H. Persson, A. Jarnac, X. Wang, H. Enquist, A. Jurgilaitis, and J. Larsson, *Studies of electron diffusion in photo-excited Ni using time-resolved X-ray diffraction*, Appl. Phys. Lett. **109**, 203115 (2016).

[PIM13]   Y. V. Petrov, N. A. Inogamov, and K. P. Migdal, *Thermal conductivity and the electron-ion heat transfer coefficient in condensed media with a strongly excited electron subsystem*, JETP Lett. **97**, 20–27 (2013).

[Pud19]   J. Pudell, A. von Reppert, D. Schick, F. Zamponi, M. Rössle, M. Herzog, H. Zabel, and M. Bargheer, *Ultrafast negative thermal expansion driven by spin disorder*, Phys. Rev. B **99**, 094304 (2019).

[Qia14]   J. Qiao, X. Kong, Z.-X. Hu, F. Yang, and W. Ji, *High-mobility transport anisotropy and linear dichroism in few-layer black phosphorus*, Nat. Commun. **5**, 4475 (2014).

[Raz17]   I. Razdolski, A. Alekhin, U. Martens, D. Diesing, M. Münzenberg, U. Bovensiepen, and A. Melnikov, *Analysis of the time-resolved magneto-optical Kerr effect for ultrafast magnetization dynamics in ferromagnetic thin films*, J. Phys. Condens. Matter **29**, 174002 (2017).

[Rei18]   A. H. Reid, X. Shen, P. Maldonado, T. Chase, E. Jal, P. W. Granitzka, K. Carva, R. K. Li, J. Li, L. Wu, T. Vecchione, T. Liu, Z. Chen, D. J. Higley, N. Hartmann, R. Coffee, J. Wu, G. L. Dakovski, W. F. Schlotter, H. Ohldag, Y. K. Takahashi, V. Mehta, O. Hellwig, A. Fry, Y. Zhu, J. Cao, E. E. Fullerton, J. Stöhr, P. M. Oppeneer, X. J. Wang, and H. A. Dürr, *Beyond a phenomenological description of magnetostriction*, Nat. Commun. **9**, 388 (2018).

[Rep16]   A. von Reppert, J. Pudell, A. Koc, M. Reinhardt, W. Leitenberger, K. Dumesnil, F. Zamponi, and M. Bargheer, *Persistent nonequilibrium dynamics of the thermal energies in the spin and phonon systems of an antiferromagnet*, Struct. Dyn. **3**, 054302 (2016).

[Rin07]   M. Rini, R. Tobey, N. Dean, J. Itatani, Y. Tomioka, Y. Tokura, R. W. Schoenlein, and A. Cavalleri, *Control of the electronic phase of a manganite by mode-selective vibrational excitation*, Nature **449**, 72–74 (2007).

[RJN87]   S. Ruhman, A. G. Joly, and K. A. Nelson, *Time-resolved observations of coherent molecular vibrational motion and the general occurrence of impulsive stimulated scattering*, J. Chem. Phys. **86**, 6563–6565 (1987).

[Roh18]   G. Rohde, A. Stange, A. Müller, M. Behrendt, L.-P. Oloff, K. Hanff, T. J. Albert, P. Hein, K. Rossnagel, and M. Bauer, *Ultrafast Formation of a Fermi-Dirac Distributed Electron Gas*, Phys. Rev. Lett. **121**, 256401 (2018).

[ROM20]   U. Ritzmann, P. M. Oppeneer, and P. Maldonado, *Theory of out-of-equilibrium electron and phonon dynamics in metals after femtosecond laser excitation*, Phys. Rev. B **102**, 214305 (2020).

[Rot12]   T. Roth, A. J. Schellekens, S. Alebrand, O. Schmitt, D. Steil, B. Koopmans, M. Cinchetti, and M. Aeschlimann, *Temperature Dependence of Laser-Induced Demagnetization in Ni: A Key for Identifying the Underlying Mechanism*, Phys. Rev. X **2**, 021006 (2012).

[Rot19]   N. Rothenbach, M. E. Gruner, K. Ollefs, C. Schmitz-Antoniak, S. Salamon, P. Zhou, R. Li, M. Mo, S. Park, X. Shen, S. Weathersby, J. Yang, X. J. Wang, R. Pentcheva, H. Wende, U. Bovensiepen, K. Sokolowski-Tinten, and A. Eschenlohr, *Microscopic nonequilibrium energy transfer dynamics in a photoexcited metal/insulator heterostructure*, Phys. Rev. B **100**, 174301 (2019).

[RPM18]   H. B. Ribeiro, M. A. Pimenta, and C. J. de Matos, *Raman spectroscopy in black phosphorus*, J. Raman Spectrosc. **49**, 76–90 (2018).

[Sai06]   E. Saitoh, M. Ueda, H. Miyajima, and G. Tatara, *Conversion of spin current into charge current at room temperature: Inverse spin-Hall effect*, Appl. Phys. Lett. **88**, 182509 (2006).

[Sch10]   A. B. Schmidt, M. Pickel, M. Donath, P. Buczek, A. Ernst, V. P. Zhukov, P. M. Echenique, L. M. Sandratskii, E. V. Chulkov, and M. Weinelt, *Ultrafast Magnon Generation in an Fe Film on Cu(100)*, Phys. Rev. Lett. **105**, 197401 (2010).

[Sch19]   R. Schoenlein, T. Elsaesser, K. Holldack, Z. Huang, H. Kapteyn, M. Murnane, and M. Woerner, *Recent advances in ultrafast X-ray sources*, Philos. Trans. R. Soc. A **377**, 20180384 (2019).

[Sei16]   T. Seifert, S. Jaiswal, U. Martens, J. Hannegan, L. Braun, P. Maldonado, F. Freimuth, A. Kronenberg, J. Henrizi, I. Radu, E. Beaurepaire, Y. Mokrousov, P. M. Oppeneer, M. Jourdan, G. Jakob, D. Turchinovich, L. M. Hayden, M. Wolf, M. Münzenberg, M. Kläui, and T. Kampfrath, *Efficient metallic spintronic emitters of ultrabroadband terahertz radiation*, Nat. Photonics **10**, 483–488 (2016).

[Sei21]   H. Seiler, D. Zahn, M. Zacharias, P.-N. Hildebrandt, T. Vasileiadis, Y. W. Windsor, Y. Qi, C. Carbogno, C. Draxl, R. Ernstorfer, and F. Caruso, *Accessing the Anisotropic Nonthermal Phonon Populations in Black Phosphorus*, Nano Lett. **21**, 6171–6178 (2021).

[She15]   Z. Shen, S. Sun, W. Wang, J. Liu, Z. Liu, and J. C. Yu, *A black–red phosphorus heterostructure for efficient visible-light-driven photocatalysis*, J. Mater. Chem. A **3**, 3285–3288 (2015).

[Siw02]   B. J. Siwick, J. R. Dwyer, R. E. Jordan, and R. J. D. Miller, *Ultrafast electron optics: Propagation dynamics of femtosecond electron packets*, J. Appl. Phys. **92**, 1643–1648 (2002).

[SM11]   G. Sciaini and R. J. D. Miller, *Femtosecond electron diffraction: heralding the era of atomically resolved dynamics*, Rep. Prog. Phys. **74**, 096101 (2011).

[SMW03]   T. Saito, O. Matsuda, and O. B. Wright, *Picosecond acoustic phonon pulse generation in nickel and chromium*, Phys. Rev. B **67**, 205421 (2003).

[Söd14]   P. Söderlind, P. E. A. Turchi, A. Landa, and V. Lordi, *Ground-state properties of rare-earth metals: an evaluation of density-functional theory*, J. Phys. Condens. Matter **26**, 416001 (2014).

[Sot15]   J. Sotor, G. Sobon, W. Macherzynski, P. Paletko, and K. M. Abramski, *Black phosphorus saturable absorber for ultrashort pulse generation*, Appl. Phys. Lett. **107**, 051108 (2015).

[Spl10]   A. Splendiani, L. Sun, Y. Zhang, T. Li, J. Kim, C.-Y. Chim, G. Galli, and F. Wang, *Emerging Photoluminescence in Monolayer MoS$_2$*, Nano Lett. **10**, 1271–1275 (2010).

[Sta07]   C. Stamm, T. Kachel, N. Pontius, R. Mitzner, T. Quast, K. Holldack, S. Khan, C. Lupulescu, E. F. Aziz, M. Wietstruk, H. A. Dürr, and W. Eberhardt, *Femtosecond modification of electron localization and transfer of angular momentum in nickel*, Nat. Mater. **6**, 740–743 (2007).

[Ste18]   M. J. Stern, L. P. René de Cotret, M. R. Otto, R. P. Chatelain, J.-P. Boisvert, M. Sutton, and B. J. Siwick, *Mapping momentum-dependent electron-phonon coupling and nonequilibrium phonon dynamics with ultrafast electron diffuse scattering*, Phys. Rev. B **97**, 165416 (2018).

[Sul12]   M. Sultan, *Ultrafast Magnetization Dynamics of Lanthanide Metals and Alloys*, PhD thesis (2012).

[Sun17]   B. Sun, X. Gu, Q. Zeng, X. Huang, Y. Yan, Z. Liu, R. Yang, and Y. K. Koh, *Temperature Dependence of Anisotropic Thermal-Conductivity Tensor of Bulk Black Phosphorus*, Adv. Mater. **29**, 1603297 (2017).

[Tau22]   S. R. Tauchert, M. Volkov, D. Ehberger, D. Kazenwadel, M. Evers, H. Lange, A. Donges, A. Book, W. Kreuzpaintner, U. Nowak, and P. Baum, *Polarized phonons carry angular momentum in ultrafast demagnetization*, Nature **602**, 73–77 (2022).

[Ten18]   P. Tengdin, W. You, C. Chen, X. Shi, D. Zusin, Y. Zhang, C. Gentry, A. Blonsky, M. Keller, P. M. Oppeneer, H. C. Kapteyn, Z. Tao, and M. M. Murnane, *Critical behavior within 20 fs drives the out-of-equilibrium laser-induced magnetic phase transition in nickel*, Sci. Adv. **4**, eaap9744 (2018).

[Thi17]   N. Thielemann-Kühn, D. Schick, N. Pontius, C. Trabant, R. Mitzner, K. Holldack, H. Zabel, A. Föhlisch, and C. Schüßler-Langeheine, *Ultrafast and Energy-Efficient Quenching of Spin Order: Antiferromagnetism Beats Ferromagnetism*, Phys. Rev. Lett. **119**, 197202 (2017).

[Thu98]   K. Thurnay, *Thermal properties of transition metals*, scientific report, Forschungszentrum Karlsruhe, FZKA-6095 (1998).

[Tia16]   Y. Tian, M. J. Gray, H. Ji, R. J. Cava, and K. S. Burch, *Magneto-elastic coupling in a potential ferromagnetic 2D atomic crystal*, 2D Mater. **3**, 025035 (2016).

[TM95]   S. Tamura and H. J. Maris, *Temperature dependence of phonon lifetimes in dielectric crystals*, Phys. Rev. B **51**, 2857–2863 (1995).

[TP15]   W. Töws and G. M. Pastor, *Many-Body Theory of Ultrafast Demagnetization and Angular Momentum Transfer in Ferromagnetic Transition Metals*, Phys. Rev. Lett. **115**, 217204 (2015).

[Tra14]   V. Tran, R. Soklaski, Y. Liang, and L. Yang, *Layer-controlled band gap and anisotropic excitons in few-layer black phosphorus*, Phys. Rev. B **89**, 235319 (2014).

[Tri10]   M. Trigo, J. Chen, V. H. Vishwanath, Y. M. Sheu, T. Graber, R. Henning, and D. A. Reis, *Imaging nonequilibrium atomic vibrations with x-ray diffuse scattering*, Phys. Rev. B **82**, 235205 (2010).

[Tri19]   D. Tristant, A. Cupo, X. Ling, and V. Meunier, *Phonon Anharmonicity in Few-Layer Black Phosphorus*, ACS Nano **13**, 10456–10468 (2019).

[Tru96]   K. N. Trueblood, H.-B. Bürgi, H. Burzlaff, J. D. Dunitz, C. M. Gramaccioli, H. H. Schulz, U. Shmueli, and S. C. Abrahams, *Atomic displacement parameter nomenclature. Report of a subcommittee on atomic displacement parameter nomenclature*, Act. Cryst. A **52**, 770–781 (1996).

[Tun19]   I.-C. Tung, A. Krishnamoorthy, S. Sadasivam, H. Zhou, Q. Zhang, K. L. Seyler, G. Clark, E. M. Mannebach, C. Nyby, F. Ernst, D. Zhu, J. M. Glownia, M. E. Kozina, S. Song, S. Nelson, H. Kumazoe, F. Shimojo, R. K. Kalia, P. Vashishta, P. Darancet, T. F. Heinz, A. Nakano, X. Xu, A. M. Lindenberg, and H. Wen, *Anisotropic structural dynamics of monolayer crystals revealed by femtosecond surface X-ray scattering*, Nat. Photonics **13**, 425–430 (2019).

[Tur16]   E. Turgut, D. Zusin, D. Legut, K. Carva, R. Knut, J. M. Shaw, C. Chen, Z. Tao, H. T. Nembach, T. J. Silva, S. Mathias, M. Aeschlimann, P. M. Oppeneer, H. C. Kapteyn, M. M. Murnane, and P. Grychtol, *Stoner versus Heisenberg: Ultrafast exchange reduction and magnon generation during laser-induced demagnetization*, Phys. Rev. B **94**, 220408(R) (2016).

[Uls15]   S. Ulstrup, J. C. Johannsen, A. Crepaldi, F. Cilento, M. Zacchigna, C. Cacho, R. T. Chapman, E. Springate, F. Fromm, C. Raidel, T. Seyller, F. Parmigiani, M. Grioni, and P. Hofmann, *Ultrafast electron dynamics in epitaxial graphene investigated with time- and angle-resolved photoemission spectroscopy*, **27**, 164206 (2015).

[Uni21]   V. Unikandanunni, R. Medapalli, E. E. Fullerton, K. Carva, P. M. Oppeneer, and S. Bonetti, *Anisotropic ultrafast spin dynamics in epitaxial cobalt*, Appl. Phys. Lett. **118**, 232404 (2021).

[van20]   J. P. van Schayck, E. van Genderen, E. Maddox, L. Roussel, H. Boulanger, E. Fröjdh, J.-P. Abrahams, P. J. Peters, and R. B. Ravelli, *Sub-pixel electron detection using a convolutional neural network*, Ultramicroscopy **218**, 113091 (2020).

[Vas18]   T. Vasileiadis, L. Waldecker, D. Foster, A. Da Silva, D. Zahn, R. Bertoni, R. E. Palmer, and R. Ernstorfer, *Ultrafast Heat Flow in Heterostructures of Au Nanoclusters on Thin Films: Atomic Disorder Induced by Hot Electrons*, ACS Nano **12**, 7710–7720 (2018).

[Vat90]   A. Vaterlaus, D. Guarisco, M. Lutz, M. Aeschlimann, M. Stampanoni, and F. Meier, *Different spin and lattice temperatures observed by spin-polarized photoemission with picosecond laser pulses*, J. Appl. Phys. **67**, 5661–5663 (1990).

[VBM91]   A. Vaterlaus, T. Beutler, and F. Meier, *Spin-lattice relaxation time of ferromagnetic gadolinium determined with time-resolved spin-polarized photoemission*, Phys. Rev. Lett. **67**, 3314–3317 (1991).

[Ves15]   S. Vespucci, A. Winkelmann, G. Naresh-Kumar, K. P. Mingard, D. Maneuski, P. R. Edwards, A. P. Day, V. O'Shea, and C. Trager-Cowan, *Digital direct electron imaging of energy-filtered electron backscatter diffraction patterns*, Phys. Rev. B **92**, 205301 (2015).

[Wal16a]   L. Waldecker, R. Bertoni, R. Ernstorfer, and J. Vorberger, *Electron-Phonon Coupling and Energy Flow in a Simple Metal beyond the Two-Temperature Approximation*, Phys. Rev. X **6**, 021003 (2016).

[Wal16b]   L. Waldecker, *Electron-Lattice Interactions and Ultrafast Structural Dynamics of Solids*, PhD thesis (2016).

[Wal17a]   L. Waldecker, T. Vasileiadis, R. Bertoni, R. Ernstorfer, T. Zier, F. H. Valencia, M. E. Garcia, and E. S. Zijlstra, *Coherent and incoherent structural dynamics in laser-excited antimony*, Phys. Rev. B **95**, 054302 (2017).

[Wal17b]   L. Waldecker, R. Bertoni, H. Hübener, T. Brumme, T. Vasileiadis, D. Zahn, A. Rubio, and R. Ernstorfer, *Momentum-Resolved View of Electron-Phonon Coupling in Multilayer* WSe_2, Phys. Rev. Lett. **119**, 036803 (2017).

[Wal23]   I. Waller, *Zur Frage der Einwirkung der Wärmebewegung auf die Interferenz von Röntgenstrahlen*, Z. Physik **17**, 398–408 (1923).

[Wan08]   X. Wang, S. Nie, J. Li, R. Clinite, M. Wartenbe, M. Martin, W. Liang, and J. Cao, *Electronic Grüneisen parameter and thermal expansion in ferromagnetic transition metal*, Appl. Phys. Lett. **92**, 121918 (2008).

[Wan10]   X. Wang, S. Nie, J. Li, R. Clinite, J. E. Clark, and J. Cao, *Temperature dependence of electron-phonon thermalization and its correlation to ultrafast magnetism*, Phys. Rev. B **81**, 220301(R) (2010).

[Wan16]   K. Wang, B. M. Szydłowska, G. Wang, X. Zhang, J. J. Wang, J. J. Magan, L. Zhang, J. N. Coleman, J. Wang, and W. J. Blau, *Ultrafast Nonlinear Excitation Dynamics of Black Phosphorus Nanosheets from Visible to Mid-Infrared*, ACS Nano **10**, 6923–6932 (2016).

[Wan18]   G. Wang, A. Chernikov, M. M. Glazov, T. F. Heinz, X. Marie, T. Amand, and B. Urbaszek, *Colloquium: Excitons in atomically thin transition metal dichalcogenides*, Rev. Mod. Phys. **90**, 021001 (2018).

[Wan94]   X. Y. Wang, D. M. Riffe, Y.-S. Lee, and M. C. Downer, *Time-resolved electron-temperature measurement in a highly excited gold target using femtosecond thermionic emission*, Phys. Rev. B **50**, 8016–8019 (1994).

[War90]   B. E. Warren, *X-ray diffraction*, Dover Publications (1990).

[WBE15]   L. Waldecker, R. Bertoni, and R. Ernstorfer, *Compact femtosecond electron diffractometer with 100 keV electron bunches approaching the single-electron pulse duration limit*, J. Appl. Phys. **117**, 044903 (2015).

[WC20]   R. B. Wilson and S. Coh, *Parametric dependence of hot electron relaxation timescales on electron-electron and electron-phonon interaction strengths*, Commun. Phys. **3**, 179 (2020).

[Wel98]   S. S. Wellershoff, J. Güdde, J. Hohlfeld, J. G. Müller, and E. Matthias, *Role of electron-phonon coupling in femtosecond laser damage of metals*, Proc. SPIE **3343**, High-Power Laser Ablation, 378–387 (1998).

[Whi07]   R. M. White, *Quantum theory of magnetism*, Springer Berlin Heidelberg (2007).

[Wie10]   M. Wietstruk, *Ultraschnelle Magnetisierungsdynamik in itineranten und Heisenberg-Ferromagneten*, PhD thesis (2010).

[Wie11]   M. Wietstruk, A. Melnikov, C. Stamm, T. Kachel, N. Pontius, M. Sultan, C. Gahl, M. Weinelt, H. A. Dürr, and U. Bovensiepen, *Hot-Electron-Driven Enhancement of Spin-Lattice Coupling in Gd and Tb 4f Ferromagnets Observed by Femtosecond X-Ray Magnetic Circular Dichroism*, Phys. Rev. Lett. **106**, 127401 (2011).

[Wie15]   S. Wienholdt, *Modeling of Laser-Induced Ultrafast Spin Dynamics in Magnetically Ordered Materials*, PhD thesis (2015).

[Win21]   Y. W. Windsor, D. Zahn, R. Kamrla, J. Feldl, H. Seiler, C.-T. Chiang, M. Ramsteiner, W. Widdra, R. Ernstorfer, and L. Rettig, *Exchange-Striction Driven Ultrafast Nonthermal Lattice Dynamics in NiO*, Phys. Rev. Lett. **126**, 147202 (2021).

[Win98]   D. L. Windt, *IMD—Software for modeling the optical properties of multilayer films*, Comput. Phys. **12**, 360–370 (1998).

[WIO71]   Y. Watanabe, H. Iwasaki, and S. Ogawa, *An X-ray Investigation of Thermal Mean-Square Atomic Displacements in Magnesium, Cadmium and Mg_3Cd*, Japanese J. Appl. Phys. **10**, 786–793 (1971).

[WLY18]   L. Webster, L. Liang, and J.-A. Yan, *Distinct spin-lattice and spin-phonon interactions in monolayer magnetic CrI_3*, Phys. Chem. Chem. Phys. **20**, 23546–23555 (2018).

[WP75]   B. T. M. Willis and A. W. Pryor, *Thermal Vibrations in Crystallography*, Cambridge University Press (1975).

[WR19]   S. T. Weber and B. Rethfeld, *Phonon-induced long-lasting nonequilibrium in the electron system of a laser-excited solid*, Phys. Rev. B **99**, 174314 (2019).

[Xu13]   M. Xu, T. Liang, M. Shi, and H. Chen, *Graphene-Like Two-Dimensional Materials*, Chem. Rev. **113**, 3766–3798 (2013).

[XWJ14]   F. Xia, H. Wang, and Y. Jia, *Rediscovering black phosphorus as an anisotropic layered material for optoelectronics and electronics*, Nat. Commun. **5**, 4458 (2014).

[You18]   W. You, P. Tengdin, C. Chen, X. Shi, D. Zusin, Y. Zhang, C. Gentry, A. Blonsky, M. Keller, P. M. Oppeneer, H. Kapteyn, Z. Tao, and M. Murnane, *Revealing the Nature of the Ultrafast Magnetic Phase Transition in Ni by Correlating Extreme Ultraviolet Magneto-Optic and Photoemission Spectroscopies*, Phys. Rev. Lett. **121**, 077204 (2018).

[Zac21]   M. Zacharias, H. Seiler, F. Caruso, D. Zahn, F. Giustino, P. C. Kelires, and R. Ernstorfer, *Efficient First-Principles Methodology for the Calculation of the All-Phonon Inelastic Scattering in Solids*, Phys. Rev. Lett. **127**, 207401 (2021).

[Zah20a] D. Zahn, P.-N. Hildebrandt, T. Vasileiadis, Y. W. Windsor, Y. Qi, H. Seiler, and R. Ernstorfer, *Anisotropic Nonequilibrium Lattice Dynamics of Black Phosphorus*, Nano Lett. **20**, 3728–3733 (2020).

[Zah20b] D. Zahn, P.-N. Hildebrandt, T. Vasileiadis, Y. W. Windsor, Y. Qi, H. Seiler, and R. Ernstorfer, *Femtosecond electron diffraction data of black phosphorus*, Zenodo, https://doi.org/10.5281/zenodo.3723318 (2020).

[Zah20c] D. Zahn, F. Jakobs, W. Windsor, H. Seiler, T. Vasileiadis, T. A. Butcher, Y. Qi, D. Engel, U. Atxitia, J. Vorberger, and R. Ernstorfer, *Data for: Lattice dynamics and ultrafast energy flow between electrons, spins, and phonons in a 3d ferromagnet*, Rodare, http://doi.org/10.14278/rodare.501 (2020).

[Zah21a] D. Zahn, F. Jakobs, Y. W. Windsor, H. Seiler, T. Vasileiadis, T. A. Butcher, Y. Qi, D. Engel, U. Atxitia, J. Vorberger, and R. Ernstorfer, *Lattice dynamics and ultrafast energy flow between electrons, spins, and phonons in a 3d ferromagnet*, Phys. Rev. Research **3**, 023032 (2021).

[Zah21b] D. Zahn, F. Jakobs, H. Seiler, T. A. Butcher, D. Engel, J. Vorberger, U. Atxitia, Y. W. Windsor, and R. Ernstorfer, *Intrinsic energy flow in laser-excited 3d ferromagnets*, arXiv:2110.00525 (2021).

[Zah21c] D. Zahn, H. Seiler, Y. W. Windsor, and R. Ernstorfer, *Global fitting approach for time-resolved polycrystalline diffraction data*, Zenodo, https://doi.org/10.5281/zenodo.5618194 (2021).

[Zah21d] D. Zahn, H. Seiler, Y. W. Windsor, and R. Ernstorfer, *Ultrafast lattice dynamics and electron–phonon coupling in platinum extracted with a global fitting approach for time-resolved polycrystalline diffraction data*, Struct. Dyn. **8**, 064301 (2021).

[Zah21e] D. Zahn, Y. W. Windsor, H. Seiler, T. Vasileiadis, T. A. Butcher, Y. Qi, D. Engel, J. Vorberger, and R. Ernstorfer, *Femtosecond electron diffraction data of nickel*, Zenodo, https://doi.org/10.5281/zenodo.4575398 (2021).

[Zah22a] D. Zahn, T. A. Butcher, H. Seiler, R. Ernstorfer, and J. Vorberger, *Calculation of the electron-phonon coupling parameter and heat capacities from DFT results*, Zenodo, https://doi.org/10.5281/zenodo.5898090 (2022).

[Zah22b] D. Zahn, H. Seiler, D. Engel, Y. W. Windsor, and R. Ernstorfer, *Femtosecond electron diffraction data of iron and cobalt*, Zenodo, https://doi.org/10.5281/zenodo.5832990 (2022).

[Zam09] F. Zamponi, Z. Ansari, C. v. Korff Schmising, P. Rothhardt, N. Zhavoronkov, M. Woerner, T. Elsaesser, M. Bargheer, T. Trobitzsch-Ryll, and M. Haschke, *Femtosecond hard X-ray plasma sources with a kilohertz repetition rate*, Appl. Phys. A **96**, 51–58 (2009).

[Zei92] H. J. Zeiger, J. Vidal, T. K. Cheng, E. P. Ippen, G. Dresselhaus, and M. S. Dresselhaus, *Theory for displacive excitation of coherent phonons*, Phys. Rev. B **45**, 768–778 (1992).

[Zew06] A. H. Zewail, *4D ultrafast electron diffraction, crystallography and microscopy*, Annu. Rev. Phys. Chem. **57**, 65–103 (2006).

[ZH04]   B. Zink and F. Hellman, *Specific heat and thermal conductivity of low-stress amorphous Si–N membranes*, Solid State Commun. **129**, 199–204 (2004).

[Zha13]   W. Zhao, Z. Ghorannevis, L. Chu, M. Toh, C. Kloc, P.-H. Tan, and G. Eda, *Evolution of Electronic Structure in Atomically Thin Sheets of WS$_2$ and WSe$_2$*, ACS Nano **7**, 791–797 (2013).

[Zha20]   W. Zhang, P. Maldonado, Z. Jin, T. S. Seifert, J. Arabski, G. Schmerber, E. Beaurepaire, M. Bonn, T. Kampfrath, P. M. Oppeneer, and D. Turchinovich, *Ultrafast terahertz magnetometry*, Nat. Commun. **11**, 4247 (2020).

List of publications

Publications discussed in this thesis

D. Zahn, P.-N. Hildebrandt, T. Vasileiadis, Y. W. Windsor, Y. Qi, H. Seiler, and R. Ernstorfer, *Anisotropic Nonequilibrium Lattice Dynamics of Black Phosphorus*, Nano Lett. **20**, 3728-3733 (2020).

D. Zahn, F. Jakobs, Y. W. Windsor, H. Seiler, T. Vasileiadis, T. A. Butcher, Y. Qi, D. Engel, U. Atxitia, J. Vorberger, and R. Ernstorfer, *Lattice dynamics and ultrafast energy flow between electrons, spins, and phonons in a 3d ferromagnet*, Phys. Rev. Research **3**, 023032 (2021).

H. Seiler, D. Zahn, M. Zacharias, P.-N. Hildebrandt, T. Vasileiadis, Y. W. Windsor, Y. Qi, C. Carbogno, C. Draxl, R. Ernstorfer, and F. Caruso, *Accessing the Anisotropic Nonthermal Phonon Populations in Black Phosphorus*, Nano Lett. **21**, 6171-6178 (2021).

D. Zahn, H. Seiler, Y. W. Windsor, and R. Ernstorfer, *Ultrafast lattice dynamics and electron–phonon coupling in platinum extracted with a global fitting approach for time-resolved polycrystalline diffraction data*, Struct. Dyn. **8**, 064301 (2021).

D. Zahn, F. Jakobs, H. Seiler, T. A. Butcher, D. Engel, J. Vorberger, U. Atxitia, Y. W. Windsor, and R. Ernstorfer, *Intrinsic energy flow in laser-excited 3d ferromagnets*, Phys. Rev. Research (accepted, 2022).

Additional publications

L. Waldecker, R. Bertoni, H. Hübener, T. Brumme, T. Vasileiadis, D. Zahn, A. Rubio, and R. Ernstorfer, *Momentum-Resolved View of Electron-Phonon Coupling in Multilayer WSe$_2$*, Phys. Rev. Lett. **119**, 036803 (2017).

T. Vasileiadis, L. Waldecker, D. Foster, A. Da Silva, D. Zahn, R. Bertoni, R. E. Palmer, and R. Ernstorfer, *Ultrafast heat flow in heterostructures of Au nanoclusters on thin films: atomic disorder induced by hot electrons*, ACS Nano **12**, 7710-7720 (2018).

T. Vasileiadis, E. N. Skountzos, D. Foster, S. P. Coleman, D. Zahn, F. Krečinić, V. G. Mavrantzas, R. E. Palmer, and R. Ernstorfer, *Ultrafast rotational motions of supported nanoclusters probed by electron diffraction*, Nanoscale Horizons **4**, 1164-1173 (2019).

Y. W. Windsor, D. Zahn, R. Kamrla, J. Feldl, H. Seiler, C.-T. Chiang, M. Ramsteiner, W. Widdra, R. Ernstorfer, and L. Rettig, *Exchange-Striction Driven Ultrafast Nonthermal Lattice Dynamics in NiO*, Phys. Rev. Lett. **126**, 147202 (2021).

H. Seiler, M. Krynski, D. Zahn, S. Hammer, Y. W. Windsor, T. Vasileiadis, J. Pflaum, R. Ernstorfer, M. Rossi, and H. Schwoerer, *Nuclear dynamics of singlet exciton fission in pentacene single crystals*, Sci. Adv. **7**, eabg0869 (2021).

M. Zacharias, H. Seiler, F. Caruso, D. Zahn, F. Giustino, P. C Kelires, and R. Ernstorfer, *Efficient First-Principles Methodology for the Calculation of the All-Phonon Inelastic Scattering in Solids*, Phys. Rev. Lett. **127**, 207401 (2021).

M. Zacharias, H. Seiler, F. Caruso, D. Zahn, F. Giustino, P. C. Kelires, and R. Ernstorfer, *Multiphonon diffuse scattering in solids from first principles: Application to layered crystals and two-dimensional materials*, Phys. Rev. B **104**, 205109 (2021).

Y. W. Windsor, S. E. Lee, D. Zahn, V. Borisov, D. Thonig, K. Kliemt, A. Ernst, C. Schüßler-Langeheine, N. Pontius, U. Staub, C. Krellner, D. V. Vyalikh, O. Eriksson, and L. Rettig, *Exchange scaling of ultrafast angular momentum transfer in 4f antiferromagnets*, Nature Materials (accepted, 2022).

Published datasets

D. Zahn, P.-N. Hildebrandt, T. Vasileiadis, Y. W. Windsor, Y. Qi, H. Seiler, R. Ernstorfer, *Femtosecond electron diffraction data of black phosphorus*, Zenodo, https://doi.org/10.5281/zenodo.3723318 (2020).

D. Zahn, Y. W. Windsor, H. Seiler, T. Vasileiadis, T. A. Butcher, Y. Qi, D. Engel, J. Vorberger, R. Ernstorfer, *Femtosecond electron diffraction data of nickel*, Zenodo, https://doi.org/10.5281/zenodo.4575398 (2021).

D. Zahn, H. Seiler, Y. W. Windsor, and R. Ernstorfer, *Femtosecond electron diffraction data of platinum*, Zenodo, https://doi.org/10.5281/zenodo.5617246 (2021).

D. Zahn, H. Seiler, D. Engel, Y. W. Windsor, and R. Ernstorfer, *Femtosecond electron diffraction data of iron and cobalt*, Zenodo, https://doi.org/10.5281/zenodo.5832990 (2022).

Published code

D. Zahn, H. Seiler, Y. W. Windsor, and R. Ernstorfer, *Global fitting approach for time-resolved polycrystalline diffraction data*, Zenodo, https://doi.org/10.5281/zenodo.5618194 (2021).

D. Zahn, T. A. Butcher, H. Seiler, R. Ernstorfer, and J. Vorberger, *Calculation of the electron-phonon coupling parameter and heat capacities from DFT results*, Zenodo, https://doi.org/10.5281/zenodo.5898090 (2022).

Statement of contributions

Chapter 2

The time-resolved diffraction setup employed in this work was designed and built by Lutz Waldecker, Roman Bertoni, and Ralph Ernstorfer [WBE15]. Hélène Seiler, Thomas Vasileiadis, Yoav William Windsor, Victoria C. A. Taylor, Yingpeng Qi, and myself contributed to the further development, optimization, and maintenance of the setup. Jannik Malter wrote and maintained the measurement software employed in the experiment. During the course of this work, cryogenic cooling was added to the setup (described in Sec. 2.2.2), which was planned and designed by Y. W. Windsor, Sven Kubala, and Dieter Bauer. Y. W. Windsor and I optimized the sample environment further by reducing its size, adding a heater, and optimizing sample transfer. I also contributed to the design of the sample holders, in particular, I designed the side pumping sample holder and the cover plates for both sample holders. Furthermore, Y. W. Windsor and I installed and tested the cooling together, with help from T. Vasileiadis, H. Seiler, and Y. Qi.

Chapter 3

R. Ernstorfer had the idea for the project. The first time-resolved diffraction measurement on black phosphorus (not presented in this work) was recorded for the bachelor project of Patrick-Nigel Hildebrandt. This measurement was carried out by T. Vasileiadis, P.-N. Hildebrandt, and myself and the results are presented in Ref. [Hil18]. Following these initial results, additional measurements were recorded by H. Seiler, Y. Qi, and myself, which are presented in Sec. 3.3, 3.4, and 3.5. P.-N. Hildebrandt prepared the thin-film sample for these measurements. Y. W. Windsor developed a fitting routine to analyze Bragg reflections, which was employed throughout this chapter. P.-N. Hildebrandt contributed to the analysis of the experimental data presented in Sec. 3.3. I extended the analysis by employing the U-matrix formalism. Furthermore, I analyzed all data of Sec. 3.4. The results of Sec. 3.5 stem from a project led by H. Seiler. I took part in the experiment and actively contributed to the discussions. All DFT calculations presented in this chapter (which were also published in Ref. [Sei21]) were performed by Fabio Caruso (Christian-Albrechts-Universität zu Kiel) and Marios Zacharias (Cyprus University of Technology). M. Zacharias calculated the diffuse scattering images presented in Sec. 3.5.

Chapter 4

R. Ernstorfer had the idea for the project. I performed all measurements, with contributions from H. Seiler, Y. W. Windsor, T. Vasileiadis, V. C. A. Taylor, and Y. Qi. The DFT calculations on iron, cobalt, and nickel (which are presented in Chapter 2) were performed by Tim A. Butcher and Jan Vorberger (Helmholtz Zentrum Dresden-Rossenberg). J. Vorberger calculated TTM inputs from the DFT results and helped me to do the calculations myself (which I employed for iron and cobalt as well as in Chapter 5). The ASD simulations were performed by Florian Jakobs and Unai Atxitia (Freie Universität Berlin). Based on these results, I calculated the nonequilibrium energy flow dynamics and the comparison to the thermal case (Sec. 4.2.3.3 and 4.2.3.4). All samples were grown by Dieter Engel (Max-Born-Institut).

Chapter 5

Y. W. Windsor had the idea for the project. I recorded the measurements together with Y. W. Windsor, with contributions from H. Seiler and V. C. A. Taylor. Evangelos Papaioannou and Camillo Ballani (Martin-Luther Universität Halle-Wittenberg) performed the SQUID measurements. The DFT+U calculations on terbium and gadolinium (also presented in Chapter 2) were performed by Haichen Wang and Miguel Marques (Martin-Luther Universität Halle-Wittenberg). The tr-MOKE measurements were recorded together with Felix Steinbach and Martin Borchert (Max-Born-Institut), employing a MOKE setup at the Max-Born-Institut [Bor21]. The samples were grown by D. Engel (Max-Born-Institut).

Acknowledgments

I would like to thank everyone in the HEED team for the great atmosphere and team work, which made my PhD a very nice experience. I thank Ralph Ernstorfer for his support, for teaching me a lot, and for always being open for questions and discussions, while at the same time giving me a lot freedom to organize my projects and develop my scientific interests. Thanks to Thomas Vasileiadis for teaching me a lot about electron diffraction and about how to use the setup, and for always being available to answer my questions. I thank Yoav William Windsor for all the fun beam times, in which he taught me how to do diffraction experiments at synchrotrons, for sharing his enthusiasm about magnetism and science in general, and for teaching me a lot about magnetism and diffraction. I thank Hélène Seiler for all her help, particularly with the optics side of the experiment, and for lots of helpful discussions and encouragement. Thanks also to Victoria Taylor, Yingpeng Qi, Patrick-Nigel Hildebrandt, and Hyein Jung for their enthusiasm about electron diffraction and their work on the experiment. Thanks to Lutz Waldecker for answering my many questions about electron diffraction and the setup. Thanks to Jannik Malter for all his help with the software side of the experiment.

I would like to thank all collaborators for their contributions to this work and for the very nice work atmosphere: Florian Jakobs, Unai Atxitia, Jan Vorberger, Dieter Engel, Felix Steinbach, Martin Borchert, Tim Butcher, Haichen Wang, Miguel Marques, Evangelos Papaioannou, Camillo Ballani, Fabio Caruso, and Marios Zacharias.

I would like to thank Martin Wolf for providing the great environment at the PC department and for organizing many opportunities for scientific exchange and discussions.

I would like to thank Tobias Kampfrath for being the second supervisor of my PhD thesis and for answering my questions about magnetism. Thanks also to Laurenz Rettig for the possibility to participate in beamtimes and learn about resonant X-ray diffraction and for always being open for questions.

The CRC/Transregio 227 - Ultrafast Spin Dynamics offered lots of possibilities for scientific exchange and training, which was very helpful during my PhD. I would like to thank the TRR 227 iRTG coordinator Britta Anstötz, the CRC Spokesperson Martin Weinelt, the CRC Vice-Spokesperson Georg Woltersdorf, and all other people who made this CRC and the iRTG possible.

In addition, I would like to thank all technicians of the PC department: Sven Kubala, Daniel Wegkamp, Marcel Krenz, Albrecht Ropers, Holger Oertel, Dieter Bauer, Reinhard Franke, Harald Kirsch, and Patrick-Nigel Hildebrandt. Without them, our research would not be possible. The same is true for the mechanical workshop, the electronic workshop, the computer support group and the administration at FHI. In particular, I would like to thank Manuel Krüger, Ines Bressel, Daria Haberland, Manya Hettwer-Schleuthner, and Thorsten Nemes for their help.

I thank all members of the PC department for great discussions during the seminars and workshops and also for lots of fun after-work gatherings. Thank you all for the great atmosphere at the institute!

I would like to thank Christian for his support.

Finally, I would like to thank my family for their support and advice and for encouraging me to do what I enjoy.

Declaration of authorship

Name: Zahn

First name: Daniela

I declare to the Freie Universität Berlin that I have completed the submitted dissertation independently and without the use of sources and aids other than those indicated. The present thesis is free of plagiarism. I have marked as such all statements that are taken literally or in content from other writings. This dissertation has not been submitted in the same or similar form in any previous doctoral procedure.

I agree to have my thesis examined by a plagiarism examination software.